Light metal amides for hydrogen storage and ammonia decomposition.

Joshua William Makepeace

Lincoln College

A thesis submitted to the University of Oxford for the degree of Doctor of Philosophy

Inorganic Chemistry Laboratory

Trinity Term 2014

The work described in this thesis was carried out between October 2010 and September 2014, under the supervision of Professor William I.F. David and Professor Peter P. Edwards. All of the work is my own unless otherwise stated, and has not been submitted previously for any degree at this or any other University.

Joshua William Makepeace

October 2014

Acknowledgements

There are relatively few times when I have had the chance to write about the people who have helped me get to this point in life, the culmination of my formal education. I am grateful for the chance to do this here.

I firstly would like to thank my principal supervisor, Professor Bill David, who has not only put a significant amount of time and energy into reading and shaping this thesis, but has been a huge influence on my development as a scientist over the past four years. I have been in the fortunate position of having a supervisor who has challenged me academically, inspired me to be a more careful and thoughtful scientist, and who has shown consistent care for my well-being and interest in my personal development.

I would also like to thank my co-supervisor, Professor Pete Edwards, for his kind and welcoming approach, and for the support and advice he has offered me. Thanks also to Linda Webb for all of the work she does organising our group.

If Martin Jones had not answered the phone to me in August some four years ago, I may never have ended up down the path I now find myself following. I thank him very much for that, but significantly more so for the interest which he has shown in me and my research, spending many long nights collecting data in beamhalls.

I have benefitted immensely from the guidance, support and companionship of my colleagues. I would like to thank them all for being so helpful to me, but would take the opportunity to single a few of them out for special thanks.

Firstly, to Dr Sam Callear, who has patiently fielded questions from me, and helped me collect data on I11, NIMROD, the XRD instruments and the IGA^n. I have learnt a huge amount from her.

Dr Tom Wood and Dr Hazel Hunter have played a huge role in the development of the ammonia work in Chapter 5, generously helped with running the beamline during the collection of the ESRF data and also helped to proof-read this thesis. Tom is responsible for the basis of the Python programs which were used to generate the contour plots presented in this thesis.

My fellow DPhil students have been valued companions through this process, and good friends. Special thanks to Nazanin, Andrew Seel, Katie and Liang for their friendship.

There are some 7500 individual diffraction patterns associated with my doctoral work! Col-

lecting these data wouldn't have been possible without the various beamline and laboratory staff who have assisted me, particularly Mark Kibble, Richie Haynes, Chris Goodway, and Ron Smith at ISIS; Chiu Tang and Julia Parker at Diamond; and Christina Dräthen at the ESRF. Also, thanks to the central facilities (STFC, Diamond and the ESRF) for the provision of the experimental time, and to STFC Innovations, embodied by Kate Ronayne, for funding the ammonia decomposition work and the latter part of my studies.

I would like to thank the people at Lincoln College for being such a welcoming College community, and for providing travel grants to enable me to attend numerous conferences. I am most grateful for the administrative assistance and unfailing personal wramth of Carmella Elan-Gaston.

Of course, I wouldn't be here at Oxford at all if it were not for the generosity of the Rhodes Trust. I have greatly appreciated the guidance and support offered to me by the staff at Rhodes House, particularly Don Markwell and Mary Eaton. To receive the Rhodes Scholarship is a true honour and a life-changing experience.

While this thesis reflects of my academic life during these four years at Oxford, it wouldn't be what it is without the people who filled out the other aspects of my life. Thank you to all my friends in Oxford, particularly Sarah, Matt S, Rachel, Jess P and Ioanna for turning what seemed a hugely daunting and overwhelming place into my second home. To my housemates, Alice, Eva, Libby, Liz, Chris, Steph, Andrew, Howard, Laura and Dan, thankyou for being my family in Oxford. I am so thankful for the friendship, support and patience of all of my Australian friends, and particularly that of Akas, Faz, Will, Courtney, Amy, Rhys, George and Jack. Every time I see you it feels like I never left.

My wonderful blended family are such an important part of my life. Thank you to my brothers and sisters and their respective families for so many great times. Thank you to my Sydney family for welcoming me to stay so often, and to my grandma, Bar, for reminding me that I can only do my best, and nothing more. My aunt Grania and uncle Gavin have been my family in the UK, and have been so generous in allowing me to escape Oxford when I needed to. My parents, Mum, Dad, Terry and Janice, have been my bedrock — from speaking to me daily when I first arrived and was miserable, to patiently enduring long periods of sparse communication when I returned to normal! I am ever grateful for their love, support, friendship and care.

Andrew has patiently borne the brunt of all the stresses of this process, and I am very blessed to have such a wonderful, kind and caring companion in my life.

I am constantly reminded of the fact that, throughout my life, many things for which I am given the primary recognition are not solitary endeavours. The people above, and many more, have contributed greatly to my experience over the past four years. The fact that I couldn't have done this without them doesn't diminish my sense of achievement, it enriches it.

Thesis abstract

Hydrogen has long been touted as an alternative fuel which could form the basis of a sustainable energy system: the hydrogen economy. This thesis advances the application of light metal amide materials in the realisation of this transformative potential.

One of the most vexing technical challenges to the widespread adoption of hydrogen in transportation applications is its low volumetric energy density, which makes the storage of a sufficient amount of hydrogen in a vehicle very difficult. In their conventional application, light metal amides ($M(NH_2)_x$),where M is a Group I or II metal) have been promoted as a means of storing large quantities hydrogen in the solid state, significantly increasing this energy density. This thesis highlights the impressive characteristics of amide-based materials, primarily the facile nature of the reversibility of the hydrogen storage reaction, as a model for the development and optimisation of solid-state hydrogen stores.

The study of the relationship between the crystal structures of the relevant materials and their hydrogen storage properties through *in situ* X-ray and neutron powder diffraction measurements is reported for the lithium amide - lithium hydride (Li-N-H) hydrogen store. These investigations provide strong evidence for ionic mobility as the basis of reversible hydrogen storage in the Li-N-H system. The hydrogen storage and release reactions are seen to progress through a continuum of non-stoichiometric states, a transformation which is facilitated by its topotactic nature. The structural and energetic properties of these non-stoichiometric phases are reported, showing that they are intrinsically disordered and thermodynamically unstable relative to their parent structures. The study of the behaviour of the Li-N-H system is extended to many tens of hydrogenation-dehydrogenation cycles to examine practical performance, confirming the mechanism of capacity loss through the formation of parasitic lithium hydride, and showing that the addition of nitrogen improves the cycling lifetime of the system.

An unexplored aspect of light metal amide chemistry is also presented, where the hydrogen storage and release reactions of sodium amide are performed simultaneously. Together, these reactions effect the chemical decomposition of ammonia. Ammonia is a high energy density liquid hydrogen carrier which has been largely overlooked, partly due to the difficulty extracting its stored hydrogen. This work demonstrates a new method of ammonia decomposition which gives comparable performance to the expensive rare-metal catalysts which are currently used for the productions of high-purity hydrogen. A survey of the ammonia decomposition efficiency of a number of light metal amides and imides is presented, showing that it is not only amides which decompose into their constituent elements (such as sodium amide) which are active in ammonia decomposition, but also imide-forming amides. Indeed, imides and imide-forming amides are shown to be advantageous from the perspective of containing the catalyst material. Neutron diffraction and isotope exchange measurements provide some initial insights into the mechanism of reaction, identifying clear avenues for development of these systems, and inviting further discussion of the potential of ammonia as a sustainable energy vector.

Contents

List of Abbreviations

2Θ	scattering angle (diffraction)
a, b, c	crystallographic axis
BET	Brunauer-Emmett-Teller (surface area)
BEV	battery electric vehicles
cm^{-1}	wavenumber (inverse centimetre)
DSC	differential scanning calorimetry
e.s.d.	estimated standard deviation
h, k, l	Miller indices
HDI	Human Development Index
HFCV	hydrogen fuel cell vehicles
HHV	higher heating value
IDLH	Immediately Dangerous to Life and Health concentration
IEA	International Energy Agency
IGA	intelligent gravimetric analysis
IGA-MS	IGA coupled to a mass-spectrometer
IGA^n	intelligent gravimetric analysis for neutrons
IR	infrared
λ	wavelength
LHV	lower heating value
LPG	liquefied petroleum gas
m/z	mass-to-charge ratio
MAC	multi-analysing crystal
MOFs	metal–organic frameworks

NMR	nuclear nagnetic resonance
NPD	neutron powder diffraction
PEHV	petrol-electric hybrid vehicles
PEM	Proton Exchange Membrane
ppm	parts per million
PXRD	powder X-ray diffraction
R_{wp}	weighted profile R-value
RF	radio-frequency
rpm	revolutions per minute
sccm	standard cubic centimetres per minute,
TGA	thermogravimetric analysis
U.S. DoE	U.S. Department of Energy

Chapter 1

Introduction

> "...what we're going to have to do at a global scale is create a new system.
> And so, we need energy miracles."
> Bill Gates, "Innovating to zero!", 2010

1.1 The energy challenge

Hydrogen fuels our Universe. It is the fusion of hydrogen nuclei that provides light to the Universe and, from our Sun, the energy that drives the development and propagation of life on Earth. Humankind has stared at the stars, constellations of 'hydrogen light', since time immemorial. As we face the future, there is a poetic symmetry in the developing use of hydrogen as an energy vector (and indeed, a fusion energy source) that forms part of a sustainable energy system for future generations. This is a grand scientific and technological challenge with many facets. One of the principal challenges is the safe, effective, and efficient storage and release of hydrogen. This is the subject of this thesis.

The search for new energy vectors is prompted by the more general energy challenge. Here, we face the competing drivers of the desire to provide sufficient energy for a growing world population with the need to dramatically curb global greenhouse gas emissions. Our success in balancing these interests will likely be a determining factor in the future prosperity of humankind, and the health of many natural systems upon which we rely.

Since the beginning of the industrial revolution, technological development and wealth have been closely linked to the provision of electricity. This remains true today; a strong correlation

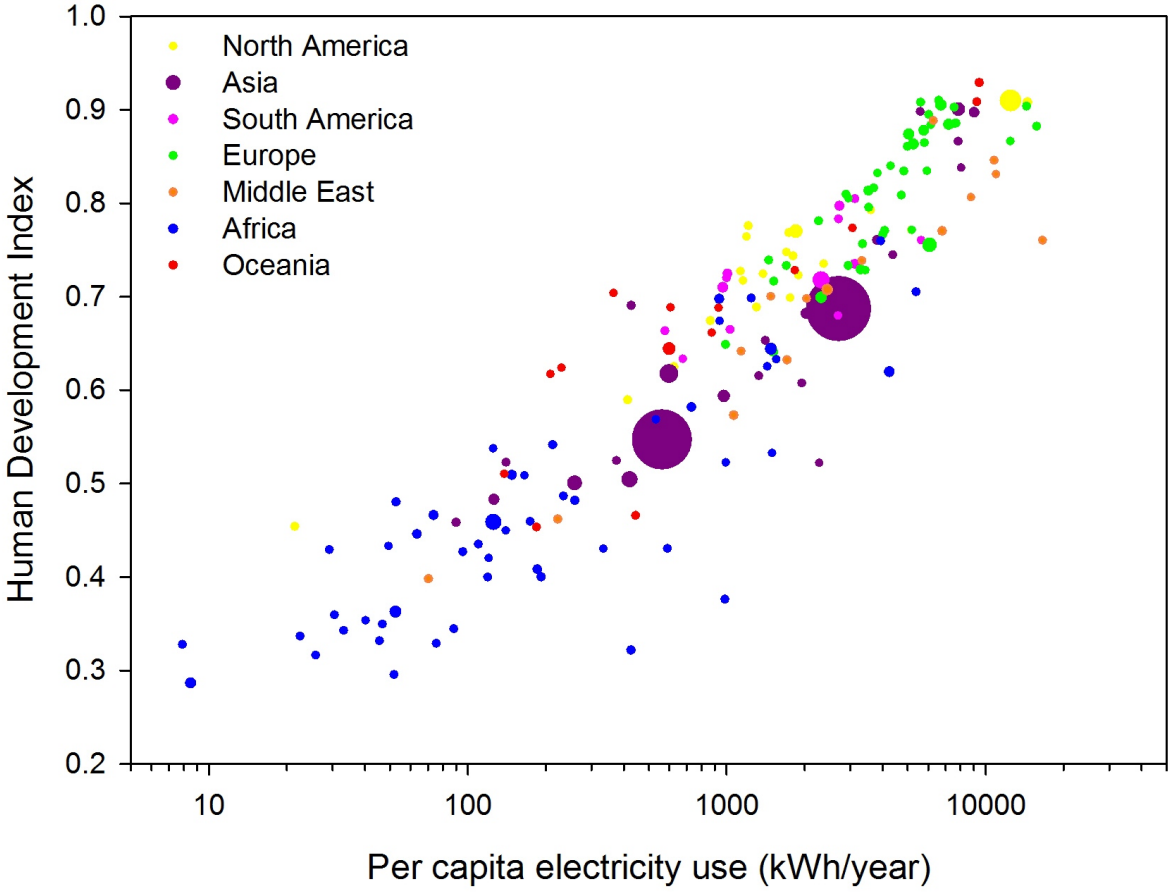

Figure 1.1: The relationship between the Human Development Index and average electricity use per capita for selected countries. Each country is represented by one point, with the size of the circle proportional to the population (ranging from a relative size of 1-8), and the colour of the circle corresponding to a broadly-defined geographic area.

between the Human Development Index (HDI)[1][1] and average electricity use per capita[2], as shown in Figure 1.1, clearly indicates that advances in human development are inexorably linked to increased access to, and use of, electricity[3].

It is clear from Figure 1.1 that for international development to continue, populations in countries with a low HDI will require increased provision of electricity. Indeed, the International Energy Agency (IEA) estimates that approximately 1.3 billion people currently live without any access to electricity[4]. In addition, 2.6 billion people rely on burning traditional biomass as their primary energy source; the replacement of this fuel with modern energy supplies is a significant

[1]The HDI combines life expectancy, mean and expected years in education, and Gross National Income per capita as a measure of national development. At the time of writing, plans had been announced by the United Nations to develop a Sustainable Human Development Index (http://hdr.undp.org/en/content/rio-20-beyond-gdp-measuring-future-we-want) to account for environmental sustainability in the development index.

priority in improving health outcomes for those people[4]. Set against the backdrop of a world population which is predicted to reach 9.6 billion by mid-century[5], it is highly probable that the forecasted one-third increase in world primary energy consumption by 2035 will be a substantial underestimate[6].

While the provision of this extra energy comes with a considerable set of logistical and economic challenges, the true test will be to reach this level of energy consumption in a sustainable manner. It is estimated that the energy sector currently accounts for between 66 and 83 % of global greenhouse gas emissions[4, 7]. If the hazardous consequences of climate change[8] are to be minimised, decarbonisation of the energy sector is paramount and essential. Thus, the development of a sustainable, decarbonised energy sector that can provide for the needs of a growing and developing human population is arguably the most fundamental and significant challenge of this century. In addressing this issue, scientific research, and particularly chemical research, must play a central role. Supplanting a set of remarkably energy-dense fuels which have been formed over millions of years and are utilised by mature technologies with extensive infrastructure is a daunting task. Indeed, with the current lack of strong international action to promote the move away from carbonaceous fuels, and if a sustainable energy system is ever to be realised, the scientific community is under increased pressure to generate alternatives which match or surpass the performance of conventional technology.

The storage of energy in a suitable vector is one of the crucial aspects of this challenge. The most obvious need for sustainable energy storage is in the area of transportation. Current vehicles are almost exclusively fuelled by petrol, diesel and natural gas. The greenhouse gas emissions from the combustion of these fuels constitute 22 % of global emissions[7], and a disproportionate percentage of these emissions are from industrialised countries. As more countries continue down the path of increased industrialisation, the global vehicle fleet will increase significantly, with the IEA predicting 800 million more cars on the road by 2050[6]. In addition to the reduction of transport-related emissions, the short- to medium-term storage of energy will become increasingly important in the broader context of a new energy system. If we are to meet the cuts in greenhouse gas emissions required to avoid significant climate change, renewable power supplies such as solar, wind, geothermal and marine power are likely to play a significant role in a future energy mix. Due to the inherent intermittency of these sources, very significant energy stores will be required

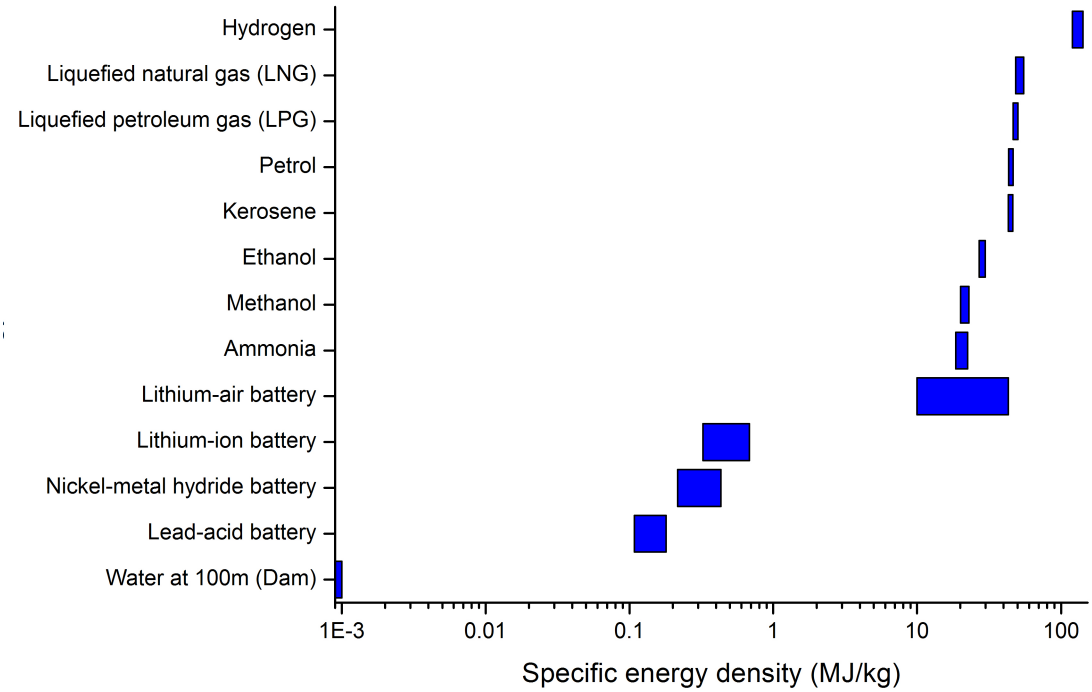

Figure 1.2: Specific gravimetric energy density of various energy storage methods. The range specified for battery methods represents the spread of commonly reported values (except the lithium-air battery, which represents the range of the theoretical maximum energy density. For chemical fuels, the ranges specified span the lower heating value (LHV) and higher heating value (HHV) of the fuel in question. The HHV includes the energy released from condensation of the water produced in the combustion reaction, whereas the LHV does not.

to be used as a buffer to balance the supply of power to the grid.

1.2 Hydrogen – promises and pitfalls

Chemical fuels are attractive energy vectors due to their high energy density relative to alternative methods such as batteries, compressed air and dam-based water storage (Figure 1.2). This energy density is of particular importance in transportation, where a large amount of energy must be stored in the vehicle in order to attain an acceptable driving range. Among the range of potential chemical fuels, hydrogen has been the subject of significant attention. Jules Verne presaged this interest in his 1874 novel "The Mysterious Island", where the character Cyrus states,

> " Yes, my friends, I believe that water will one day be employed as fuel, that hydrogen and oxygen which constitute it, used singly or together, will furnish an inexhaustible source of heat and light, of an intensity of which coal is not capable."

Verne captured two of the most attractive characteristics of hydrogen as a fuel. The oxidation of hydrogen, according to Equation 1.1, releases 120 $\mathrm{MJ\,kg^{-1}}$, approximately three times more energy than that released during the combustion of petrol, without the concomitant release of carbon dioxide. Furthermore, its use in a fuel cell offers significant efficiency gains over traditional internal combustion engines.

$$\mathrm{H_2 + O_2 \rightarrow H_2O} \tag{1.1}$$

Of course, hydrogen is not the only option which has been actively considered. Much has been made of comparisons of the various low-carbon transportation options: hydrogen fuel cell vehicles (HFCV), battery electric vehicles (BEV) and petrol-electric hybrid vehicles (PEHV). However, the most likely future scenario is one where a mixture of these technologies is present. BEV are optimal for short trips, but are limited in range by the battery weight and recharging times. Longer trips, and trips taken by heavy vehicles, currently constitute the bulk of the greenhouse gas emissions from transportation[9], and it is here that HFCV and PEHV are the more suitable replacement. Therefore, the development of chemical fuel alternatives is of significant importance to the overall goal of decarbonising transportation.

Despite the promise of hydrogen as a fuel, if it is to achieve widespread use as a sustainable energy vector, a number of technical challenges must be addressed. An idealised version of a hydrogen economy is shown in Figure 1.3. Technical challenges associated with each part of the system are summarised below, though the reader is pointed to a number of publications that address each more completely[10–15].

1.2.1 Hydrogen production

Although hydrogen is ubiquitous, on Earth it is almost exclusively found in combined chemical forms, making the cheap, efficient and sustainable production of hydrogen a requisite component of the new energy system. In the ideal conception of a 'hydrogen economy', hydrogen would be produced from water by electrolysis using either renewable electricity sources, thermolysis from waste heat generated by nuclear power stations, or via a sustainable thermochemical cycle. In this way, hydrogen would be a near zero emissions fuel. Despite electrolysis processes being relatively efficient (56–73 % system efficiency[14]), the electricity costs render hydrogen production in this

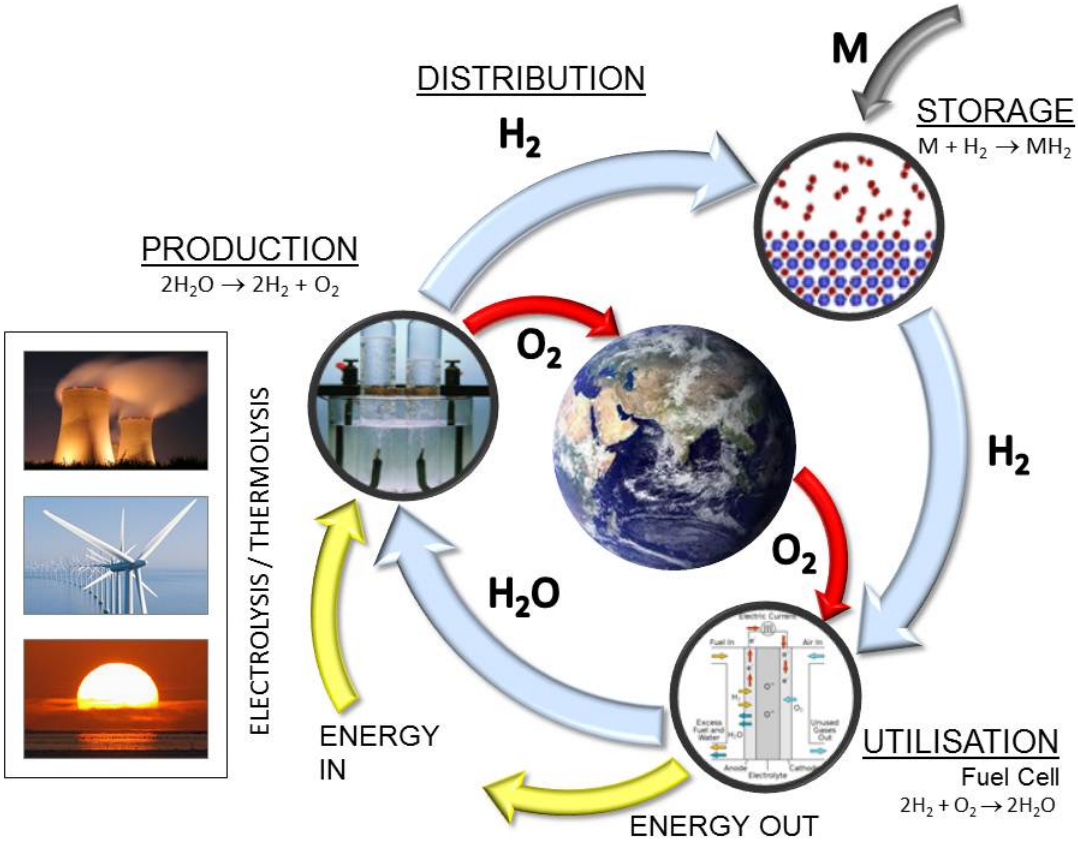

Figure 1.3: The hydrogen cycle, showing the four major technical components of the hydrogen economy. Ideally, hydrogen is synthesised from the electrolysis of water using renewable electricity. From there, the hydrogen is distributed to fuel stations, and stored onboard vehicles as a metal hydride (or equivalent). The hydrogen is delivered from the store for utilisation in a fuel cell to drive a vehicle, or extract energy for another purpose.

way uncompetitive when compared with production of hydrogen from fossil fuels[13]. As a result, the vast majority of current hydrogen production is by steam reformation of methane (Equation 1.2)[14].

$$CH_4 + 2H_2O \rightarrow 4H_2 + CO_2 \tag{1.2}$$

While the release of carbon dioxide in this synthesis method precludes methane reformation as a long-term solution to decarbonisation of the transport sector, it has been shown that switching to hydrogen produced from methane as a vehicular fuel does result in a significant decrease (around 50 %) in the greenhouse gas emissions relative to petrol[16]. As such, it may play an important bridging role until carbon pricing and/or technological advances make the production of hydrogen from water cost-competitive.

1.2.2 Distribution of hydrogen

As a gaseous fuel, the distribution requirements of hydrogen will require the development of a significantly different infrastructure to the current system for petrol distribution. The development of this infrastructure is complicated by the technical requirements for pressurised or liquefied hydrogen transportation and dispensation, and the embrittlement of various metals on long-term exposure to hydrogen. While these issues do not prevent the development of an effective hydrogen infrastructure, significant expenditure will be required to build and maintain it: a recent analysis estimates the construction of a hydrogen distribution and refuelling network for 1 million fuel cell vehicles across Europe by 2020 would cost approximately €3 billion[9]. Given the total active European road vehicle fleet is estimated at roughly 280 million vehicles, infrastructure to service a completely decarbonised transportation sector would require significantly higher levels of investment. Individual compressed hydrogen refuelling stations have been estimated to cost of the order of $3–5 million[17]. However, recent analysis has suggested that the costs associated with HFCV infrastructure (including retail outlets, production and distribution) are significantly lower than those for a similar roll-out of BEV[9].

1.2.3 Utilisation of hydrogen

The combination of hydrogen and oxygen to release energy, as described in Equation 1.1, can be achieved either via conventional combustion as with fossil fuels, or electrochemically using a fuel cell. Fuel cells are significantly more expensive than internal combustion engines, but remain the favoured technology for hydrogen utilisation due to the superior system efficiency which can be reached.

Fuel cells are a subset of galvanic electrochemical cells where the reactants are in continuous supply. For simplicity, here we will examine a Proton Exchange Membrane (PEM) fuel cell, which is the most extensively-researched type of fuel cell for transportation applications due to its compactness and low operating temperature. Other fuel cell varieties are more suited for different tasks, though they may yet find application in transportation, as will be discussed later. A PEM fuel cell consists of an anode and cathode which are usually made of platinum, separated by a proton conducting membrane electrolyte, and are connected by an external electrical circuit. Hydrogen is flowed across the anode, where is is decomposed into protons and electrons (Equation 1.3). The protons pass through the electrolyte, and the electrons pass through the electric circuit. They recombine to reduce oxygen to water at the cathode, as shown in Equation 1.4.

$$\mathrm{H_2}(g) \rightarrow 2\mathrm{H^+} + 2\mathrm{e^-} \tag{1.3}$$

$$\mathrm{O_2}(g) + 4\mathrm{H^+} + 4\mathrm{e^-} \rightarrow 2\mathrm{H_2O}(l) \tag{1.4}$$

PEM fuel cells operate at 80–120 °C, are quiet and have system efficiency values in the range of 40–60 % (compared to ~25 % for a conventional internal combustion engine). The two most significant issues with the use of PEM fuel cells are i) sensitivity to even low levels (parts per million, ppm) of contaminants, forcing very high purity hydrogen to be used, and ii) high cost. For large production volumes, almost half the cost of the fuel cell is related to the platinum catalyst[18]. In the last decade, significant progress has been made in reducing the amount of platinum used in PEM fuel cells, with the U.S. Department of Energy (U.S. DoE) claiming an 80 % reduction in the mass of platinum through their research program since 2005[19]. The clear benchmark is to reduce the level of platinum to the same as is found in existing vehicular catalytic converters, or to find cheaper and more abundant catalyst materials which are as effective as

platinum.

1.2.4 Hydrogen storage

The principal technical barrier to the uptake of hydrogen comes from the fact that the volumetric, not gravimetric, energy density is the most practical measure for the comparison of energy storage methods. By this metric, hydrogen, a gas under standard conditions, is approximately 3000 times less energy-dense than petrol. For transportation, therefore, the central issue becomes the discovery of a method of storing hydrogen onboard in a sufficiently dense manner to realise the driving range of modern vehicles. This is of the order of 500 km per tank of fuel, which equates to around 5 kg of hydrogen, or 55 m^3 of hydrogen gas. This challenge is the main subject of this thesis.

The density of hydrogen can obviously be increased by the simple liquefaction or compression of hydrogen gas. However, even when liquified at 20 K, hydrogen is still a factor of four less energy-dense than petrol. Liquefaction is an energy intensive process, requiring up to 30 % of the stored energy of the hydrogen. This, along with concerns about the loss of useable hydrogen from cryogenic tanks, has meant that liquid hydrogen has largely been passed over in favour of compressed hydrogen gas. Indeed, the majority of hydrogen vehicles scheduled for production are proceeding with pressurised hydrogen tanks. However, this method is not without its own drawbacks, as to achieve comparable range to petrol vehicles, 700 bar hydrogen tanks must be employed. While the energy costs associated with pressurisation to this level are not as high as they are for liquefaction, they do constitute a significant amount (10–20 %) of the stored energy of the fuel. Furthermore, the tank technology required to support such high pressures is bulky, expensive, and restricted in terms of the possible geometry of the tank. Despite rigorous safety testing, it is likely that high pressure hydrogen tanks will encounter some degree of resistance from the public based on perceived safety issues.

The combination of all of the above factors has led to a significant research effort aimed at discovering new ways of storing hydrogen that are advantageous compared with pressurised tanks. Much of this effort has focussed on the potential of solid-state hydrogen storage, where a solid material is used to bind hydrogen at high density under moderate conditions.

1.3 Solid-state hydrogen storage

Storing hydrogen in a solid requires a different set of considerations than compression, since there is now a bonding interaction between the hydrogen and the solid material. A successful materials approach to the storage of hydrogen must be grounded in the thermodynamics required for practical application. The most fundamental of these requirements is that the hydrogen has the potential to be *reversibly* stored under practical conditions. PEM fuel cell systems require hydrogen to be delivered at 3–12 bar, and the release of the stored hydrogen from the material should be achieved using only the waste heat from the fuel cell, which operates at approximately 85 °C[2]. Therefore, the change in Gibbs free energy (Equation 1.5) for the hydrogen storage and release equilibrium must be approximately zero under these conditions of temperature and pressure in order for both the forward and reverse reactions to be easily accessible.

$$\Delta G = \Delta H - T\Delta S \tag{1.5}$$

If we take a simple hydrogen storage and release equilibrium such as that shown in Equation 1.6, we can express the Gibbs free energy for that reaction in terms of the activities of the relevant chemical species, shown in Equation 1.7. This type of analysis holds for almost all varieties of hydrogen storage material; a small (but important) number of exceptions are discussed later.

$$\mathrm{MH}_{x(s)} \rightleftharpoons M_{(s)} + \frac{1}{2}x\mathrm{H}_{2(g)} \tag{1.6}$$

$$\ln \frac{(p_{\mathrm{H}_2})(a_M)}{a_{\mathrm{MHx}}} = \frac{\Delta S}{R} - \frac{\Delta H}{RT} \tag{1.7}$$

If we assume that the activities of the solid species, M and $\mathrm{MH_x}$, are unity, then the parameters which determine and describe the thermodynamic behaviour of the system are the change in enthalpy (ΔH), change in entropy (ΔS), hydrogen partial pressure (p_{H_2}), and the temperature of the reaction (T). The change in entropy for most hydrogen storage reactions is dominated by the entropy term for hydrogen gas ($S^o_{\mathrm{H}_2}$= 130 J mol^{-1} K^{-1}). Taking this into account, and considering a maximum working temperature of 85 °C to deliver a working pressure of ca. 5

[2]Higher temperatures of hydrogen release are possible, but would require a proportion of the energy produced by the fuel cell to heat up the hydrogen store. As such the further the operating temperature of the store is from 85 °C, the lower the system efficiency.

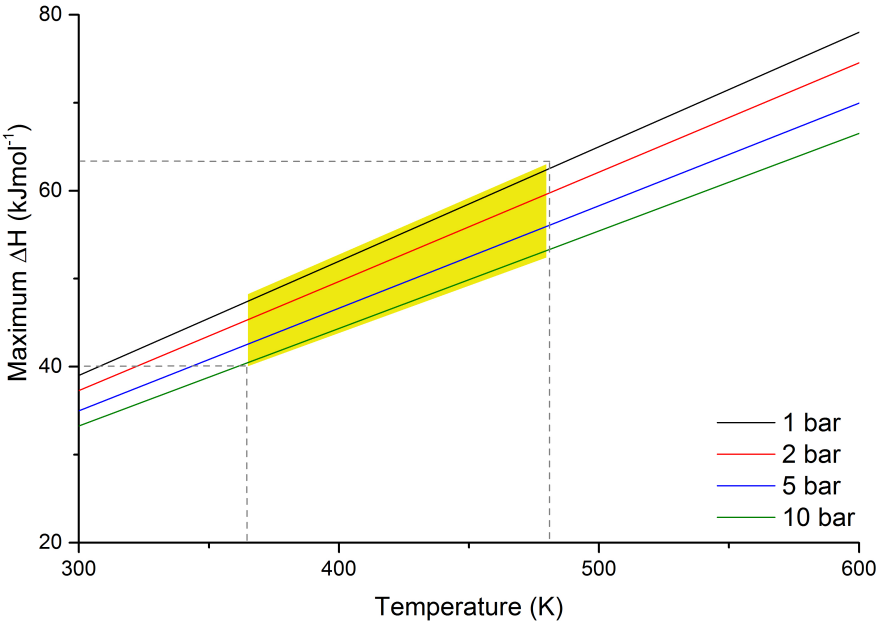

Figure 1.4: The relationship between the operating temperature of a hydrogen store and the maximum enthalpy of the hydrogen release reaction to delivery the required pressure of hydrogen at that temperature. The relationship is shown for a series of equilibrium hydrogen pressures.

bar, substitution into Equation 1.7 gives a maximum change in enthalpy of 41.7 $kJmol^{-1}$ for the desorption reaction. Of course, there is some flexibility in the operating parameters of the system. Figure 1.4 shows the relationship between working temperature and maximum enthalpy change for a selection of hydrogen output pressures, with a workable region for PEM fuel cell operation (80–200 °C) shown in yellow. These thermodynamic requirements constitute the first set of parametric constraints for an effective hydrogen storage material.

Of course, the requirements for a practical hydrogen store are more diverse than simply those which are dictated by thermodynamics. The U.S. and Japanese governments ha've been the major public drivers of the targets for practical use, which have guided research into solid-state hydrogen storage. In particular, the U.S. DoE has issued materials targets covering the various requirements for the delivery of hydrogen to a PEM fuel cell[20], covering the following areas:

- System (materials and associated technology) cost
- Gravimetric and volumetric hydrogen content (reversibly stored)
- Purity of the produced hydrogen flow
- Refuelling time

- Minimum and maximum operating temperature/pressure
- Minimum cycle lifetime
- On-board and "well to wheels" system efficiency
- Hydrogen delivery rates
- Start up and transient response times
- Safety (encompassing hydrogen loss, toxicity etc)

While the advantages of the targets in terms of their role in guiding the direction of hydrogen storage research are debatable, the categories do provide a useful means of comparing the various material classes. Of the list given by the U.S. DoE, gravimetric hydrogen density has been the central focus of the majority of recent hydrogen storage research, resulting in an extensive materials discovery program, uncovering new or hybrid materials with high hydrogen content. Figure 1.5 shows the volumetric and gravimetric hydrogen density of a selection of these materials, as well as some other important compounds (such as octane, water, ammonia, compressed hydrogen and liquid hydrogen) for comparative purposes. To provide a relatable measure, the density is expressed in terms of the mass or volume of material required for the storage of 5 kg of hydrogen, which is the approximate amount necessary for a 500 km car journey.

As can be seen in Figure 1.5, the different classes of hydrogen storage materials can principally be segregated on the basis of their hydrogen content. However, this graph only considers one of the relevant characteristics in the U.S. DoE list. As such, it is worth examining the properties of each class in more detail.

1.3.1 Porous materials

The simplest extension of compression or liquefaction using materials is to create some sort of porous material which can act as a hydrogen sponge (light blue materials in Figure 1.5). A variety of materials have been explored in this category, with the main classes being activated carbons and metal-organic frameworks (MOFs). The mechanism of hydrogen storage in these systems is based on physisorption, where the hydrogen molecule remains intact and is bonded to the surface via weak van der Waals type interactions with bond enthalpy values typically in the

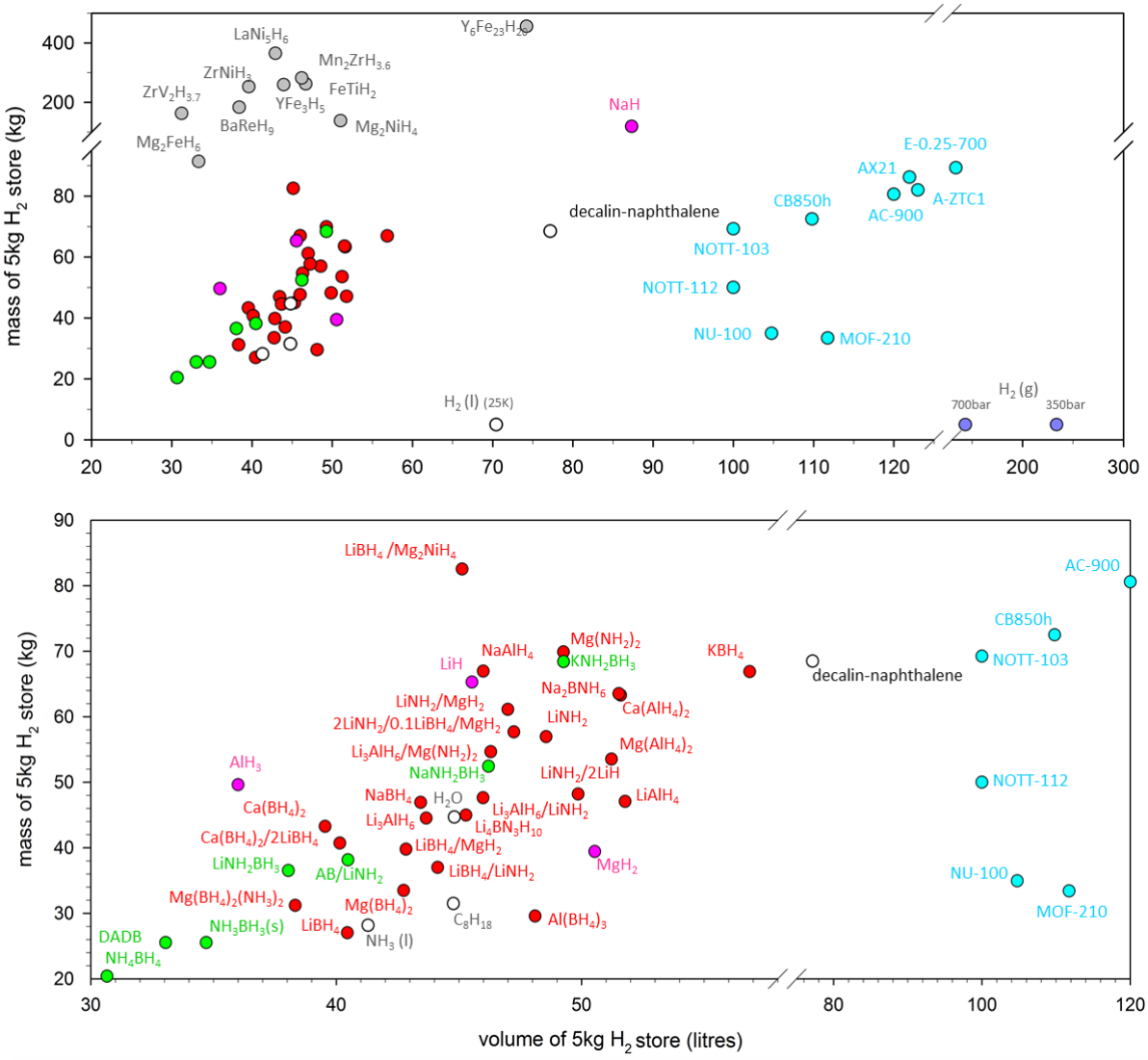

Figure 1.5: A plot of the volumetric and gravimetric hydrogen density values for selected materials, given in terms of the volume/mass of material required to store 5 kg of hydrogen. Note that these values reflect the total hydrogen content of the material, and as such do not give a complete description of the reversible hydrogen content. The top panel shows all of the materials, while the bottom panel is an enlarged view of the higher-density materials. The materials are sorted into various classes by colour. Dark blue is pure hydrogen, light blue are hydrogen sorbents (where the value represents the hydrogen density at 77 K at various hydrogen pressures, usually around 60 bar), magenta are alkali and alkaline earth hydrides, grey are transition/rare earth hydrides, red are complex hydrides, green are chemical hydrides, and white are other important hydrogen-containing materials. Packing fractions are not accounted for for solid materials in this plot. Adapted from Ref. [12] with permission from The Royal Society of Chemistry.

region of 5–10 kJ mol^{-1}. These weak bonds lead to highly reversible hydrogen storage but also result in very low hydrogen capacity (generally 0–1 wt%) at room temperature. As such, most sorbent materials only adsorb significant amounts of hydrogen at liquid nitrogen temperature under moderate to medium hydrogen pressure (10–100 bar). For this reason, sorbent materials can be thought of as providing a means to reduce the pressure of high pressure hydrogen storage and to reduce the boil off of hydrogen when compared to liquid hydrogen. The gas storage of these materials is well-correlated with their Brunauer–Emmett–Teller (BET) surface area, with an average increase in hydrogen uptake of around 1.5 wt% per 1000 m^2 g^{-1}. As can be seen in Figure 1.5, their volumetric hydrogen density lies somewhere between pressurised and liquid hydrogen. There have been no studies which suggest that the volumetric density of hydrogen in these systems will ever surpass that of liquid hydrogen, and thus, by this measure, porous materials are inferior to the other classes of hydrogen storage material.

Carbonaceous materials, specifically nanostructured carbons, were the first sorbents investigated for their hydrogen storage potential. They are attractive choices as they are generally low cost (certainly the starting materials are generally cheap), abundant, can be synthesised in a range of morphologies and possess good chemical and cycling stability. A plethora of these materials have been investigated, including activated carbons, single- and multi-walled carbon nanotubes, graphite nanofibers[21] and even exotic materials such as carbon nanohorns[22]. Zeolitic carbons, produced by templating with a zeolite[23, 24], and superactivated carbons [24, 25] have also shown particular promise. However, the field has suffered from a lack of consistency in experimental results, with some of the most promising results[21, 26, 27] failing to be replicated in subsequent investigations, and even being disproved[28]. It is clear that synthetic and analytical methodology, the quality of the adsorption gas and even inconsistency in the terminology used for hydrogen uptake have had significant impacts on the precision of results reported for hydrogen uptake in supposedly identical materials.

Despite these inconsistencies, the field is certainly not without promise. In the effort to increase hydrogen uptake at temperatures above 77 K, the introduction of metal centres into carbonaceous materials has shown favourable results — indeed, there are suggestions that some of the spuriously high results for hydrogen capacity in carbonaceous materials are due to contaminant metal from the synthesis process. The effect of the metal centres is essentially to create

a hybrid physisorption-chemisorption system, increasing the enthalpy of the hydrogen bonding, and thus increasing its stored hydrogen content at a given temperature. It has also been suggested that the presence of metal centres results in 'spillover' of dissociated hydrogen from the metal centre into the carbon network, a mechanism for enhanced hydrogen adsorption. This concept has been the subject of significant debate [29–31], and will not be addressed further here.

A logical progression from the doping of carbonaceous materials with metals is to construct a porous system where the metal centres are an integral part of the structure: MOFs. The first report of hydrogen storage in a MOF was by the Yaghi group in 2003[32]. MOFs are attractive research materials due to the vast number of possible frameworks which can be generated, the high degree of control over the chemistry and porosity of the materials, and their generally high degree of crystallinity. These characteristics seem to reduce the degree of uncertainty associated with hydrogen storage measurements, though consistency in synthetic methodology remains an important factor in the reproducibility of results in these systems[33]. Due to the chemical flexibility of these systems, a huge number of MOFs have been synthesised and investigated for their hydrogen storage potential; these results have been reviewed in significant detail[34–36]. The most common approaches to increasing the hydrogen storage capacity in MOFs are similar to those used for carbonaceous materials: higher surface area, larger pore size, and increased bonding enthalpy. These strategies have had a significant degree of success — some representative examples of each of these strategies taken to their extreme are shown in Table 1.1.

The combination of very high surface areas and large pore volumes in PCN-610, MOF-210 and NOTT-112 results in impressive gravimetric hydrogen density values, comparable to that of petrol, at elevated hydrogen pressure. At low pressure, hydrogen content does not have a good correlation with surface area beyond approximately 2000 $m^2\,g^{-1}$[34]. While there are indications that surface areas in excess of 14,000 $m^2\,g^{-1}$ are theoretically accesible for MOF structures[44], the difficulties in synthesising stable, non-interpenetrated structures with these surface areas (and the desired larger pore sizes) should not be underestimated. Given these difficulties, post-synthetic modification of MOF structures have been a popular method for attempting to improve their hydrogen storage characteristics. Incorporation of lithium ions into MOFs via exchange with organic cations[45] or the formation of lithium alkoxides by reaction with pendant hydroxl

Table 1.1: Surface area, pore volume, hydrogen storage capacity and enthalpy of adsorption for selected MOFs.

Material	Short name	BET surface area ($m^2\,g^{-1}$)	Pore volume ($cm^3\,g^{-1}$)	H_2 uptake (excess/total, wt%) at 77 K, pressure (bar)	ΔH_{ads} ($kJ\,mol^{-1}$)	Ref
Cu_3(ttei)	PCN-610 NU-100	6143	2.82	9.05/14.1, 56	6.1	[37]
$Zn_4O(bte)_{4/3}$(bpdc)	MOF-210	6240	3.60	7.92/15.0, 50	-	[38]
Cu_2(bbtei)	NOTT-112	3800	1.69	7.07/9.0, 35	5.6	[39]
$Co_4(H_2O)_4(mtb)_2$	SNU-15'	356*	0.74	0.74, 1	15.1	[40]
$Cd_5(tz)_9(NO_3)_3$		310	0.75	0.75, 1	13.5	[41]
Ni_2(dhtp)	CPO-27-Ni	1218	0.47	2.10, 1	12.9	[42, 43]

ttei = 5,5',5"-(((benzene-1,3,5-triyltris(ethyne-2, 1-diyl))tris(benzene-4,1-diyl))tris-(ethyne-2, 1-diyl))triisophthalate, bte = 4,4',4"-[benzene-1,3,5-triyl-tris(ethyne-2, 1-diyl)]tribenzoate, bpdc = 4,4'-biphenyldicarboxylate, bbtei = 5,5',5"-(benzene-1,3,5-triyltris(benzene-4,1-diyl))triisophthalate, mtb = methanetetrabenzoate, tz = 3,5-bis(trifluoromethyl)-1,2,4-triazolate, dhtp = 2,5-dihydroxyterephthalate, *Langmuir surface area

groups[46] has been remarkably effective in increasing the hydrogen storage content of a number of MOFs. The use of bulky ligand or counterion groups has been shown to act as a kind of gate on the pores of some MOFs, resulting in hysteresis in the adsorption-desorption behaviour of the MOF. Variation in the size of such cations in the channels of NOTT-200 has been shown to tune the hysteretic behaviour of the hydrogen storage and release reactions[47].

As with carbonaceous materials, an effort to increase the enthalpy of adsorption of hydrogen on MOFs, and thus reduce the need for expensive and bulky cooling systems, has been prominent in the literature in this field. In MOFs such as SNU-15' and CPO-27-Ni, the introduction of coordinatively-unsaturated (or 'open') metal centres in the structure has been successful in engineering the largest adorption enthalpy values yet recorded for MOFs[40, 43]. Indeed, the inclusion of open metal centres has been shown to generally increase hydrogen storage content relative to the closest analogue without an open metal centre. In an alternative approach, MOFs such as $Cd_5(tz)_9(NO_3)_3$ achieve a similar increase in the adsorption enthalpy through the inclusion of electron rich groups in the organic linker species, which can also bind to hydrogen. Further increases will be needed; it has been estimated that a hydrogen adsorption enthalpy closer

to 20 kJ mol^{-1} is optimal for the practical requirement of a vehicular storage system operating at room temperature, charging at 120 bar and delivering hydrogen at 1.5 bar[48]. Currently, the highest enthalpies of adsorption have been achieved by systems with relatively small surface areas and pore volumes, and thus low hydrogen density.

It seems that porous materials will always be restricted to a lower volumetric density than that demanded by the U.S. DoE targets. However, their facile reversibility may yet prove sufficiently attractive compared with 700 bar tanks if a system can be synthesised which combines very high surface area (and/or pore volume) with an enthalpy of hydrogen adsorption in the region of 20 kJ mol^{-1} . Alternatively, porous materials may be considered as a suitable method of raising the operating temperature of cryogenic hydrogen storage systems, reducing boil off due to their endothermic desorption. In these scenarios, porous materials could be a suitable compromise candidate for vehicular hydrogen storage.

1.3.2 Simple metal hydrides

The alternative approach to physisorption of hydrogen onto the surface of a material is the chemisorption of hydrogen at the surface and subsequent diffusion into the bulk of the material resulting in the formation of a metal hydride. A generalised reaction for the chemisorption of hydrogen into a metal is shown in Equation 1.8.

$$M + H_2 \rightarrow MH_2 \tag{1.8}$$

The simple binary (AH_x) and ternary ($A_mB_nH_x$) metal hydrides are the family of compounds which sparked interest in solid-state hydrogen storage (magenta and grey data points in Figure 1.5, respectively). Particularly well-known examples include a number of transition metal hydrides, including lanthanum-nickel hydride ($LaNi_5H_6$), palladium hydride ($PdH_{0.8}$) and iron-titanium hydride ($FeTiH_2$), renowned for their high volumetric hydrogen density and facile reaction kinetics. The ease with which hydrogen is stored and released in these materials is due to facile hydrogen dissociation at the metal surface, and the fact that the hydrogen occupies interstitial sites in the crystal structures. This renders the hydrogenation and dehydrogenation reactions essentially topotactic, lowering the energetic barriers to reaction. They also display impressively high volumetric hydrogen density. Unfortunately, from a gravimetric perspective,

hundreds of kilograms of metal would be required to store a sufficient quantity of hydrogen for vehicular use, rendering them an impractical choice for this purpose. Complex transition metal alloys such as $Ti_{25}V_{50}Cr_{20}Mo_5$ have been considered as additions to high pressure hydrogen storage tanks to improve the volumetric hydrogen density, and thus lower the pressure required[49] in a similar way to that described for porous materials. However, commercial production of hydrogen vehicles containing high-pressure tanks is currently proceeding without the presence of a metal hydride[50].

Binary metal hydrides based on early period Group I-III metals have much higher gravimetric hydrogen density values than transition metal hydrides. However, these hydrides, which include species such as lithium hydride (LiH), sodium hydride (NaH) and calcium hydride (CaH_2), are generally very stable, and only release hydrogen at temperatures far in excess of the preferrred range for PEM fuel cell vehicles. Beryllium hydride (BeH_2) has a lower decomposition temperature but is extremely toxic. Only two of these binary hydrides continue to be the subject of extensive research efforts, and are considered as possible candidates for vehicular hydrogen storage: aluminium hydride (alane, AlH_3) and magnesium hydride (MgH_2).

Alane is a tantalising hydrogen storage candidate due to its high hydrogen content (10.1 wt%, 138.9 $kg\,m^{-3}$), low cost, and low hydrogen desorption temperature (around 100 °C). The decomposition of alane to aluminium is exothermic, and therefore the hydride is only kinetically stable. While this instability results in a low decomposition temperature, it also means that the reverse reaction, the hydrogenation of aluminium, is very difficult, requiring 28 kbar of hydrogen at 300 °C. Indeed, the hydrogenation must be performed in solution such that the hydrogenation is thermodynamically feasible. Astounding improvements in these reaction conditions would be required for alane to be viable for on-board hydrogen storage applications.

Magnesium hydride contains 7.6 wt% hydrogen, is cheap, abundant, non-toxic and easy to prepare. The main drawbacks in its use are that the temperature of dehydrogenation is quite high (in excess of 300 °C), and the kinetics of both the storage and release of hydrogen are prohibitively slow. The analogy of the topotactic reactions in the transition metal hydrides can be used in order to understand why this is so: magnesium adopts a close-packed hexagonal array under standard conditions (Figure 1.6a), while its hydride adopts the rutile structure (Figure 1.6b). This effect, along with the lesser ability of magnesium to dissociate hydrogen, means that

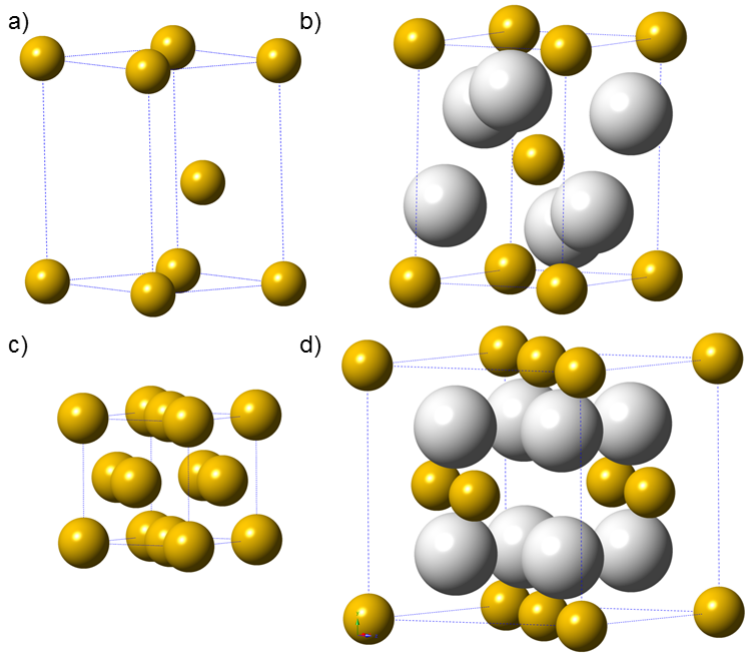

Figure 1.6: The crystal structures of low pressure phases a) α-Mg and b) α-MgH_2 compared with c) a theoretical cubic Mg structure and d) high pressure phase β-MgH_2. Magnesium atoms are shown in orange, with hydrogen atoms in grey.

the hydrogenation and dehydrogenation reactions for the Mg-MgH_2 system require significantly elevated temperatures compared with the transition metal hydrides mentioned earlier.

Traditional routes to improved kinetics have proved successful in the magnesium hydride system; nanosizing of the hydride particles, generally achieved by high-energy ball milling, has been shown to reduce the activation energy for dehydrogenation. Indeed, the milling is essential in order for complete reaction to be observed. Doping with transition metals and their oxides has proven a successful strategy in futher improving the hydrogen absorption kinetics [51–53], with the additives thought to assist with the dissociation of hydrogen during chemisorption.

In addition to these traditional methods for improving the kinetics, there have been efforts to modify the thermodynamics of the reaction by alloying the magnesium with other metals in order to create a topotactic hydrogenation-dehydrogenation reaction scheme. Magnesium hydride is known to adopt a cubic structure at elevated pressure (Figure 1.6d), so if alloying could cause the magnesium to adopt a cubic type structure (Figure 1.6c) and stabilise cubic magnesium hydride, then a topotactic transformation could occur.

This strategy has been employed successfully with the synthesis of Mg_7MH_x compounds,

where M is titanium, vanadium, niobium, tantalum, zirconium and hafnium[54]. These materials adopt a face-centred cubic structure, stabilising the high-pressure form of magnesium hydride and, as expected their hydrogen emission occurs up to 190 °C lower than that of pure magnesium. The zirconium analogue maintains the cubic structure in the dehydrogenated state, giving the desired topotactic transition[55]. However, these alloys only release approximately half the hydrogen content of magnesium hydride, and require gigapascal pressure obtained in a diamond anvil cell for their synthesis, which is not practical on the large scale.

Despite the advances made, the restrictions imposed by the slow kinetics of hydrogen storage and release in these systems mean that it is likely that the use of magnesium hydride as a hydrogen store will be confined to stationary applications. In this area, it has already found commercial application for use in industry processes which only require low pressure hydrogen, where storage in magnesium hydride removes the need for expensive compression equipment[56].

1.3.3 Complex and chemical metal hydrides

Interest in the use of solid-state hydrides for vehicular hydrogen storage was revitalised by the work of Schwickardi and Bogdanovic[57], who showed that complex metal hydrides (and specifically, sodium aluminium hydride — sodium alanate) were viable high-density hydrogen stores. In this discussion, complex hydrides should be taken to mean that the hydrogen is chemically bonded to an element (or multiple elements) to form a complex anion (or anions), which itself forms an ionic bond with one or more cations. Three complex anions have been the principal focus of complex hydride hydrogen storage research: amide (NH_2^-), alanate (AlH_4^-) and borohydride (BH_4^-). It is worth noting here the innacuracy of the term 'hydride' as applied to the amide anion, where the hydrogen atoms are not hydridic. However, the widely-used convention of referring to them as commplex hydrides will be used in this thesis. The majority of complex hydrides (shown in red in Figure 1.5) investigated for hydrogen storage consist of one of these anion types bound to an alkali or alkaline earth metal cation, although more exotic species have also been investigated.

The use of complex hydrides is advantageous as a lightweight Group I or II metal can store significantly more hydrogen in a complex hydride than the simple hydride. However, this additional hydrogen content comes at a cost: the enhanced chemical stability of the covalent bonds of

the complex anion often results in very high decomposition temperatures Additionally, the fact that the anions are molecular species means that in some cases complex hydrides are susceptible to the formation of gaseous byproducts which can contaminate the hydrogen gas stream.

Amide-based complex hydrides are the main subject of this thesis, and will be discussed in more detail in Section 1.4. Hydrogen release from amides is usually facilitated by mixing the amide with a metal hydride, which together decompose upon heating to form the metal imide with the release of hydrogen (Equation 1.9).

$$MNH_2 + MH \rightarrow M_2NH + H_2 \tag{1.9}$$

Alkali metal alanates usually follow the two-step decomposition mechanism outlined in Equations 1.10-1.11, forming the metal hydride and aluminium via a hexa-alanate species. Alkaline earth metal alanates usually form the same products, though often by different reaction mechanisms. Alanates are attractive because, unlike other complex hydrides, they do not give off other gaseous byproducts, releasing a pure hydrogen stream similar to that of the simple hydrides.

$$MAlH_4 \rightarrow \frac{1}{3}M_3AlH_6 + \frac{2}{3}Al + H_2 \tag{1.10}$$

$$M_3AlH_6 \rightarrow 3MH + Al + \frac{3}{2}H_2 \tag{1.11}$$

The pioneering work of Schwickardi and Bogdanovic showed that sodium alanate doped with a small amount of titanium (III) chloride could reversibly store 4.5 wt% hydrogen under moderate conditions; this was a significant advance on the gravimetric hydrogen capacity of traditional transition metal hydrides. Although many alanates have been studied since [10, 11], sodium alanate remains the best performing material. Lithium alanate, for example, releases hydrogen at relatively low temperatures, but is not easily reversible.

As with many complex hydrides, one of the main challenges facing the use of sodium alanate is to increase the reaction kinetics, lowering the required temperature of operation. Many metal additives have been tested on sodium alanate, but none have surpassed the activity of titanium-based additives[58–65]. Titanium-catalysed systems have been shown to give a stable hydrogen content of approximately 4 wt% over hundreds of cycles[66], and have even been scaled up into

prototype fuel tanks[67–69]. Although the system hydrogen storage capacities reported for these tanks are only around 2 wt%, far lower than the U.S. DoE target levels, sodium alanate is the material which has come closest to commercial application, and the construction of a functioning prototype is an admirable achievement.

Borohydrides, which possess some of the highest hydrogen densities among the complex metal hydrides, display more diverse decomposition pathways than the alanates and amides. Alkali metal borohydrides decompose according to Equation 1.12 or 1.13, while alkaline earth metal borohydrides can follow analogous paths, or decompose to the metal hydride and metal hexaboride[10].

$$\mathrm{MBH_4} \rightarrow \mathrm{MH} + \mathrm{B} + \frac{3}{2}\mathrm{H_2} \tag{1.12}$$

$$\mathrm{MBH_4} \rightarrow \mathrm{MB} + 2\mathrm{H_2} \tag{1.13}$$

The alkali metal borohydrides typically decompose at temperatures far in excess of the PEM fuel cell operating temperatures, and are very difficult to rehydrogenate. The alkaline earth metal borohydrides, however, have attracted a significant amount of research interest. Magnesium borohydride, in particular, decomposes at more moderate temperatures (onset around 330 °C) to release up to 14 wt% of hydrogen[70], with calcium borohydride releasing around 9 wt% [11]. The decomposition of magnesium borohydride has been the subject of some discussion, with the mechanism thought to involve the formation of a range of polyborane species[71]. The formation of these species may explain the fact that, despite favourable thermodynamics, magnesium borohydride is still very difficult to rehydrogenate.

Almost all of the complex metal hydrides share the need to lower the temperature of hydrogen release. A few different strategies have been employed to achieve this in addition to the normal approaches of particle size reduction and doping with transition metals and their salts. Generally, the release of hydrogen from a complex hydride requires the break-up of the complex anion. Thus, being able to reduce the strength of the X–H bonds in the anion is an obvious way of trying to reduce the temperature required for hydrogen release. Indeed, partial substitution of fluorine for hydrogen in the sodium alanate system results in a decrease in the decomposition temperature,

albeit with an associated drop in the hydrogen storage density[72].

The stability of the complex metal hydride is also related to the bonding between the cation and the complex anion; changing to a metal cation with higher electronegativity weakens the ionic bond between the metal and the complex anion, destabilising the structure[73, 74]. This logic has been used to target mixed metal borohydrides and alanates with more favourable decomposition properties, with some success in species such as $LiK(BH_4)_2$ and mixed lithium-potassium alanates[75, 76].

Yet another strategy to lower the decomposition temperature of the complex hydrides has arisen from consideration of the charge distribution on the complex hydrides. The hydrogen atoms in the amide ion carry partial positive charges. However, for alanates and borohydrides, bonding to the more electropositive aluminium and boron atoms results in a partial negative charge on the hydrogen atoms. It was rationalised that the formation of complex metal hydrides with mixed anions would result in lower hydrogen release temperatures due to the energetically favourable combination of hydridic and protic hydrogen between the two complex anions, the so-called '$\delta^+ - \delta^-$' mechanism. This concept has been borne out in the synthesis of various mixed amide-borohydrides and amide-alanates, which tend to show reduced temperatures of dehydrogenation[77–82], but do not address the issues associated with reversibility.

The '$\delta^+ - \delta^-$' mechanism underpins the remaining class of solid-state hydrogen store discussed in this thesis: the chemical hydrides (shown in green in Figure 1.5). Here, we use David's definition of the chemical hydride as a hydrogen-containing compound which also contains "two or more chemically distinct non-hydrogen atoms where some of these atoms form bonds with one another"[12]. This definition encompasses the metal amide-borohydrides described above, along with ammonia borane and metal amidoboranes. Ammonia borane, NH_3BH_3, combines protic and hydridic hydrogen atoms in a single molecule. The '$\delta^+ - \delta^-$' dihydrogen bonds formed between these hydrogen atoms are crucial in explaining why ammonia borane is solid at room temperature. Its hydrogen content is impressive: almost 20 wt% and 145 $kg\,m^{-3}$. It releases hydrogen in multiple stages, with 13 wt% released by 150 °C according to Equations 1.14 and 1.15). The release of such a large amount of hydrogen at temperatures close to the target range has fuelled much research into ammonia borane and its related compounds.

$$NH_3BH_3 \rightarrow [NH_2BH_2]_n + nH_2 \tag{1.14}$$

$$[NH_2BH_{2n}] \rightarrow [NHBH]_n + nH_2 \tag{1.15}$$

Unfortunately, small amounts of ammonia and borazine contaminate the hydrogen released from ammonia borane, species which would cause irreparable damage to low temperature PEM fuel cells. Replacement of one of the N–H hydrogens with an alkali metal ion to form an amidoborane (MNH_2BH_3, M = Li, Na, K), reduces the hydrogen capacity, but improves the kinetics of the hydrogen release and prevents the formation of borazine[83, 84].

Despite these generally positive characteristics, the now-familiar refrain must be invoked for the aforementioned chemical hydrides: none of these materials exhibit facile reversibility.

1.3.4 Elusive reversibility

Despite the impressive quantities of hydrogen contained within complex and chemical hydrides, the amount of hydrogen which can be reversibly stored under conditions which might be acceptable for on-board hydrogen refuelling is generally very low. To illustrate this point, Figure 1.7 shows both the hydrogen storage content of a selected range of hydrogen storage materials and their reported reversible hydrogen storage content. Even with the generous definition of 'reversible hydrogen content' used here (hydrogenation temperatures between -196 °C and 400 °C, pressure up to 150 bar, and no requirement of fast hydrogenation kinetics), most of the high-capacity hydrogen stores show very little potential for on-board regeneration.

Indeed, none of the chemical hydrides have been shown to be reversible except in the case of the use of long exposure to 10 bar of hydrazine and liquid ammonia[85–87]. These kinds of procedures would require specialist regeneration undertaken in chemical factories, rather than refuelling at a hydrogen fuel station. The difficulties regenerating these materials comes from the fact that the decomposition of the ammonia borane family results in the formation of polymeric B–N species, and the hydrogenation of these B–N bonds is very difficult. Similar chemical regeneration procedures are required for lithium alanate[88–90] and alane[75] due to their exothermic dehydrogenation reactions, which makes rehydrogenation of their solid decomposition products

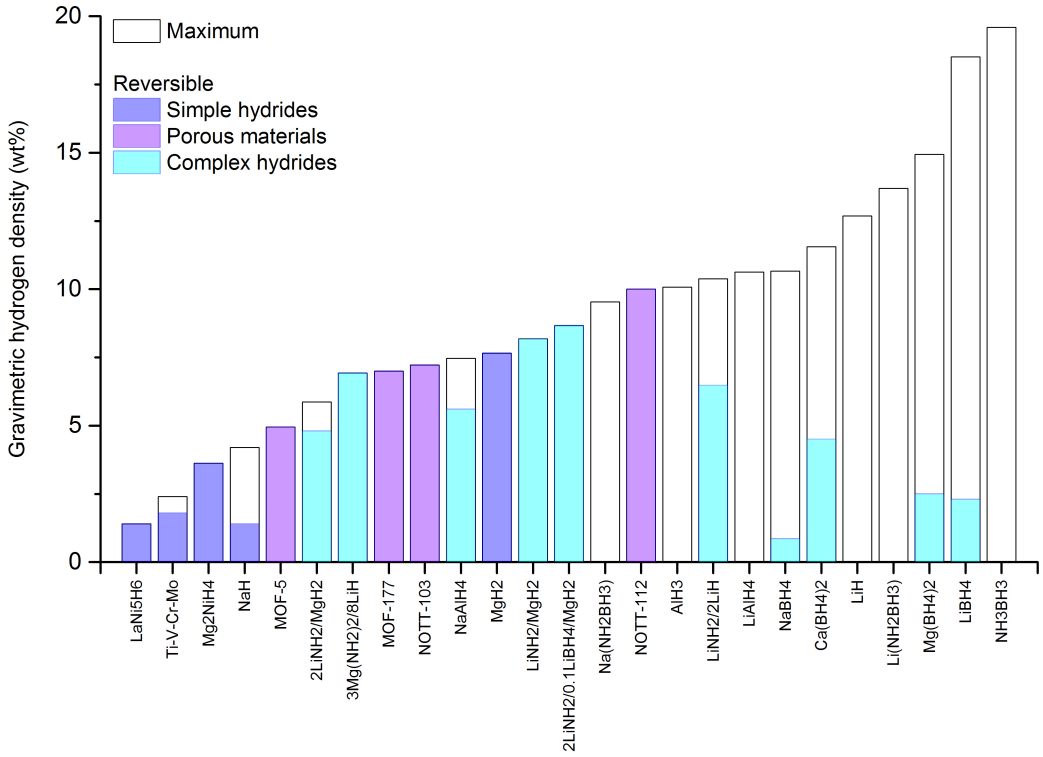

Figure 1.7: A plot of the maximum (unfilled columns) and reversible (filled columns) gravimetric hydrogen storage content for selected simple hydrides (blue), porous materials (purple) and complex hydrides (light blue). For the purposes of this figure, the reversible hydrogen content was defined as the hydrogen ad/absorption content reported for hydrogenation conditions of 77–674 K, with up to 150 bar of hydrogen pressure.

thermodynamically unfavourable.

The metal borohydrides are also poorly reversible, with bulk magnesium borohydride showing only minor reversibility (2.5 wt%) under strong hydrogenation reaction conditions[91], with full reversibility only achieved after 100 hours at 400 °C and 950 bar of hydrogen[92]. Calcium borohydride shows partial reversibility after 12 hours exposure to 150 bar of hydrogen at 350 °C[93]. Full reversibility for magnesium borohydride and lithium borohydride, and partial rehydrogenation for sodium borohydride, can be achieved using more moderate conditions when the hydride is encapsulated in a porous carbon matrix[94–96]. However, encapsulation dramatically reduces both the gravimetric and volumetric hydrogen storage capacity, as evidenced by the low reversible weight percentages obtained for lithium and sodium borohydride in Figure 1.7. The value for full hydrogenation of encapsulated magnesium borohydride is less than that obtained for the partial hydrogenation of the bulk sample.

It can be argued that the hydrogen storage community has not given sufficient focus to the criterion of *reversible* hydrogen storage, and instead expended a disproportionate amount of energy finding hydrides with ever-greater hydrogen content. The vast majority of these materials are best considered as one-shot hydrogen stores, in a similar way that the alkaline battery is a one-shot electrical energy store. In order for them to be used in vehicles, a system of exchanging the spent fuel for fresh material would be required, with the hydrogen store subsequently regenerated at a central location. It seems unlikely that this would be a cost-competitive model for transportation. Despite this critique, there are many applications for one-shot energy stores which may benefit from the increased power density of hydrogen stores over batteries. In these cases, irreversible hydrogen stores may be of commercial interest. However, for vehicular transportation, reversible hydrogen stores are likely to be the most practical and cost-effective option.

Figure 1.7 does show that transition metal hydrides and porous materials are easily reversible. However, given the aforementioned concerns about the volumetric capacity of porous materials and the gravimetric capacity of transition metal hydrides, the most promising reversible hydrogen stores for on-board use are amide-based materials and sodium alanate. While sodium alanate has been the subject of a vast research effort, the amides have not been examined in as much detail as might be expected given their position as one of the few reversible complex hydrides. This thesis aims to shed more light on the potential of these amide materials.

1.4 Lithium amide - lithium hydride: the Li-N-H system

Metal amides, compounds which contain metals bonded to one or more NRR‘ groups (where R and R’ are hydrogen, alkyl, aryl or silyl groups), are reported for almost every known element. Their diverse structural chemistry has been studied extensively, and their use as bases and ligand transfer agents in synthetic organic chemistry underpins many important synthetic pathways. In recent years, their use in synthetic chemistry has broadened to include reactions such as cyclisations, polymerisation, and even nitrogen and nitrous oxide activation[97].

In the field of hydrogen storage, the study of metal amides has been mostly restricted to the simplest amide ligand (NH_2) combined with light elements, in order to maximise gravimetric and volumetric hydrogen density. The potential for their use in this field was first highlighted by Chen *et al.* in 2002, who examined the behaviour of the lithium amide - lithium hydride composite material[98]. They expanded on work from the early 20th Century by Dafert and Miklauz, who had shown that lithium nitride (Li_3N) could take up hydrogen to form a compound with an empirical formula of Li_3NH_4[99]. Chen *et al.* clarified that this empirical formula was actually a 1:2 mixture of lithium amide and lithium hydride (the Li-N-H system), and that the absorption of hydrogen by lithium nitride occurs in two stages, with the initial formation of lithium imide and one equivalent of lithium hydride (Equation 1.16) followed by a second hydrogenation, resulting in the formation of the amide and second equivalent of lithium hydride (Equation 1.17).

$$Li_3N + H_2 \rightarrow Li_2NH + LiH \tag{1.16}$$

$$Li_2NH + H_2 \rightarrow LiNH_2 + LiH \tag{1.17}$$

Combined, the overall reaction results in a hydrogen storage capacity of 10.4 wt%, with a corresponding volumetric hydrogen density of 100.3 $kg\,m^{-3}$, values which make the Li-N-H system a viable option for transportation applications. While the decomposition of lithium amide on its own was previously known to form the imide with the release of ammonia[100], Chen *et al.* showed that through the combination of the amide and hydride, the storage and release of hydrogen occurred in reversible reactions, sparking a wave of interest in these materials.

Although reversible, the first stage of hydrogenation of lithium nitride is highly exothermic

and thus the complete dehydrogenation (reverse reaction of Equation 1.16) will only occur above 350 °C. Hence, the vast majority of the research effort of the hydrogen storage community has focussed on the interconversion of lithium imide and lithium amide plus lithium hydride, which as an individual reaction stores an appreciable amount of hydrogen (6.5 wt%, 67.3 $kg\,m^{-3}$), with a much lower theoretical enthalpy (45 $kJ\,mol^{-1}$). The dehydrogenation reaction occurs at around 200 °C. Although this is in excess of the desired temperature range, the Li-N-H system has inspired significant research interest primarily due to the facile nature of the reversibility. The hydrogenation reaction requires only a few bar of hydrogen pressure to proceed with reasonable kinetics, and was quickly shown to cycle with relatively stable capacity[101]. As can be seen from our survey of other hydrogen storage materials, this quality is remarkably rare amongst complex and chemical hydrides. The conditions for reversibility in the Li-N-H system are significantly more practical than those for sodium alanate, the other flagship reversible complex hydride. Therefore, the study of the Li-N-H system has been prompted not only by a desire to improve the properties of the system itself, but to understand the nature of its reversibility in order to inform the study of other complex and chemical hydride materials.

The key challenges in the development of practical Li-N-H hydrogen storage centre on the improvement of the low-temperature kinetics of the hydrogenation and dehydrogenation reactions, and the need to minimise the formation of ammonia as a contaminant in the hydrogen gas stream, to which amide systems are susceptible. Ammonia, even at parts-per-million levels, has catastrophic effects on PEM fuel cells[102], and so must be removed or, preferably, not produced in the first place.

Efforts to improve the hydrogen storage characteristics of the Li-N-H hydrogen store have followed similar routes to those employed for sodium alanate. A range of additives have been employed, with varying levels of success in improving the kinetics of dehydrogenation[103–107]. Of the additives used, titanium (III) chloride ($TiCl_3$) is the most intensively studied, and, as was observed for sodium alanate, appears to be the most effective of the small number of materials studied to date. The addition of a few molar percent of titanium (III) chloride has been reported to reduce the onset temperature of dehydrogenation by 30–50 °C, with the effect shown to be maintained over a small number of hydrogenation-dehydrogenation cycles[103, 104]. In terms of gaining an understanding of why this effect is observed, little progress has been made. X-

ray absorption spectroscopy (XAS) results suggest that the additive has some form of electronic effect on the lithium amide rather than the lithium hydride[108], with the hypothesis put forward that the titanium ions could substitute on to lithium sites in the amide[109]. A follow-up XAS study suggested that the X-ray absorption structure of the titanium ions in a doped Li-N-H sample was very similar to that of the penta-ammoniate of titanium chloride ($TiCl_3(NH_3)_5$)[110]. Alternatively, it has been claimed on the basis of *in situ* transmission electron microscopy that the titanium may facilitate movement of ions between lithium amide and lithium hydride[111]. Based on these few studies, the form and mechanism of action of the titanium dopant are not clear.

Aside from metal additives, halide doping has also been used as a way to destabilise the Li-N-H structure. It has been found that halides may be incorporated into the lithium amide structure in various stoichiometric and non-stoichiometric ratios, and can improve the kinetics of decomposition of the amide and imide[112, 113]. Of course, the use of halides to destabilise the amide causes a concomitant decrease in the reversible hydrogen content. However, it has been shown that useful improvements in the hydrogen release kinetics can be achieved whilst maintaining an acceptable level of hydrogen storage. These systems are also fully reversible[112].

Various studies have used ball milling to reduce the particle size, and have shown that this results in a reduction in the hydrogen desorption temperature[114, 115]. Furthermore, Nuclear Magnetic Resonance (NMR) experiments have shown that milling can change the electronic structure in the Li-N-H system by inducing defects[116, 117], with low-temperature milling used to stabilise those defects[118]. However, there are concerns about the cost of milling commercial samples, and to what extent this kinetic effect is maintained over many hydrogen storage and release cycles. Nevertheless, it remains a popular method of sample homogenisation and mixing.

In addition to the use of dopants and mechanical methods, the development of chemical variants of the Li-N-H system, using different combinations of alkali and alkaline earth metal amides and hydrides, has been widely investigated as a means for reducing the reaction temperature. These have included Li-Na-N-H[119], Li-Ca-N-H[120, 121], Mg-Na-N-H[122], Mg-N-H[123–125], and Li-Mg-N-H. Of these, the Li-Mg-N-H system has been the most successful. Magnesium amide decomposes at a lower temperature than lithium amide, but a magnesium amide - magnesium hydride composite suffers from poor hydrogen release kinetics[123]. However, combinations of

Table 1.2: The various Li-Mg-N-H systems.

Reaction	wt% H_2	T_{peak}(°C)	Reversible wt% H_2 (temp, pressure)	Ref.
$MgH_2 + LiNH_2 \rightarrow LiMgN + 2H_2$	8.18	220	8.18 (160 °C, 138 bar)	[126]
$MgH_2 + 2LiNH_2 \rightarrow Li_2Mg(NH)_2 + 2H_2$	5.87	195	4.8 (200 °C, 32 bar)	[127]
$3Mg(NH_2)_2 + 8LiH \rightarrow Mg_3N_2 + 4Li_2NH + 8H_2$	6.93	190	6.93 (200 °C, 30 bar)	[128, 129]
$3Mg(NH_2)_2 + 12LiH \rightarrow Mg_3N_2 + 4Li_3N + 12H_2$	9.15	180-400	8.0 (250 °C, 350 bar)	[129, 130]

magnesium amide and lithium hydride or lithium amide and magnesium hydride show promising results. Indeed, the combination of amide and hydride used appears to be incidental, as the cations readily metathesise, either with ball milling or upon undergoing a hydrogenation-dehydrogenation cycle. A number of different ratios of the two materials have been investigated and are summarised in Table 1.2. As can be seen, the investigations into these systems have been fruitful, identifying a number of additional reversible systems with reasonably large hydrogen content and, in some cases, better dehydrogenation kinetics than the Li-N-H system. Uniformly, the hydrogenation kinetics are poor compared with the nascent Li-N-H system, which is reflected in the higher hydrogen pressures required for hydrogenation. However, pressures in the region of 30 bar are still more practical than most alternative systems.

The chemical intuition involved in the development of these mixed systems, and the trial-and-error approach of using additives, have achieved impressive results. However, the further advances that are necessary for practical application of metal amide systems are likely to come from a deeper understanding of the mechanisms by which amide-hydride composite systems store and release hydrogen.

A number of groups have attempted to elucidate the precise mechanism of hydrogen storage in the Li-N-H system, and thus identify the physical parameters that govern the conditions of these hydrogenation/dehydrogenation processes. Hydrogen release from lithium amide and lithium hydride was initially proposed to be a simple combination of protic ($\delta+$) hydrogen from the amide and hydridic ($\delta-$) hydrogen from the hydride to form molecular hydrogen[131], as is the

case for ammonia borane, or mixed anion complex hydrides. However, an alternative model was also proposed in which the hydrogen release in the Li-N-H system is mediated by ammonia[132]. In this model, the release of hydrogen is a two-step process, whereby the ammonia released from the decomposition of lithium amide to lithium amide (Equation 1.18) is captured by lithium hydride to form lithium amide (Equation 1.19), with the concomitant release of hydrogen. Each of these reactions is known to occur in isolation.

$$2LiNH_2 \rightarrow Li_2NH + NH_3 \tag{1.18}$$

$$LiH + NH_3 \rightarrow LiNH_2 + H_2 \tag{1.19}$$

A number of subsequent experimental studies reported results which supported the ammonia-mediated mechanism. Studies of isotopically labelled Li-N-H systems ($LiNH_2$+LiD and $LiND_2$+ LiH pairs) gave a mixture of not only HD, as would be expected from a protic-hydridic mechanism, but also H_2/D_2, consistent with ammonia mediation[133]. Hu and Ruckenstein conducted elegant experiments using layered lithium amide-lithium hydride samples to show that flowing argon gas through a layer of lithium amide followed by a layer of lithium hydride produced hydrogen, whereas through a layer of hydride followed by amide resulted in ammonia[134]. *In situ* NMR studies also detected the sequential formation of ammonia followed by conversion to hydrogen[135].

A similar debate between these two mechanisms occurred for the Li-Mg-N-H system. Eventually, a single ammonia-mediated mechanism was able to account for the range of results with different lithium to magnesium ratios[129]. Indeed, the generally improved kinetics of the Li-Mg-N-H systems can be understood by the fact that magnesium amide releases ammonia at a lower temperature than lithium amide.

With mounting evidence supporting the ammonia-mediated model, the next significant development in the understanding of the reaction mechanism came from *ex situ* synchrotron X-ray powder diffraction studies on hydrogenated and dehydrogenated Li-N-H samples. The use of the synchrotron afforded the necessary resolution for a more comprehensive mechanism to be proposed[136]. Complex microstructure observed in the diffraction peaks of lithium amide and

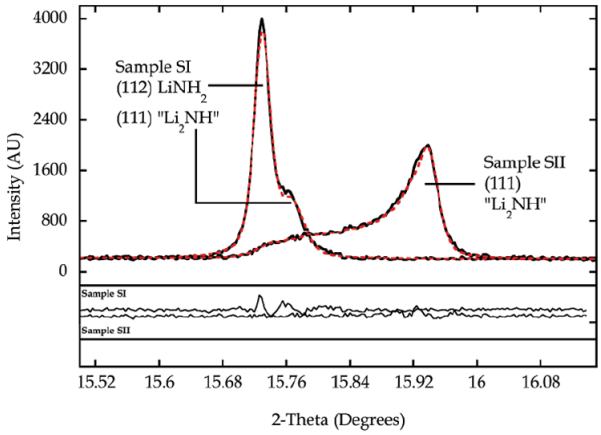

Figure 1.8: Complex peak shapes observed in synchrotron x-ray powder diffraction peaks for hydrogenated (SI) and dehydrogenated (SII) Li-N-H samples. Reprinted with permission from [136]. Copyright 2007 American Chemical Society.

imide (shown in Figure 1.8) indicated significant deviation in stoichiometry for samples supposedly at the end of their hydrogenation and dehydrogenation cycles, respectively. In the dehydrogenated sample, in particular, diffraction intensity was observed in a continuum from the position of the amide (112) to the imide (111) peak. From these peak shapes, it was inferred that the system could adopt the full range of stoichiometry values between lithium amide and lithium imide, with the intermediate stoichiometries being described by the formula $Li_{1+x}NH_{2-x}$, where x=0 is lithium amide, and x=1 is lithium imide.

The presence of these non-stoichiometric phases was then used as the basis for a proposed mechanism for hydrogen storage and release based on the diffusion of lithium ions through the crystal structures of the amide and imide. Looking at the structures of each phase as they are conventionally depicted, their similarity is not immediately apparent. Lithium amide crystallises in a tetragonal spacegroup ($I\bar{4}$), while, above 80 °C, lithium imide adopts a cubic anti-fluorite structure ($Fm\bar{3}m$). However, if the conventional origin of the imide structure, which has the nitrogen atoms at the (0,0,0) position, is shifted by $(\frac{1}{4},\frac{1}{4},\frac{1}{4})$ such that the lithium atoms are at the origin (Figure 1.9a), it can be seen that the lithium amide structure (Figure 1.9b) is an ordered $a\times a\times 2a$ supercell of lithium imide, with half of the lithium sites vacant (Figure 1.9c). Progressive filling of the vacant lithium sites in lithium amide to approach the lithium imide structure as the material dehydrogenates provides an explanation of the appearance of non-stoichiometric phases.

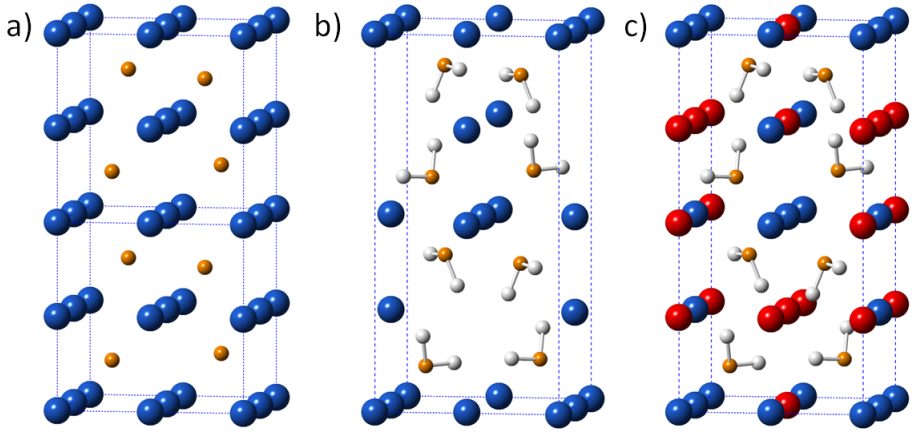

Figure 1.9: The crystal structures of the Li-N-H system, with lithium ions shown in blue, nitrogen shown in orange, and hydrogen in white. a) An $a \times a \times 2a$ superstructure of the high-temperature phase of Li_2NH with the disordered hydrogen atoms omitted for clarity, b) the $LiNH_2$ structure, and c) $LiNH_2$ with vacant lithium sites shown in red[137]. Reproduced by permission of The Royal Society of Chemistry.

Of course, whether this migration is likely under the experimental conditions is a separate question. Lithium imide has a very similar topology to lithium oxide, which also crystallises in the anti-fluorite structure. Studies on the diffusion of lithium ions within the lithium oxide structure show that tetrahedral to tetrahedral site hopping (such as was proposed for the lithium amide-imide transition) is present at relatively low temperatures, with tetrahedral to octahedral site hopping seen at higher temperatures[138]. Thus, the migration of lithium ions in the Li-N-H system seems plausible.

Lithium amide has a low observed ionic conductivity (2.6×10^{-5} S cm^{-1} at 520 K), but lithium imide has very high lithium conductivity (5.3 S cm^{-1}at 533 K)[139], suggesting that once dehydrogenation begins, the diffusion of lithium ions becomes very favourable.

A series of elementary steps can be written out for this mechanism: they are listed in Equations 1.20- 1.24, and shown graphically in Figure 1.10. The dehydrogenation may be described by the formation of a lithium ion Frenkel defect pair, where a lithium ion in lithium amide moves to an interstitial site (Equation 1.20, Figure 1.10a), leaving behind a lithium vacancy ($\square$), with an exposed NH_2^- unit. The local charge balance can be restored by the ejection of a proton from this NH_2^- unit (Equation 1.21, Figure 1.10b), and the ejected proton is then able to migrate through the structure as a transitory ammonia unit, which can be understood as a Grotthus-type

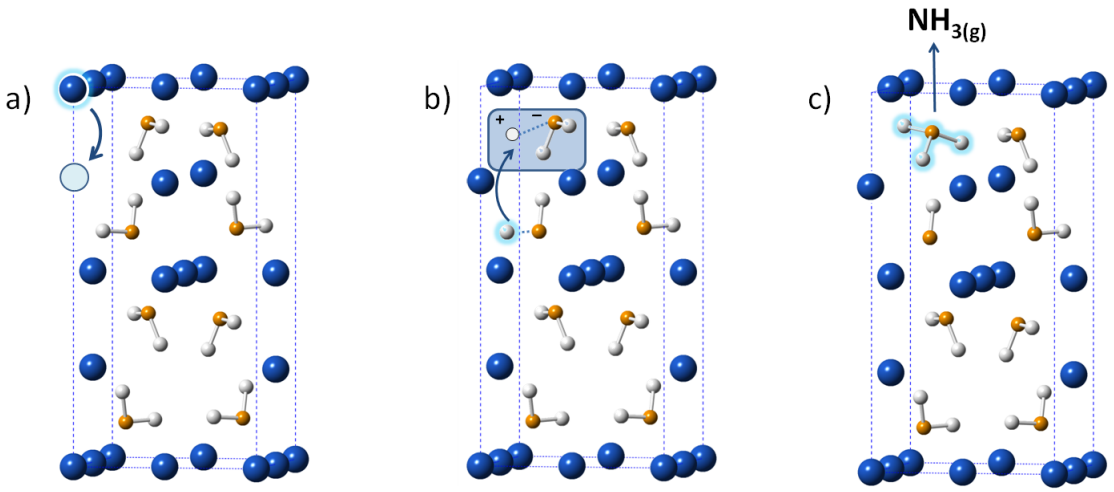

Figure 1.10: A graphical representation of the proposed mechanism of dehydrogenation of the Li-N-H system, showing a) Frenkel defect formation, b) charge-balancing by proton ejection, and c) emission of ammonia from the amide [137]. Reproduced by permission of The Royal Society of Chemistry.

mechanism (Equation 1.22-1.23). Once it reaches the surface of a grain, it can be released as an ammonia molecule, where it can then react with lithium hydride to form lithium amide and hydrogen (Equation 1.24, Figure 1.10c).

$$LiNH_2 + LiNH_2 \rightarrow [\square NH_2{}^-] + [LiLiNH_2{}^+] \tag{1.20}$$

$$[LiLiNH_2{}^+] \rightarrow Li_2NH + H^+ \tag{1.21}$$

$$[\square NH_2{}^-] + H^+ \rightarrow NH_3 \tag{1.22}$$

$$NH_3 + NH_2{}^- \rightarrow NH_2{}^- + NH_3 \tag{1.23}$$

$$NH_3 + LiH \rightarrow LiNH_2 + H_2 \tag{1.24}$$

The hydrogenation reaction can also be described in this way, where an interstitial lithium ion formed on the lithium imide lattice (Equation 1.25) reacts with a hydrogen molecule to form lithium hydride and an interstitial proton (Equation 1.26), which can then migrate to combine

with the other half of the Frenkel defect, the lithium vacancy, to form lithium amide (Equation 1.27).

$$Li_2NH \rightarrow Li^+ + [\square LiNH^-] \tag{1.25}$$

$$Li^+ + H_2 \rightarrow LiH + H^+ \tag{1.26}$$

$$[\square LiNH^-] + H^+ \rightarrow LiNH_2 \tag{1.27}$$

The fact that non-stoichiometric phases are formed, rather than simple nucleation and growth of the product imide or amide phase, can be explained by another migration of protons via a Grotthus-type mechanism, which allows amide and imide units to diffuse throughout the structure (Equation 1.28). It would seem to be entropically favourable for the amide and imide units to disorder via this mechanism, resulting in the formation of bulk non-stoichiometric phases.

$$NH_2{}^- + NH^{2-} \longleftrightarrow NH^{2-} + NH_2{}^- \tag{1.28}$$

The defect structures and ionic mobility suggested by these mechanisms have been studied in a number of Density Functional Theory modelling investigations, which have all broadly endorsed the feasibility of such a mechanism[139–142]. There has been some debate as to whether the defect formation occurs in the bulk, close to the surface, or both.

In summary, the structural similarity between lithium amide and lithium imide appears to facilitate a topotactic transition between the two structures, mediated by the migration of both lithium ions and protons, which result in the formation of non-stoichiometric phases. In common with the reversible interstitial hydrides, this is likely to underpin the facile solid-state reversibility observed in the Li-N-H system. However, this mechanism was based on the analysis of post-reaction samples. A full *in situ* diffraction study is necessary to confirm the participation of these non-stoichiometric phases in the hydrogenation and dehydrogenation processes, and to examine more fully the proposed mechanism in order to understand the behaviour of this prototypical system.

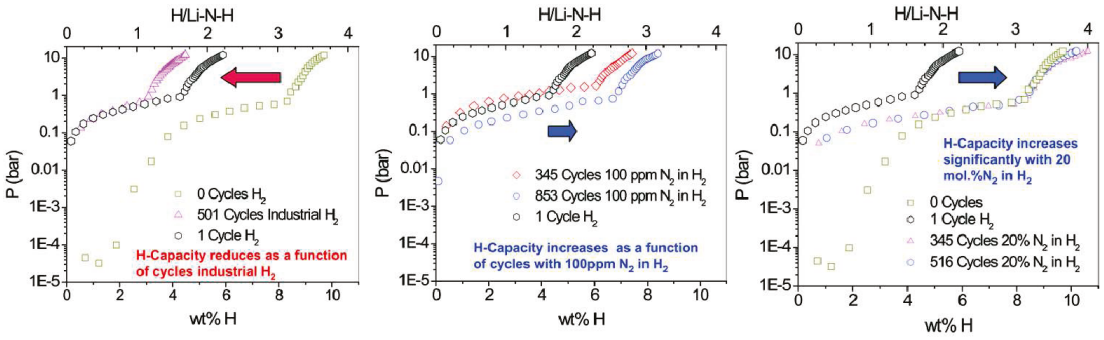

Figure 1.11: The variation in the reversible hydrogen storage content observed for the Li-N-H system as a function of cycle number with (left) pure hydrogen gas, (middle) 100 ppm nitrogen in hydrogen gas and (right) 20 mol% nitrogen in hydrogen gas as the hydrogenation gas. Reprinted with permission from [143]. Copyright 2011 American Chemical Society.

Indeed, there has been some evidence in recent work that the behaviour of the Li-N-H system may be more complex than what is described above. Lamb and co-workers performed a number of experiments subjecting the Li-N-H system to hundreds of hydrogenation-dehydrogenation cycles[143], as would be required for a practical system[144]. Their results are summarised in Figure 1.11. They found that by cycling in pure hydrogen for 501 cycles, the reversible hydrogen storage capacity of the system dropped by roughly one-half. However, introduction of 100 ppm of nitrogen gas into the hydrogenation gas stream resulted in an increase in the stored hydrogen content by a similar amount over 853 cycles, and increasing the proportion of nitrogen in the hydrogenation gas stream to 20 mol% resulted in a two-thirds increase in the hydrogen storage content over 516 cycles, approaching the capacity which would be expected from full dehydrogenation to lithium nitride. This is a remarkable, and indeed counter-intuitive result, given the usually inert nature of molecular nitrogen.

The authors attribute the loss of capacity under pure hydrogen to the formation of parasitic lithium hydride. They also contend that lithium metal is formed during the hydrogenation-dehydrogenation reactions, which reacts with the hydrogen gas to form lithium hydride (Equation 1.29). Lithium metal is one of the few materials with which molecular nitrogen will readily react. Therefore, it has been postulated that the inclusion of nitrogen results in the preferential formation of lithium nitride (Equation 1.30), which can subsequently hydrogenate and thus keep all of the lithium as an active part of the reaction.

$$\mathrm{Li} + \mathrm{H_2} \rightarrow 2\mathrm{LiH} \tag{1.29}$$

$$3\mathrm{Li} + \frac{1}{2}\mathrm{N_2} \rightarrow \mathrm{Li_3N} \tag{1.30}$$

These hypotheses are based only on pressure-composition isotherm data — more rigorous investigation is required in order to elucidate the role of nitrogen in the Li-N-H system, particularly its apparent ability to cause the hydrogen storage capacity to exceed the normally-accessible level. Importantly, there is currently no direct evidence for the formation of lithium metal, nor any detail about how the reaction mechanism is altered by the presence of nitrogen. However, if these results can be corroborated, they would represent a significant step towards the development of a practical amide-based hydrogen store.

1.5 Ammonia: the new paradigm?

Despite all of the advances made in the development of hydrogen storage materials, there are significant challenges that must still be addressed to develop a system which is suitable for transport applications. Porous materials and transition metal hydrides at best provide a means to lower the maximum pressure required in high pressure hydrogen storage tanks, though not sufficiently to enable the use of low-cost and lightweight tank materials. The current generation of complex and chemical hydrides either operate above the target temperature range, requiring a sacrifice in efficiency, or are poorly reversible, and thus would function only as one-shot stores which would need to be exchanged and regenerated separately.

The challenges of on-board refuelling go beyond just the materials question of whether rehydrogenation is chemically feasible in the desired range of conditions. There is a technical challenge in the management of heat during refuelling for any materials-based hydrogen store. Considering even a very small hydrogenation enthalpy of -10 $\mathrm{kJ\,mol^{-1}}$, as observed for many physisorption-based hydrogen stores, then refuelling to store 5 kg of hydrogen gas (approximately 2480 moles) will release 24.8 MJ of heat. Accounting for a refuelling time of five minutes, this would require the management of 82 kW of heat. For chemical and complex hydrides, with more exothermic hydrogenation reactions, this value is significantly higher. The management of this heat is challenging from an engineering perspective, requiring the addition of heat management devices which effectively reduce the system hydrogen storage density.

While there remain many valid paths of scientific enquiry towards practical solid-state hydrogen stores, some which are explored in this thesis, it is important also to be mindful of potential alternatives to solid state hydrogen storage in the event that the 'Goldilocks zone' of materials properties as outlined by the U.S. DoE cannot be achieved. One such alternative is ammonia.

1.5.1 Ammonia as a fuel and hydrogen store

The Haber-Bosch process for the industrial synthesis of ammonia has, over the past century, led to a global revolution in agriculture to the extent that almost half the crops grown across the world today depend on ammonia-based fertilisers[145]. As a fertiliser feedstock chemical, ammonia is a vector for the nitrogen which feeds plants. As a fuel, its use would be as a hydrogen vector. In this way, the reverse Haber-Bosch reaction (Equation 1.31) may have a similarly transformative potential, where the decomposition of ammonia into nitrogen and hydrogen enables the provision of hydrogen for a low-carbon energy economy[146–150].

$$2\mathrm{NH_3} \rightarrow \mathrm{N_2} + 3\mathrm{H_2} \tag{1.31}$$

Liquid ammonia has a very high gravimetric (17.8 wt%) and volumetric (121 $\mathrm{kg\,m^{-3}}$) hydrogen density, a characteristic which makes it attractive as a hydrogen vector. One can envisage an ammonia cycle which is similar to the hydrogen cycle in Figure 1.3. In this modified cycle, storage of the hydrogen occurs prior to its distribution. Ammonia is produced centrally or through a highly distributed network using the Haber-Bosch process: the combination of hydrogen and nitrogen gas at high temperature (400–600 °C) and elevated pressure (200–400 bar) over an iron catalyst. This process is highly energy efficient, but also energy intensive, accounting for around 1–2 % of annual global energy use[151]. Around 200 million tonnes of ammonia are produced annually, making ammonia one of the highest volume industrially-produced chemicals[151]. Of course, this level of production would need to increase dramatically to supply a significant proportion of the global transportation fuel requirement. An estimated five-fold increase in production would be required to cover the US and UK fuel consumption alone (at 2013 levels[152, 153]), based on the relative energy densities of ammonia and gasoline, and assuming an average equal efficiency. Additionally, ammonia faces the same issues around sustainable production as are present for hydrogen, since hydrogen is required for ammonia synthesis. Nevertheless, there are early-stage

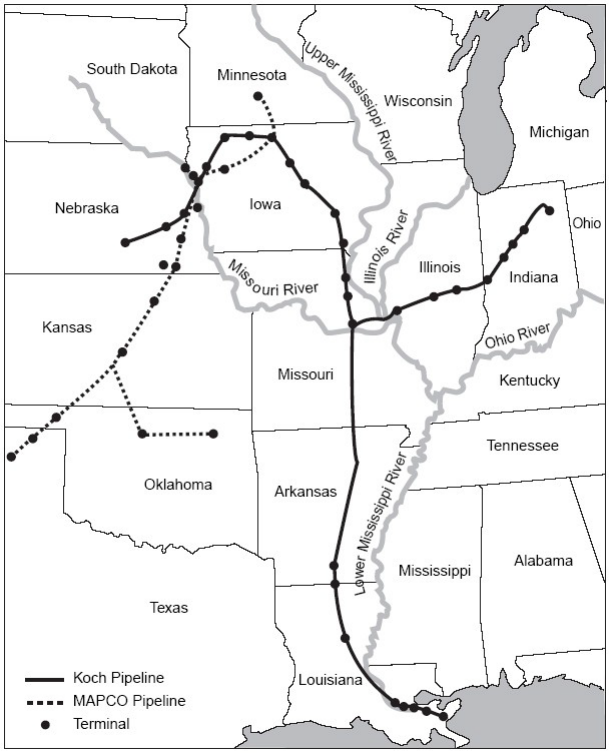

Figure 1.12: Existing ammonia distribution network in the United States of America (reproduced from [155]).

efforts underway to produce ammonia electrochemically directly from air and water[154], running in parallel to efforts to improve the electrolysis of water to give hydrogen, which could then be turned into ammonia with via the Haber-Bosch process.

Once produced, the ammonia must be distributed for use. Due to the fact that ammonia liquefies under modest pressure (approximately 10 bar at room temperature), ammonia is much more easily transported through pipes than hydrogen, and has existing mature infrastructure because of its widespread use for fertilliser production (see Figure 1.12 for the US distribution network). Therefore, the roll-out of large-scale distribution networks for ammonia would not be expected to be more technically challenging or expensive than alternatives such as liquefied petroleum gas (LPG).

Refuelling with ammonia would be compatible with the current paradigm of fuel stations and user-operated systems; again, it would have very little practical difference to LPG, and would not require the complex and expensive high-pressure gas delivery technology that is necessary for 700 bar pressurised hydrogen storage. The ~10 bar pressure required to maintain ammonia as

Table 1.3: Physical, toxicity, flammability and explosivity data for selected fuels.

Fuel	Vapour pressure (bar @ 293 K)	IDLH[a] (ppm)	Toxicity[b]	Flammability range (% in air)	Explosive range (% in air)
Petrol	0.047	750	63	1.4–7.6	1.1–3.3
Methanol	0.13	6000	21.6	6–36	5.5–44
Hydrogen	-	n/a	n/a	4–74	18.3–59
Natural gas	-	n/a	n/a	5.3–15	5.7–14
Liquid ammonia	8	300	27000		16–25

[a]Immediately Dangerous to Life and Health concentration. [b]Toxicity value is calculated by dividing the vapor pressure at 293 K by the partial pressure of the IDLH concentration. Adapted from Ref. [149] with permission from The Royal Society of Chemistry.

a liquid means that inexpensive and lightweight tanks would be sufficient for on-board storage.

Given all of this potential, it begs the question why ammonia has been largely overlooked as a serious contender for the storage and distribution of hydrogen? There are two central reasons: safety, and the ability to extract the stored hydrogen.

Ammonia is a toxic chemical. Its toxicity, explosivity and flammability limits, along with some pertinent physical characteristics, are shown in Table 1.3. The high toxicity level of ammonia is primarily due to its high vapour pressure. However, it is difficult to quantify the dangers associated with a chemical in a single number. For example, ammonia is lighter than air, and so will clear from the scene of a spillage quite rapidly. This is in contrast to methanol and petrol.

As with all safety issues, there are real and perceived risks. Although it has been well-argued that the low limit of detection of ammonia by human smell (a few ppm) is advantageous due to the early detection of leaks, the repellant sensory effect of ammonia and its association with harsh cleaning products and piscine decay should not be underestimated in stalling widespread public acceptance of ammonia as a fuel. Assurance of the safety of ammonia in a technical sense is a distinct issue from that of convincing the general public that it is safe. As a bulk industrial chemical, ammonia is transported around the world, with a very good safety record. Of course, the widespread use by the general public brings a different set of risks. Some analyses have determined that while the risks associated with using ammonia as a fuel (in terms of transport, delivery and use in vehicles) are somewhat higher than for gasoline, they are lower than those

for LPG[156]. There are also options for storing ammonia in the solid state as metal halide ammines such as magnesium chloride hexaammoniate ($MgCl_2(NH_3)_6$)[148, 149, 157, 158]. In some of these complexes, the ammonia density is very similar to that of liquid ammonia. These compounds reduce the vapour pressure of the ammonia to millibar levels, and in doing so would effectively render the ammonia non-toxic. However, they would then require the input of energy to liberate the ammonia for use in the vehicle, presenting a similar range of technical issues as those encountered for hydrogen storage materials.

Fundamentally, the issue of the safety of ammonia for transportation is a societal and regulatory debate. Undoubtedly, ammonia is a hazardous chemical, requiring controlled use and suitable safety precautions, but the safe use of ammonia does not require significant development of new technology, apart from perhaps more extensive development of ammonia capture materials. The principal technical challenge to the use of ammonia is the effective, efficient and cheap decomposition of ammonia to release its stored hydrogen.

1.5.2 Ammonia cracking

Like most alternative fuels, ammonia could be used either in a fuel cell or a combustion engine, with the energetic pathways of these two methods summarised in Figure 1.13. Both of these routes require some degree of decomposition of ammonia into nitrogen and hydrogen. For use in low temperature fuel cells such as PEM fuel cells, the ammonia must be completely decomposed to nitrogen and hydrogen (Figure 1.13a), with the hydrogen produced then delivered to the fuel cell (Figure 1.13b). Although there are high temperature fuel cells which could use ammonia directly as a fuel, they are not considered practical for transportation. Alternatively, the ammonia may be combusted directly (Figure 1.13c). It is difficult to ignite pure ammonia, so partial decomposition (around 15%) of the ammonia is required to provide sufficient hydrogen to enable optimal combustion to occur[159].

As can be seen in Figure 1.13, the end products of ammonia use in either pathway (fuel cell or combustion engine) are the same; there is no thermodynamic advantage to either route. Therefore, the preference for one method over the other is determined on the merits of the technology associated with each system. The efficiency of each route can be characterised as the product of the efficiency of the ammonia decomposition unit with the efficiency of the power

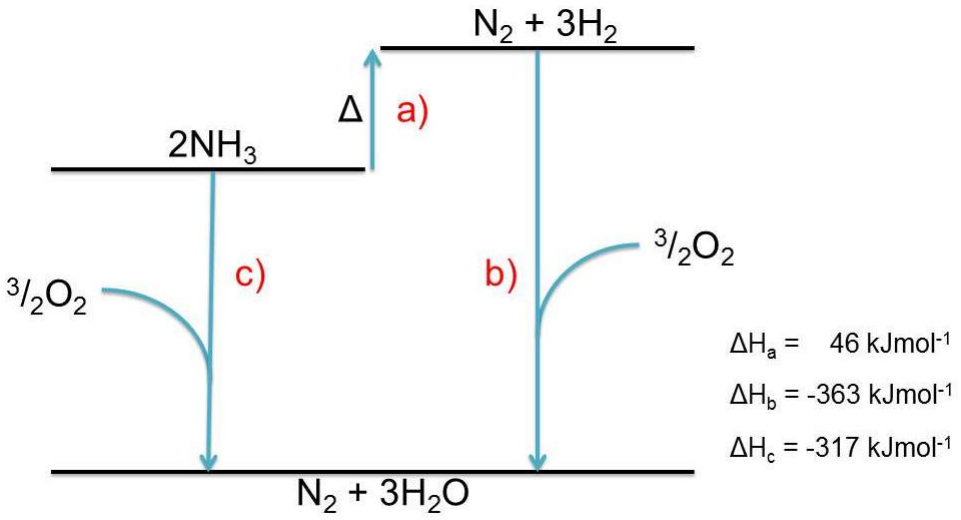

Figure 1.13: Enthalpy diagram for a) decomposition of ammonia into hydrogen and nitrogen, followed by b) reaction of the hydrogen in a fuel cell, or c) the direct combustion of ammonia. The change in enthalpy (ΔH) values indicated are all per mole of ammonia.

converter (the fuel cell/combustion engine). The efficiency of the cracking unit for the combustion route is likely to be higher than that of the fuel cell cracker when taken as a system efficiency, since only a fraction of the ammonia needs to be decomposed for complete combustion to occur. Therefore, which method has the advantage in terms of efficiency comes down to the magnitude of the difference in the efficiency of the fuel cell compared with that of the combustion engine. Here, it is useful to address a common misconception about the relative efficiencies of fuel cells and internal combustion engines. It is often stated that the Carnot cycle efficiency limits the efficiency of an internal combustion engine, meaning that fuel cells will always maintain an efficiency advantage over combustion engines. However, an analysis of the efficiency of both technologies in terms of the chemical reaction fuelling them shows that the efficiency of both (η) is expressed in terms of the enthalpy and entropy of the reaction (Equation 1.32)[160].

$$\eta = \frac{\triangle G}{\triangle H} = \frac{\triangle H - T\triangle S}{\triangle H} = 1 - \frac{T\triangle S}{\triangle H} \tag{1.32}$$

As this expression holds both for combustion engines and fuel cells, there is no inherent difference in the maximum efficiency of the two technologies. While is is true that current fuel cells are generally more efficient than an average combustion engine, it is not unreasonable to assume that next-generation combustion engines will approach the overall efficiency of a fuel cell.

Of course, efficiency is not the only factor in comparing the systems, as cost and robustness are highly relevant. In these areas, combustion engines have a distinct advantage over fuel cells.

Whichever energy conversion route is deemed optimal, a highly efficient and effective ammonia decomposition process is required. Thermodynamically, the decomposition of ammonia is favourable above 463 K; the equilibrium conversion of ammonia for various temperatures and pressures is shown in Figure 1.14. Here, the challenge for ammonia-sensitive PEM fuel cells becomes apparent. Even at 1173 K, at a pressure of 10 bar, there remains 0.15 % (1500 ppm) unreacted ammonia[155], far in excess of the 0.1 ppm ammonia concentration required for safe operation of a PEM fuel cell. The dominance of PEM fuel cells in the fuel cell vehicle market has been one of the main reasons ammonia has been avoided as a hydrogen vector. However, by using the metal halides outlined previously to trap unwanted ammonia in the outlet gas stream it has been shown that the removal of 500 ppm of ammonia for an equivalent driving range of 1800 miles can be achieved using 1.2 kg of adsorbent material[161]. Alternatively, a change in the type of fuel cell used, such as to an alkaline fuel cell, which is not sensitive to significant amounts (up to 10 %) of ammonia in the gas stream[162], could be considered. For these systems, clean up would only be required post fuel cell to reduce the ammonia concentration down to a level which was deemed safe as per environmental and health regulations.

Of course, thermodynamic conversion is not obtained in kinetically limited situations, such as the high flow rates used in a vehicle, and the decomposition reaction must be catalysed. Most ammonia decomposition catalysts do not effect significant levels of ammonia decomposition under flowing gas conditions below approximately 620 K. It is unlikely that full ammonia decomposition will be achieved using only the waste heat from a fuel cell or combustion engine. Some power will be required for heating the cracking reactor. Given the very high hydrogen density of ammonia, this can be accommodated up to a point, but the very high temperatures used with some catalysts (1100 K or above) will decrease the system efficiency to an unacceptable level. Therefore, for transport applications, the search for more active catalyst materials is paramount.

Ammonia decomposition catalysts have, to date, been exclusively transition metals, which act as classic heterogeneous catalysts. These have been investigated primarily as an indirect method for examining the kinetics of the ammonia synthesis reaction, since the conditions of ammonia decomposition are more straightforward to achieve in an average laboratory. The

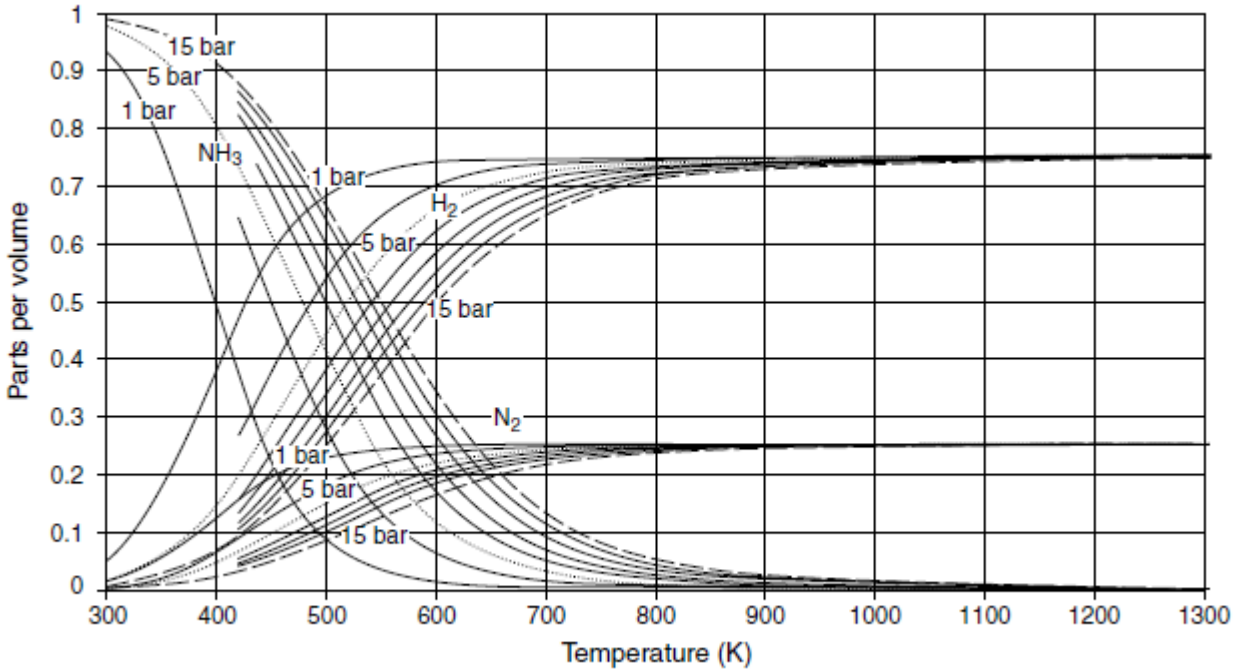

Figure 1.14: The equilibrium mixture for $NH_3 \rightarrow \frac{1}{2}N_2 + \frac{3}{2}H_2$ between 300 K and 1300 K, and for various pressures. Reproduced with permission from [163].

metal-catalysed mechanism of ammonia decomposition is generally accepted to occur via the following elementary steps (Equations 1.33-1.38)[164]:

$$NH_3 \longleftrightarrow NH_{3ads} \tag{1.33}$$

$$NH_{3ads} \longleftrightarrow NH_{2ads} + H_{ads} \tag{1.34}$$

$$NH_{2ads} \longleftrightarrow NH_{ads} + H_{ads} \tag{1.35}$$

$$NH_{ads} \longleftrightarrow N_{ads} + H_{ads} \tag{1.36}$$

$$2H_{ads} \longleftrightarrow H_2 \tag{1.37}$$

$$2N_{ads} \longleftrightarrow N_2 \tag{1.38}$$

There are disagreements about which step is rate determining out of the cleavage of the N–H bond (Equation 1.33), or the combinative desorption of nitrogen (Equation 1.38). The desorption of nitrogen appears to be the most commonly reported slow reaction step, although it has also

been suggested that the rate determining step could possibly vary between different metals, and even different reaction conditions[165].

The effectiveness of the transition metals in the decomposition of ammonia has been correlated in classic 'volcano' plots, showing that the peak in ammonia decomposition activity across the metal series is correlated with an ideal intermediate value of nitrogen absorption enthalpy, the energy level of the d-band centre, or ammonia adsorption enthalpy[166, 167]. These volcano plots have also been rationalised by invoking a change in rate determining step, with an initial rise in activity correlated with increasing nitrogen absorption enthalpy up to the peak value, and the subsequent decrease correlated with increasing N–H scission enthalpy[164]. These types of approaches have been successful in predicting high activity for bimetallic catalysts based on an average nitrogen absorption enthalpy[166].

Ruthenium is widely acknowledged as the most active metal for ammonia decomposition[168, 169], and so has been the focus of studies attempting to achieve full decomposition of ammonia. Iron- and nickel-based catalysts have also been widely investigated because of their lower cost and the fact that iron is the catalyst used in the vast majority of commercial ammonia synthesis. Some modified iron catalysts do show catalytic activities similar to supported ruthenium for an equivalent total mass basis[170] (i.e. catalyst plus support — ruthenium particles are more active than iron per mole of metal).

The activity of the metal catalyst depends greatly on the manner in which the catalyst is presented. There have been a range of published studies examining the effects of different support architectures and additives for ruthenium catalysts[165, 171]. Ruthenium catalysts are often distributed on some form of support structure, which not only provides a means for increasing the surface area and ensuring the effective dispersion of the catalyst into nanosized domains, reducing the amount of the expensive catalyst material required, but also appear to have an electronic effect on the catalyst which in turn affects its ammonia decomposition performance[172–174]. Traditional supports include metal oxides such as alumina, silica, zirconia and titania[169]. However, the most recent work has involved more exotic support structures such as carbon nanotubes and blends of nanotubes with metal oxides[175], which have proved to be the most active. Studies of a range of these materials have concluded that those which possess a basic nature, good conductivity, high surface area and good thermal stability under the operating conditions are

the most effective catalyst supports[165, 175]. A small number of studies have also investigated the effect of encapsulating the metal particles in the support structure[176, 177].

In addition to supports, so-called promoter materials are added to improve further the catalytic activity of the metal catalysts[158, 172, 173, 178–189]. These are normally alkali or alkaline earth metal salts. At the temperature of operation, most of these salts would form the oxide or hydroxide. In the case of ruthenium, caesium- and potassium-based promoters appear to have the strongest effect, which is generally rationalised in terms of electron donation to the metal centre, influencing the electronic interaction with the ammonia and the desorption of nitrogen from the catalyst surface.

Overall, ammonia shows significant potential as a viable replacement for petrol. It benefits from a mature synthesis technology, which takes the most plentiful component of Earth's atmosphere (nitrogen) and combines it with hydrogen. The geopolitical advantages of a fuel synthesised from air and water alone are immense. Ammonia is easily transported, and its use in transportation would not require significant changes to current methodologies. However, its use will rely upon the continual development of new materials to unlock its stored hydrogen more effectively. Ideally, these materials should consist of cheap and abundant materials and show high ammonia decomposition activity.

1.6 Thesis Aims

This thesis aims to explore the function of light metal amides as energy materials in two specific capacities: their function as hydrogen stores and their activity as catalysts for the decomposition of ammonia.

Firstly, their role as hydrogen stores. The Li-N-H system has arguably the most straightforwardly reversible hydrogen content among the complex and chemical hydrides. A more complete description of the mechanism of hydrogen storage and release in the Li-N-H system would be very helpful in informing efforts to impart this reversibility to other hydrogen stores, and would facilitate efforts to improve the hydrogen storage properties of the Li-N-H system itself. By taking advantage of new developments in sample environments at central facilities, the collection of *in situ* X-ray and neutron diffraction data on the Li-N-H and related systems will be used to

give direct insight into the mechanisms of hydrogen storage and release within the the Li-N-H system. In parallel, elucidation of the properties and functions of the component reactions of Li-N-H, the decomposition of lithium amide and the reaction of lithium hydride (and other alkali hydrides) with ammonia, will be investigated. Furthermore, and in an effort to gain insight into the Li-N-H system as it might behave in a commercial system, the effects of multiple storage and release cycles will be studied. These studies will be used to identify possible mechanisms of capacity loss, and investigate the remarkable effects of adding nitrogen into the hydrogenation gas stream on the reversible hydrogen capacity over many cycles.

Secondly, the need for new methods to decompose ammonia into hydrogen and nitrogen has been outlined. This work will seek to achieve this by examining the role that alkali metal amides could play in catalysing the decomposition of ammonia. It is hoped that this work may instigate renewed research interest and dialogue regarding the potential role of ammonia in facilitating the transition to a sustainable energy economy.

Chapter 2

Experimental

2.1 General sample handling and preparation

2.1.1 Reagent List

Details of the reagents used in the work in this thesis are shown in Table 2.1.

2.1.2 Air/moisture-sensitive sample handling

The substantial majority of the materials used in this thesis are sensitive to one or both of oxygen and water. Thus, in order to ensure reliable and reproducible analysis, great care was taken to maintain the samples under air- and moisture-free conditions. This was primarily achieved through the handling of samples in argon-filled glove boxes, mainly the mBraun Unilab series glove box. These glove boxes are equipped with a gas recirculation system which passes the argon through a catalyst bed in order to remove trace amounts of oxygen and water. Normal operation of this system maintains the levels of both species below 0.1 ppm, which is sufficient for most sample handling procedures.

Where access to a glove box was not possible or impractical due to size restrictions, polypropylene glove bags (Sigma Aldrich) were used as an alternative. These bags do not possess the active purification system of the glove box, and so must, as a consequence, be sequentially filled and purged with argon gas (usually at least five times) before work can commence.

Table 2.1: Reagents used in the work presented in this thesis.

Reagent name	Chemical Formula	Form	Supplier	Purity (%)
Lithium amide	$LiNH_2$	powder	Sigma Aldrich	95, 99
Sodium amide	$NaNH_2$	powder	Sigma Aldrich	95, 99
Lithium hydride	LiH	powder	Sigma Aldrich	95
Sodium hydride	NaH	powder	Sigma Aldrich	95
Sodium	Na	solid	Sigma Aldrich	99.9
Potassium hydride	KH	powder	Sigma Aldrich	-
Lithium deuteride	LiD	powder	Fisher Scientific	99
Calcium hydride	CaH_2	powder	Sigma Aldrich	90-95
Magnesium hydride	MgH_2	powder	Sigma Aldrich	98
Titanium (III) chloride	$TiCl_3$	powder	Sigma Aldrich	99.99
Ammonia	NH_3	liquefied gas	CKGas/Sigma Aldrich	99.98
Ammonia - d3	ND_3	liquefied gas	CKGas/Sigma Aldrich	99
Hydrogen	H_2	gas	CKGas	99.99999
Lithium nitride	Li_3N	powder	Sigma Aldrich	99.5
100 ppm nitrogen in hydrogen		gas	CKGas	99.99999
20 mol% nitrogen in hydrogen		gas	CKGas	99.99999
3% ruthenium on alumina		powder	Sigma Aldrich	-
65% nickel on silica/alumina		powder	Sigma Aldrich	-

2.1.3 Powder mixing/grinding

Solid-state samples are often ground either as a preparatory method of particle size reduction and homogenisation, or for the creation of an intimate mixture of reactants prior to solid-state reaction. Two methods of mixing/grinding of powder samples were used in this work: hand grinding and ball-milling.

Hand grinding was performed using agate mortar and pestles. Usually samples were ground by hand for five minutes, or five minutes per gram of sample for large samples.

Samples which were ball-milled (usually 1–2 g) were initially ground by hand, then placed inside a tungsten carbide-interior grinding jar (Retsch, 125 mL) filled with eight, 10 mm diameter

tungsten carbide grinding balls. The mill was sealed and placed in a planetary ball mill (Retsch, PM100). When the mill is operational, the main "sun wheel" of the mill rotates in the opposite direction to the grinding jar (equal rotational velocity in the PM100), causing the grinding balls to repeatedly crush and grind the powder sample. Samples were milled at 400 rpm for the specified duration. The total milling time was generally broken up into 15 minute intervals, with a 2 minute rest period between each segment to ensure that there was no excessive heating of the sample. The direction of rotation was also reversed after each segment in order to minimise the formation of 'dead zones', where powder accumulates without being subject to continuous milling.

2.2 Synthetic techniques

2.2.1 Solid-gas reactions

The solid-gas reactions employed in this work were generally for the synthesis of simple amides. A number of experimental setups were used for these reactions. The reactions performed, and their various experimental conditions, are recorded in Table 2.2.

Intelligent gravimetric analysis (IGA) — the sample (<1 g, held in a stainless steel bucket) was placed in the Intelligent Gravimetric Analysis for neutrons (IGA^n) apparatus (described in section 2.3.1) under argon. The sample was then evacuated at 100 mbar min^{-1}, and then exposed to the desired pressure of gas (100 mbar min^{-1}). Once at pressure, the sample was heated to the required temperature at a chosen heating rate (1–5 °C min^{-1}), and maintained at that temperature until the mass gain reached the expected level. The gas pressure was held constant throughout the experiment.

Flowing gas — the sample was placed inside a custom-designed stainless steel reactor (see section 2.6) and reactive gas was flowed across the sample at a chosen flow rate (10–100 standard cubic centimetres per minute, sccm) at 1 bar (atmospheric) pressure using a custom-designed gas delivery panel. The sample was then heated to the required temperature at 5 °C min^{-1} using a vertical tube furnace (Severn Thermal Solutions). The reaction progress was monitored by mass spectrometry where appropriate.

High pressure hydrogenation — the metal was loaded into a stainless steel pressure reactor

Table 2.2: Summary of solid-gas reactions used in this thesis.

Solid reactant	Reactive gas	Desired product	Temp (°C)	Pressure (bar)	Method
Li_3N	NH_3/ND_3	$LiN(H/D)_2$	150-300	1–3	IGA
Li_3N	H_2	$LiNH_2$ + 2LiH	150-300	1–3	IGA
LiH/LiD	NH_3/ND_3	$LiN(H/D)_2$	200-250	1	IGA/FG
NaH/NaD	NH_3/ND_3	$NaN(H/D)_2$	100-200	1	IGA/FG
KH	NH_3/ND_3	$KN(H/D)_2$	100-200	1	IGA/FG
Na	D_2	NaD	700	40–80	HPH

IGA = intelligent gravimetric analysis, FG = flowing gas, HPH = high-pressure hydrogenation.

(Parr Instruments), evacuated and then filled with the desired pressure of deuterium gas. The reactor was then heated to 700 °C at 5 °C min^{-1}, and held at that temperature until completion.

2.2.2 Solid-solid reactions

Similar methods were used for all of the solid-solid reactions between two starting materials. A list of these reactions is shown in Table 2.3. The reactants were hand ground and then ball-milled together as described in Section 2.1.3. After milling, the sample was heated under flowing gas using one of two methods. In the first method, the sample was placed into a cylindrical alumina crucible, and inserted into a quartz tube (sealed at one end). The open end of the tube was then sealed using a metal adaptor with a rubber O-ring, and a glass T-piece fitted with three Young's taps, as shown in Figure 2.1. The gas supply was connected to one of the Young's taps via a concentrated sulfuric acid bubbler to remove moisture, with the gas exhaust connected via the other tap to a paraffin oil bubbler. Gas was flowed through the upper section of the glass T-piece for five minutes before the tap to the sample was opened. The quartz tube was then placed inside a horizontal tube furnace (Carbolite), and heated to the desired temeperature. The second method used for these solid-solid reactions was identical to that described for the flowing gas solid-gas reactions, see Section 2.2.1.

2.3 Thermal Analysis

Thermal analysis is central to hydrogen storage research, since the primary aim of this research is to tune the temperature and pressure conditions required for hydrogen absorption and desorption.

Table 2.3: Summary of solid-solid reactions used in this thesis.

Reactants	Desired product	Mixing	Flowing gas	Temp (°C)	Duration
$LiNH_2$ + Li_3N	Li_2NH	BM, 1h	Ar	250	12 h
$LiND_2$ + Li_3N	Li_2ND	BM, 1h	Ar	250	12 h
$LiNH_2$ + Li_3N	$Li_{1+x}NH_{2-x}$	BM, 1h	Ar	250	12 h
$2LiNH_2$ + CaH_2	$Li_2Ca(NH)_2$	BM, 4h	Ar/NH_3	350	12 h
$2LiNH_2$ + MgH_2	$Li_2Mg(NH)_2$	BM, 4h	Ar/NH_3	350	12 h

BM = ball-milling

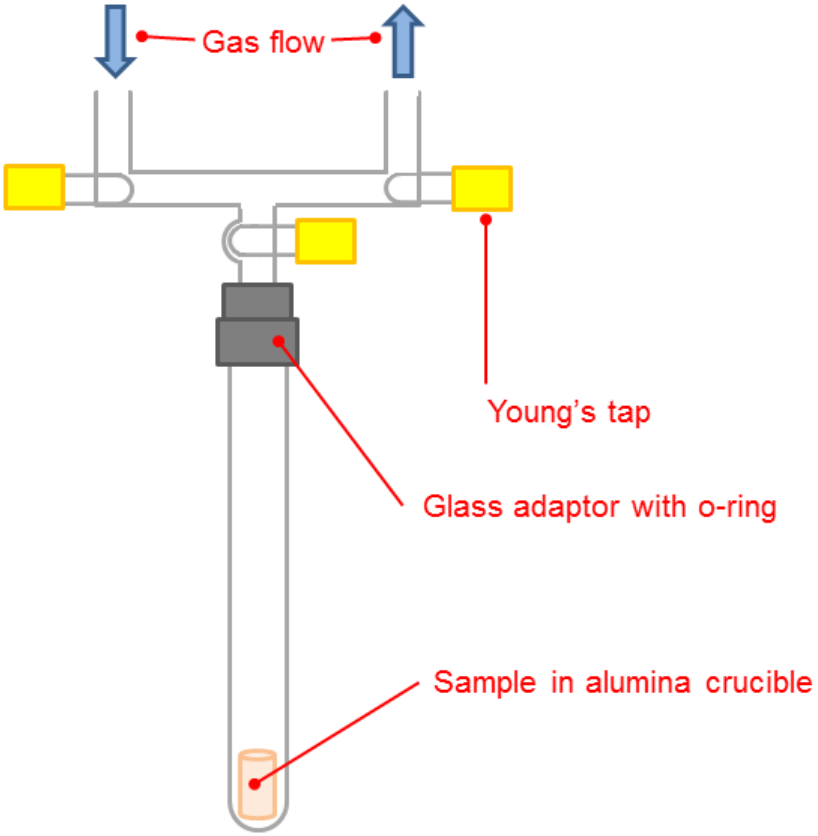

Figure 2.1: Flowing gas setup for solid-solid synthesis using a quartz tube.

Thermal analysis allows for this fundamental information to be collected, along with both the kinetic and thermodynamic properties of hydrogen storage materials.

2.3.1 Thermogravimetric analysis (TGA)

TGA is the workhorse technique of thermal analysis, where the mass of the sample is monitored over time under a controlled temperature regime, usually linear ramps in temperature with isothermal regions occasionally included. In most cases, the experiments are performed under flowing gas conditions. In hydrogen storage research, TGA is used to monitor the amount of hydrogen released from a sample, the kinetics of that mass loss, and the steps in which it occurs. By performing multiple experiments at different heating rates, the activation energy of the process can also be calculated by the Kissinger method.

TGA was performed using a variety of instruments, often with multiple functions which will be discussed below. For TGA-only experiments, a Setaram SETSYS Evolution TGA housed in a nitrogen-filled glove box was used. After zeroing the balance with the empty sample bucket (alumina, $20\,\mu L$), samples with a mass of 1–10 mg were placed in the bucket and attached to the balance hang down. The samples were then lowered into the furnace. During the TGA experiment, the sample was subject to a flowing argon atmosphere.

2.3.2 Intelligent gravimetric analysis (IGA)

IGA is an extension of TGA, with the additional feature of more flexible control over the atmosphere to which the sample is exposed. This flexibility allows for gas absorption studies to be undertaken more readily.

Two IGA instruments were used in this study. Both of the instruments contain common basic elements, which are shown in Figure 2.2. Two mass flow controllers, one at the gas inlet and one at the exhaust, are used to control the pressure and flow of gas in the reactor.

The first IGA instrument used was an IGA coupled to a mass-spectrometer (IGA-MS, Hiden Isochema). The IGA-MS can operate in two measurement modes: static and dynamic mode. In static mode, the pressure and composition of the sample atmosphere are controlled, but a flowing gas environment is not utilised. Alternatively, dynamic mode allows the chosen gas (or a mixture of two gases) to flow over the sample, and this gas is then sampled by a quadrupole mass

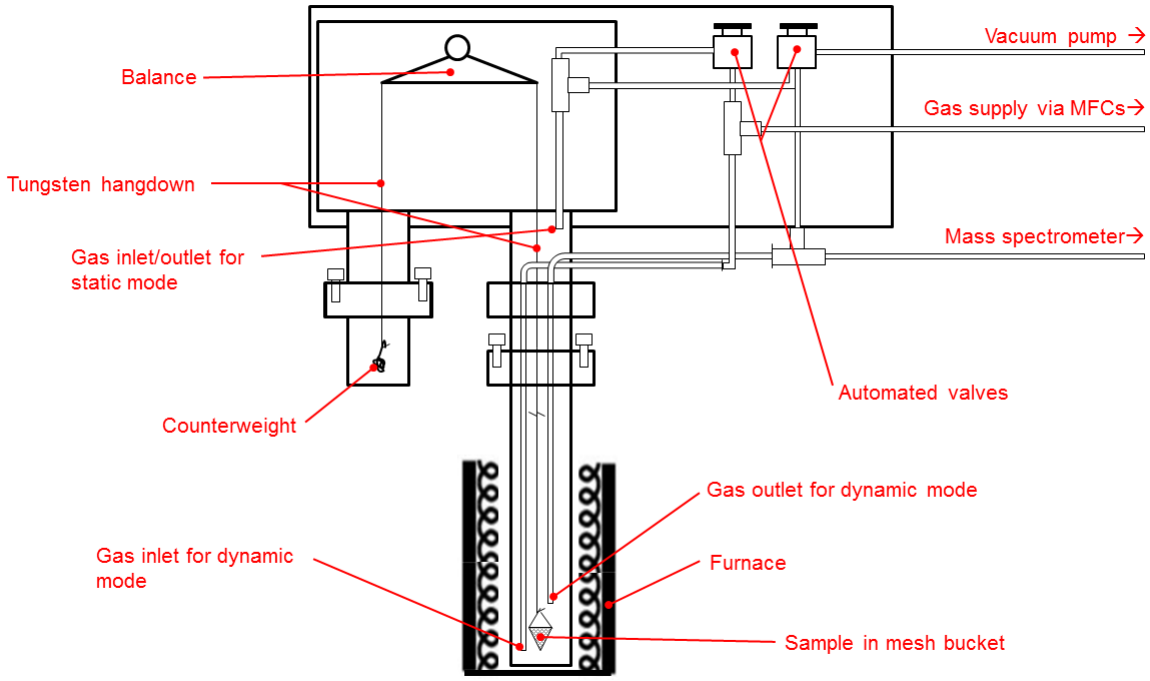

Figure 2.2: A simplifiied schematic of the IGA instrument showing the principal components of the apparatus.

spectrometer. The mass spectrometer takes the sampled portion of the gas outflow into a vacuum chamber where electrons generated from a filament are accelerated into the gas flow, ionising the gas molecules. From there, the ionised molecules pass into a quadrupole mass analyser: four parallel metal rods consisting of two pairs of opposite electric polarity. A variable radio-frequency (RF) voltage is applied to the rods. Together with a DC voltage, this variable voltage serves to stabilise the trajectory of ions of a selected mass-to-charge ratio (m/z) as they travel through the quadrupole. The selected ions pass through the quadrupole, and are neutralised in a metal cup, called a Faraday cup. Ions of m/z not selected for analysis will not have a stable trajectory, and will impinge on one of the metal rods, where they are neutralised. The current generated at the cup is proportional to the number of ions hitting it, and so by monitoring the current, the amount of a particular m/z in the gas stream can be quantified. By scanning through the RF-voltage applied to the quadrupole, a range of m/z values can be analysed. The experiments in this thesis were generally run in MID mode, where a particular set of m/z values are monitored. By correlating the changes in the mass of the sample with the composition of the gas stream, the IGA experiment is used to probe reaction mechanisms, identifying the gaseous

species responsible for mass loss and/or the byproducts of reactions with a reactive gas.

A general procedure for the use of the IGA-MS is as follows: samples (10–200 mg) were held within either a stainless steel mesh cone to allow gas flow through powder samples, or a stainless steel bucket for samples which liquefy. The sample was loaded inside a glove box, and then sealed in a transport vessel which was subsequently inserted into the dry loader, a container attached around the IGA reactor for air sensitive sample loading. With the sample transport vessel inserted, the dry loader was purged with argon for approximately 1 hour prior to exposing the sample. Each IGA sample container possesses a wire handle which hooks onto the balance hang-down as shown in Figure 2.2. A metallic 'arm' in the dry loader was used to pick up the sample container and hook it onto the balance hang-down. The reactor was then sealed using a copper gasket, and the dry loader was dismantled and replaced with the furnace. Once sealed, the reactor was evacuated (100 mbar min^{-1}) and then refilled with the chosen gas. A TGA-type experiment could then progress.

The second IGA instrument (IGA^n, Hiden Isochema) is unique in that it has been designed especially for use in conjunction with neutron scattering experiments at the ISIS Facility. It is quite similar in general layout and functionality to the IGA-MS, except that it does not have the option of a flowing gas mode, which precludes the use of mass spectrometry. It is, however, proofed for use with elevated pressures of ammonia, a feature which was used to advantage in this study as a synthesis method, as well as for neutron experiments. The balance and reactor components of the IGA^n are fixed to a standard Tomkinson flange (the standard flange used for ISIS instrument tanks) which allows for flexible use across the neutron scattering instruments available at ISIS. For sample loading and for experiments not involving the use of neutrons, the flange is bolted onto a custom-designed glove box, depicted in Figure 2.3. The glove box relies on a constant flow of argon to keep the atmosphere free of water and oxygen, rather than the recirculating purification system used in more advanced glove boxes. The glove box was purged for approximately 2 hours prior to sample loading.

Because of its application to neutron scattering experiments, which require larger sample sizes to compensate for the weak interaction of the neutron with most samples, the IGA^n can accommodate samples with a mass of up to 1 g. For neutron experiments, the best sample can is a bucket made of vanadium, which is essentially transparent to neutrons. Unfortunately, for

experiments which evolve or use hydrogen, vanadium will decrepitate, necessitating the use of other sample buckets. Quartz is amorphous, and so a good choice for diffraction experiments, although stainless steel is less reactive with alkali metal amides. The sample bucket was loaded onto the balance hang down, and the balance was then zeroed.

The sample was then loaded into the bucket (Figure 2.3b and c), hooked onto the balance hang-down, and then sealed into the reactor. The IGA^n has a choice of two reactors: a quartz reactor which does not give any diffraction peaks, but can only be used up to 1200 mbar and 400 °C, or a stainless steel reactor which can operate at up to 20 bar and 500 °C, but will give steel peaks in the diffraction data. For the neutron diffraction experiments examining the reaction of the alkali metal hydrides with ammonia, the quartz reactor was used with a vanadium sample bucket. For general synthesis reactions, the stainless steel reactor and bucket were used.

Once loaded, the reactor was then evacuated (100 mbar min^{-1}) and refilled with gas as required by the particular experiment. For neutron diffraction experiments, the IGA^n was then unbolted from the glove box and craned into the neutron instrument prior to the commencement of the experiment. Heating in the IGA^n was accomplished using heating elements above and below the sample.

2.3.3 Differential scanning calorimetry

The determination of the enthalpy of the reactions with associated mass loss, and the identification of thermal events without a change in the mass of the sample is useful ancillary information. Differential scanning calorimetry (DSC) is a method for measuring such enthalpic events in a sample. The DSC experiment involves placing the sample in a sample pan (usually alumina or aluminium) which is then placed on a heater. In parallel, a reference pan of the same type as the sample pan is located on a second heater. Both pans have a sensor which measures the heat flow to the pan. The pans are heated/cooled according to a defined temperature regime. By recording the difference between the heat flow required to keep the sample at the programmed temperature with that of the reference pan, the heat flow to or from the sample can be calculated. Most DSC experiments in hydrogen storage materials involve a linear increase in temperature. In these experiments, if the sample undergoes an endothermic transition (phase change, melting, decomposition...), then more heat will be required to keep heating the sample at the same rate as

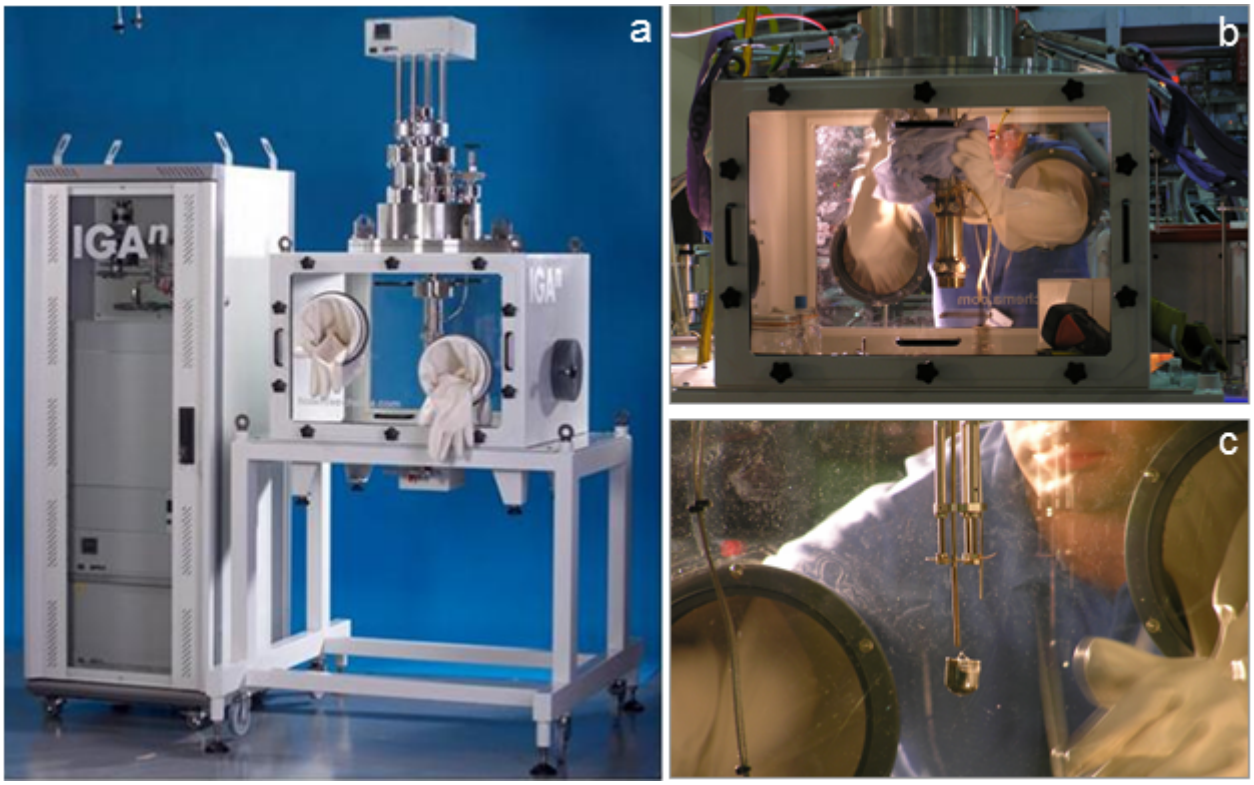

Figure 2.3: a) The IGA^n apparatus, with b) sample loading and c) the loaded position of the sample. Image credit STFC.

the reference pan. This is seen as a peak in the DSC heat flow trace. For exothermic events, the reverse is true, and a trough will be seen in the heat flow trace. The integral of the peak/trough gives the enthalpy of the transition.

DSC data in this thesis were collected on a Perkin Elmer STA 6000, which collects simultaneous DSC and TGA data, allowing the user to distinguish the thermal events which correlate with changes in the mass of the sample. The instrument was housed within a glove bag which was purged with argon prior to operation. For all DSC experiments, sample sizes in the range of 5–10 mg were used, loaded into open-lidded 30 μL alumina buckets without lids, and all of the experiments were performed under flowing argon gas atmospheres (30 sccm).

2.4 Structural Analysis

Structural analysis is a central component of the experimental work in this thesis, connecting the hydrogen storage properties of a material to its solid structure. In order to go beyond the determination of how much hydrogen is released from a material under a certain set of

experimental conditions and to examine the actual mechanism of hydrogen storage and release, structural analysis is an indispensable tool.

2.4.1 X-ray scattering

X-rays are the principal probe used for the structural analysis of crystalline materials. When X-rays are shone at a sample, they will be scattered by that sample. This scattering is largely due to the interaction of the X-rays with the electrons of the atoms in the sample. Interatomic spacings in solid materials are comparable to the wavelength of X-rays ($\sim 10^{-10}$ m, 1 Å), and so when the X-rays are scattered by the atoms in the solid, they will diffract. For crystalline materials, which consist of well-ordered planes of atoms in a repeating structure, the scattered X-rays will be coherent, and so will constructively interfere at predictable points in space. The well-known Bragg condition (Equation 2.1) relates the angle between the incoming X-ray beam and the constructive interference (θ) with the wavelength of the X-rays (λ) to give the spacing between the planes of atoms in the sample which gives rise to that interference (d, d-spacing).

$$2d \sin\theta = \lambda \tag{2.1}$$

For powder (or polycrystalline) samples, which are the subject of this work, diffraction from randomly-orientated crystallites results in constructive interference occurring in cones emanating from the sample, as shown in Figure 2.4, as opposed to the discrete spots observed for single crystal samples. In most experimental setups, a point (1D) detector is scanned through an arc around the sample, intersecting these cones at single points. Recording the intensity of the scattered X-rays in this way results in the classic powder X-ray diffraction (PXRD) pattern: a plot of scattered X-ray intensity versus angle with various peaks (Bragg peaks) corresponding to the regions of constructive interference. Of course, the use of an area (2D) detector allows the user to sample the entire ring of diffraction intensity, giving much higher intensity and more information on the nature of the polycrystalline sample. The intensity of the rings can then be integrated to generate the PXRD pattern.

The collection of diffraction data in this way allows the spacings of planes of atoms to be determined from the Bragg relation, which in turn gives the symmetry of the arrangement of the atoms in the crystal structure. This symmetry may be described in a systematic manner from

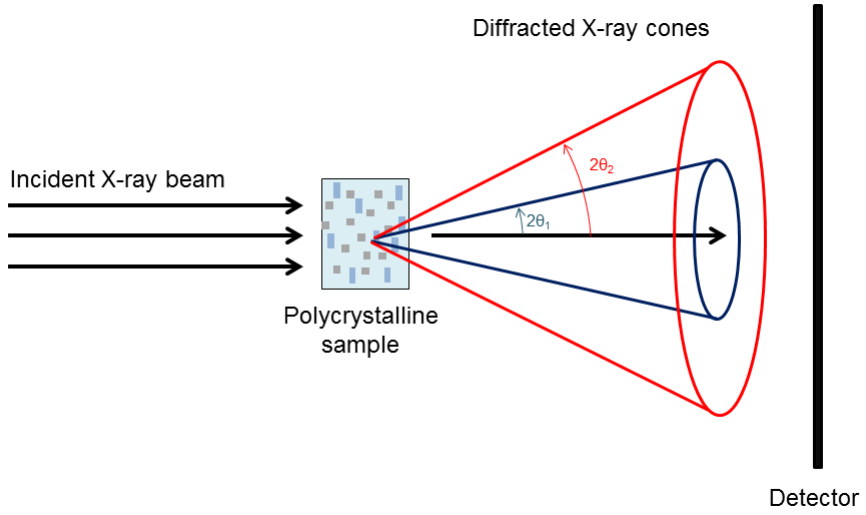

Figure 2.4: Depiction of the diffraction of X-rays from a polycrystalline sample.

the starting point of the asymmetric unit, the simplest description of the relative positions of the atoms in the structure. This unit is translated into the unit cell, the smallest representation of the bulk crystal structure, by the application of symmetry operations to the asymmetric unit; the combination of symmetry elements is called the space group of the crystal structure. In total there are 230 space groups, built up from the combination of the various symmetry elements. Firstly, crystal structures may be defined by the lattice family, of which there are seven. Lattice families are described by the relationship between the lengths of the axes of the unit cell (a, b, c) and the values of the angles between those axes (α, β, γ). These seven families expand into 14 basic lattices (Bravais lattices) when different centering of the lattice points are considered. The various lattice families and Bravais lattices are described in Table 2.4. These lattices describe the basic translational symmetry of the unit cell. Next, there are 32 crystallographic point groups. These groups describe a set of symmetry operations (rotations, reflections, inversions) around the central point in the lattice which can be applied to the lattice without changing the position of any of the atoms. Finally, there are translational symmetry elements (glide planes, screw axes) which combine translation of atoms through the lattice with a reflection or rotation, respectively. Taken together, these symmetry elements combine to give the 230 unique space groups, which encompass all possible crystal structures.

The angular positions of the Bragg peaks give some insight into the symmetry of the unit cell, but do not describe the precise locations of the atoms inside the unit cell. This information is

Table 2.4: The lattice families and their associated Bravais lattice types used to describe crystal structures.

Lattice family	Lattice centring types	Axial length relations	Axial angle values
Cubic	Simple, body-centred, face-centred	$a = b = c$	$\alpha = \beta = \gamma = 90°$
Tetragonal	Simple, body-centred	$a = b \neq c$	$\alpha = \beta = \gamma = 90°$
Orthorhombic	Simple, body-centred, base-centred, face-centred	$a \neq b \neq c$	$\alpha = \beta = \gamma = 90°$
Hexagonal	Simple	$a = b \neq c$	$\alpha = \beta = 90°, \gamma = 120°$
Rhombohedral	Simple	$a = b = c$	$\alpha = \beta = \gamma \neq 90°$
Monoclinic	Simple, base-centred	$a \neq b \neq c$	$\alpha = \beta = 90°, \gamma \neq 90°$
Triclinic	Simple	$a \neq b \neq c$	$\alpha \neq \beta \neq \gamma$

contained within the intensity of the peaks. However, the intensity of the scattering is determined by a number of factors aside from the precise location of the atoms in the structure, including the the diffracting power of the atoms present, how that diffracting power varies with the diffraction angle, the character of the powder sample, the thermal motion of the atoms in the structure and the multiplicity of the reflection (how many equivalent atomic planes have a particular d-spacing). In this study, the analysis of diffraction patterns was simplified in that crystal structures for the main species were already known, removing the need to solve the crystal structure *ab initio*. A summary of these structures is shown in Table 2.5. These known structures were used as starting points for analysis of the experimental data, with the structures then refined against the experimental data as described in Section 2.4.3. Once a satisfactory unit cell is obtained, the average long-range crystal structure can be described by replicating the unit cell in three dimensions.

PXRD for the purposes of pre- and post-reaction phase identification and quantification was performed using laboratory X-ray diffractometers. Three instruments were used for this work: a PANalytical X'Pert Diffractometer was used for phase identification, while a PANalytical Empyrean and a Rigaku SmartLab diffractometer were each used for high-resolution studies and

Table 2.5: Selected data from the crystal structures of the most commonly-studied materials in this thesis.

Compound	Space group	a, b, c (Å)	α, β, γ (°)	Notes
Lithium hydride, LiH	$Fm\bar{3}m$	4.08321(6)	90, 90, 90	
Lithium amide, $LiNH_2$	$I\bar{4}$	5.04309(7), 5.04309(7), 10.2262(3)	90, 90, 90	
Lithium imide, Li_2NH	$Fm\bar{3}m$	5.0769(1)	90, 90, 90	High T phase
Lithium oxide, Li_2O	$Fm\bar{3}m$	4.610	90, 90, 90	
Sodium hydride, NaH	$Fm\bar{3}m$	4.89	90, 90, 90	
Sodium amide, $NaNH_2$	$Fddd$	8.949(6), 10.456(5), 8.061(4)	90, 90, 90	
Sodium, Na	$Im\bar{3}m$	4.30	90, 90, 90	
Potassium hydride, KH	$Fm\bar{3}m$	5.704	90, 90, 90	
Potassium amide, KNH_2	$Fm\bar{3}m$	6.129	90, 90, 90	High T phase
Lithium magnesium imide, $Li_2Mg(NH)_2$	$Iba2$	9.8937, 4.9914, 5.2238	90, 90, 90	
Lithium calcium imide, $Li_2Ca(NH)_2$	$P\bar{3}m1$	3.5664(3), 3.5664(3), 5.9540(8)	90, 90, 90	
Calcium imide, CaNH	$Fm\bar{3}m$	5.143(1)	90, 90, 90	

quantitative phase analysis. The principles of operation of these instruments are very similar, and so will be discussed together.

In laboratory diffractometers, electrons generated by passing a current through a filament are accelerated through a 45 kV potential difference high voltage tube. At the end of the tube, the electrons impact a metal anode (copper in the case of these three instruments). As the electrons lose energy, they emit a range of wavelengths of radiation that includes X-rays. The wavelength range emitted has a number of peaks which correspond to electronic transitions in the copper atoms. These peaks arise due to the fact that the incident electrons have sufficient energy to remove core shell electrons from the copper atom. When this occurs, electrons from higher shells will drop down energy levels to take their place, losing energy in the form of X-rays with the characteristic energy for that energy level transition. One of these transitions, the copper $K_{\alpha 1}$ transition (λ= 1.54051 Å), is selected for the PXRD experiment through the use of a germanium (111) crystal, which acts as a monochromator.

For the PANalytical instruments, a flat plate sample geometry was used. The sample was hand-ground in a glove box, and placed on a microscope slide coated in a thin film of vacuum grease. Care was taken to ensure that the powder sample was as flat as possible. The slide was then inserted into an airtight sample container with a polyvinyl acetate window for X-ray transmission. For the Rigaku SmartLab, borosilicate capillaries (0.7 mm i.d.) were used to house the sample, sealed at the end using vacuum grease. Diffraction data were generally collected in the angular range of 3-80°.

For instances where the speed and/or resolution of laboratory-based diffractometers are insufficient, synchrotron-based diffractometers are the instrument of choice. Synchrotrons are large facilities that can accelerate electrons to very high energies (GeV). Instead of accelerating electrons towards a metal target, bunches of electrons are generated in an electron gun, accelerated through a linear accelerator and then injected into a booster synchrotron. In the synchrotron, variable magnetic fields are used to guide the electrons around a pseudo-circular path so they repeatedly pass through electric field regions until they attain their target energy. Once they reach this energy, they are then passed into the main storage ring, the largest component of the synchrotron complex. The storage ring is a type of synchrotron where the electron energy is kept constant; acceleration sections are used to replace energy lost through generation of synchrotron

radiation rather than to increase the energy of the electrons. The ring in fact consists of a number of straight sections joined together by magnets which bend the bunch of electrons around the ring. In the process of this bending, the electrons lose energy in the form of electromagnetic radiation such as X-rays. By tuning the magnetic field which the electrons are subject to, the characteristics of the radiation can also be tuned. The light produced during this bending is guided into an experimental hutch (beamline) for scientific use: in this case, for PXRD analysis. The use of X-rays generated by a synchrotron is advantageous primarily because of the very high brilliance of the light produced (at least five orders of magnitude more intense than that of the best laboratory instruments), which allows for the very rapid collection of high quality data. This leads to more reliable phase quantification with lower detection limits for minor phase components. This intensity also facilitates kinetic experiments where diffraction data can be collected in seconds to monitor the course of fairly rapid chemical reactions, a property which has been used extensively in this work. Furthermore, the wavelength of the X-rays can be effectively tuned to the requirements of the experiment, minimising the potential for beam damage and excessive absorption of the X-rays.

Two synchrotron PXRD beamlines were used in this work: I11[190] at the Diamond Light Source and ID31 at the European Synchrotron Radiation Facility (ESRF). Diamond Light Source is a 3 GeV facility, whereas the ESRF is 6 GeV. Once again, the principles of operation of these beamlines are very similar. Both beamlines use multi-analysing crystal (MAC) detector banks for high-resolution studies. These units consist of a bank of nine detectors which are preceded by silicon (111) crystals which ensure that only X-rays scattered at precisely the specified angle proceed to the detector. ID31 has a single MAC bank, whereas I11 has five MAC detector banks. Diffraction data were collected by scanning the MAC detector/s through the 2-theta arc around the sample. Data were collected in steps of 0.002°, though for kinetic analysis, were generally re-binned to 0.005° steps to improve the signal-to-noise ratio. Data were collected in the 2-theta range of 0.002–28° on ID31, where the wavelength of the X-rays was 0.39982 Å. On I11, the data were collected in the range of 0.002–150°, with a wavelength of 0.81861 Å.

For all of the work in this thesis, samples were housed in capillaries; 0.7 mm i.d. borosilicate capillaries were used for room temperature sample measurements, and 1 mm i.d. single crystal sapphire capillaries for the *in situ* studies. On I11 there is a facility for automated measurement

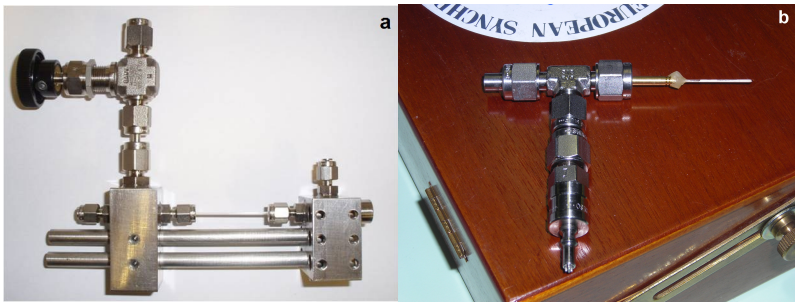

Figure 2.5: The *in situ* gas cells used on a) I11 and b) ID31, showing sapphire capillaries attached to the two Swagelok manifolds.

of capillary samples, the I11 robot. For these samples, the powdered sample was loaded into the borosilicate capillary and flame sealed using a propane torch. The sealed capillary was then mounted onto a brass sample holder and attached to a magnetic base. For analysis, the robot arm picked up the sample holder and placed it on the magnetic mount on the diffractometer. These samples were spun while the diffraction data were collected in order to minimise any preferred orientation effects.

A number of the *in situ* experiments required sample environments which could deliver gas to the capillary. The two setups used are shown in Figure 2.5. The sapphire capillaries into which the samples were loaded are capable of withstanding pressures up to 200 bar, far in excess of the pressures required for these experiments. They are also chemically inert to alkali metal amides at high temperatures, unlike borosilicate and quartz capillaries. As the experiments involved variation in gas pressure, plugs of quartz wool were placed at either side of the powder sample to minimise the potential for the sample to dislodge with changing pressure.

The gas cell used at I11 was set up for use with up to 150 bar of gas pressure[191]. The capillary, open at both ends, was screwed into the cell in a glove box and the cell was then sealed via the Swagelok valve. Single crystal sapphire is not very resistant to torsional strain, so care was taken to alternate between tightening each side of the cell to avoid unnecessary strain. The cell was then mounted on the diffractometer and connected to the gas line. The delivery of gas to the cell was controlled using a custom-built gas panel, with the pressure monitored by a digital display on the panel. Gas loading of the cell was performed slowly to prevent rapid changes in pressure which might have dislodged the sample. Due to the geometrical setup of the surrounding cell, and the high thermal conductivity of the sapphire capillary, it was necessary to

Table 2.6: Reaction conditions used during in situ PXRD for hydrogenation-dehydrogenation of the Li-N-H hydrogen store

Beamline	Initial Sample	Temp (°C)	Hydrogenation pressure (bar)	Hydrogenation time (min)	Dehydrogenation time (min)
I11	Li_3N	230, 265, 290	0.5, 1.0, 3.0	Variable	Variable
I11	Li_3N+ 0.03 $TiCl_3$	230	0.5, 1.0, 3.0	Variable	Variable
I11	Li_2NH+LiH (cycled)	265	3.0	120	60
ID31	Li_3N	265	2.0 (100 ppm N_2)	60	90
ID31	Li_3N	265	2.0 (20 mol% N_2)	60	90

conduct a temperature calibration for the I11 setup. A sample of annealed platinum was heated from 50–400 °C in steps of 50 °C. The *a* lattice parameter extracted by Rietveld refinement of the diffraction data at each temperature was compared with literature values[192] and, using the known thermal expansion of platinum, a temperature calibration equation constructed. Based on these data, the calibration equation used to relate the temperature of the hot air blower to the actual sample temperature, where T is temperature (°C) was: $T_{sample} = 0.69(2) * T_{blower}$.

On ID31, the gas cell used has a slightly simpler design as it is intended for use with gas pressures of less than 10 bar. The sapphire capillary was sealed at one end with epoxy resin, the sample was loaded and then placed in a cylindrical brass sample holder, held in place with resin. This holder was then screwed into the Swagelok cell, attached to the gas delivery system and mounted on the diffractometer. The pressure in the capillary was controlled by an automated system.

Table 2.6 shows the various reaction conditions used for the in situ experiments, which are discussed in more detail in the relevant results Chapter.

In the analysis outlined up to this point, the scattering data which does not form part of a Bragg peak is largely ignored, with the background modelled as a polynomial function. However, there is structural information present in all of the scattering data which is collected in a diffraction experiment. The Bragg peaks gives an indication of average structure, but examining

all of the scattering data (total scattering data) can give insight into local and mesoscale structure, including order and disorder which is not observed in the average structure. Structural information can also be determined for amorphous or liquid materials, which do not give Bragg peaks. These kinds of insights are gathered from analysis of total scattering data. For example, taking the Fourier transform of these data can be used to give a pair distibution function, which shows the density of atom pairs at a given radial separation in a sample.

X-ray total scattering data were collected on a PANalytical X'Pert Diffractometer equipped with a silver X-ray source, which is better suited to total scattering analysis than a copper source because of the shorter-wavelength X-rays produced, giving scattering information over a wider length scale.

2.4.2 Neutron scattering

Of course, X-ray scattering does have some limitations. In particular, it is difficult to observe light elements using X-rays, since the scattering is proportional to the number of electrons in the atom. Figure 2.6a shows the X-ray coherent scattering cross-sections for the main elements studied in this thesis, showing clearly that, in the presence of other elements, it is essentially impossible to see hydrogen with X-rays. One way to avoid this problem is to use a different probe: neutrons. By wave-particle duality, neutrons of the correctly chosen energy will have a wavelength which is applicable for diffraction analysis of materials. However, they differ from X-rays in that they are scattered by nuclei, rather than electrons. Furthermore, there is no clear trend in the scattering cross-section with atomic number. Indeed, even different isotopes of the same element can have markedly different interactions with neutrons. As can be seen in Figure 2.6b, hydrogen has a reasonably large coherent neutron scattering cross-section compared with the other elements of interest, which should make it reasonably straightforward to observe with neutrons.

Unfortunately, for diffraction experiments the situation is not quite that simple — as well as a coherent neutron scattering cross-section, each element also has an incoherent scattering cross-section. Incoherent scattering does not result in the constructive interference which is the basis of diffraction; rather, it causes uniform scattering in all directions, essentially increasing the background signal of the measurement. Hydrogen has the largest incoherent neutron scattering

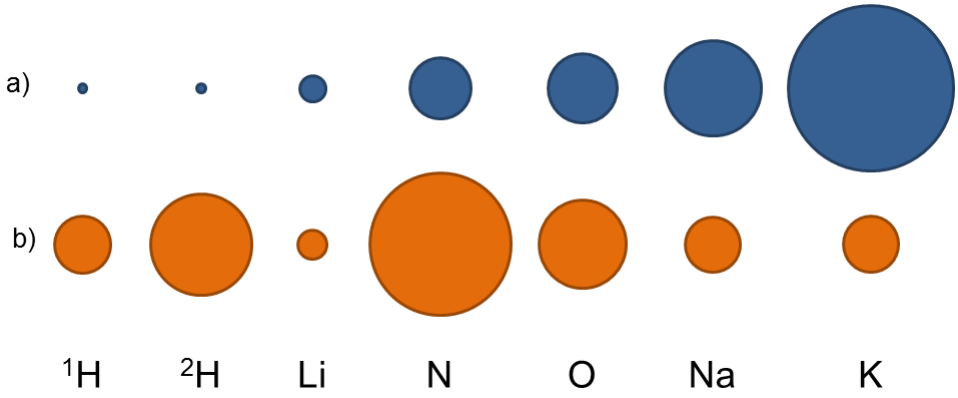

Figure 2.6: a) X-ray and b) neutron coherent scattering cross-sections for selected elements and isotopes[193, 194]. Cross-sections are relative sizes and are accurate within the group (i.e. the X-ray and neutron values for a single element are not directly comparable).

cross-section of all the elements, and so getting useable signal-to-noise ratios in the presence of significant quantities of hydrogen is difficult. Thankfully, due to the isotopic variation in scattering cross-sections, deuterium is a good substitute for hydrogen in neutron powder diffraction (NPD); it has a much smaller incoherent neutron scattering cross-section, and a larger coherent neutron scattering cross-section, than hydrogen. Of course, the effect of isotopic substitution should be considered in the interpretation of results collected from deuterated analogues, however, in NPD the differences appear to be minimal in most cases. As such, deuterated analogues were used wherever possible in the NPD work presented in this work.

NPD also has some practical differences to PXRD. Firstly, neutrons are more difficult to produce than X-rays, and so generally NPD experiments are restricted to central facilities such as ISIS, described below. It is also difficult to produce a high flux of neutrons, which, combined with the fact that neutrons are weakly interacting particles, means that the collection times for equivalent signal-to-noise are significantly higher using neutrons than for X-rays. Thus, significantly larger sample sizes tend to be used in NPD experiments (of the order of 100–1000 mg). However, the weak interaction also means that neutrons penetrate the sample well, providing a probe of the bulk sample behaviour, and that more complex sample environments can be readily used, since there is less problem with obstruction of the signal.

All of the neutron scattering experiments reported in this thesis were performed at the ISIS facility, the United Kingdom's neutron source. A schematic of the facility is shown in Figure 2.7. ISIS produces neutrons via a process called spallation. Similarly to a synchrotron X-ray

source, the process of producing neutrons in a spallation neutron source begins with particle acceleration. However, in order to produce neutrons, the particles which must be accelerated are protons, rather than electrons. At ISIS, the ion source actually generates hydride anions initially, which are accelerated down a linear accelerator. As they come into the synchrotron, they pass through a thin sheet of aluminium oxide, which strips them of their electrons, leaving the desired protons. The protons are accelerated to 800 MeV in two bunches in the synchrotron, and once they reach their target energy, they are guided towards one of the target stations. The target is a heavy metal. In the case of ISIS, it is tungsten. When the protons strike the target, they are travelling at around 84 % of the speed of light, and so have sufficient energy to destabilise the nucleus of a tungsten atom. Once this destabilisation occurs, the nucleus may release neutrons. Typically, 20–30 neutrons are released for each proton which impinges on the target.

The neutrons formed by spallation are much too energetic to be useful for diffraction experiments. In order to reduce their energy to the useful range, the neutrons emitted from the target encounter a moderator which dissipates the energy of the neutrons through intermolecular collisions. Depending on the application, the moderator may be water (298 K), liquid (100 K) or solid (26 K) methane, or liquid hydrogen (20 K). Once the neutrons are moderated, they travel down a guide to the instrument where they are used for experiments. This cycle is repeated with a frequency of 50 Hz, with four out of every five pulses directed towards Target Station 1, and the remainder to Target Station 2.

The production of neutrons in this way influences the manner of collecting diffraction data. The other main method of neutron production, from a nuclear reactor, closely resembles X-ray diffraction, where the neutrons are constantly produced, monochromated, and then the diffracted intensity is measured across the desired angular range. Instead, with spallation, the neutrons are produced in pulses, so the time of the production of the neutrons can be known precisely. This gives the opportunity to use all the neutron wavelengths present in the moderated neutron pulse for the diffraction experiment, giving a significantly higher flux than that of a nuclear source. In order to do this, you must conduct a fixed angle, variable wavelength experiment: the detectors are kept stationary, and the time the neutrons arrive at the detector is measured. Hence, this form of NPD is termed time-of-flight NPD. The time-of-flight of the neutrons relates to their energy, and, therefore, their wavelength. Higher energy (shorter wavelength) neutrons have a

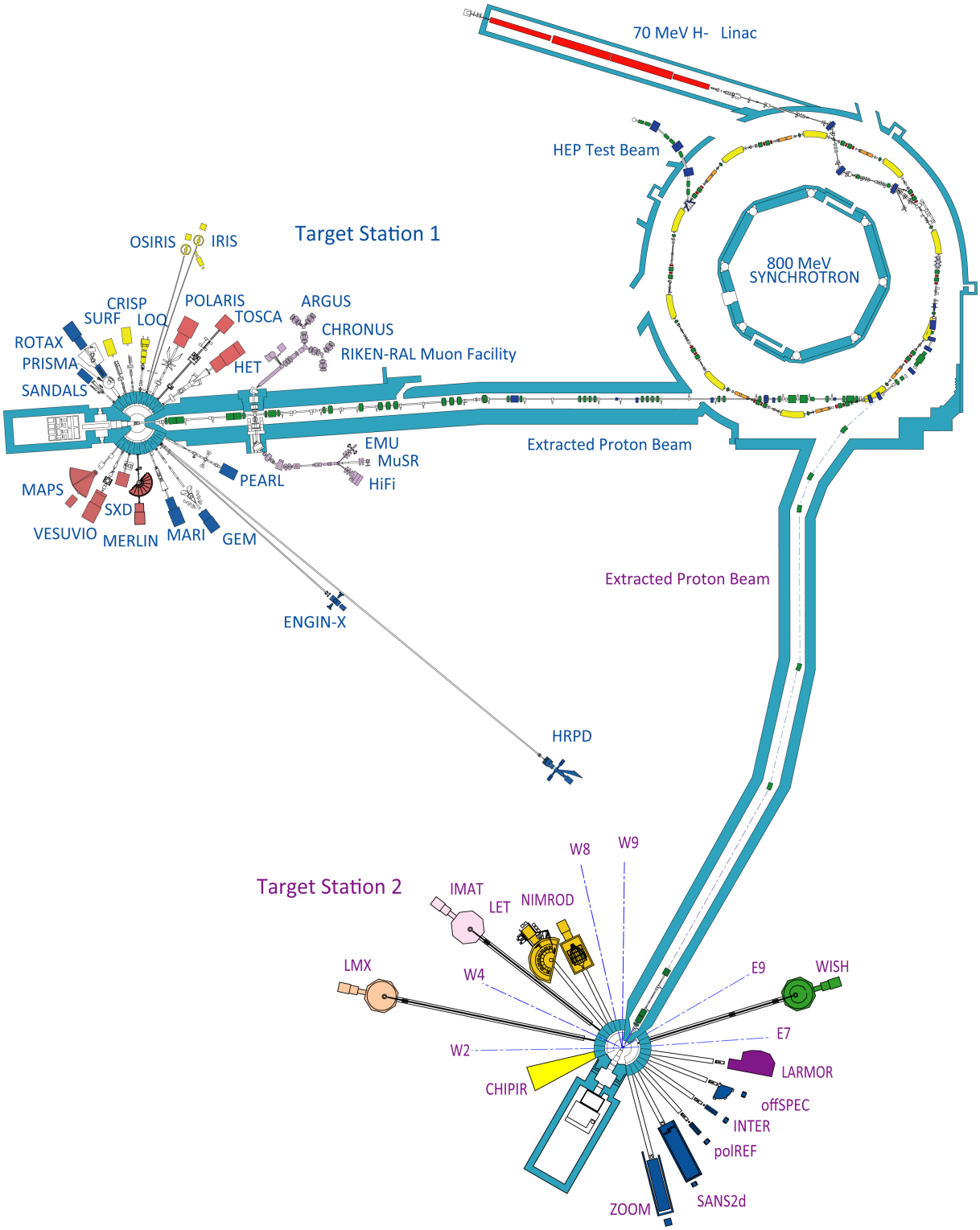

Figure 2.7: The ISIS neutron and muon facility, showing the synchrotron, two targets stations and their associated instruments. Image credit STFC.

higher velocity and so will arrive at the detectors first. Each static detector will collect a different range of neutron energies, depending upon the angle of the detector.

Three ISIS instruments were used to collect the elastic neutron scattering data in this thesis: GEM[195], POLARIS[196] and NIMROD[197]. As can be seen in Figure 2.7, GEM and POLARIS are on Target Station 1, whereas NIMROD is on Target Station 2.

GEM and POLARIS are both high-flux, medium-resolution diffractometers, and have very similar setups. The sample tanks of the instruments are shown in Figure 2.8. For reference, these tanks are 2–3 metres tall. Typically, a Tompkinson flange is bolted onto the sample port (the circular hole shown on each tank). For standard measurements, the sample was loaded into a 6 or 8 mm i.d. cylindrical vanadium can sealed with indium wire in a glove box, and then screwed onto a centre stick which is inserted into the flange to hold the sample in the beam position (normally approximately 30 cm below the flange height). Once inserted, the sample tank was evacuated to reduce air scattering, and then the measurements were completed. The sample tanks consist of a series of detector banks surrounding the sample position, covering a significant portion of the solid angle around the sample to increase the proportion of scattered neutrons detected. The detector banks are situated from very low angles to high-angle backscattering detector banks. The resolution of the diffraction pattern improves with increasing angle (the resolution varies with cot θ), so the backscattering detectors have the highest resolution.

NIMROD, the third instrument used at ISIS, is similar to the other diffractometers, but its setup is optimised to collect scattered neutrons over a very wide range of length scales — from less than 1Å up to as large as 300 Å. The purpose of collecting neutron scattering data over such a wide range is to allow for the collection of good total scattering data. In a total scattering experiment, all of the scattered neutrons are analysed. Therefore, much care must be taken in collecting the experimental data, with a series of background scans collected in addition to the sample data, such that the scattering due to the sample can be isolated from that of the background, instrumentation and sample environment.

2.4.3 Rietveld Refinement

Once powder diffraction data is collected, it must be analysed in order for useful structural information to be extracted. One of the most effective methods for doing this for crystalline

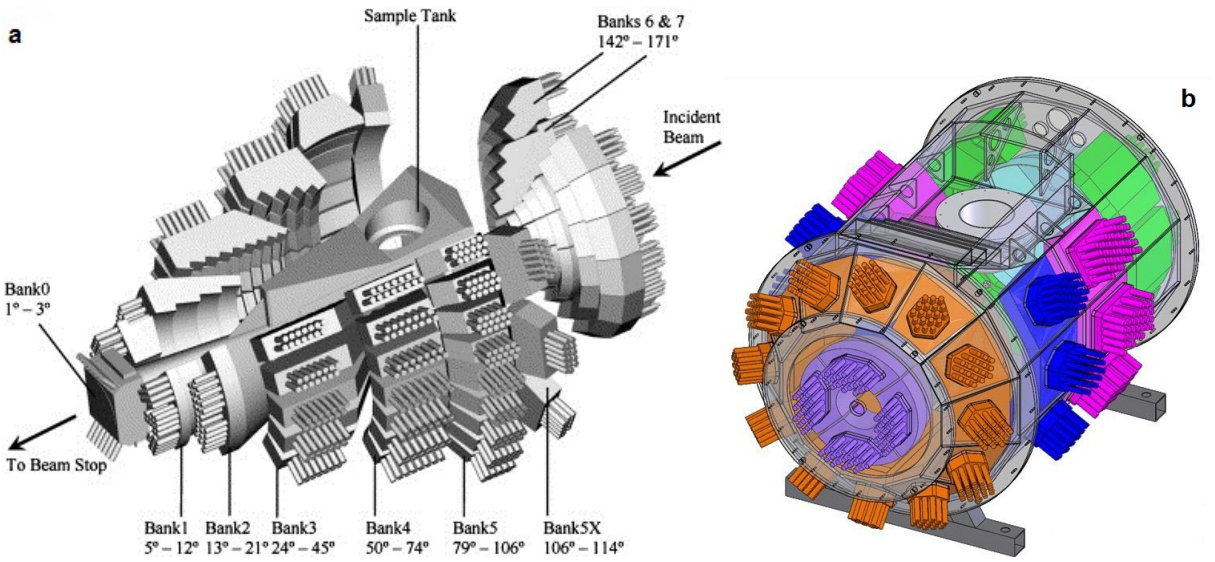

Figure 2.8: The sample tanks of the a) GEM and b) POLARIS diffractometers at ISIS, showing the positions of the different banks of neutron detectors. Part a) is reproduced from Ref. [195]. Copyright 2005 Elsevier. Part b) image credit STFC.

structures is the Rietveld method, a weighted least-squares refinement method developed in the 1960s[198]. The basic principle of the method is as follows: the user inputs a starting structural model, including the space group, unit cell parameters, atomic coordinates, thermal parameters, and crystallite size and strain parameters. Combined with inputs on the nature of the experimental data (source, wavelength, peak shapes etc), this generates a calculated model of the experimental data. Each calculated data point ($y_{i(calc)}$) is then compared to the observed data ($y_{i(obs)}$), with the squared difference between them weighted by the inverse of the squared error in the data point (w_i). A weighted residual chi-squared function (χ_0^2) is then calculated across all of the data points (Equation 2.2):

$$\chi_0^2 = \sum_{i=1}^{n} w_i \left[y_{i(obs)} - y_{i(calc)} \right]^2 \tag{2.2}$$

The purpose of the refinement is to minimise the residual, such that the calculated data optimally fits the observed data. This is achieved by the user determining the parameters which should be varied. A change which improves the residual is accepted, and the process then continues in an iterative fashion. The goodness of the refined profile fit to the experimental data is generally measured using a weighted profile R value (R_{wp}), Equation 2.3. This value is compared to an expected R value (R_{exp}, Equation 2.4), which is calculated on the basis of the

number of observables (N_o) and the number of refined values (N_v) in the model system.

$$R_{wp} = \left[\frac{\chi_0^2}{\sum w_i y_{i(obs)}^2} \right]^{0.5} \tag{2.3}$$

$$R_{exp} = \left[\frac{N_o - N_v}{\sum w_i y_{i(obs)}^2} \right]^{0.5} \tag{2.4}$$

The iterative refinement generally continues until the R factor converges, hopefully on a value close to the expected R factor. In practice, the goodness-of-fit is assessed by a combination of the R factor and a visual assessment of the match between the calculated and observed diffraction patterns; often small discrepancies are not effectively accounted for by simple use of the R factor. A difference plot showing the absolute intensity difference between the obeserved and calculated patterns is often included with graphs of diffraction data as a guide to the eye.

In the refinement, care must be taken in the choice of which and how many parameters to vary in any one cycle. Chemical knowledge must be used to assess the sensible range of a given parameter, and a knowledge of the covariance of the various parameters is an important guide. In practice, the most common approach is to first allow the lattice parameters of the structure to vary, along with the background (which is modelled by a high-order polynomial expression), the zero error correction and the scale factor, which determines the magnitude of the diffraction peaks. Once these values are acceptable, the atomic positions, thermal parameters, size and strain can begin to be varied, until a suitable structural model is obtained. For multiphase mixtures, the various scale factors can be converted into a percentage composition, which is crucial for kinetic analysis and determination of sample purity.

In this work, TOPAS Academic[199] was the program used to conduct these refinement procedures. The program uses a least-squares approach with additional minimisation methods included[200, 201]. In all cases, the model diffraction pattern is generated in a text file which is input into the TOPAS Academic program, which then performs the optimisation routine. The program is very flexible in that the user is free to define their own peak shape functions and variables as required. This allows the user to generate physical models for peak shapes based on their particular experimental setup. For example, the neutron diffraction data is modelled using a custom-defined peak shape for the ISIS neutron source, developed by David[202] and based

upon the peak shapes proposed by Ikeda and Carpenter[203]. The flexibility of the program allows for a multi-file refinement to be undertaken, where data from multiple detector banks in a NPD experiment can be used to refine a structural model simultaneously.

Another very useful feature of the TOPAS Academic program is the ability to run in batch mode. In this process, a refinement is carried out on an initial data set and a script is generated which uses this refinement as the starting point for the refinement of the next data set. The output from the second refinement is then used as the initial script for the third data set, and so on. Critical parameters in the refinement are output at the end of each refinement in the series, allowing for easy extraction of refined physical parameters such as weight percent, cell parameter etc.

It is worth noting that the batch approach works best when only small changes occur between the data sets. In order to prevent unrealistic features being incorporated into the batch refinement process, the physical parameters of each phase were carefully constrained. As an example, for the purposes of monitoring the progress of a reaction at a given temperature the lattice parameters, crystallite size and strain parameters and isotropic thermal parameters for each phase were generally held constant, while the scale factors were allowed to vary. The initial appearance and final disappearance of phases were generally refined manually.

2.4.4 Total scattering analysis

The silver-source X-ray and NIMROD data were analysed using the GudrunX and GudrunN programs[204, 205], respectively, which were developed by Soper at the ISIS Facility. This program takes the raw diffraction data and applies a set of corrections to obtain the true differential scattering cross-section of the sample. The software performs corrections to the data for multiple scattering, absorption, and subtracts the various background data sets described above to give the scattering from the sample alone. Once this is obtained, the data may be transformed to give pair distribution functions, or used to model the structure directly.

2.5 Vibrational analysis

In terms of understanding the behaviour of the various hydrogen storage materials, information about the dynamics of the species involved is valuable. Phonon modes and intramolecular vibrations give important insights into the bonding in the sample, and can help to unravel reaction mechanisms. Although some of this information can be inferred from structural analysis, measuring these dynamics directly is advantageous, and can be achieved rapidly using laboratory-scale apparati.

2.5.1 Raman spectroscopy

Along with infrared spectroscopy, Raman spectroscopy is the primary laboratory-scale method for vibrational analysis. Raman differs from infrared in that it is a light-scattering technique, whereas infrared involves the absorption of infrared radiation which has energy corresponding to a vibration in the sample. In Raman, monochromatic light from a laser is shone on the sample, and the energy of the scattered light is measured. The vast majority of the light scattered from the sample will do so elastically. However, a small amount will be scattered inelastically. The change in energy is related to the vibrations of the sample: when the light impinges on the sample, it will raise the energy of the sample to a higher 'virtual' energy state. If the scattering is inelastic, and the light causes the sample to relax from that higher energy state into an excited vibrational state, the frequency of the light will change. The change in frequency of the inelastically-scattered light relates directly to the energy of the vibration in the sample. Usually, Raman spectroscopy measures energy loss in the scattered light, although energy gains are possible as well.

In this work, Raman spectra were recorded using a Bruker Senterra Raman microscope system. Samples for analysis were loaded into 0.7 mm i.d. borosilicate capillaries and sealed with vacuum grease. The sample was then placed on the microscope stage, aligned and brought into focus using the motorised XY stage. Once a grain of the sample was in focus in the correct position, the system doors were locked and the light used for focussing was extinguished. Raman analysis was performed using a 532 nm laser light, chosen depending on the quality of the signal obtained, and whether any fluorescence was observed. After checking the quality of the signal, the Raman spectrum was recorded using two co-additions of two-second data collections.

2.6 Ammonia decomposition experiments

Ammonia decomposition reactions were performed in two cylindrical, 316 stainless steel reactors with internal volumes of 46.9 cm^3 and 21.3 cm^3, fitted with an inlet gas pipe running from the reactor lid to approximately 5 mm from the base of the reactor, an outlet gas pipe from the lid, and a thermocouple monitoring the internal temperature, shown in Figure 2.9a. For some of the later experiments, the internal surfaces of these reactors were coated with nickel using an electroless plating method in order to prevent degradation of the reactor surface, which was influencing experimental reproducibility. Ammonia gas was supplied to the reactor via a custom-designed gas control panel (Figure 2.9b) where the inlet gas flow was controlled using a mass flow controller (HFC-302, Teledyne Hastings Instruments) and the outlet gas flow was measured using a mass flow meter (HFM-300, Teledyne Hastings Instruments). The gas species exiting the reactor were characterised using a Hiden Analytical HPR-20 QIC R&D mass spectrometer system. The sensitivity factors[1] of the gas species measured were calibrated using a certified gas mixture of composition ammonia (2 %), hydrogen (2 %), nitrogen (2 %) and argon (94 %, balance). The mass spectrometer was set to auto-range for the gas values, with detection using a Faraday cup detector. The mass spectrometry data were recorded at the same time as the flow in to and out of the reactor, the reactor temperature and system pressure. The m/z values routinely monitored in these experiments were m/z = 2 (H_2), 17 (NH_3), 28 (N_2), 32 (O_2) and 40 (Ar).

Conversion efficiencies were calculated using a custom-written program written by Dr Thomas Wood using the Python code. This program removes the background signals of the ammonia, nitrogen and hydrogen traces (the signals observed during argon flow, and the hydrogen and nitrogen signals seen when ammonia is flowing through the reactor at room temperature), and accounts for the discontinuities in the signals when the detector switches which range it is using (seen as a vertical discontinuity in the mass spectrometry plot). Once these signals are corrected, the conversion efficiency is calculated by expressing the ammonia signal as a percentage of the total signal, and thus the conversion efficiency is 100 % minus the percentage of ammonia in the gas stream.

[1] the sensitivity factors account for the difference in the ease of ionisation of different species, and for the fragmentation of those species in the mass spectrometer, which has the effect of artificially lowering their signal.

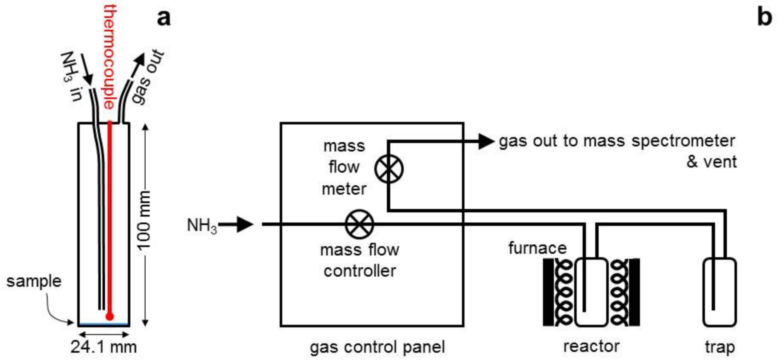

Figure 2.9: Reactor and experimental setup: a) A typical 46.9 cm^3 reactor showing ammonia inlet, gas outlet and thermocouple temperature probe positions, with 0.5 g $NaNH_2$ drawn to scale and b) experimental setup, where the inlet ammonia gas flow is controlled prior to the reactor and the outlet gas flow is monitored by a mass flow meter and analysed by a mass spectrometer. Reprinted with permission from [206]. Copyright 2014 American Chemical Society.

Chapter 3

The Li-N-H hydrogen store

3.1 Overview and Experimental

The lithium amide - lithium hydride hydrogen storage system is set apart from other complex hydrides by the facile nature of its reversible hydrogen storage. The hydrogen storage and release reaction considered in this Chapter, the interconversion of lithium amide and lithium imide shown in Equation 3.1, is reversible at around 200 °C, and requires only a few bar of hydrogen to achieve appreciable hydrogenation kinetics at these temperatures.

$$LiNH_2 + LiH \longleftrightarrow Li_2NH + H_2 \tag{3.1}$$

This chapter considers the mechanism by which the Li-N-H system stores and releases hydrogen both as a means to uncover the limiting factors in the system itself, and as a model for reversible hydrogen storage in other complex metal hydrides. As was discussed in the Introduction, there has been significant interest in this reaction mechanism.

In the first part of this Chapter, the results of an *in situ* synchrotron X-ray powder diffraction study of Equation 3.1 are reported. In this study, two samples were used: lithium nitride and lithium nitride doped with 3 mol% of titanium (III) chloride. For each sample, the powder was loaded into a sapphire capillary and housed in the I11 Gas Cell described in Section 2.4.1. The cell was then mounted on the beamline, and the capillary holding the sample was evacuated to remove residual argon from the glove box, then filled with helium gas to the working pressure and tested for leaks. The helium was then removed and replaced with hydrogen gas. Diffraction

data were collected at room temperature for 30 minutes. Due to the use of the gas cells, full spinning of the sample was not possible. Instead, the cells were rocked over a 60° range. The samples were heated using a hot air blower to hydrogenate the lithium nitride to lithium amide and lithium hydride. Dehydrogenation reactions were performed under dynamic vacuum, with the pressure in the cell reading less than 10 mbar. Diffraction data were collected using the MAC detectors, with a counting time of 1–3 minutes for each dataset during the reactions.

An investigation into the structure and bonding of non-stoichiometric Li-N-H phases is then reported. Samples of particular target average stoichiometry values were synthesised by ball-milling hand-ground mixtures of lithium nitride and lithium amide of the appropriate molar ratio for one hour at 400 rpm, followed by heating of the milled mixture to 250 °C in an alumina crucible under flowing argon for 12 hours. The as-synthesised samples were then analysed by PXRD by being placed into 0.7 mm borosilicate capillaries and measured for one hour using the Rigaku SmartLab diffractometer. The non-stoichiometric phases were also analysed by Raman spectroscopy, again in 0.7 mm borosilicate capillaries, exposed to 532 nm light for two co-additions of two second data collections. Deuterated analogues of the non-stoichiometric phases were synthesised following the same procedure as outlined above, except using deuterated lithium amide, which had itself been produced by the reaction of lithium nitride with 3 bar of deuterated ammonia at 250 °C in the IGA^{n}. These samples were analysed by NPD, being placed into 6 mm i.d. vanadium cans, followed by diffraction data collection for one hour on the POLARIS instrument.

In order to examine the behaviour of the system under conditions approaching that of a practical hydrogen store, the Li-N-H system was subjected to a series of hydrogenation-dehydrogenation cycles, under pure hydrogen and mixtures of hydrogen and nitrogen. The combined thermogravimetric and diffraction studies detailed in the last section of this Chapter examine long term changes in the hydrogen storage behaviour of the system and seek to probe the effect of the addition of nitrogen gas on the reversible hydrogen storage content over many cycles.

The first set of cycling data concerns the behaviour of the Li-N-H system under pure hydrogen. For these experiments the IGA-MS was programmed to perform the cycling automatically using the sequence mode in the instrument software. A sample of lithium nitride was loaded onto the instrument, exposed to 3 bar of hydrogen pressure and heated to 265 °C, a temperature

which was held constant for the duration of the experiment. The sample was hydrogenated for an initial period of three hours, then subject to a programmed sequence of 100 minutes dehydrogenation under dynamic vacuum followed by 30 minutes hydrogenation at 3 bar of hydrogen, for the chosen total number of cycles (1, 2, 5, 10, 25 and 45 cycles). This effected the cycling back and forth between lithium amide plus two equivalents of lithium hydride, and lithium imide plus one equivalent of lithium hydride. Each cycled sample was then subjected to one further hydrogenation-dehydrogenation cycle, under the same reaction conditions, on the I11 beamline at Diamond. The PXRD data collection was identical to that described for the first *in situ* study.

The investigation of the effect of nitrogen gas on the cycling behaviour of the Li-N-H system was also explored, with all of the cycling reactions performed on the ID31 beamline at the ESRF. Lithium nitride samples were loaded into the ESRF gas cell described in Section 2.4.1, evacuated and then exposed to 2 bar of either 100 ppm nitrogen-in-hydrogen or 20 % nitrogen-in-hydrogen gas. The sample was then heated to 265 °C and hydrogenated for an initial period of 2 hours, followed by cycles of 90 minutes dehydrogenation under dynamic vacuum followed by 60 minutes hydrogenation under 2 bar of the reactive gas. Diffraction data were collected using the MAC detector in 3 minute datasets throughout the experiment.

3.2 Hydrogen storage and release mechanism by *in situ* X-ray diffraction

3.2.1 Evidence for the Frenkel defect mechanism

The initial investigation into the reaction mechanism of hydrogen storage and release in the Li-N-H system was an *in situ* synchrotron X-ray powder diffraction study on I11 at Diamond. The lithium nitride sample was subjected to hydrogenation-dehydrogenation reactions under a series of temperature and pressure regimes, summarised in Table 3.1. The order in which each reaction was performed is also given. This order is important given that a single sample was used for all of these experiments, meaning that the interpretation of results for a given set of reaction conditions must also take into account the degree of cycling which had been performed, although this study was not explicitly designed to study cycling effects.

A few points are worth noting at this initial juncture. Firstly, a worthwhile question of a

sample which has been subjected to over 24 hours of continous synchrotron radiation is whether the sample exhibited any effects attributable to radiation damage, and how this might affect the results obtained in this study. Indeed, radiation damage is a significant problem in the study of ammoniaborane, amidoboranes and borohydrides. Slight discolouration of the samples was observed over the first hour of exposure, although this discolouration did not intensify significantly after this point. Given that identical reaction conditions were used at various points in this study, the extent of radiation damage was evaluated by examining the positions of the Bragg peaks of lithium amide and lithium hydride in the diffraction data over time. Radiation damage would be expected to cause defects in the crystal structure, resulting in substantial lattice variation. However, no such expansion of the lattice was seen in this study, nor any noticeable strain broadening of the diffraction peaks. Hence, it was concluded that the sample was not subject to a significant level of radiation damage, thus precluding the effect of the radiation as being responsible for the effects observed in the study.

Secondly, it was decided to use a sample of lithium nitride as the starting material in this study, and to perform the hydrogenation to lithium amide and two equivalents of lithium hydride. This provides an extra equivalent of lithium hydride than is necessary for Equation 3.1, since full dehydrogenation to the nitride requires excessively high temperatures. An alternative choice would be simply to mix together single equivalents of lithium amide and lithium hydride. The nitride reaction route was chosen because it allowed for some examination of the hydrogenation of lithium nitride in addition to the hydrogen storage and release reactions of the Li-N-H system. Furthermore, the extra equivalent of lithium hydride allowed for more detailed analysis of its role in the reaction. The main disadvantage of the chosen approach is that the *in situ* hydrogenation appears to result in larger average particle sizes than those which can be achieved by ball milling the sample. This may have influenced the extent of reaction of the sample achieved in these experiments.

A broad view of the reaction progression is detailed in Figure 3.1 , which shows contour plots of four regions of interest in the diffraction data from the experiment. There is a significant amount of information contained within these data, so a preliminary survey of the highlighted regions will be conducted before delving into a more detailed analysis. crystallographic information used in the refinements given in Appendix A, with individual diffraction patterns showing the observed

Table 3.1: Summary of pressure and temperature regimes for the *in situ* X-ray diffraction measurements on the Li-N-H system. Letter designations given to the right of each set of reaction conditions indicate the sequence in which each reaction was performed. All dehydrogenations were performed under dynamic vacuum.

Process	Temperature (°C)	H_2 pressure (bar)	Order
$Li_3N + 2\,H_2 \rightarrow LiNH_2 + 2\,LiH$	25-290	3	A
$LiNH_2 + LiH \rightarrow Li_2NH + H_2$	290	<0.01	B
	290	<0.01	D
	263	<0.01	F
	235	<0.01	H
	235–290	<0.01	J
$Li_2NH + H_2 \rightarrow LiNH_2 + LiH$	290	3	C
	263	3	E
	235	3	G
	235	1	I
	235	0.5	K

patterns and the calculated fit to the data are given for the beginning of each process outlined in Table 3.1 in Appendix B.

Segment (a) shows the (001) reflection of α-lithium nitride, in the angular region $2\theta = 12.16$–$12.32°$. The commercial sample was determined to be free of crystalline impurities other than a very small (3 %) amount of lithium oxide, containing a mixture of α- and β-lithium nitride (see Figure 3.2). Upon heating, the β phase rapidly converts into the α phase, as the β phase is unstable except at elevated pressure[207]. The α-lithium nitride is consumed during the hydrogenation, although it can be seen that the phase does not completely disappear until the second hydrogenation reaction.

Segment (b) of Figure 3.1 shows the region of the diffraction pattern corresponding to the (002) lithium amide superlattice reflection ($2\theta = 9.20$–$9.55°$). The (002) superlattice reflection appears as a consequence of the characteristic doubled cubic cell structure of the tetragonal form of lithium amide[208]. This region was used as the definitive indicator of the presence of tetragonal lithium amide, given that diffraction intensity from some non-stoichiometric Li-N-H phases coincides with the more intense (112), (020) and (024) lithium amide reflections. As expected, the appearance and disappearance of this reflection correlates well with the hydrogenation and

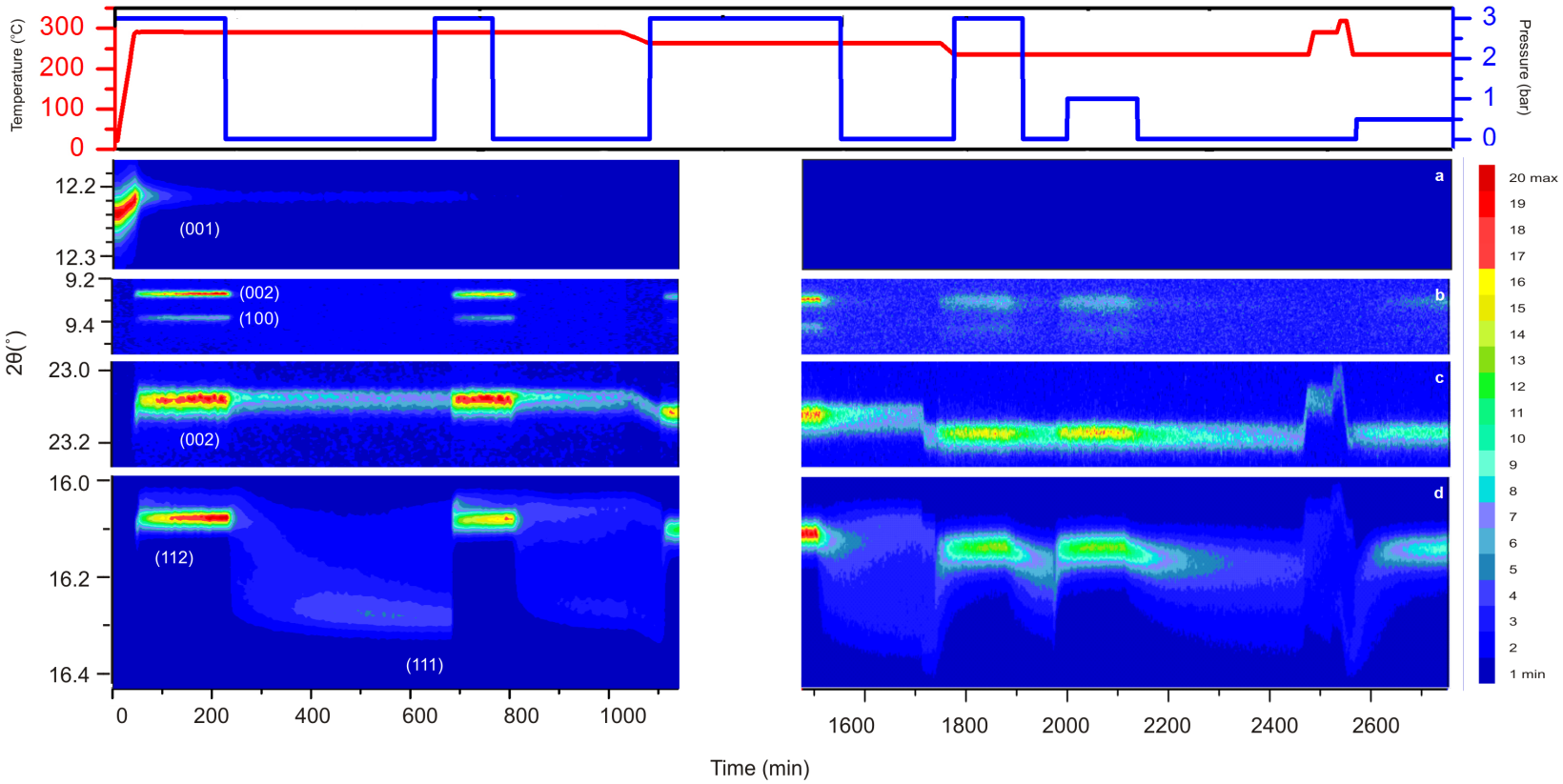

Figure 3.1: Contour plot showing selected regions of the diffraction patterns obtained for the hydrogenation/dehydrogenation cycles over time for the Li-N-H system. The panels show a) the α-Li_3N (001) reflection, b) the superlattice region of $LiNH_2$: the (002) and (100) reflections, c) the LiH (002) reflection and d) the "Li-N-H" region, bounded by the $LiNH_2$ (112) reflection and the Li_2NH (111) reflection. The top panel indicates the experimental conditions during the course of the experiment. The colour bar on the right hand side indicates the range of diffraction intensity within an individual panel. Individual reflections are indicated in white.

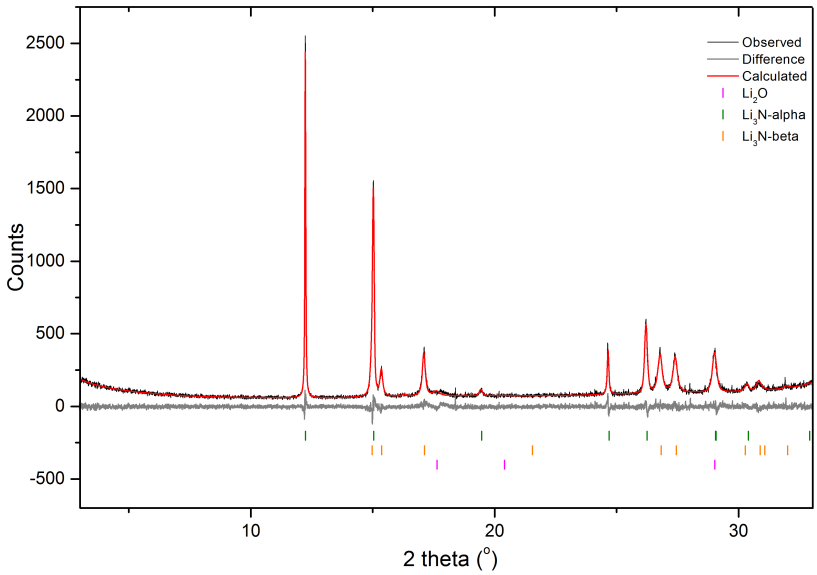

Figure 3.2: PXRD pattern for the lithium nitride sample used as starting material, showing the observed (black) data, the calculated pattern from Rietveld refinement (red) and the difference between the two (grey). Tick marks for the phases included in the refinement are shown. The Rwp for the fit to the data was 8.291.

dehydrogenation of the system, respectively. In this segment, the appearance of a Bragg reflection at a 2θ value of 9.385° is also observed. As the intensity of this reflection follows closely the rise and fall of the (002) reflection and appears to be associated with lithium amide, it is assumed that this reflection is the (100) of lithium amide; the 2θ value is consistent with this assignment. This reflection is not observed for the $I\bar{4}$ structure of lithium amide, suggesting that the amide is no longer body-centred, and the primitive tetragonal space group $P\bar{4}$ was assigned as the appropriate space group for lithium amide in this study. For the purposes of the subsequent analysis, lithium amide was treated as a line phase with $P\bar{4}$ symmetry, and included an anisotropic strain broadening term to account for asymmetry in the peak shape, which may or may not relate to stoichiometry variation in the tetragonal phase.

Segment (c) shows the (002) reflection for lithium hydride (θ = 22.9–23.3°), which forms two molar equivalents during the hydrogenation of lithium nitride, with one equivalent consumed and then reformed during the dehydrogenation and hydrogenation of the system between lithium amide and lithium imide, respectively. As such, the LiH Bragg peak intensity is a good indicator of the extent of reaction.

Segment (d) shows the (112) Bragg peak of lithium amide and the (111) of lithium imide

(2θ = 15.95–16.45°). As the c axis of lithium amide is approximately double that of lithium imide (as an $a \times a \times 2a$ superstructure), these Miller indices represent analogous planes in each structure. The dominant feature in the data is the presence, most clearly during the dehydrogenation reactions, of diffraction intensity in the angular region intermediate between the stoichiometric lithium amide and lithium imide peaks. This confirms the previous *ex situ* observations[136]. This represents shrinking of the cubic lattice parameter during the transition from the hydrogenated lithium amide structure to dehydrogenated lithium imide as a result of the migration of lithium ions through the structure, forming a continuum of intermediate states. The details of this transition will be discussed in greater detail below, but we note that this observation is clear evidence for the existence of non-stoichiometric phases as proposed by David *et al.*[136], and for their intimate involvement in the dehydrogenation mechanism of the Li-N-H system.

Some more detailed information can be extracted from the analysis of a single reaction from this large dataset. High-resolution contour plots for three of the lithium amide-imide Bragg peak pairs during the first dehydrogenation reaction (220–660 minutes in Figure 3.1d) are shown in Figure 3.3, indicating that the same complex development of the lineshape was observed for all of the cubic Bragg reflections. A more rigorous assessment of the lineshape is provided in Figure 3.4, which depicts a strain analysis for these regions: a plot of the normalised peak intensity in terms of the change in d-spacing (Δd) across the breadth of the peak divided by the d value for the relevant lithium amide peak. This analysis suggests that the continuum of intermediate states is isotropic in the Li-N-H structure, and therefore is not the result of a different microstructural effect such as anisotropic strain broadening. Thus, the best explanation for the change in lineshape seen during the reaction is the presence of non-stoichiometric phases.

Closer examination of the contour plots of the diffraction data shows more complex stoichiometry variations than a simple linear transformation between lithium amide and lithium imide. The subsequent description of these variations divides the non-stoichiometric continuum into three distinct groups: stoichiometry values close to that of lithium amide ($Li_{1.1}NH_{1.9}$, $Li_{1.2}NH_{1.8}$, $Li_{1.3}NH_{1.7}$) are termed lithium-poor phases, those close to lithium imide ($Li_{1.7}NH_{1.3}$, $Li_{1.8}NH_{1.2}$, $Li_{1.9}NH_{1.1}$) are termed lithium-rich phases, and the remaining stoichiometry values ($Li_{1.4}NH_{1.6}$, $Li_{1.5}NH_{1.5}$, $Li_{1.6}NH_{1.4}$) are termed intermediate phases.

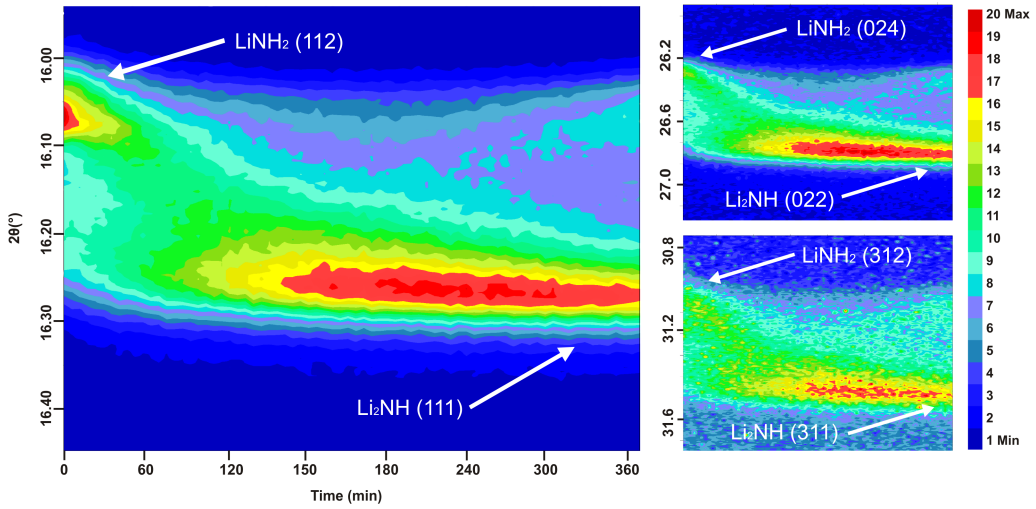

Figure 3.3: Contour plot of three sections of synchrotron X-ray diffraction data for the dehydrogenation of $LiNH_2$ under vacuum at 290 °C, showing the transformation via a continuum of intermediate intensity. Relevant Bragg reflections for $LiNH_2$ and Li_2NH are indicated on each panel. The colour bar to the right indicates the relative intensity of the diffraction data. [137] Reproduced by permission of The Royal Society of Chemistry.

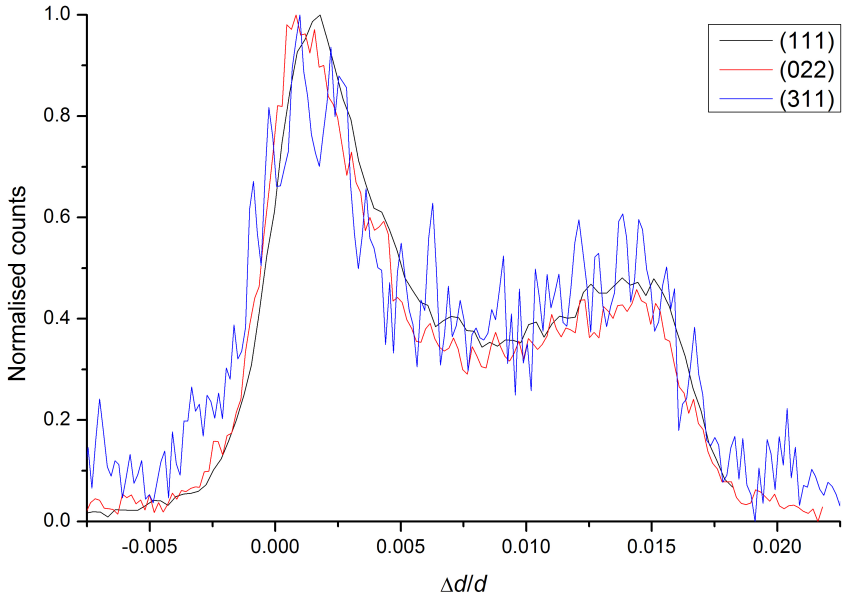

Figure 3.4: Strain analysis for three $LiNH_2$ Bragg reflections for the Li-N-H sample obtained at the end of the first dehydrogenation reaction at 290 °C. Each reflection has had a background subtraction applied before normalisation of the diffraction data for comparison. [137] Reproduced by permission of The Royal Society of Chemistry.

In the Rietveld analysis of these data, the non-stoichiometric continuum is modelled as the combination of the individual phases described above (see also Chapter 2). Figure 3.5 shows an example of how the total refinement is built up for the final pattern in the first dehydrogenation reaction, showing the portion of the refined pattern that each phase contributes. The granularity used in the refinement of the continuum is a compromise between providing a sufficiently structured description of the peakshape and reducing the number of refined parameters.

Of course, this method of refinement is a simplification of the system. As such, it is worth identifying how well it approximates the behaviour of the system. The goodness-of-fit of the data to the observed data is a useful place to start. Rather than reporting the R-values for the refinements, a contour plot of the calculated diffraction data in the lithium amide-imide region for the first dehydrogenation (process B) is shown in Figure 3.6b, along with the contour plot of the measured data in the same region (Figure 3.6a). These plots indicate a very good agreement between the observed and calculated patterns, suggesting that a sufficient level of detail is captured by the structural model used in the refinement process. This is important for the assessment of the kinetics of the reaction and the determination of the overall stoichiometry. However, it could be argued that given there are 12 phases modelled in that region it is unsurprising that the data fit well. At the very least, it does indicate that the granularity used in the non-stoichiometric continuum is sufficiently fine. As is explained in Chapter 2, the refinements were carefully constrained to minimise the potential for non-physical fitting of the data. The crystallite size and strain terms were constrained, and the lattice parameters were fixed for a given temperature, and linked between the non-stoichiometric phases by Vegard's Law, giving a linear variation in the lattice parameter with stoichiometry. The decision to contrain the crystallite size and strain parameters should be considered in the conclusions presented in the analysis of the diffraction data in this thesis, as an possible effects on the size and strain, particularly with the multiple cycle experiments, will not be assessed by this analysis.

As an alternative measure of how well the refinement reflects the behaviour of the Li-N-H system, the relative molar amounts of each element, lithium, nitrogen and hydrogen, were extracted from the refined fractions of each phase in the refinement. The data in Figure 3.7 show the variation in these values (summed over all phases) over the course of the first dehydrogenation. These values would be expected to be in the ratio of 3:1:4 in the hydrogenated sample, and 3:1:2

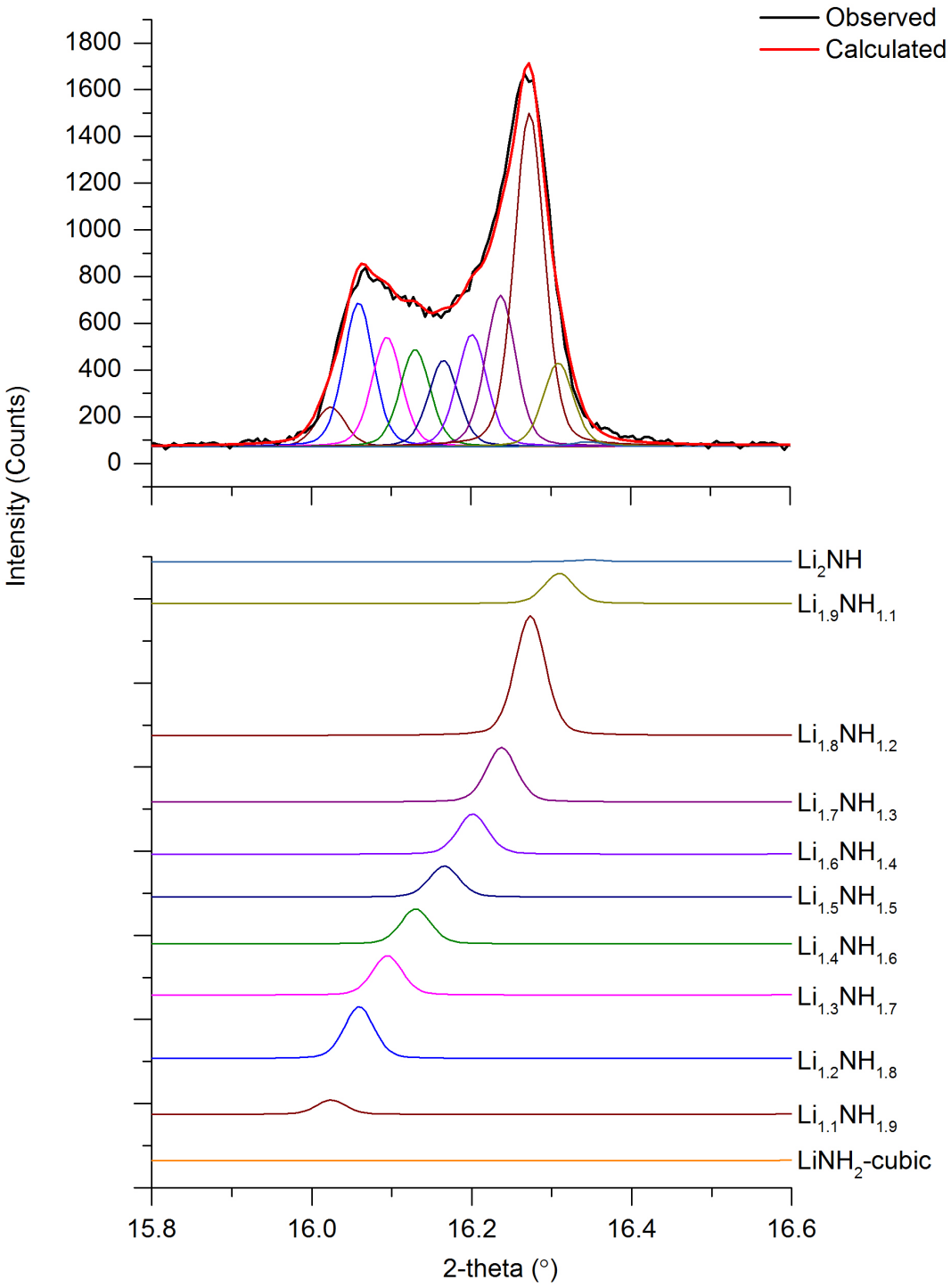

Figure 3.5: An example of the way in which the non-stoichiometric continuum is modelled in the Rietveld refinement. The top panel shows the observed (black) and total calculated (red) diffraction patterns for the dehydrogenated sample, which shows a continuum of intensity between the $LiNH_2$ (112) and Li_2NH (111) reflections. The calculated pattern consists of a series of eleven phases, which are shown together in the top panel, and individually in the bottom panel.

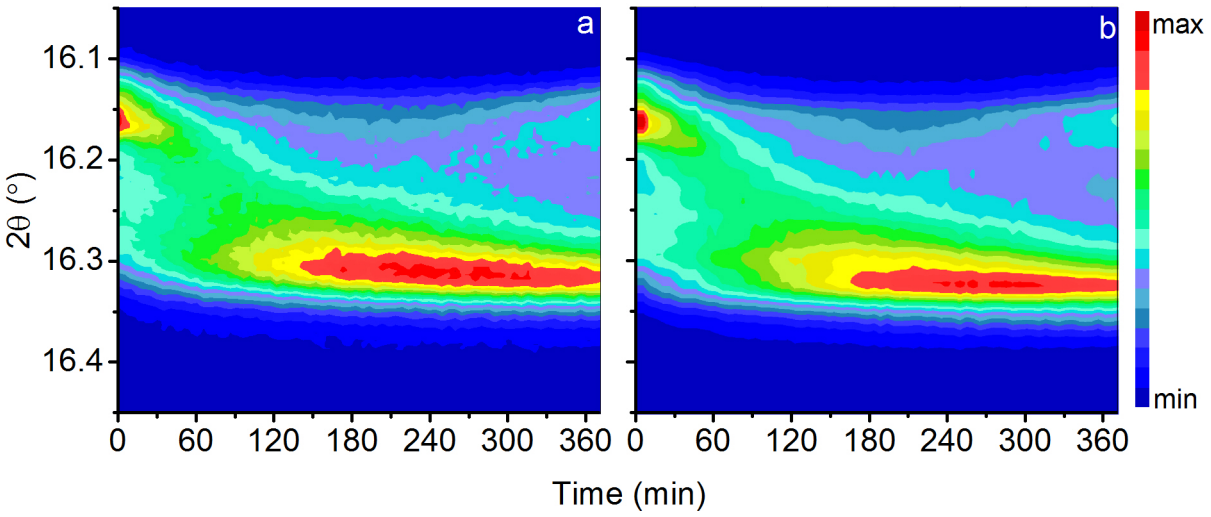

Figure 3.6: A comparison of contour plots of the a) observed and b) calculated diffraction data for the (112) lithium amide - (111) lithium imide region for the first dehydrogenation reaction (process B)

in the dehydrogenated sample (Li:N:H). There is a small difference in the lithium to nitrogen ratio compared with the expected values, with a lower proportion of nitrogen than would be expected from the amount of lithium. This may be due in part to the presence of lithium oxide in the sample, which raises the lithium to nitrogen ratio. Importantly, the amount of lithium and nitrogen in the sample stays relatively constant over the course of the dehydrogenation. This is an indication that the phases are providing a physically reasonable fit to the data, as well as a satisfactory goodness-of-fit value. A small decrease in the nitrogen content may be due to loss of ammonia which has not been captured by lithium hydride. This will be discussed in more detail later in this Chapter. Further evidence for the accuracy of the refinement comes from the fact that the hydrogen content, as expected, decreased over the course of the reaction. While this in itself is not a startling result (modelling only the lithium hydride peaks effectively would give this trend), the starting ratio of the hydrogen to the lithium content follows closely that expected from the stoichiometric equations, and approaches the expected final ratio as the reaction progresses. This analysis confirms that the reaction model used in the refinements effectively reproduces the behaviour of the Li-N-H system.

Looking closely at Figure 3.3, it can be seem that from 260 minutes the diffraction signal intensity diverges away from region close to the midpoint between lithium amide and lithium imide, separating into the lithium-poor and lithium-rich end members. This effect can be seen

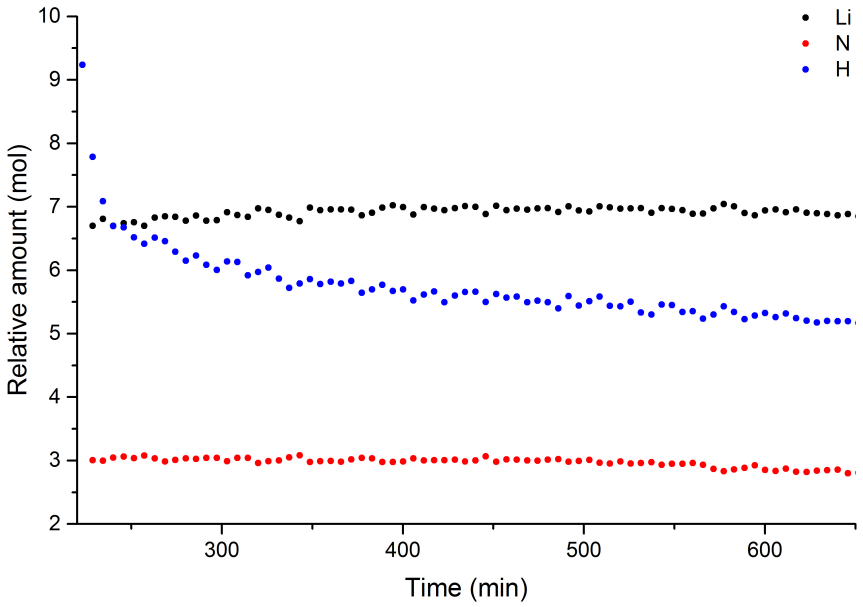

Figure 3.7: The summed relative molar amounts of lithium (black), nitrogen (red) and hydrogen (blue) in all of the phases in the Rietveld refinement for the first dehydrogenation of the Li-N-H sample (process B). Average standard deviations are ±0.08 mol for nitrogen, ±0.08 mol for lithium, and ±0.54 mol for hydrogen.

clearly in Figure 3.8, where the evolution of the molar fraction of each of the refined non-stoichiometric phases during the dehydrogenation is shown. The lithium-poor phases are seen to increase in magnitude during the latter stages of the reaction at the expense of the intermediate stoichiometries. The lithium-rich components increase for the duration of the reaction.

The depletion of these intermediate components to produce lithium-rich phases is the normal progression of the reaction from lithium amide to lithium imide. However, the simultaneous formation of lithium-poor phases requires further explanation. The reactions outlined for the proposed reaction mechanism do show that lithium amide is reformed during the dehydrogenation process (from the reaction of ammonia and lithium hydride). However, it was expected that the lithium amide formed in this reaction would then be rapidly consumed to form intermediate range stoichiometry species, and eventually lithium imide. It would not be expected to be a mechanism for a net increase in lithium-poor phases.

Moreover, the increase in lithium-poor stoichiometry described above occured at a plateau in the intensity of the lithium hydride peaks (Figure 3.1c), indicating that dehydrogenation reaction is at equilibrium while this process occurs. Taken together, these observations suggest that the change in distribution of the non-stoichiometric phases in fact indicates that the in-

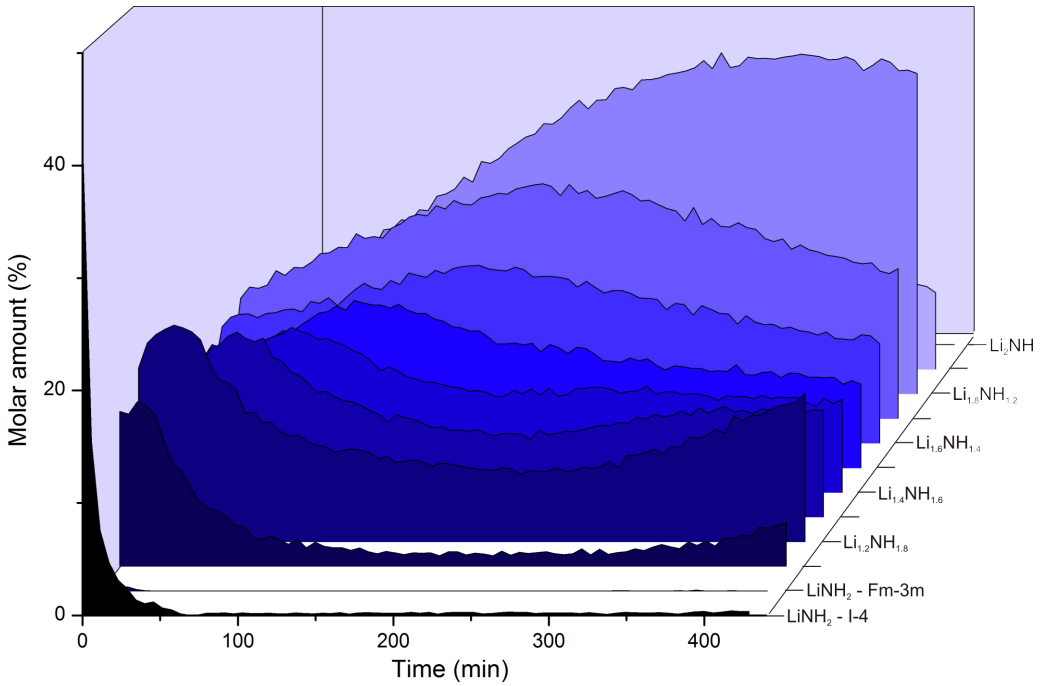

Figure 3.8: Stacked plots of the relative molar amounts of each of the refined phases in the $LiNH_2$-Li_2NH continuum for the duration of the first dehydrogenation cycle at 290 °C (process B). The relative estimated standard deviations for the molar amount of each phase are in the range of ±2–5 % of the stated value. [137] Reproduced by permission of The Royal Society of Chemistry.

termediate stoichiometry values are of lower thermodynamic stability than the lithium-rich and lithium-poor phases. This effect is reproduced — albeit in a less dramatic form — for each dehydrogenation reaction observed in this experiment. This instability is consistent with the recent first-principles analysis by Zhang *et al.*[209], which showed that a proposed $Li_{1.5}NH_{1.5}$ structure [210] is unstable at T = 0 K with respect to phase separation into lithium amide and lithium imide. Their study was a response to work which suggested that the $Li_{1.5}NH_{1.5}$ phase should be a stable intermediate[210], a theory which has been invoked in some experimental studies of the decomposition of lithium amide[113]. The data presented here suggest that all non-stoichiometry in the Li-N-H system is kinetically stabilised.

Considering the topological similarity of the structures of the end members, this phase separation may be considered to be an ordering of the lithium vacancies present in the non-stoichiometric continuum to form lithium amide and imide. The intermediate stoichiometry values are likely to be disordered relative to lithium amide and lithium imide, and therefore the depletion of these phases is unlikely to be an entropic process, but rather enthalpic in nature. Hence, it might be expected that the relative amounts of the end members would increase when

a range of stoichiometry values are annealed after the completion of dehydrogenation. Clearly, the relative stability of non-stoichiometric Li-N-H phases is a subject worthy of a future detailed investigation.

The exothermic hydrogenation reaction is more rapid than the dehydrogenation at a given temperature, and so precise observation of the non-stoichiometric intermediates during the hydrogenation in the initial runs at the highest temperature is difficult. However, the (112) peak shape of the lithium amide at the end of the hydrogenation at 290 °C and 3 bar of hydrogen (process A) is instructive. This is shown in Figure 3.9a. As can be seen, there is very little diffraction intensity to the right of the (112) peak corresponding to the lithium-rich and intermediate stochiometries, suggesting that the hydrogenation reaction had progressed to completion. However, there is a shoulder on the left hand side of the peak, corresponding to a larger d-spacing. By analogy with the justification of the d-spacing of the non-stoichiometric phases, diffraction intensity at higher d-spacing than the amide would imply that there are phases with stoichiometry beyond that of the amide (ie $Li_{1-x}NH_{2+x}$) — these phases are not known to exist.

What is more likely is that this shoulder represents the presence of a form of lithium amide with a long-range cubic structure similar to the non-stoichiometric continuum. Since the c-axis of lithium amide is slightly longer than twice the a and b axes, an average cubic structure would have a slightly larger d-spacing for the (111) reflection compared with the (112) reflection of the amide. Hence its appearance at a smaller angle than the lithium amide (112) peak. This is not a known phase of lithium amide, and thus is unlikely to be an equilibrium structure. Indeed, examination of a contour plot of the diffraction intensity in this region over the course of the hydrogenation of the lithium nitride (Figure 3.9b) shows that there was a more intense shoulder earlier in the hydrogenation, which then anneals into the main (112) peak. This probably represents the ordering of lithium amide into the long-range tetragonal symmetry structure.

At lower temperatures and hydrogen pressures, the reaction process could be monitored more effectively. One such hydrogenation (process K) is shown in Figure 3.10. Here, the lithium imide (111) and lithium amide (112) reflections are shown for the hydrogenation at 235 °C under 0.5 bar of hydrogen. Under these milder hydrogenation conditions, the shoulder at larger d-spacings is not observed, strengthening the suggestion that this phase is a kinetic product.

As was the case for the dehydrogenation, it can be seen that hydrogenation reaction progresses

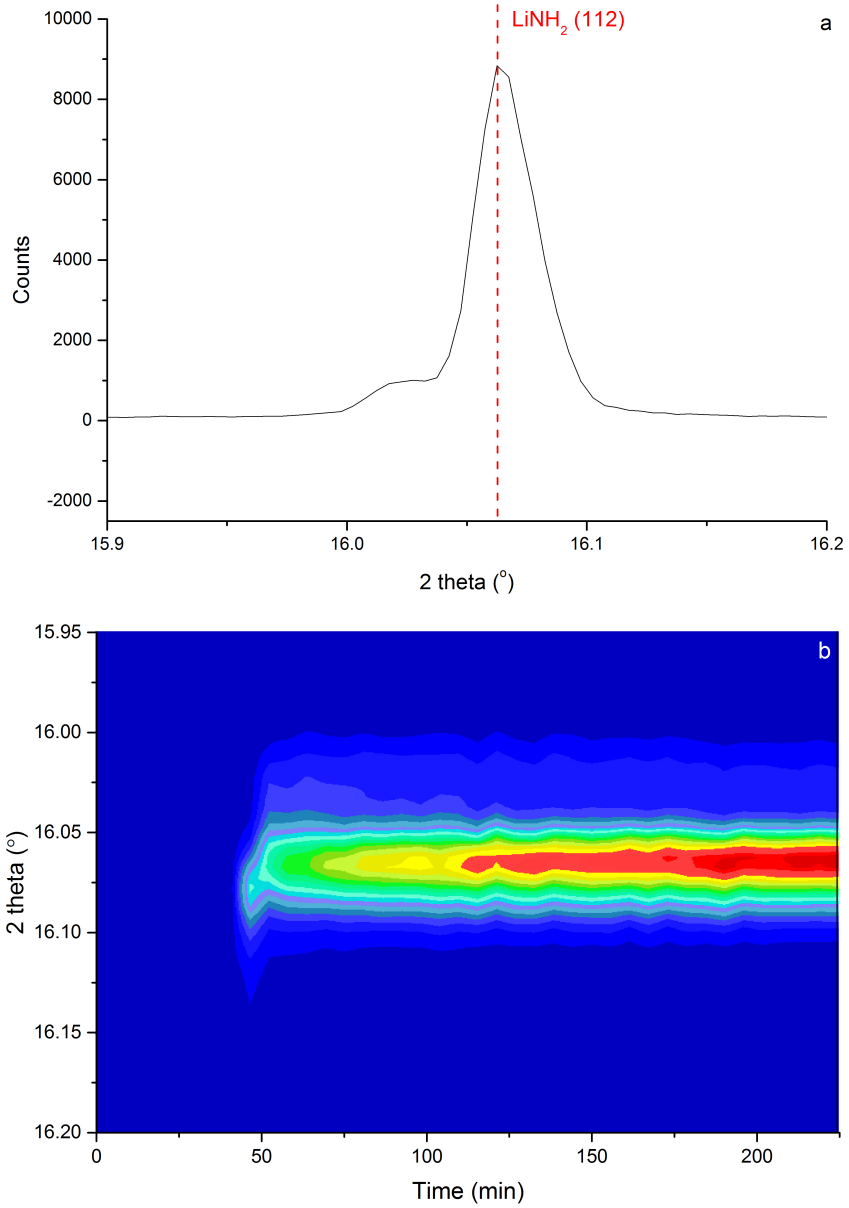

Figure 3.9: a) A section of the PXRD pattern for the hydrogenated sample (end of Process A), showing the shape of the lithium amide (112) peak, which contains a shoulder at lower 2-theta values. The expected position of the (112) reflection is shown in red. b) Contour plot of the PXRD data showing the evolution of the (112) peak shape during the hydrogenation reaction

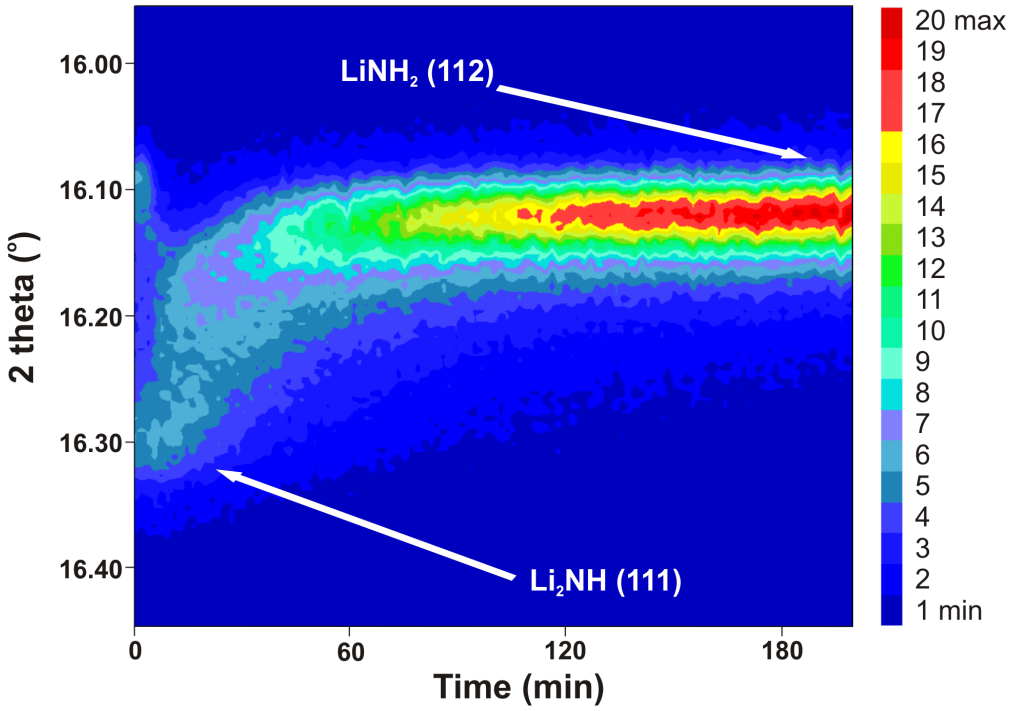

Figure 3.10: Contour plot of a section of synchrotron X-ray diffraction data for the hydrogenation of Li_2NH under 0.5 bar of H_2 gas at 235 °C (process K), showing the transformation via a continuum of intermediate intensity. Relevant Bragg reflections are indicated. The colour bar to the right indicates the relative diffraction intensity. [137] Reproduced by permission of The Royal Society of Chemistry.

through the full non-stoichiometric continuum. The refined phases in the hydrogenated state were found to be a mixture of tetragonal stoichiometric lithium amide with smaller amounts of lithium-poor non-stoichiometric cubic phases. Clearly, there must be a point where, as the stoichiometry approaches lithium amide, the equilibrium structure adopts long-range tetragonal symmetry[100, 136]. This transformation is most clearly marked by the appearance of the (002) superlattice reflection of tetragonal lithium amide. While the lithium-poor non-stoichiometric phases observed here appear to have long-range cubic symmetry (because the characteristic superlattice reflections for tetragonal lithium amide are absent) the short-range order of these phases is anticipated to be tetragonal. It is worth noting that, during dehydrogenation, while the overall rate of dehydrogenation was relatively modest, the disappearance of the superlattice reflection of lithium amide is very rapid. This observation is consistent with a reaction model whereby a small deviation in stoichiometry causes the long range tetragonal symmetry to collapse, presumably via a short-range twinning mechanism.

There may be a (small) range of stoichiometry values for which the Li-N-H species retain the

long-range tetragonal symmetry of the pure amide phase. The appearance of the (100) reflection described earlier could be indicative of a structural variation associated with a small shift in the average stoichiometry of long-range tetragonal lithium amide. However, no differences in the relative intensity of the (100) reflection were observed compared to other Bragg peaks in the amide phase during reaction, as might be expected if the interconversion of any these species was occuring. Thus, while the loss of body-centring indicates a subtle displacement of the lithium and nitrogen positions, the exact nature of this displacement remains unclear.

In the previous *ex situ* synchrotron X-ray diffraction study, slightly different lattice constants were observed for lithium hydride in the hydrogenated and dehydrogenated states of the Li-N-H system [136]. Here, a single peak analysis of the lithium hydride (002) reflection provides further evidence for a change of lattice parameter on hydrogenation, and this is shown in Figure 3.11. The position and intensity of the peak are shown for the first two hydrogenation-dehydrogenation cycles. The average 2θ position of the peak during hydrogenation was 23.1001(16)°, while the position during dehydrogenation was 23.0963(17)°, with an independent t-test showing the two data sets to be statistically different ($p<0.01$). This corresponds to a 0.02 % increase in the lattice constant during dehydrogenation.

Pressure effects alone cannot account for the discrepancy observed in the lithium hydride lattice parameter on hydrogenation and dehydrogenation, as X-ray diffraction data of lithium hydride taken under vacuum, 3 bar of hydrogen and 3 bar of helium showed no discernible difference in the peak position (See Appendix E). This suggests that there was a significant difference in the defect structure formed during hydrogenation and dehydrogenation. Considering the role of lithium hydride in the dehydrogenation reaction, the formation of hydrogen in the Li-N-H system is understood to result from the action of interstitial hydrogen (H^+) formed in lithium amide and mobilised in the structure as transitory ammonia units: one of these units may combine with lithium hydride, producing hydrogen and lithium amide (Figure 3.12). Recent theoretical studies have shown that lithium hydride is capable of producing surface interstitial hydride ions as part of a Frenkel defect in order to facilitate this reaction[142]. Thus, the reaction of lithium hydride with ammonia involves the removal of hydride to form hydrogen (Figure 3.12a), and the subsequent reaction of a lithium ion with the amide unit to reform lithium amide (Figure 3.12b). The net reaction is therefore the removal of Li^+/H^- pairs from the lithium hydride phase, forming a

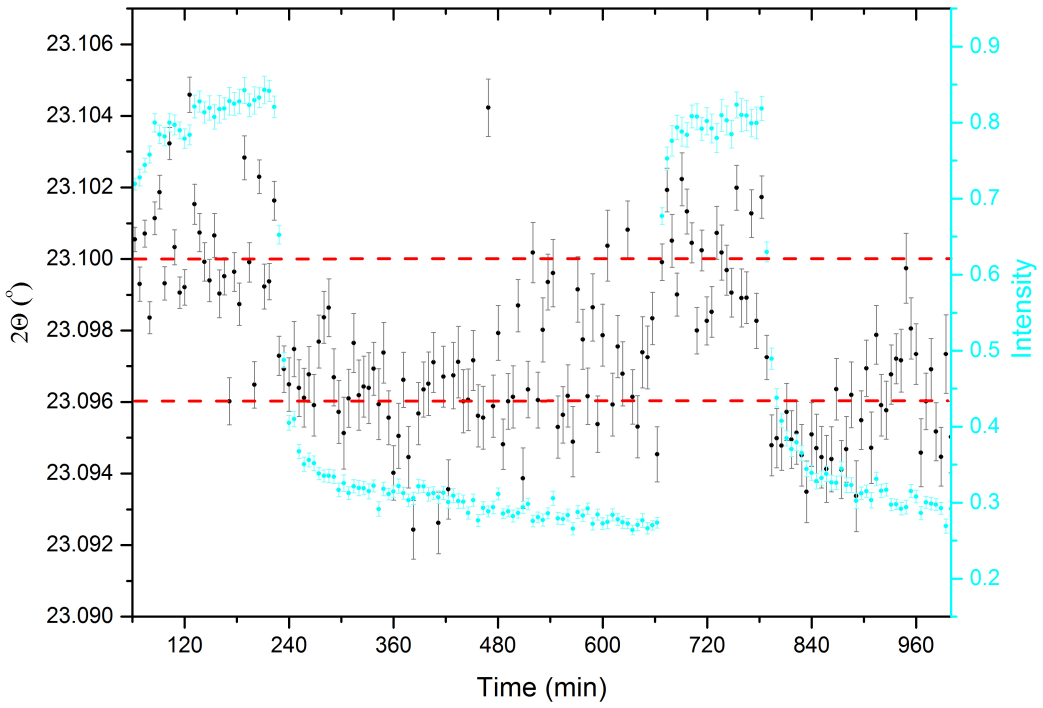

Figure 3.11: Peak position (black) and intensity (dark blue) of the (002) reflection of LiH for the first two hydrogenation-dehydrogenation cycles at 290 °C (processes A-D), obtained from single peak analysis. The average peak positions during hydrogenation and dehydrogenation are shown as dotted lines. [137] Reproduced by permission of The Royal Society of Chemistry.

Schottky defect (Figure 3.12c).

It is proposed that the increase in the lattice parameter in lithium hydride during dehydrogenation arose as a result of the formation and removal of these ion pair defects as outlined above. The formation and migration of such defects are known to cause volume expansion in alkali metal halides[211]. Recently, Symeonides calculated that the formation of Schottky pairs in lithium hydride is accompanied by an increase in cell volume as the lattice rearranges around the defect site[212]. The observation of this microstructural effect was possible due to the presence of an excess equivalent of lithium hydride from the hydrogenation of lithium nitride. During hydrogenation, the formation of lithium hydride does not involve the migration of defect species to the surface, and so the formation of Schottky defects is not expected. Thus, the average cell volume of lithium hydride was lower during hydrogenation.

One advantage of an *in situ* X-ray diffraction study is the ability to extract kinetic information from the data. The relative amounts of each phase extracted from the batch Rietveld analysis are

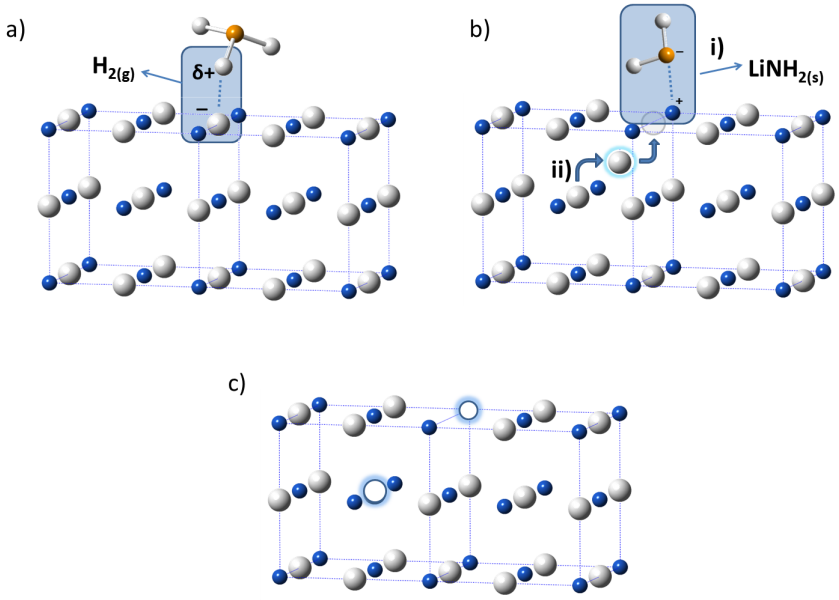

Figure 3.12: The formation of Schottky defects in LiH. Once an NH_3 unit reaches the surface of $LiNH_2$, it is free to interact with lithium hydride, where the partially positively charged hydrogen on the NH_3 molecule will react with a hydride anion to form hydrogen gas (a). The remnant NH_2^- unit can then react with a lithium ion to form lithium amide (b-i), and hydride anions can migrate to the surface (b-ii). The remaining lithium hydride now contains a Schottky defect (c). [137] Reproduced by permission of The Royal Society of Chemistry.

shown in Figure 3.13b. For clarity of presentation, all of the non-stoichiometric phases (cubic $LiNH_2$-Li_2NH) are summed to give a total "Li_2NH" value. In order to give a more accurate depiction of the overall extent of the reaction, the average stoichiometry of the lithium amide-imide continuum (compared with a constant nitrogen stoichiometry of 1) is given in Figure 3.13a, along with the temperature and pressure. This value was calculated as an average across all of the refined phases:

$$\frac{n_{Li} + n_{Li-cubic} + 1.1n_{Li1.1} + 1.2n_{Li1.2} + 1.3n_{Li1.3} + \ldots + 1.8n_{Li1.8} + 1.9n_{Li1.9} + 2.0n_{Li2.0}}{n_{Li} + n_{Li-cubic} + n_{Li1.1} + n_{Li1.2} + \ldots + n_{Li1.8} + n_{Li1.9} + n_{Li2.0}} \quad (3.2)$$

The break in the time axis in Figure 3.13 was a period where the synchrotron beam failed, and so the sample was maintained under a constant temperature and pressure during this malfunction. When the production of X-rays resumed, data collection was restarted with a smaller time interval of one minute collections (three minute collections were used prior to the beam-off period). This explains the change in the y-axis scale after this point, since this value is derived from the scale factor in the Rietveld analysis, which is an absolute measure of the intensity of the signal for a

given phase, and so will be smaller for shorter collection times.

While the data are not of sufficiently high resolution to allow a more detailed analysis of the kinetics through the application of stretched exponentials or other solid-state kinetic models[213], simple exponential models give acceptable fits to molar amounts of lithium hydride and lithium amide extracted from the Rietveld analysis of these data. The functions used are given in Equations 3.3 and 3.4, and relate the molar amount of a phase (n_t) to the maximum level (n_{max} for hydrogenation) or the initial level ($n_{initial}$ for dehydrogenation) and the time (t) using an indicative rate constant (k):

$$n_t = n_{max}(1 - e^{-kt}) \tag{3.3}$$

$$n_t = n_{initial}(e^{-kt}) \tag{3.4}$$

An example of the fits obtained for one hydrogen storage and release cycle (processes H–I) is shown in Figure 3.14, and the rate constants for lithium hydride and lithium amide extracted for all of the reactions are shown in Table 3.2. These values are formation rate constants during hydrogenation, and consumption rate constants during dehydrogenation.

These rate constants show a significant decrease in the reaction rate with decreasing temperature, as expected. Although only three temperatures were used, the data follow Arrhenius type behaviour (R^2>0.90 for modelling both lithium hydride and lithium amide Bragg peak intensity on hydrogenation and dehydrogenation). The rates extracted from the lithium hydride intensity are equivalent to the overall rate of reaction, and thus the activation energy extracted from the lithium hydride Arrhenius plot indicates the activation energy of the process (see Appendix F). The activation energy extracted is 38(8) kJ mol^{-1} for hydrogenation, and 70(15) kJ mol^{-1} for dehydrogenation. This implies an enthalpy change for the reaction of 32(17) kJ mol^{-1}, compared with the expected value of 45 kJ mol^{-1} from standard enthalpies of formation[214], and approximately 50–70 kJ mol^{-1} from various experimental determinations (calorimetric data)[109, 215, 216]. The large errors on these values indicate that the approximation to a simple exponential kinetic model is only suitable for a very general description of the kinetics of the system. Additionally, the use of sequential measurements at different temperatures is a less useful experiment than using

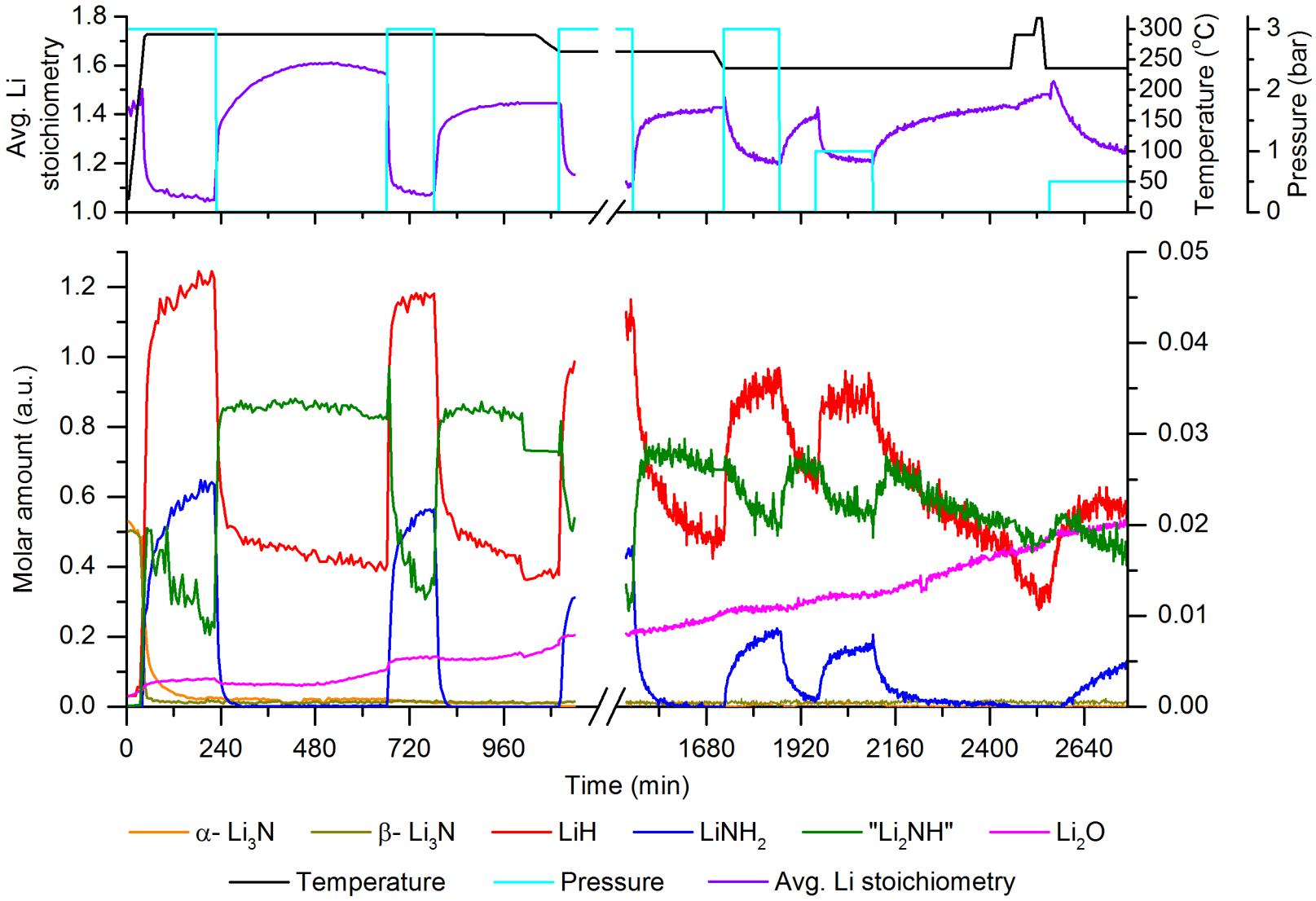

Figure 3.13: The lower panel shows the relative molar amount of each of the phases extracted from the Rietveld refinement, where the 'Li_2NH' value is the sum of each of the non-stoichiometric phases and stoichiometric Li_2NH. The left y-axis corresponds to the data before the x-axis break, and the right y-axis corresponds to data after the break. The upper panel shows the reaction temperature and pressure, and the average lithium stoichiometry of the $LiNH_2 - Li_2NH$ phases. Average relative standard deviations before the break in the data are ±5% for lithium hydride, ±6% for lithium amide, ±6% for "lithium imide" phases, ±2% for lithium oxide and both lithium nitride phases. After the break in the data, these average errors were ±10% for lithium hydride, ±8% for lithium amide, ±11% for "lithium imide" phases and ±5% for lithium oxide.

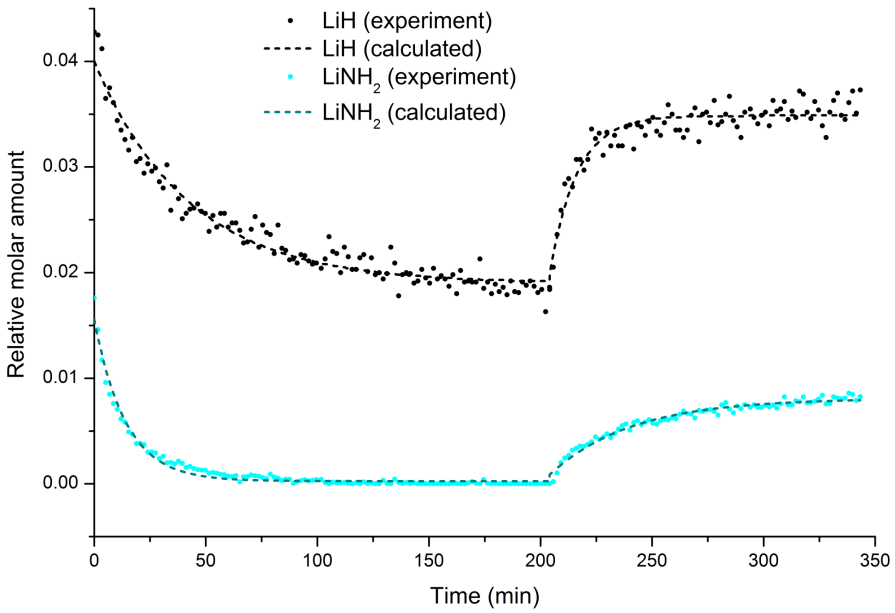

Figure 3.14: An example of the kinetic fits obtained for the dehydrogenation and hydrogenation of the Li-N-H sample at 235 °C (processes H–I). The data points and dashed lines represent the experimental and calculated molar amount of each phase, respectively, with black as lithium hydride, and blue as lithium amide. Relative standard deviations calculated from fits to the data are ±6 % for lithium amide and ±15% for lithium hydride. [137] Reproduced by permission of The Royal Society of Chemistry.

Table 3.2: Rate constants from exponential fits to the LiH and $LiNH_2$ amount for each of the reaction processes in this experiment. Errors in the extracted rate constant are given in brackets.

Process	Starting material, reaction conditions	k(LiH) (min^{-1})	k($LiNH_2$) (min^{-1})
	Hydrogenation reactions		
A	Li_3N, 290 °C, 3 bar	0.065(4)	0.044(3)
C	Li_2NH, 290 °C, 3 bar	0.22(1)	0.067(5)
E	Li_2NH, 263 °C, 3 bar	0.126(5)	0.061(2)
G	Li_2NH, 235 °C, 3 bar	0.082(7)	0.027(2)
I	Li_2NH, 235 °C, 1 bar	0.11(1)	0.042(2)
K	Li_2NH, 235 °C, 0.5 bar	0.035(3)	0.0050(8)
	Dehydrogenation reactions		
B	$LiNH_2$, 290 °C	-0.073(4)	-0.114(3)
D	$LiNH_2$, 290 °C	-0.063(5)	-0.120(4)
F	$LiNH_2$, 263 °C	-0.024(1)	-0.071(2)
H	$LiNH_2$, 235 °C	-0.020(4)	-0.052(3)
J	$LiNH_2$, 235 °C	-0.0054(4)	-0.03(1)

a fresh sample at each temperature. The activation energy calculated for lithium amide formation during hydrogenation was found to be 32(10) kJ mol^{-1}, and 42(9) kJ mol^{-1} for consumption during dehydrogenation.

Unlike temperature, the effect of the hydrogen pressure on the hydrogenation rate is less clear. At a hydrogenation temperature of 235 °C, the rate constant increased from 0.082(7) min^{-1} with 3 bar of hydrogen to 0.11(1) min^{-1} with 1 bar, before decreasing to 0.035(3) min^{-1} with 0.5 bar. For the fastest hydrogenation reaction, at 290 °C with 3 bar of hydrogen, the rate constant of 0.22(1) min^{-1} (lithium hydride Bragg peaks) translates to a half life for the reaction of 3.14 minutes. Using this result, we would expect the reaction to be 95 % complete in approximately 12.5 minutes. While vastly superior to the recharge times of current electric vehicles[217], this value is significantly in excess of the 2.5 minute target value for vehicular applications[20], especially given the high temperature used to achieve that hydrogenation rate in this experiment. The rate could be increased by the use of moderately higher hydrogen pressure, however a trade-off emerges between the speed and practicality of refuelling, principally in terms of heat management during the exothermic refuelling process. For a 12.5 minute refuel of 5 kg of hydrogen (~500 km range), with an assumed reaction enthalpy of -45 kJ $molH_2^{-1}$, the average heat energy generated would be 150 kW. As outlined in the Chapter 1, this would require significant heat management and related penalties in the system hydrogen storage density.

In order to examine the kinetic behaviour of the non-stoichiometric continuum, stacked plots of the percentage molar amounts of each of lithium amide, lithium imide and the refined non-stoichiometric phases are shown in Figure 3.15 for each dehydrogenation reaction (processes B, D, F, H and J). The dehydrogenations were chosen due to their slower reaction kinetics. In all of the reactions, it can be seen that the lithium-poor phases were consumed to form lithium-rich phases — this is the normal course expected for the dehydrogenation reactions. Each of the dehydrogenation reactions also show that towards the end of the reaction, the proportion of intermediate stoichiometry values decreased to form both lithium-rich and lithium-poor phases, i.e. the phase separation described earlier for the first dehydrogenation reaction. This is particularly apparent in Figure 3.15e, where the temperature increase at 370 minutes results in dramatic segregation of the non-stoichiometric continuum.

In addition to the kinetics of the reaction under the various experimental conditions, the

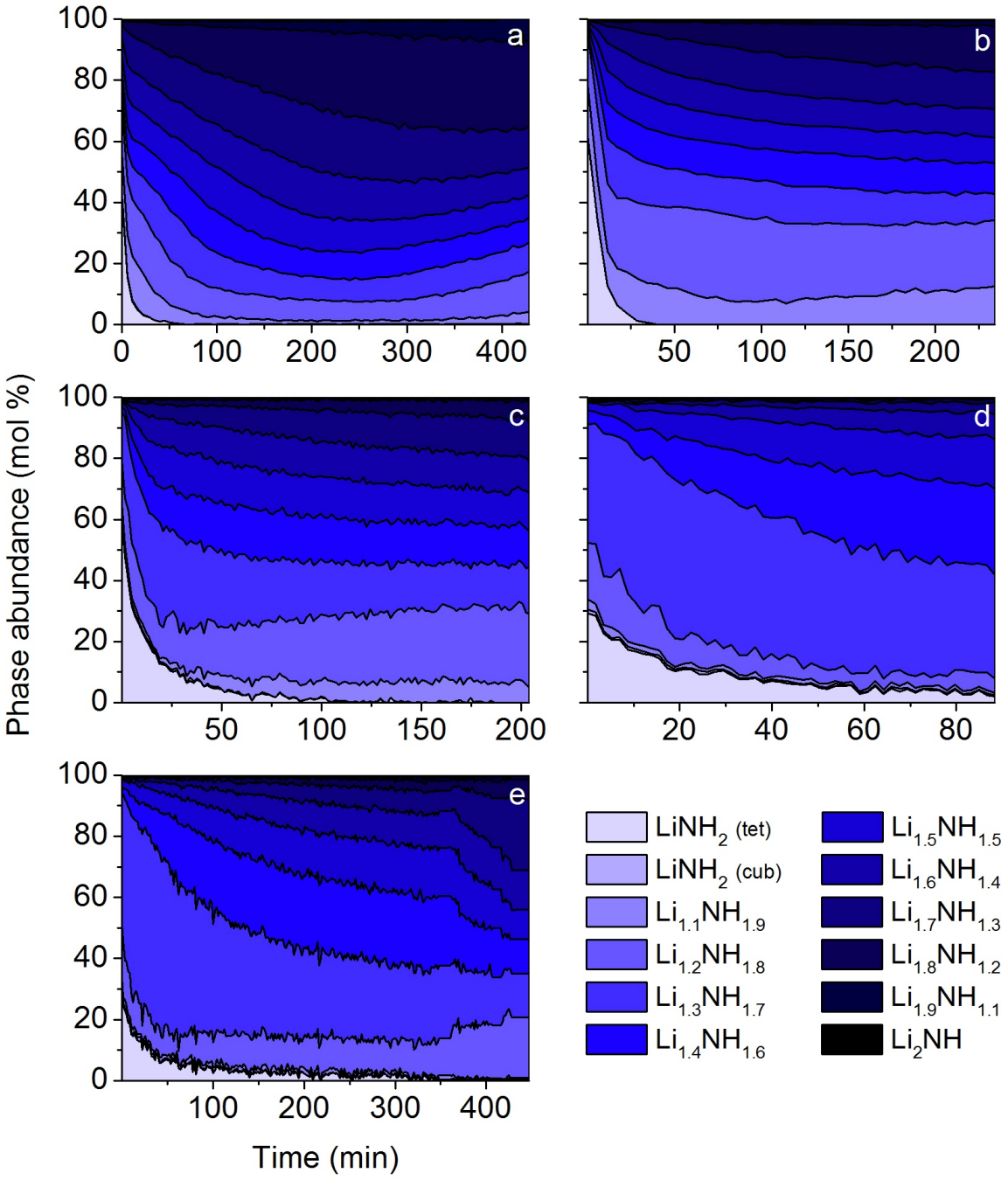

Figure 3.15: Stacked plots of the percentage molar amounts of each of lithium amide, lithium imide, and each of the intermediate phases over the course of each dehydrogenation reaction: (a) 290 °C, 1st cycle (Process B), (b) 290 °C, 2nd cycle (Process D), (c) 263 °C (Process F), (d) incomplete reaction at 235 °C, 1st cycle (Process H), (e) 235 °C, 2nd cycle, heated to 290 °C at 370 min (Process J). Average relative standard deviations in each phase are ±2 % for Processes B and D, and ±4% for Processes F, H and J.

relative extent of reaction is of interest, giving insight into the accessible proportion of the stored hydrogen, and the diminution of capacity upon cycling or changes in reaction condition. Given the complexity associated with modelling the Li-N-H region for Rietveld analysis, the lithium hydride signal is a convenient initial measure of this parameter. Further results from the single peak analysis of the intensity of the lithium hydride (002) reflection described earlier are shown in Figure 3.16. Here, the average percentage change in the peak scale factor during each hydrogenation and dehydrogenation process and an indication of the extent of reaction are shown, taking the first hydrogenation and dehydrogenation endpoints as 100 %. It can be seen that the variation in the magnitude of the lithium hydride peak was significantly greater than the maximum change expected from stoichiometry according to the expected reaction (–50 % for dehydrogenation and +100 % for hydrogenation). As such, this analysis is not sufficiently reliable to produce a direct correlation to the lithium amide - lithium imide concentrations. However, the scale of the lithium hydride peaks can be used as a guide to the relative extent of hydrogenation/dehydrogenation in the system under different reaction conditions.

By this measure, it can be seen that the most significant parameter affecting the hydrogen storage and release capacity of the Li-N-H system was the temperature of the reaction, with the relative extent of hydrogenation from lithium imide to lithium amide dropping from 100 % at 290 °C to 74 % at 263 °C and 66 % at 235 °C, and the relative dehydrogenation extent from lithium amide to lithium imide decreasing from 100 % at 290–263 °C to 95 % at 235 °C. These results suggest that the hydrogenation reaction was more sensitive to changes in temperature at this level than the dehydrogenation reaction, although these observations do not take into consideration any oxidation of the sample by reaction with the capillary, which occurred primarily during dehydrogenation. Oxidation, to form lithium oxide (Li_2O) will increase the apparent extent of reaction during dehydrogenation measured in this way, as lithium hydride is likely to be the species preferentially consumed by oxidation. However, it will diminish the extent of reaction of the subsequent hydrogenation, as the lithium from oxidised lithium hydride is sequestered. The amount of oxide increased slowly over the course of the cycling, reaching 16 mol% after process I.

Hydrogen pressure did not appear to affect the extent of hydrogenation over the range of pressures studied at 235 °C, with no significant difference in hydrogenation extent observed for

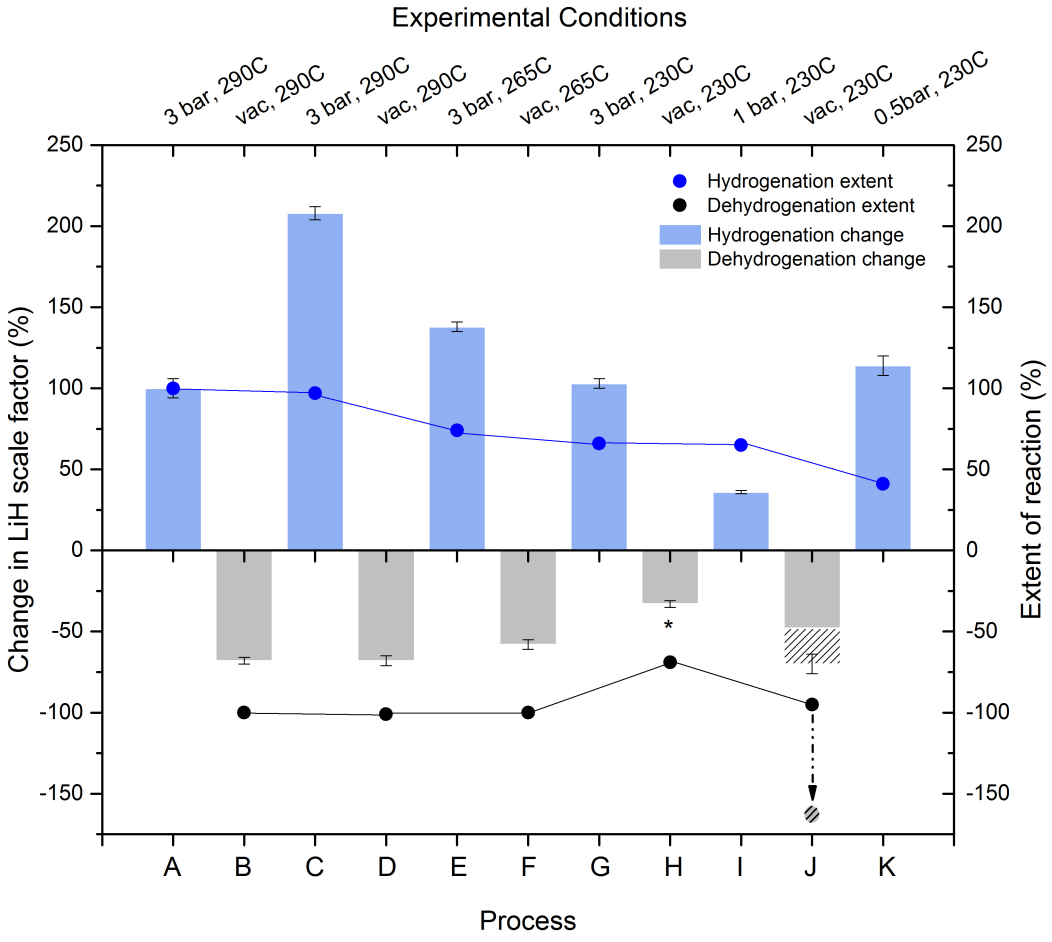

Figure 3.16: Variation in the magnitude of the LiH (002) peak during each reaction, shown as a column graph, and the extent of reaction relative to the first hydrogenation-dehydrogenation cycle shown as points. The shaded column and point represent the change in lithium hydride scale and extent of reaction upon heating the 235 °C sample to 290 °C. The starred column indicates a partially complete reaction. [137] Reproduced by permission of The Royal Society of Chemistry.

hydrogenations performed at 3.0 bar and 1.0 bar (processes G and I). The lowest extent of hydrogenation was observed with 0.5 bar of hydrogen (process K). Examination of the increase in the lithium oxide peak during the previous dehydrogenation (process J, where an elevated temperature of 290 °C was utilised in an attempt to drive the reaction to completion), from 16 mol% to 38 mol%, indicates that oxidation of the sample is the most likely explanation for this drop in capacity.

The extent of reaction was also examined by studying the diffraction information for the lithium amide-imide continuum. Figure 3.17 shows plots of the diffraction intensity for the Li-N-H region at the end of each dehydrogenation cycle, and a histogram of the refined molar percentage of each non-stoichiometric phase at that point, encompassing the range of reaction temperatures used in the experiment. The average stoichiometry of the sample is indicated in each panel. Clearly, there is a range of distributions of the non-stoichiometric phases among the different reaction conditions. In particular, a significant difference in behaviour may also be observed between high- and low-temperature dehydrogenation. After high-temperature desorption, a bimodal distribution of the $Li_{1+x}NH_{2-x}$ stoichiometry is observed, with a slight excess of lithium-rich stoichiometry ($x \geq 0.8$) for cycle 1 (Figure 3.17a) and lithium-poor ($x \leq 0.2$) for cycle 2 (Figure 3.17b). The excess of lithium rich phases in Figure 3.17(a) may be attributed to this material approaching complete dehydrogenation and the more even profile of phases in the second cycle at 290 °C (Figure 3.17b) resulting from incomplete dehydrogenation.

In Figure 3.17c and d, showing the data for dehydrogenation at 263 °C and 235 °C, respectively, considerably less complete reaction is observed compared with (a) and (b). In contrast to the high-temperature reaction, the distribution of phases after the low-temperature dehydrogenation reactions shows stoichiometry dominated by the intermediate $0.3 \leq x \leq 0.7$ range, with concomitant decreases in the average stoichiometry values relative to the high temperature experiments. A second cycle at 235 °C (Figure 3.17e) is visibly similar to the first cycle at 235 °C (Figure 3.17d), although with a slightly increased proportion of lithium-rich phases. Given the discussion of Figure 3.3, it is reasonable to say that the high-temperature dehydrogenations also form a similar distribution, albeit with a shift to more lithium-rich average stoichiometry, and subsequently segragate into the bimodal stoichiometry distribution seen in the final patterns.

The phase composition profiles of Figure 3.17 suggests a system where the progress of the

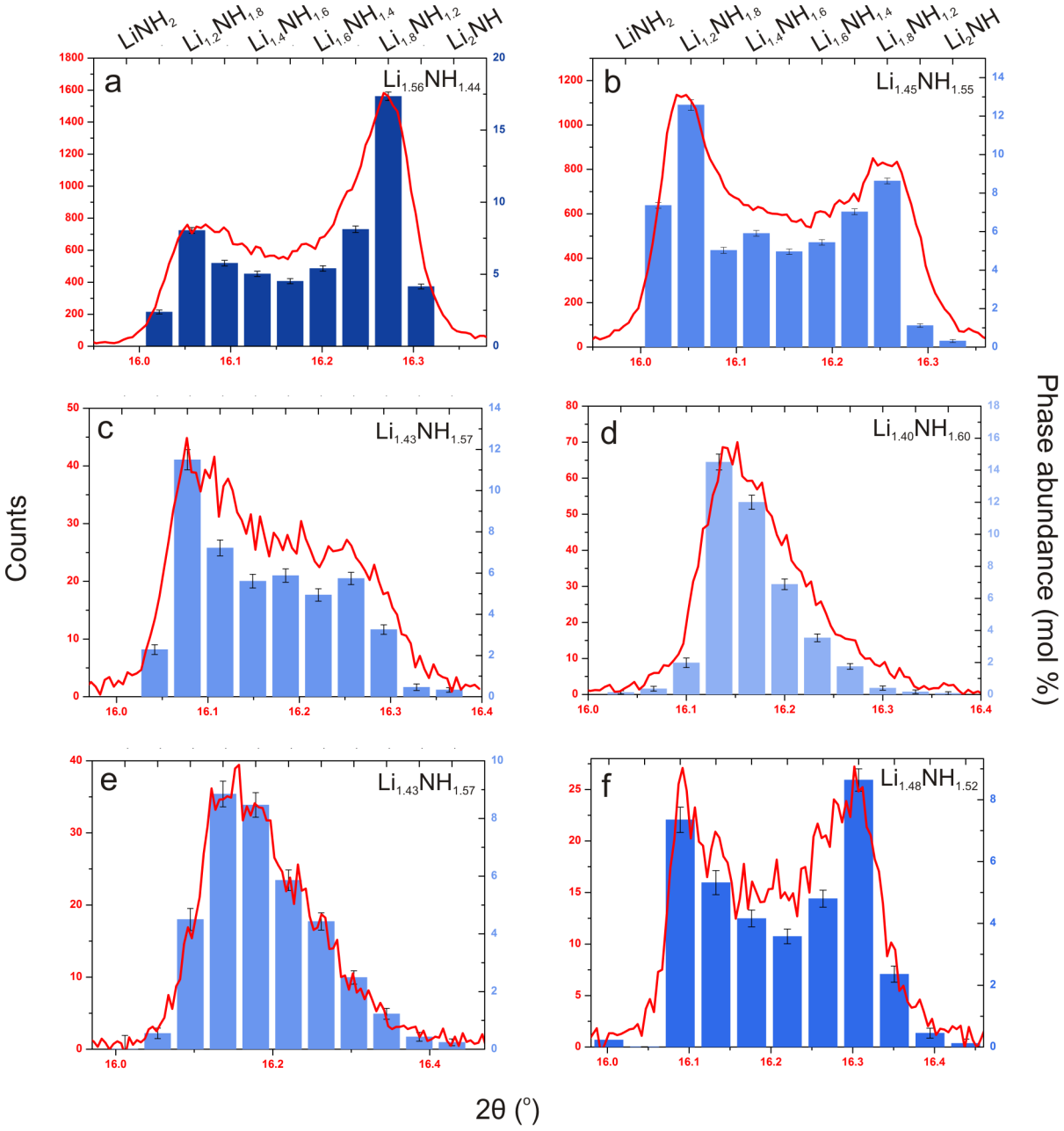

Figure 3.17: Diffraction peak profiles for the Li-N-H region (111) reflection (red) and histograms of refined amounts of Li-N-H stoichiometry values (blue bars) at the end of dehydrogenation reactions at (a) 290 °C, 1st cycle (Process B), (b) 290 °C, 2nd cycle (Process D), (c) 263 °C (Process F), (d) incomplete reaction at 235 °C, 1st cycle (Process H), (e) 235 °C, 2nd cycle (Process J), (f) 290 °C, heated from (e). Lighter blue reflects an average stoichiometry value closer to $LiNH_2$, with darker blue closer to Li_2NH. The average stoichiometry of the sample at the end of each dehydrogenation is indicated in the relevant panel. [137] Reproduced by permission of The Royal Society of Chemistry.

reaction is limited by temperature. In other words there was insufficient thermal energy to form the most lithium-rich compositions, particularly in the low-temperature cycles. This, in turn, suggests the presence of a different activation barrier for lithium/proton migration in lithium-poor materials compared to lithium-rich materials. The structural similarity of the amide and imide phases notwithstanding, variation might be expected as lithium amide has many more vacant potential hopping sites for lithium cations and protons than the imide. Furthermore, the driving potential for lithium motion — the negative charge of the NH_2^- and NH^{2-} units — is more shielded in lithium rich compounds, and the potential for Li^+–Li^+ repulsion (ionic conductivity scattering events) is greater where there is a greater concentration of lithium cations. However, ionic conductivity data for lithium amide and lithium imide show that the conductivity of the imide is at least two orders of magnitude higher than the amide[139]. This means that despite the arguments above, the activation energy to migration is significantly higher in the amide than in the imide. Indeed, there is an important distinction between the number of vacancies and the energy required to move to a vacant site. The variation in activation barrier has been reported to arise from a difference in high temperature behaviour of NH_2^- and NH^{2-}[218].

In addition to the possibility of differential stability and ionic-mobility barriers, particle-size equilibration may be important in the dehydrogenation kinetics, and extent of reaction indicated in Figure 3.17. Particle size has been suggested to influence the balance between bulk/surface mechanisms in the Li-N-H system[141, 142]. Given the doubling of lithium density during dehydrogenation, it is not unreasonable to assume that the lithium amide or imide particles decrepitate during this process. However, the initial particle sizes of the lithium amide and lithium hydride may play a significant role in the extent of reaction for a given temperature. The samples in this experiment were hand ground, but mechanochemical milling has been shown to reduce the activation energy for the reaction[114, 115]. This may be reflected in the fact that, even at the highest temperatures used in this experiment, the extent of reaction as determined from the average stoichiometry of the Li-N-H phases was only 56 %.

In this investigation, the dual effects of kinetic and thermodynamic stability have been observed in the Li-N-H system. The facile reversibility of the hydrogen storage reactions in this system is facilitated by the formation of a non-stoichiometric continuum ($Li_{1+x}NH_{2-x}$), which appear to be stabilised because of its disordered nature. However, the relative thermodynamic

stability of these phases is low compared with the end members, lithium amide and imide, and so with annealing, and increased temperature, phase separation into these species is observed. These dual effects are illustrated by the comparison of Figure 3.17e and f, where the heating of the sample from 235 °C to 290 °C under vacuum facilitates the transformation from the kinetic distribution of phases seen in the low temperature reaction (Figure 3.17e) to the bimodal thermodynamic distribution seen at high temperatures (Figure 3.17f). The close interplay of these effects is likely to be central to the reversibility of the Li-N-H system.

3.2.2 The effect of additives: titanium (III) chloride

The second sample analysed by *in situ* PXRD on the I11 beamline was lithium nitride doped with 3 mol% of titanium (III) chloride. The room temperature PXRD pattern (Figure 3.18) shows that the titanium chloride is observed in the crystalline mixture, with extra peaks matched by the crystal structure of the chloride. The refined weight percent from the Rietveld refinement is 0.61 %, significantly lower than the expected weight percent of 7 %. This discrepancy may reflect a lack of crystallinity of the titanium (III) chloride phase, or that a reaction has occurred with lithium nitride. The titanium (III) chloride crystal structure does not fit the experimental data well; the (010) and (011) peaks are not observed. Furthermore, the data also do not fit any of the predicted transformations of the chloride.

The doped sample was subjected to hydrogenation-dehydrogenation reactions in the same manner as for the undoped sample. Due to time constraints, all of the reactions were isothermal at 235 °C. The conditions are summarised in Table 3.3. Contour plots of selected regions of the diffraction pattern are shown in Figure 3.19. The panels in Figure 3.19a-d capture the same regions of the diffraction pattern as those is Figure 3.1, with an additional panel in Figure 3.19e which shows the titanium (III) chloride (112) reflection. Individual diffraction patterns showing the observed patterns and the calculated fit to the data are given for the beginning of each process outlined in Table 3.3 in Appendix C, with crystallographic information used in the refinements given in Appendix A.

The features of the contour plots for the doped sample are broadly similar to those of the nascent sample. The lower temperature and pressure used for the hydrogenation of the lithium nitride allows for a more clear observation that the reaction to form lithium amide (and lithium

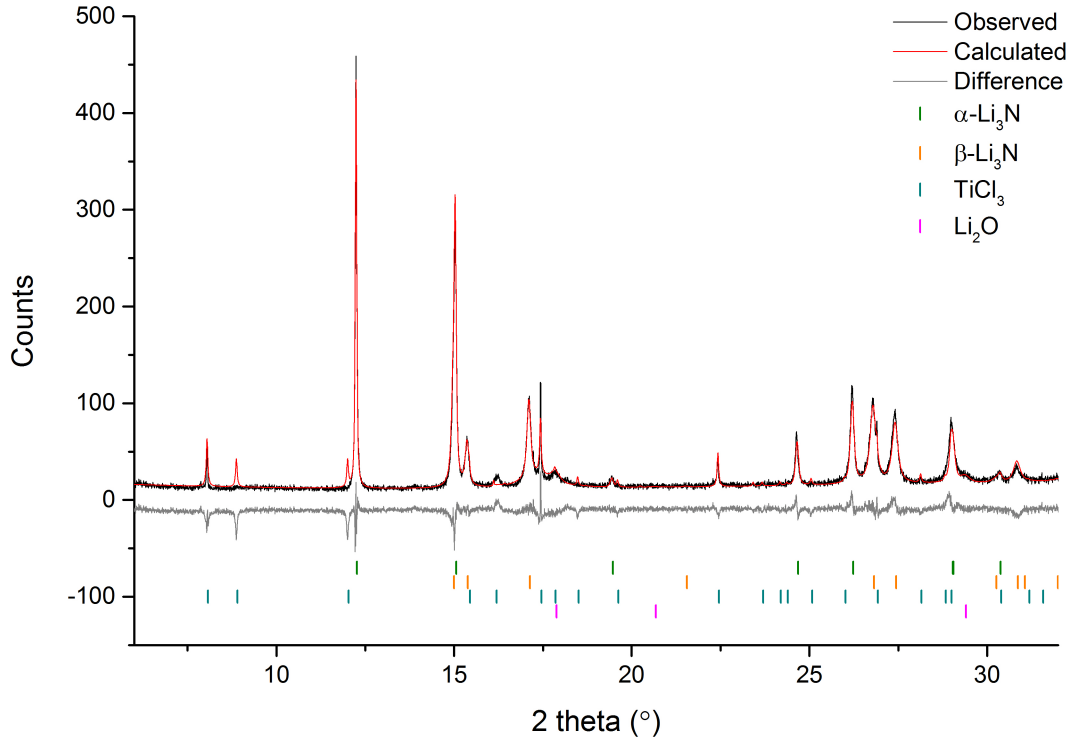

Figure 3.18: PXRD pattern of the starting material, $Li_3N + 0.03TiCl_3$, showing the observed (black) and calculated (red) patterns, with tick marks for reflections of the identified crystalline phases included in the refinement shown. The difference between the observed and calculated patterns is shown in grey. The Rwp for the fit to the data was 16.099.

Table 3.3: Summary of pressure and temperature regimes for the *in situ* X-ray diffraction measurements on the Ti-doped Li-N-H system. Letter designations given to the right of each set of reaction conditions indicate the sequence in which each reaction was performed. All dehydrogenations were performed under dynamic vacuum.

Process	Temperature (°C)	H_2 pressure (bar)	Order
$Li_3N + 2\,H_2 \rightarrow LiNH_2 + 2\,LiH$	235	0.5	L
	235	3	M
$LiNH_2 + LiH \rightarrow Li_2NH + H_2$	235	<0.01	N
	235	<0.01	P
$Li_2NH + H_2 \rightarrow LiNH_2 + LiH$	235	0.5	O
	235	1.0	Q

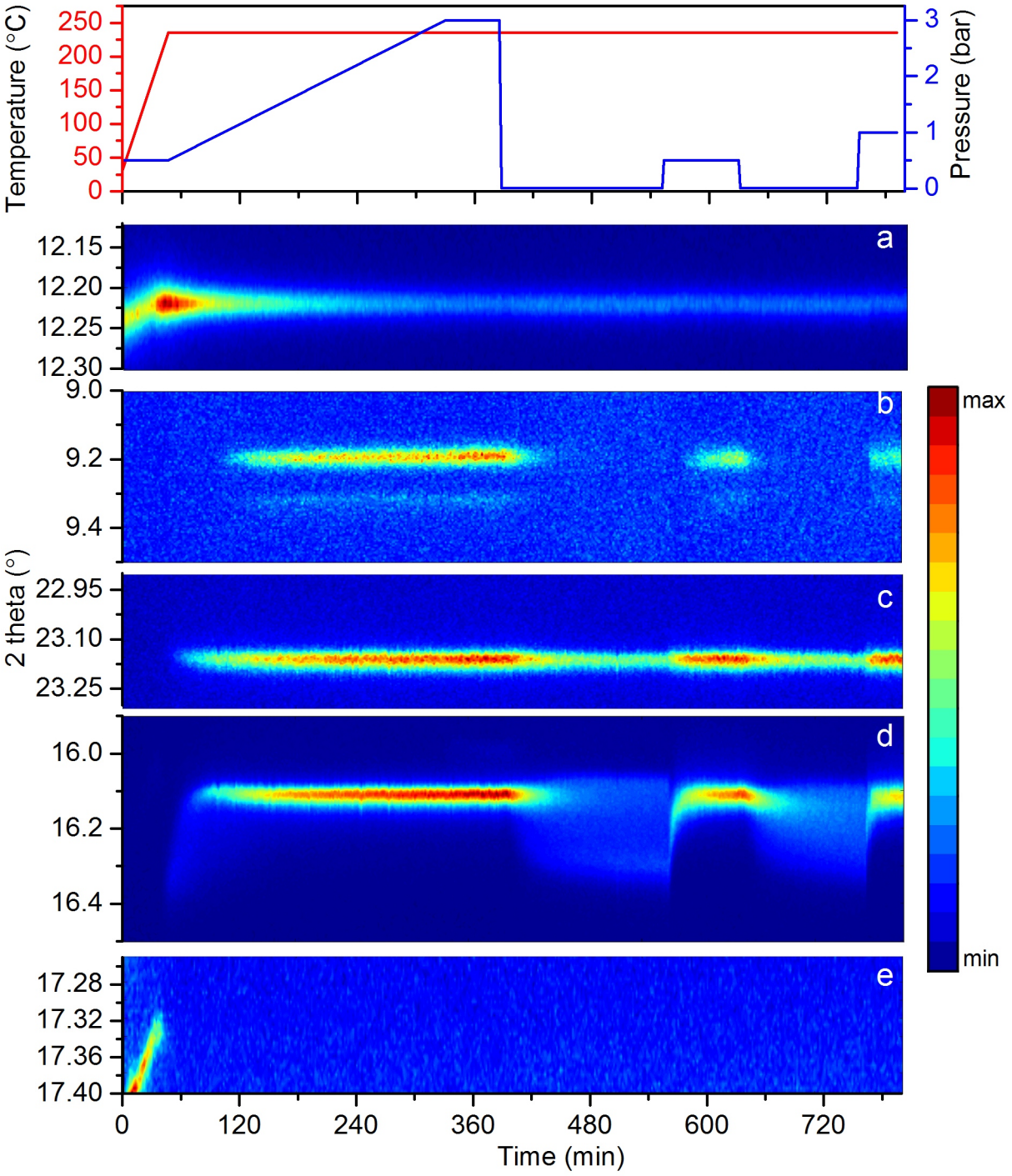

Figure 3.19: Contour plot showing selected regions of the diffraction patterns obtained for the hydrogenation/dehydrogenation cycles over time for the Ti-doped Li-N-H system. The panels show a) the α-Li_3N (001) reflection, b) the superlattice region of $LiNH_2$: the (002) and (100) reflections, c) the LiH (002) reflection d) the "Li-N-H" region, bounded by the $LiNH_2$ (112) reflection and the Li_2NH (111) reflection and e) the (112) reflection $TiCl_3$. The top panel indicates the experimental conditions during the course of the experiment.

hydride) does proceed via the non-stoichiometric continuum described for the amide-imide transformations than was possible for the undoped sample. This is evidenced by the diffraction intensity which appears between the lithium amide and lithium imide reflections during the hydrogenation of lithium nitride. The presence of the lithium nitride hydride (Li_4NH) or superstoichiometric lithium imide phases (referred to as either $Li_{2+x}NH$ or $Li_{2+x}NH_{2-x}$) which have been previously reported[219, 220] were not observed in these data. The reaction pathways which form these species during the hydrogenation of lithium nitride have been proposed to be pressure-dependent, although similar reaction conditions were used in these experiments as in the studies which reported the existence of these phases. In these experiments, diffraction intensity is only observed starting at the region expected for lithium imide and then progressing through the non-stoichiometric continuum toward the amide.

The lithium amide structure formed during the hydrogenation again shows the presence of the (001) reflection, giving the $P\bar{4}$ space group. The refined PXRD pattern for the end of the first hydrogenation reaction is shown in Figure 3.20. As can be seen, the reaction did not go as far to completion as the undoped sample, because of the lower temperature used. Although the titanium (III) chloride phase disappeared during the hydrogenation reaction (Figure 3.19e), three peaks appeared which are unaccounted for in the Rietveld analysis, and were not present in the undoped sample. They are indicated with asterisks in Figure 3.20. These peaks were not able to be assigned to a specific phase — those tested included metallic titanium, oxides of titanium, and nitrides of titanium and lithium. It is, however, reasonable to suggest that these phases are associated in some way with the titanium (III) chloride, since they were not present in the undoped sample.

In sodium alanate, doping with titanium (III) chloride is believed to reduce the titanium (III) ion to titanium metal according to Equation 3.5, which then reacts to form titanium-aluminium alloys upon dehydrogenation[221]. There is not an analogous reaction in the lithium amide system, since lithium amide is not a reducing agent, and alloys of lithium and titanium are not known[222].

$$3NaAlH_4 + TiCl_3 \rightarrow Ti + 3NaCl + 3Al + 6H_2 \tag{3.5}$$

The peak at 15.8° is close to the position expected for the lithium chloride (111) reflection,

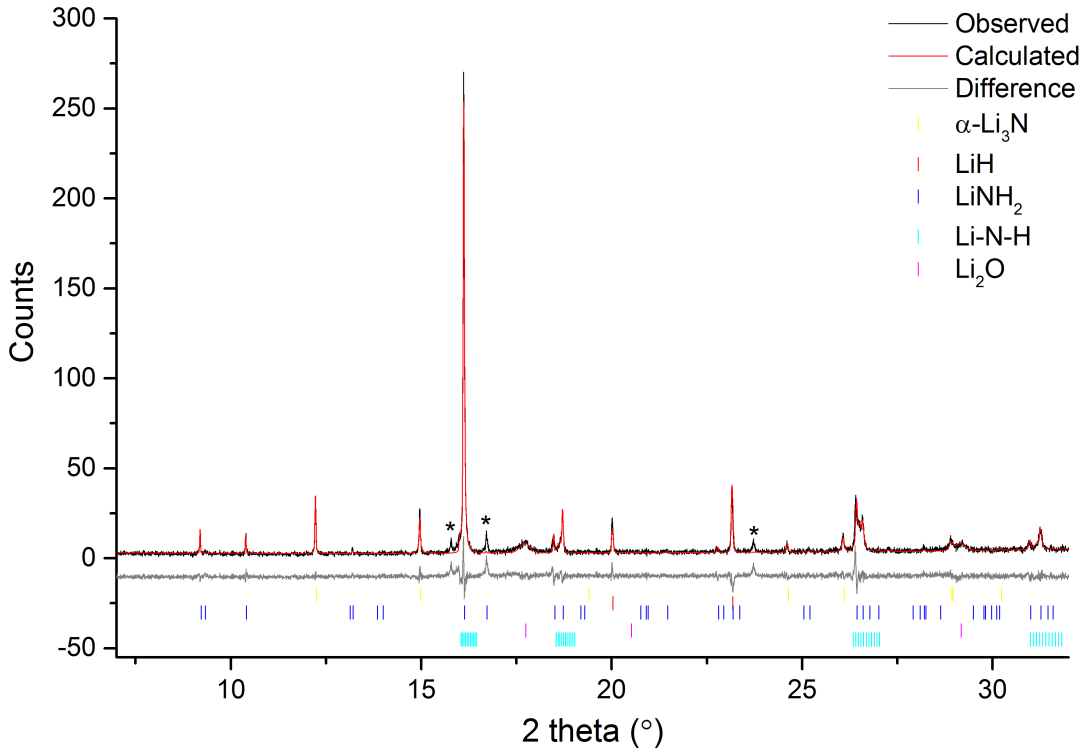

Figure 3.20: PXRD refinement of the titanium-doped lithium nitride sample after the first hydrogenation reaction, showing the observed (black) and calculated (red) diffraction patterns, and the difference between the two (grey). The tick marks for Bragg peaks of the phases included in the Rietveld refinement are shown. Peaks which are not assigned to a particular phase are marked with an asterisk. The Rwp for the fit to the data was 20.633.

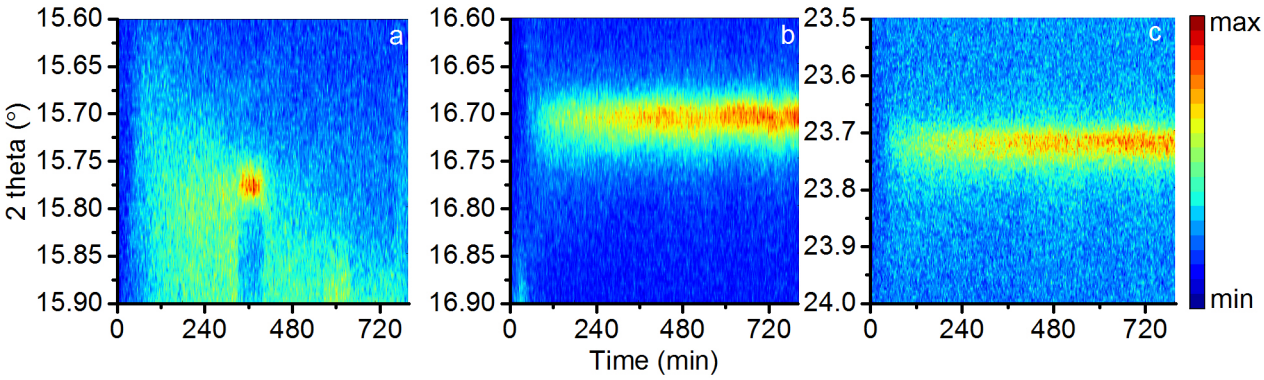

Figure 3.21: Contour plots of the three unassigned Bragg peaks in the PXRD data of the course of the hydrogenation-dehydrogenation reactions in the titanium-doped Li-N-H system.

which might be expected as a byproduct of the reaction of lithium amide and titanium (III) chloride, however no other peaks for lithium chloride are observed. In fact, contour plots of the regions associated with these three peaks across the duration of the experiment in Figure 3.21 show that the 15.8° peak (Figure 3.21a) is only observed at the end of this first hydrogenation reaction, and only for the period when the sample was under 3 bar hydrogen pressure. This may indicate the presence of a hydrogenated structure, though without any other peaks to associate it with, assigning the peak to a specific phase is not straightforward. In contrast, the other two unknown peaks at 16.7° and 23.7° are observed throughout the experiment (Figure 3.21b and c), and their magnitude does not appear to be correlated with the hydrogen pressure; both peaks increase steadily over the course of the experiment. It is unclear whether they are associated with inert phases which increase over the course of the reaction in a similar fashion to oxide peaks, for example, or whether they are the active form of the titanium dopant.

Other studies have presented evidence for possible active forms of the titanium dopant. Tsumuraya *et al.* found that the best fit to the XAS data collected for the titanium-doped system was a substitution of the titanium into lithium amide [223]. They inferred that this would be energetically stable by noting that there are similarities in the structure of lithium-titanium nitrides with the amide-imide structures, where the titanium ion is four-coordinate with nitrogen in the same way that lithium ion is in the amide structure. The substitution of a titanium for one of the lithium sites ($Li_3Ti(NH_2)_4$) produced a theoretical XAS spectrum which matched the main features of the experimental data. The data presented here fit well with an unaltered lithium amide structure — although with the low percentage of titanium doped into

the sample, and the similar ionic radii of lithium and titanium, this is perhaps unsurprising.

Lithium titanate ($Li_2Ti_2O_4$) was also suggested on the basis of *in situ* X-ray diffraction on single crystals in a microscopy study[111]. This phase does not fit any of the peaks present in the data here. An alternative explanation given for the XAS data on the doped system based on experimental data was that the best fit to the titanium absorption edge of the active form of the dopant was an ammoniate of titanium (III) chloride ($TiCl_3(NH_3)_x$)[110]. IGA^n data for the adsorption and desorption of ammonia from titanium (III) chloride are shown in Figure 3.22. These data suggest that even under 1 bar of ammonia — significantly higher than the pressures which are likely to be present locally during the hydrogen storage and release reactions of the Li-N-H system — the tri-ammoniate is the highest degree of ammonia basorption obtained, making the penta-ammoniate suggested in the XAS study an unlikely species to be present in the sample. These data also show that the ammoniate is not stable under elevated temperatures, with the formation of the di-ammoniate observed at 150 °C, and complete ammonia desorption as the sample is heated to 250 °C.

A diffraction pattern of the tri-ammoniate does show peaks in the region of those in Figure 3.21b and c, along with a number of other reflections (see Appendix G). While this could be an indication that the ammoniate is present in the *in situ* data, it is unclear why it would have increased thermal stability when doped into the Li-N-H system, and the presence of two corresponding peaks is not sufficient information to clearly identify this as the active form of the titanium dopant.

Identifying the active form of the catalyst is only part of the effort to understand its action. The observed effect on the kinetics of the reaction is also crucial to determining the usefulness of doping the sample. Figure 3.23 shows the evolution of the relative molar amount of each of the phases included in the Rietveld analysis for the reactions of the Ti-doped sample, along with the reaction conditions and the extent of reaction assessed by the average lithium stoichiometry in the lithium amide-imide continuum. Due to the lower temperature used, the extent of reaction was generally lower than that observed for the earlier cycles in the undoped sample. The effect is also seen in the proportion of non-stoichiometric phases which remained at the end of the hydrogenation reactions; higher temperatures would result in more complete formation of lithium amide.

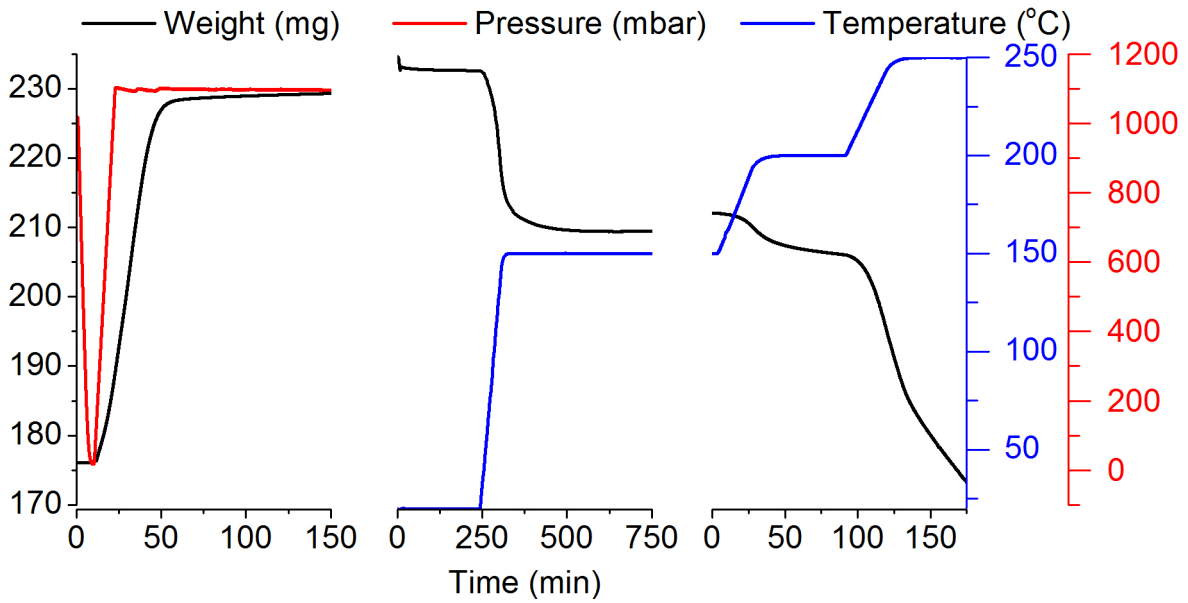

Figure 3.22: IGA^n data for the (left) absorption and (right) stepwise desorption of ammonia by titanium (III) chloride, showing the variation of the mass of the sample (black) with changes in the ammonia pressure (red) and the temperature (blue). The adsorption experiment was performed under 1 bar of ammonia, while the desorption experiment was performed under 1100 mbar of argon.

The extracted molar amounts were fitted to the same exponential equations that were used for the undoped sample (Equations 3.3 and 3.4). The rate constants extracted from these fits are shown in Table 3.4. Due to the different thermal histories of the doped and undoped samples, comparison of these rate constants should be considered qualitatively. Nevertheless, the lithium hydride rate constants, which indicate the overall reaction rate, were significantly higher than the rates for the equivalent hydrogenation reactions in the undoped sample, and the average rate of dehydrogenation across processes N and P was also higher than the average rate for processes H and J in the undoped sample. These values corroborate the general reports that the addition of titanium (III) chloride improves the reaction kinetics of the Li-N-H system [103, 104, 106].

Without further experimental data, it is not possible to be conclusive as to how the dopant improves the reaction kinetics, particularly given the lack of consensus on the rate determining step in the hydrogen storage and release reactions[141, 142, 224, 225]. The most likely effects are: weakening of N–H bonds, enhanced ionic conductivity, improved ammonia transport between lithium amide and lithium hydride, or faster kinetics of chemisorption of hydrogen. Contour plots of the diffraction data for the lithium amide-imide region are shown in Figure 3.24, and follow similar patterns to the low-temperature processes in the undoped sample. The same low-

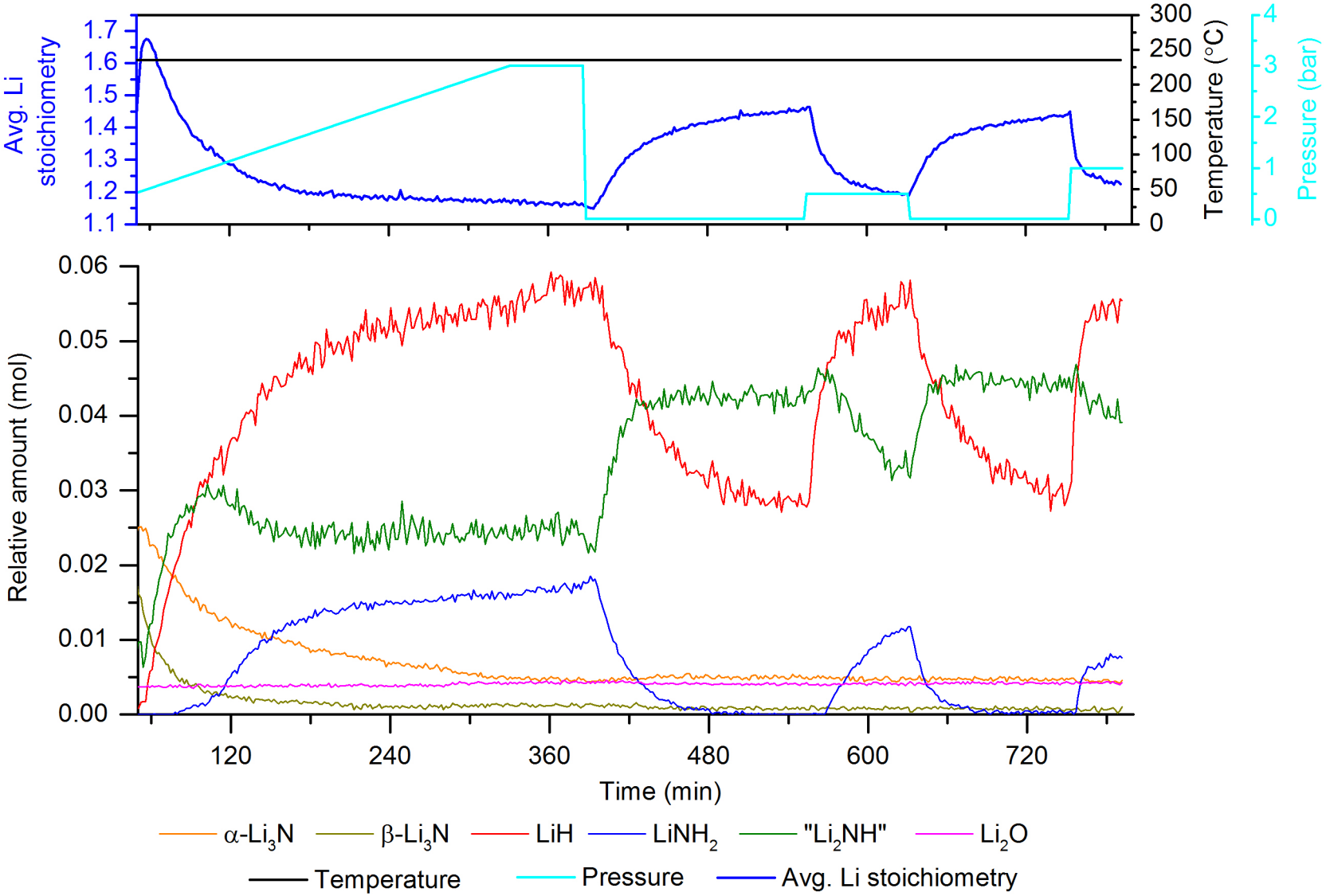

Figure 3.23: The lower panel shows the relative molar amount of each of the phases extracted from the Rietveld refinement of the Ti-doped Li-N-H sample, where the 'Li$_2$NH' value is the sum of each of the non-stoichiometric phases and stoichiometric Li$_2$NH. The upper panel shows the reaction temperature and pressure, and the average lithium stoichiometry of the LiNH$_2$ – Li$_2$NH phases. Average relative standard deviations in the data are ±5% for lithium hydride, ±3% for lithium amide, ±7% for "lithium imide" phases, ± 5% for lithium oxide and ± 4% for both lithium nitride phases.

Table 3.4: Rate constants from exponential fits to the LiH and $LiNH_2$ molar amounts for each of the reaction processes in the Ti-doped Li-N-H experiment. Uncertainties in the extracted rate constant are given in brackets.

Process	Starting material, reaction conditions	k(LiH) (min^{-1})	k($LiNH_2$) (min^{-1})
Hydrogenation reactions			
L,M	Li_3N, 235 °C, 3 bar	0.0150(3)	0.0188(4)
O	Li_2NH, 235 °C, 0.5 bar	0.074(5)	0.025(1)
Q	Li_2NH, 235 °C, 1 bar	0.22(2)	0.14(3)
Dehydrogenation reactions			
N	$LiNH_2$, 235 °C	-0.020(1)	-0.0363(1)
P	$LiNH_2$, 235 °C	-0.028(2)	-0.083(2)

temperature distribution of the non-stoichiometric continuum was observed as was seen for the undoped sample. The difference between the first dehydrogenation relative and the subsequent dehydrogenation reactions was less stark than for the undoped sample. Whether this indicates an effect of the dopant or is as a result of the lower temperature that was used remains to be seen.

3.3 Properties of non-stoichiometric Li-N-H phases

The involvement of the non-stoichiometric continuum in the hydrogenation and dehydrogenation reactions of the Li-N-H system indicates that their properties may be important in understanding and improving its hydrogen storage characteristics. The first challenge in studying this continuum is to prepare various stoichiometry values in isolation; while the first consideration would be to attempt to quench the dehydrogenation of a 1:1 mixture of lithium amide and lithium hydride at various stages of reaction, it is clear from the *in situ* diffraction data presented in this chapter that this would result in a broad stoichiometry range. This would make the determination of stoichiometry-specific properties quite difficult. Therefore, an alternative method was devised based on the work of Hu and Ruckenstein, who showed that lithium imide could be synthesised by the rapid reaction of lithium nitride and lithium amide[226], according to Equation 3.6. This reaction proceeds rapidly at low temperatures, which was deemed advantageous for avoiding the phase separation of the non-stoichiometric phases observed after annealing at high temper-

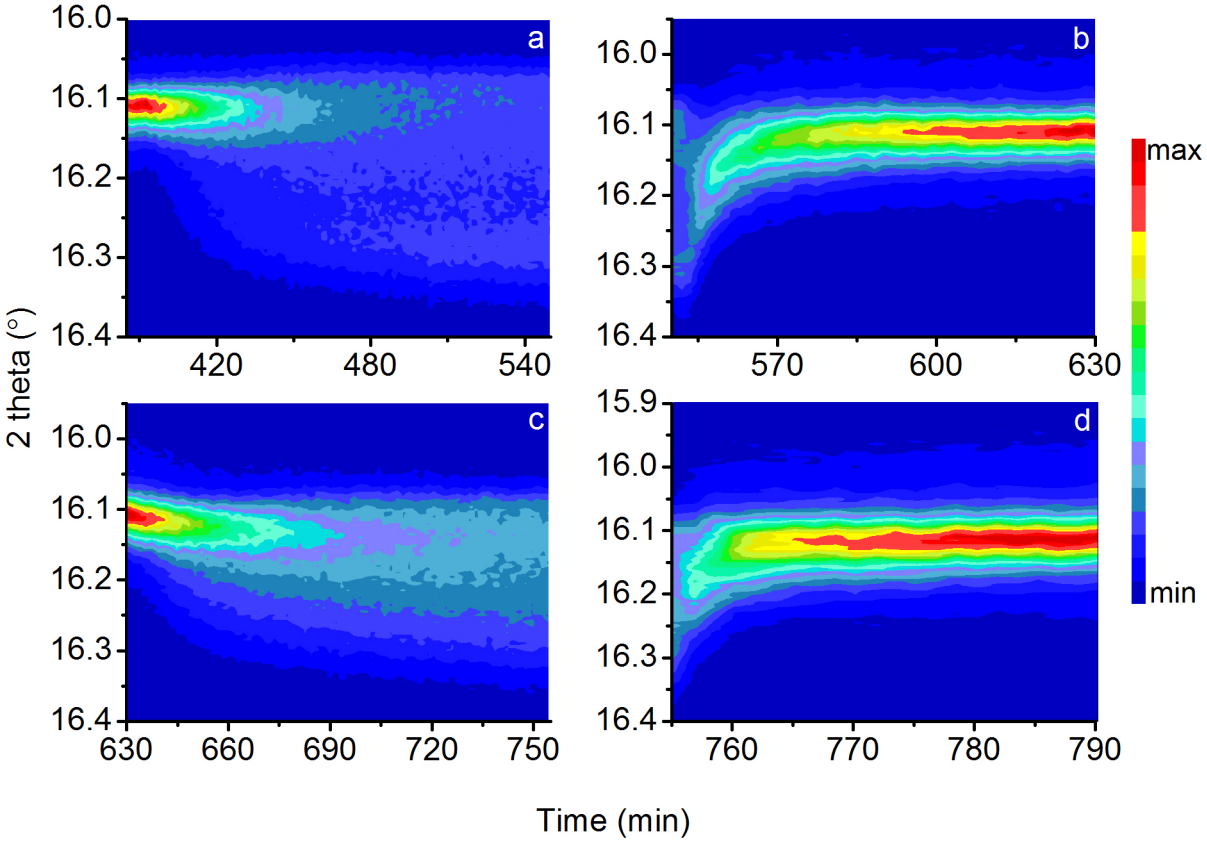

Figure 3.24: Contour plots of the PXRD data of the lithium amide (112) reflection and the (111) peak of both lithium imide and the various non-stoichiometric phases for (a) the first dehydrogenation (process N), b) hydrogenation under 0.5 bar of hydrogen (process O), c) the second dehydrogenation (process P) and d) hydrogenation under 1.0 bar of hydrogen (process Q).

ature. The ratio of lithium amide to lithium nitride was altered to synthesise ostensibly narrow stoichiometric distribution non-stoichiometric samples, according to Equation 3.7.

$$Li_3N + LiNH_2 \rightarrow 2Li_2NH \tag{3.6}$$

$$(1-x)Li_3N + (1+x)LiNH_2 \rightarrow 2Li_{2-x}NH_{1+x} \tag{3.7}$$

The PXRD patterns of the phases synthesised by this method are shown in Figure 3.25, with sections of the patterns highlighted in Figure 3.26. These patterns show a clear transformation from the tetragonal amide structure to the cubic structure expected for the non-stoichiometric and lithium imide phases. In the lithium-poor samples, no lithium nitride was observed, indicating that all of the lithium nitride has reacted with the lithium amide to form the imide. Minor impurities of lithium nitride are observed in the lithium-rich samples, although no lithium amide was observed. This could indicate incomplete mixing of the reactants. The persistence of a number of the tetragonal lithium amide peaks throughout the lithium-poor samples could be taken to indicate that the tetragonal phase exists across a broader stoichiometry range than was observed in the *in situ* data. However, the peak positions of the tetragonal phase did not vary between samples, indicating that the tetragonal phase does not accommodate significant variation in stoichiometry. This implies that those samples contain significant quantities of stoichiometric lithium amide.

A number of conclusions could be drawn from this observation. Firstly, it could be asserted that the amide and nitride simply reacted according to Equation 3.6, resulting in a mixture of stoichiometric amide and imide, rather than the bulk formation of a non-stoichiometric phase. However, this is clearly not the case for the lithium-rich compounds: beyond the nominally $Li_{1.5}NH_{1.5}$ sample, no crystalline lithium amide is seen in the samples. This indicates that bulk formation of non-stoichiometric phase is possible by variation of the reactant ratios according to Equation 3.7. The relative molar amounts of the tetragonal amide and the cubic 'imide' phase in each sample are shown in Figure 3.27a. This demonstrates what is observed qualitatively from examination of the PXRD data, that there is no tetragonal phase remaining in the lithium-rich stoichiometry phases.

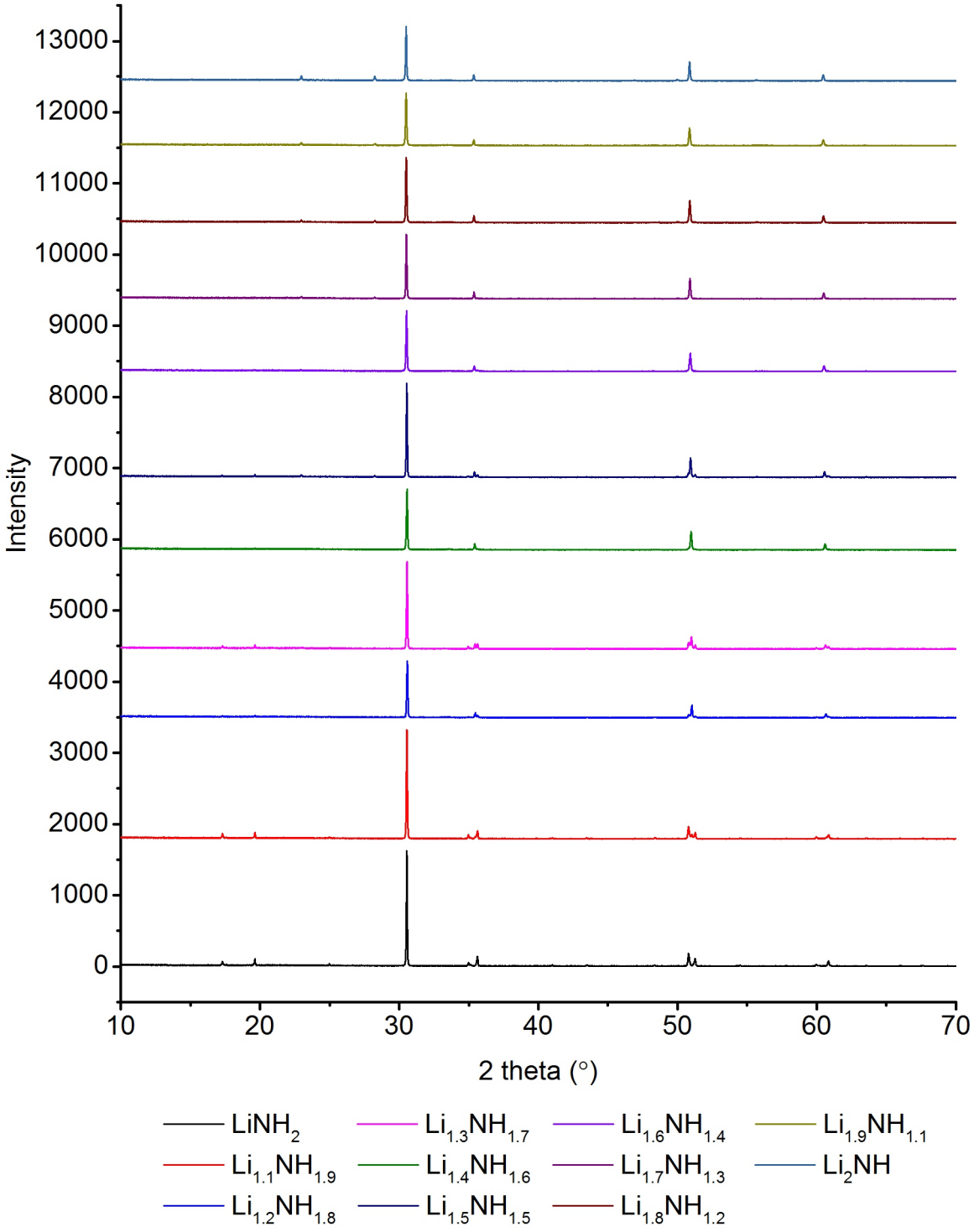

Figure 3.25: Full PXRD patterns of each of the phases synthesised in the continuum between lithium amide and lithium imide. The intensity values are offset from each other for clarity of presentation.

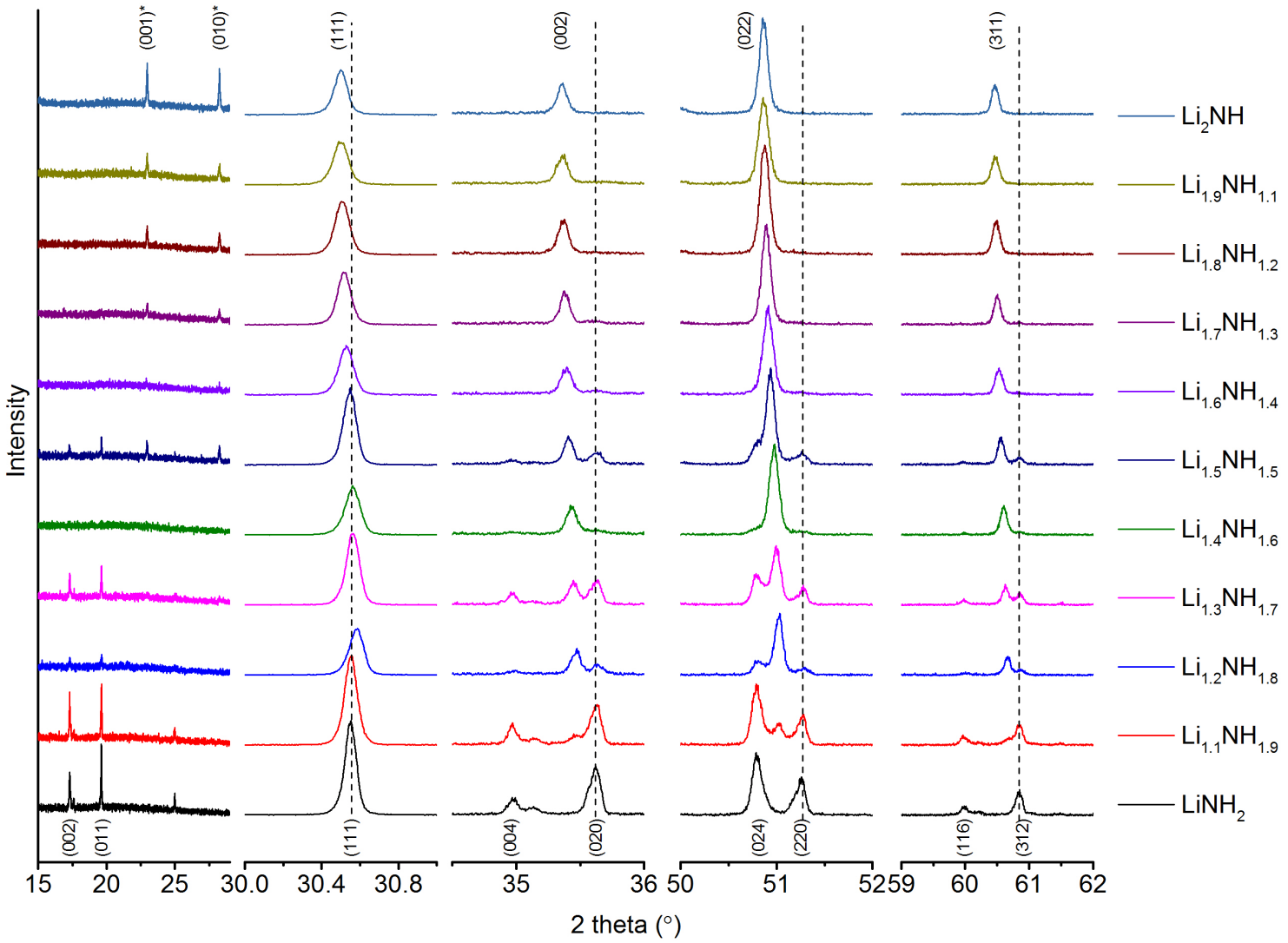

Figure 3.26: Selected sections of PXRD patterns of each of the phases synthesised in the continuum between lithium amide and lithium imide. The intensity values are offset from each other for clarity of presentation. Vertical lines showing the position of selected lithium amide peaks are shown as a guide to the eye. Selected Miller indices for the lithium amide phase are shown below the patterns, with indices for the cubic Li-N-H phases shown above the patterns. The starred Miller indices are from alpha lithium nitride.

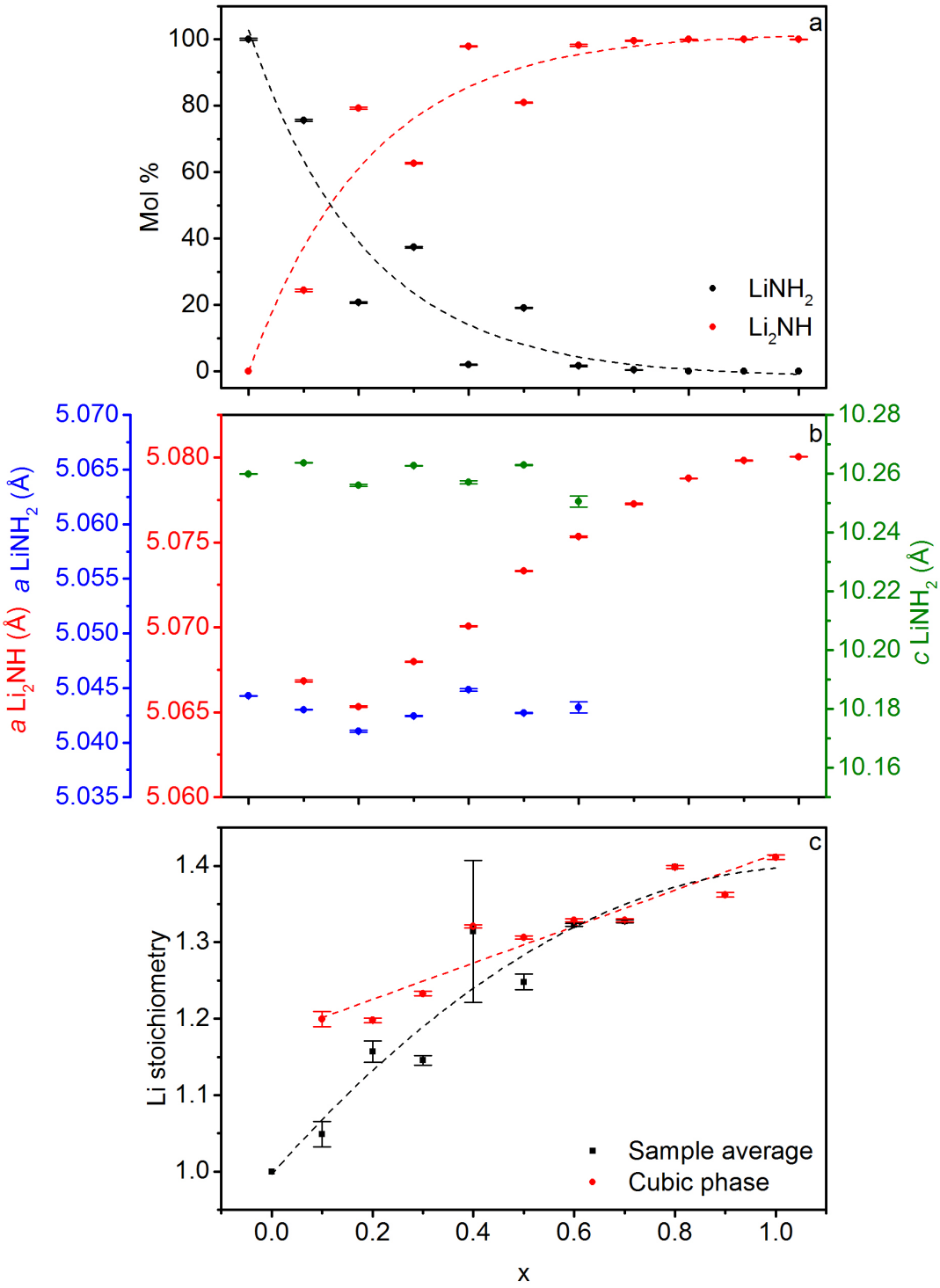

Figure 3.27: Results of Rietveld analysis of PXRD data for the non-stoichiometric phases, showing the variation with x, where the nominal stoichiometry of the phase is intended to be $Li_{1+x}NH_{2-x}$, of a) the molar percentage of lithium amide and the cubic phase (designated as lithium imide), b) the lattice parameters of the two phases and c) the average lithium stoichiometry in the cubic phase, and across both phases.

A possible explanation of the persistence of the amide phase is that the lithium-poor phases are susceptible to phase separation back to the amide and imide, as predicted from first-principles analysis by Zhang *et al*[209]. That study suggested that deviations from amide stoichiometry by less than or equal to 0.25 would not be stable, while those with a stoichiometry within 0.25 of lithium imide would be stable. While the stable ranges for the lithium-rich stoichiometry values observed here are somewhat larger than those predicted ranges, the trend suggested by their modelling is borne out for these samples. This is, however, in contrast to the results of the *in situ* PXRD studies in this Chapter, in which the entire range of intermediate stoichiometry values were unstable to annealing, and long-range tetragonal symmetry lithium amide was never reformed.

What is perhaps a more likely explanation is that, upon reaction of the lithium nitride and lithium amide to form lithium imide, the subsequent formation of a bulk non-stoichiometric sample requires the diffusion of protons and, crucially, lithium ions through the structure. As mentioned earlier, lithium amide has poor lithium ion conductivity, and so it is possible that the temperatures used in these synthesis reactions were insufficient to enable bulk formation of the non-stoichiometric phase in samples which contained a significant proportion of lithium amide. Repetition of this experimental work at higher temperatures would help to elucidate whether this effect is the cause of these results (varying the reaction time may also be useful and indicate the effect of phase separation).

Whatever the origin of the stoichiometric lithium amide, there remain a number of useful pieces of information which can be extracted from the Rietveld analysis of these data. The peak shapes of the cubic phases in these patterns are not as complex as those observed in the *in situ* PXRD studies. This reflects the desired formation of relatively narrow bands of stoichiometry, although this is also, to an extent, due to the lower resolution of the instrument compared with the synchrotron. The symmetry of the peaks allowed for a simple structural model composed of the tetragonal lithium amide phase and a single, variable stoichiometry cubic amide-imide phase. Since hydrogen atoms are only weakly visible by PXRD, the average stoichiometry values of the cubic phases were determined by allowing the lithium occupancy in the lithium imide structure to refine between 0.5 (cubic lithium amide) and 1.0 (stoichiometric imide).

The variation of the lattice parameters of lithium amide and the cubic phase, and the average

stoichiometry of the sample and the stoichiometry of the cubic phase are shown in Figure 3.27b and c, respectively. Reflecting a visual assessment of the diffraction data, it can be seen that the tetragonal amide phase did not undergo a significant change in either of its lattice parameters with varying target stoichiometry values, supporting the hypothesis that the tetragonal phase is essentially stoichiometric. In contrast, the lattice parameter of the cubic phase varied steadily across the samples, implying a variation in stoichiometry. The deviations from a linear variation in lattice parameter as would be expected from Vegard's Law are likely due to incomplete reaction as detailed earlier. Although the stoichiometry of the cubic phase increased in an approximately linear fashion, the narrow range of lithium-poor stoichiometry values obtained (1.2–1.4) suggests that the stoichiometry is not well modelled in the refinement of these data. The variation in the lattice parameter is of a similar magnitude to that seen for the full range of stoichiometry values in the *in situ* diffraction experiments, suggesting that a much wider range of stoichiometry values should have been obtained.

In order to gain a complementary insight into the structure of these phases, a series of deuterated non-stoichiometric phases were synthesised and analysed by NPD. Their full patterns are shown in Figure 3.28, with selected sections highlighted in Figure 3.29. The results largely mirror those from the X-ray analysis, with the lithium-poor samples modelled as a mixture of tetragonal lithium amide and a cubic imide-like phase, while the lithium-rich samples adopted a single cubic phase.

However, the most remarkable result of these diffraction data is that the lattice parameters of the non-stoichiometric phases vary in the opposite direction to that which was observed in the hydrogen storage and release reactions of the Li-N-H system detailed earlier in this Chapter; the non-stoichiometric phases have larger unit cells than lithium amide. This is seen in both the X-ray and neutron data, raising significant questions about the nature of the defect structures in the these different situations. Clearly there are differences in the reaction pathway used to generate these non-stoichiometric phases compared with those of the *in situ* work. It seems likely that a different defect structure may be involved, perhaps resulting from contrasting effects of lithium nitride compared with lithium hydride. For example, it is possible that the intimate mixture of the lithium amide-imide phase with lithium hydride causes some crystallographic strain, or 'clamping'. A number of avenues for further investigation are presented in the concluding remarks

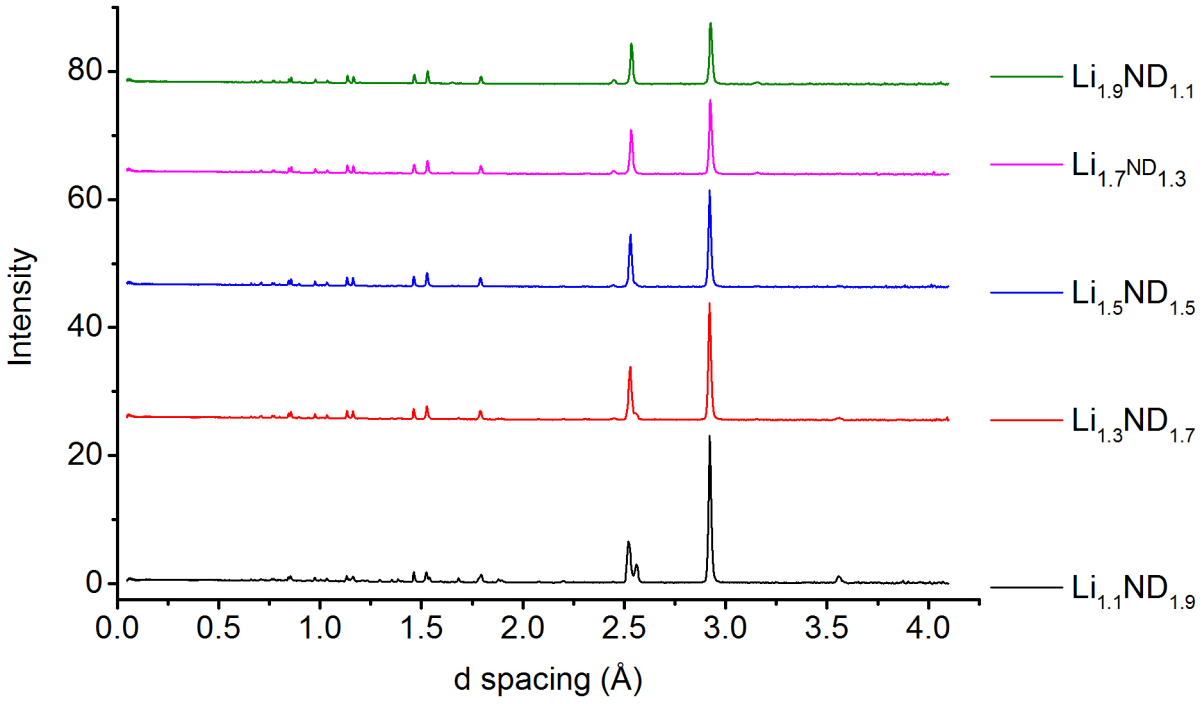

Figure 3.28: NPD patterns for each of the synthesised non-stoichiometric Li-N-D phases, collected on bank 4 of the POLARIS instrument. The patterns are offset from each other for clarity of presentation.

of this Chapter.

In addition to the structural investigation, the bonding in the amide and imide anions was probed by Raman spectroscopy, with the N–H stretching region for each of the phases shown in Figure 3.30, along with those of lithium amide and lithium imide, for reference. Lithium amide shows characteristic vibrations for an NH_2 unit: the large peak at 3260 cm^{-1} is the symmetric N–H stretch band, while the two smaller peaks at 3313 and 3323 cm^{-1} are the asymmetric N–H stretches. The linear imide ion, on the other hand, cannot undergo an asymmetric stretch, and so only exhibits a single N–H stretch, the broad band at 3185 cm^{-1}.

Examination of Figure 3.30 shows that the transition through the range of stoichoimetry values does not result in a simple linear decrease in the amide peaks, and a concomitant increase in the imide peak: additional peaks are observed in the spectra, which are most pronounced in the intermediate stoichiometry range. Given the significant differences in the intensity of the signals given by the various samples, it is difficult to compare the peak heights or areas directly, so most of the discussion of these data is limited to a comparison of relative peak areas and the position of the peaks. Fitting of the data provides some insight into the composition of the

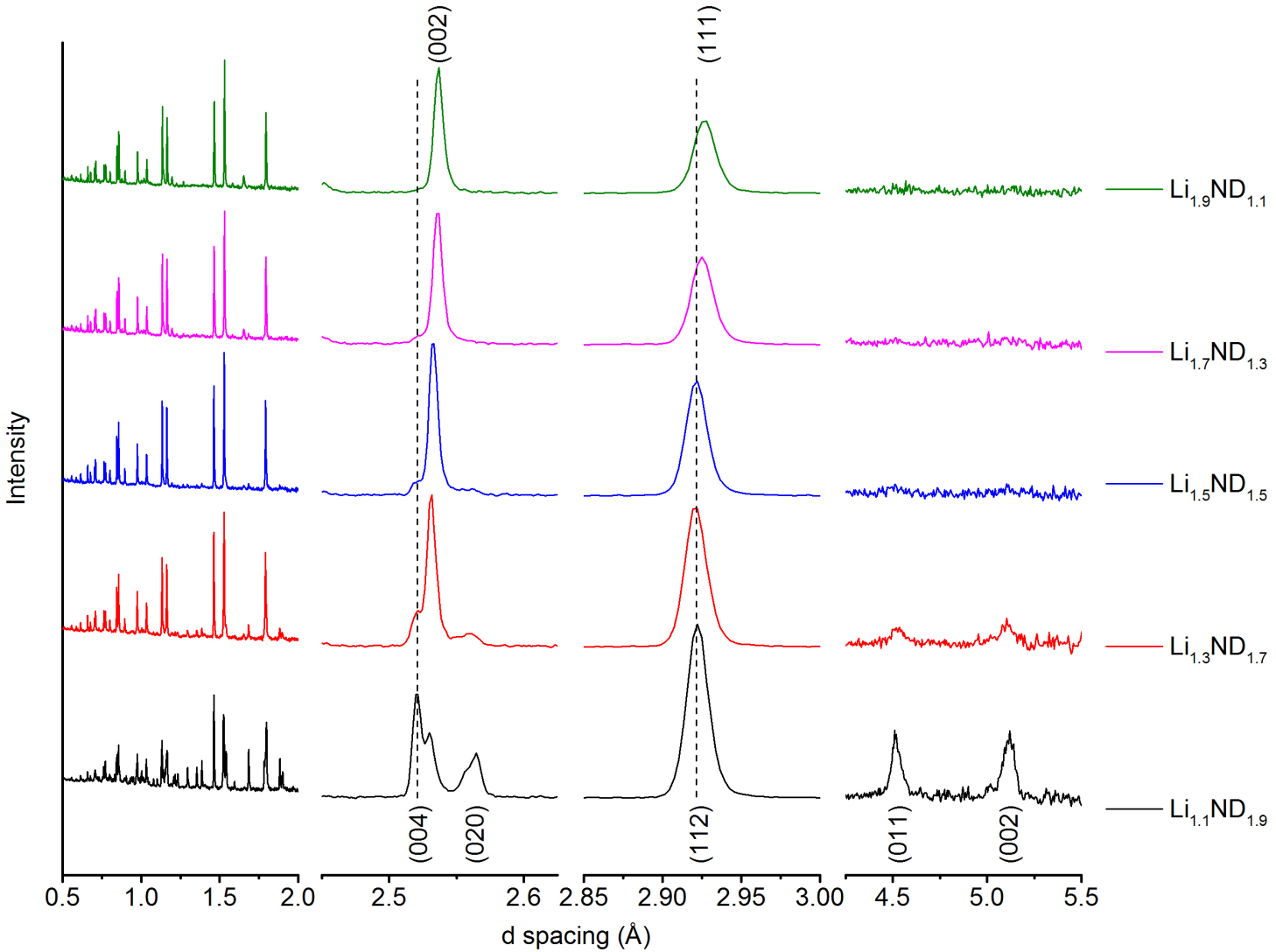

Figure 3.29: Selected regions of NPD patterns for each of the synthesised non-stoichiometric Li-N-D phases, collected on the POLARIS instrument. The intensity values are offset from each other for clarity of presentation. The data shown for the regions 0.5–2.0 and 2.4–2.65 Å are from bank 5 detectors, 2.85–3.00 Å are from bank 4, and 4.25–5.50 Å are from bank 3. Vertical lines showing the position of selected lithium amide peaks are shown as a guide to the eye. Selected Miller indices for the lithium amide phase are shown below the patterns, and above the patterns for indices of the cubic Li-N-D phases.

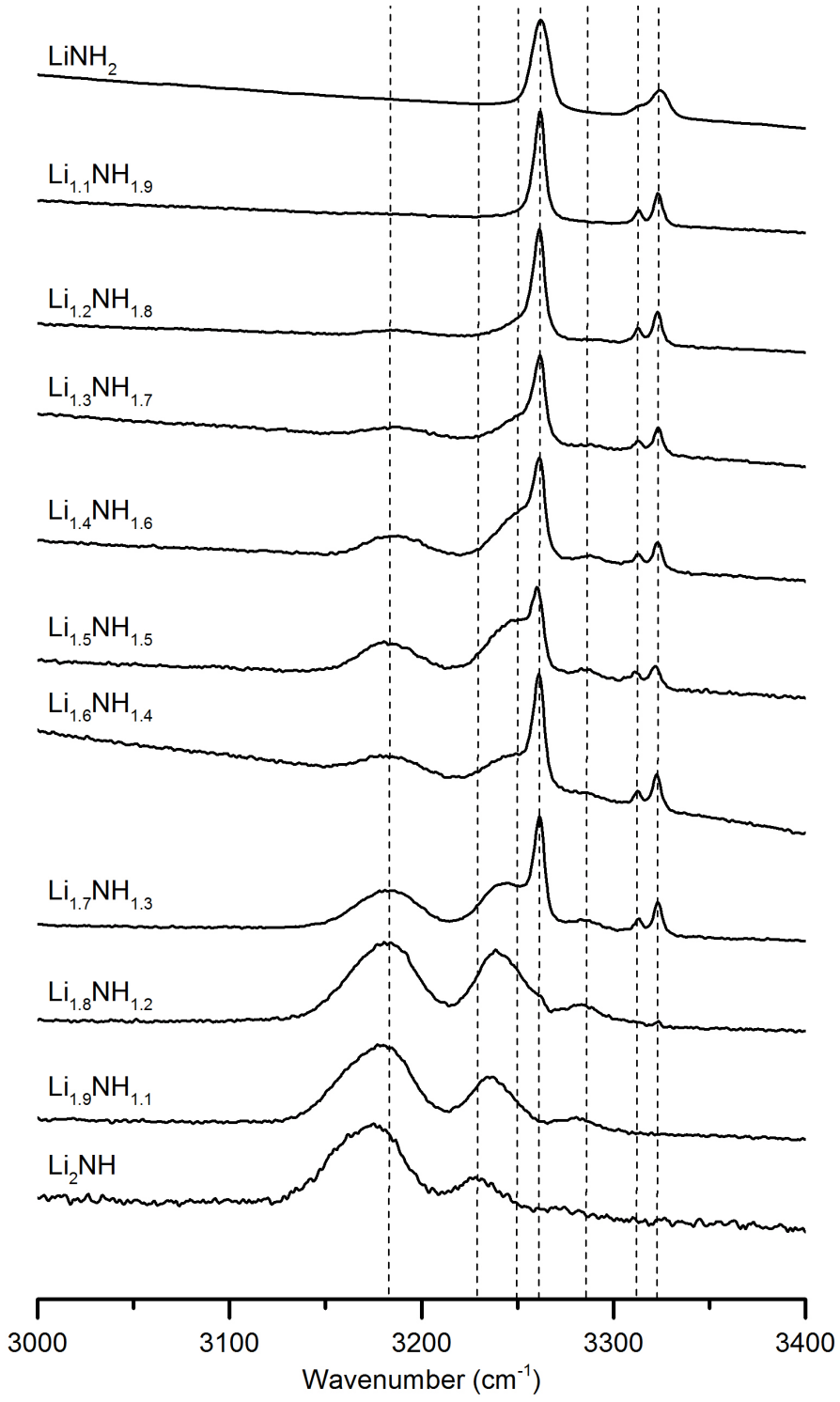

Figure 3.30: The N–H stretch region of the Raman spectra obtained for each of the phases synthesised in the continuum between lithium amide and lithium imide. The intensity values are offset from each other for clarity of presentation. The dashed vertical lines indicate the position of the peaks assigned as (L-R) the imide N–H stretch, Unknown 2, Unknown 1, the amide N–H symmetric stretch, Unknown 3, and the amide N–H asymmetric stretch.

spectra, with the best fit to the data obtained by the inclusion of three additional N–H stretch peaks. The positions of each of the peaks are indicated as dashed lines on Figure 3.30. One low-intensity peak occurs between the symmetric and asymmetric amide stretch bands (at around 3280 cm^{-1}), with the shoulder of the symmetric amide stretch fit to two peaks (around 3230 and 3250 cm^{-1}). These peaks have not been reported previously for the Li-N-H system. The most relevant study of the system by Raman spectroscopy details the results of a variable temperature experiment for the decomposition of lithium amide into lithium imide. In this experiment, a broadening of the amide peaks was observed, along with a transition to lower wavenumber[227]. However, this was explained as a temperature effect, rather than being due to a change in the stoichiometry.

The relative peak areas for each of the refined peaks are shown in Figure 3.31. The top panel details the peak areas of the amide and imide N–H stretches for the various samples, which broadly reflect what would be expected expected of the transition from lithium amide to lithium imide through mixed phases, supporting the hypothesis that reaction according to Equation 3.6 proceeded, but that subsequent formation of the non-stoichiometric phases was not completely successful. The bottom panel details the peak areas of the three unknown phases (Unknown 1–3). From this plot, it is clear that Unknown 2 and Unknown 3 are related peaks, with Unknown 1 being associated with a different motif. The relative energies and intensities of Unknowns 2 and 3 are similar to those of the lithium amide N–H stretches, and so are tentatively assigned as a second set of amide symmetric and asymmetric stretches[1].

The appearance of a second set of amide N–H stretches in the non-stoichiometric phases could be indicative of a second chemical environment for the amide anion. This would be consistent with the formation of a non-stoichiometric phase, as the increase in lithium ion density as the stoichiometry approaches that of the imide would undoubtedly have an effect on the strength of the N–H bonds in the amide groups, and hence the frequency of the vibration of those bonds. Indeed, computational analysis has indicated that the bond strength of the N–H bond in the imide anion is weaker than in the amide anion[228]. Thus, it is not unreasonable to suggest that the bond strength of an N–H bond would decrease as the stoichiometry moves from amide to imide, which is consistent with the data shown in Figure 3.30. On this basis, it is hypothesised

[1]The resolution of these peaks makes the observation of two discrete asymmetric stretch peaks unlikely.

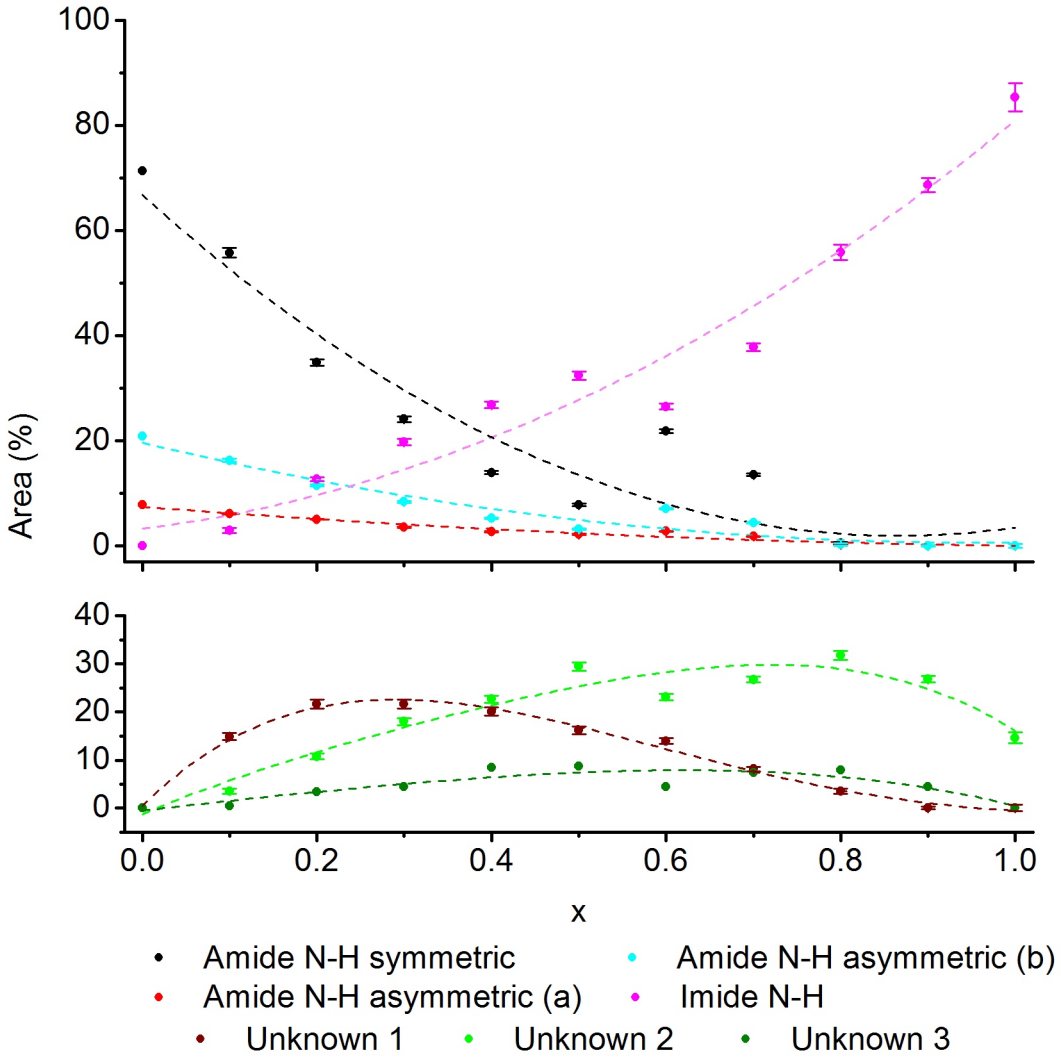

Figure 3.31: Relative peak areas for each of the refined peaks in the Raman spectra of the lithium amide - imide continuum. Polynomial fits to the data are included as dashed lines.

that the Unknown 2 and 3 peaks are associated with amide units in the non-stoichiometric phases. If this is the case, the fact that there remains a significant signal from the original amide N–H stretches in the lithium-poor phases ($x \leq 0.5$) is consistent with the PXRD and NPD data which show that these phases contain crystalline domains of tetragonal lithium amide. Following this line of argument, it is logical to suggest that the remaining Unknown 1 peak is due to the imide N–H stretch, for imide units which are present in non-stoichiometric phases.

A summary of the various N–H stretching peaks described is given in Table 3.5. The positions of the lithium imide N–H stretch, and the three intermediate peaks, all vary with changing value of x, with a consistent magnitude of change across all four peaks. This indicates that the shift in wavenumber in all of these peaks is associated with a common change in chemical environment. This not only supports the assertion that the unknown peaks are due to the non-stoichiometric phases, but also suggests that the imide N–H stretch may not be due simply to stoichiometric lithium imide, but also represents non-stoichiometric imide units. If this is the case, then it could be asserted that the unknown 1 peak could represent imide units in an amide-like environment. In contrast, the amide N–H stretch peaks show only a very small change in wavenumber with changing stoichiometry, supporting the assertion of the presence of a discrete amide phase in these samples, and that the tetragonal amide phase does not support significant stoichiometry variation.

The fact that the peaks can be divided into those representing the (almost) stoichiometric phases and those in the non-stoichiometric phases is indicative that the bulk formation of the non-stoichiometric phases was not entirely successful, as was indicated by the diffraction data. If bulk phases were synthesised, it would be expected that a single set of amide and imide N–H stretches would be observed, with the peak area changing linearly with stoichiometry. What can be inferred from the data shown in Figure 3.31 is that the amide/imide ions enter non-stoichiometric phases when the overall stoichiometry is far from their respective line phases, but as the stoichiometry approaches one of the end members, the relative anion tends to order into the line phase (this effect is perhaps exaggerated for the imide, which appears to show some stoichiometry variation in its 'line phase' N–H stretch peak as discussed above). This is consistent with the results from the *in situ* diffraction study, which showed that the intermediate phases were unstable with regard to separation into lithium amide and lithium imide. Clearly,

Table 3.5: Summary of the N–H stretch peaks observed in the non-stoichiometric Li-N-H samples. Errors in refined peak positions are all less than 1 cm^{-1}.

Peak	Peak position (cm^{-1})	Position change per 0.1 stoichiometry (cm^{-1})	Phase assignment
Amide symmetric	3260	-0.340(5)	Tetragonal lithium amide
Amide asymmetric a)	3313	-0.340(5)	Tetragonal lithium amide
Amide asymmetric b)	3323	-0.340(5)	Tetragonal lithium amide
Imide	3185	-2.78(4)	Lithium imide and imide-like stoichiometry
Unknown 1	3258	-2.78(4)	Imide in non-stoichiometric phases
Unknown 2	3244	-2.78(4)	Amide in non-stoichiometric phases (symmetric)
Unknown 3	3291	-2.78(4)	Amide in non-stoichiometric phases (asymmetric)

this factor would need to be taken into account, along with the potential for incomplete reaction described earlier, in any further attempts to synthesise specific non-stoichiometric phases.

3.4 Effects of cycling in the Li-N-H system

Most reversible solid-state hydrogen storage materials show a loss in capacity after multiple hydrogenation-dehydrogenation cycles. However, there have not been many investigations of capacity loss mechanisms, and the majority invoke particle size effects to explain the diminishment of reversible hydrogen content. If a hydrogen storage material is to be used in a practical setting, it must deliver a relatively stable amount of hydrogen over many hundreds, possibly thousands, of cycles. Therefore, an understanding of how cycling effects influence the fundamental reaction mechanism is a crucial step on the path to commercial application.

In the *in situ* diffraction study reported in Section 3.2.1, there were some indications of these effects, despite this not being the focus of that study. There was a significant difference in the behaviour of the intermediate phases between the first and second cycles at 290 °C, as detailed in contour plots of the PXRD data for the lithium amide-imide region of these two processes, shown in Figure 3.32. While the basic mechanism was clearly conserved, there was a far less

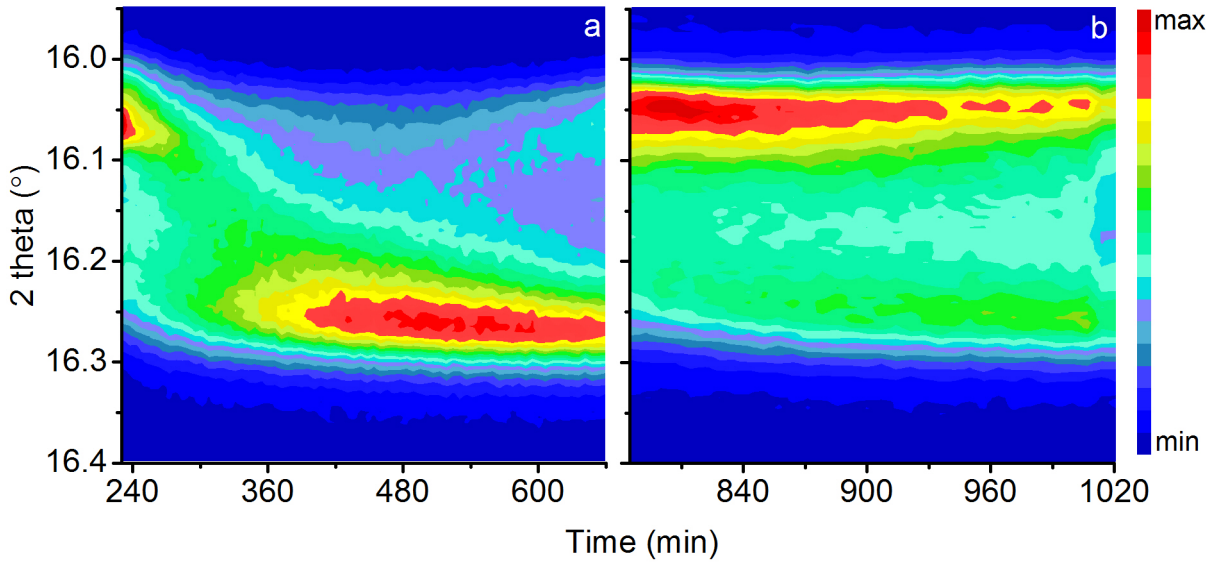

Figure 3.32: A comparison of the contour plots of the PXRD data of lithium amide-imide region, bounded by the lithium amide (112) and lithium imide (111) reflections for a) the first and b) the second dehydrogenation reactions of the undoped Li-N-H sample at 290 °C (processes B and D).

complete transition to the imide in the second cycle. This demonstrates that diffraction data can provide insight into cycling effects beyond a simple decrease in the stored hydrogen content as assessed by TGA or pressure-composition insotherms.

It is not straightforward to separate the changes in capacity observed in the original study which are due to cycling from those caused by changes in the temperature and hydrogenation pressure. However, some initial indications of capacity loss can be observed. Figure 3.33 shows the relative molar amounts of lithium, nitrogen and hydrogen through all of the reactions of the undoped Li-N-H sample, summed across all of the phases included in the Rietveld analysis of the diffraction data. The changes in the hydrogen content reflect the various hydrogenation and dehydrogenation reactions, with the magnitude of the change in the hydrogen content (and thus, the extent of reaction) affected by the experimental conditions. However, there was also clearly some capacity loss in the sample: while the amount of lithium remained fairly constant across the course of the reactions, there was a steady decrease in the amount of nitrogen in the system. This represents a decrease in the maximum capacity of the system, since the hydrogen storage and release reactions do not involve the emission of nitrogen-containing species.

Loss of nitrogen from the system has previously been identified as a potential mechanism of capacity loss, although there are a number of potential explanations for this effect. Loss

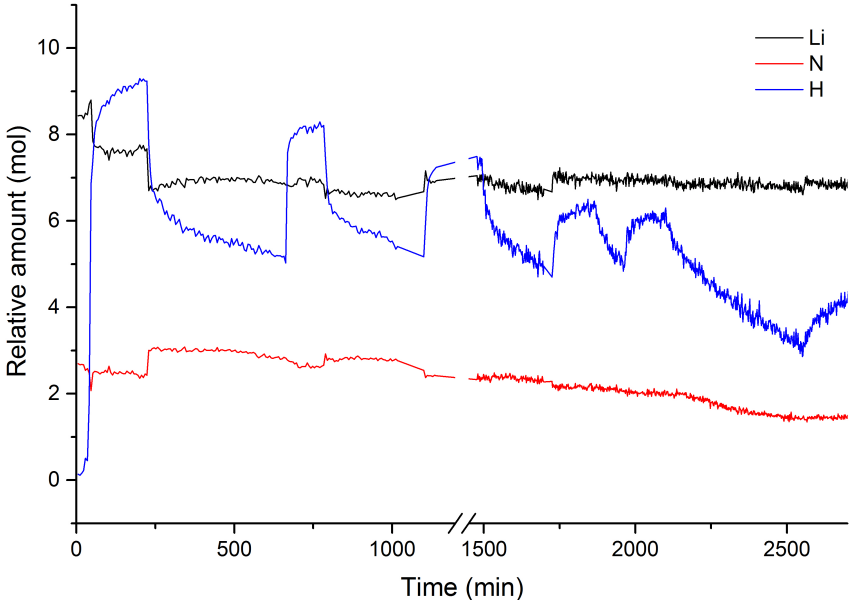

Figure 3.33: The summed relative molar amounts of lithium (black), nitrogen (red) and hydrogen (blue) in all of the phases in the Rietveld refinement for the undoped Li-N-H sample across all of the hydrogenation-dehydrogenation processes. Average standard deviations before the break in the data are ±0.08 mol for nitrogen, ±0.08 mol for lithium, and ±0.54 mol for hydrogen. After the break in the data, the average standard deviations are ±0.2 mol for nitrogen, ±0.2 mol for lithium, and ±0.8 mol for hydrogen

of nitrogen as ammonia during dehydrogenation could be ascribed to the ineffective mixing of the amide and hydride phases, meaning that the ammonia released from the decomposition of the amide (Equation 3.8) is not completely captured by the hydride to form hydrogen. Loss of ammonia in this way has been reported in a number of studies on the Li-N-H system[98, 106], and may explain why hydrogen released from the Li-N-H system is prone to contamination with ammonia.

The second potential avenue for the loss of nitrogen is the conversion of lithium amide to lithium hydride and ammonia under hydrogen pressure (Equation 3.9), the reverse reaction of the hydrogen release step in the normal operation of the Li-N-H system. This was highlighted as a potential issue for the commercial use of the Li-N-H system by Pinkerton[224], and has been demonstrated as a stoichiometric reaction[229]. Lithium hydride formed in this way is in addition to the stoichiometric amount required for the hydrogen release reaction, and so sequesters lithium from active participation in the hydrogen storage and release reactions, as well as reducing the amount of amide which can react.

$$2LiNH_2 \rightarrow Li_2NH + NH_3 \tag{3.8}$$

$$LiNH_2 + H_2 \rightarrow LiH + NH_3 \tag{3.9}$$

The other obvious path by which nitrogen could be removed from the system is by oxidation of the amide/imide species by reaction with the capillary or contaminant oxygen or water, which would also likely involve the release of ammonia. This reaction is the simplest to observe — examination of Figure 3.13 shows a steady increase in the amount of lithium oxide in the sample over the course of the reactions. Clearly this will have an impact on the capacity of the sample, and appears to give a reasonably good correlation with the loss of nitrogen from the sample.

With regard to the other two paths of capacity loss outlined above, the situation is less clear. It is not obvious that the decrease in nitrogen was more associated with one of the reactions over the other. Without the ability to characterise the gas coming off the sample, or the gas mixture during hydrogenation, it is difficult to ascertain whether a significant amount of ammonia was released in any of the reactions. If there was significant formation of lithium hydride via the reaction indicated in Equation 3.9, it would be evident in the ratio of lithium hydride to the amide-imide phases. It is also true that release of ammonia from the decomposition of the amide to the imide would also result in the formation of excess lithium hydride when that imide was subsequently hydrogenated. Therefore, an increase in the hydride to amide-imide ratio would be indicative of either of these paths of capacity loss occurring. A plot of this ratio over the course of the reactions of the undoped sample is shown in Figure 3.34, indicating that the ratio did not increase significantly over the course of the experiment.

It is clear that too few cycles were performed in these initial experiments to obtain a reliable indication of the mechanisms of capacity loss. In the remainder of this Chapter, further *in situ* measurements on the hydrogen storage and release behaviour of the Li-N-H system shifted focus from the underlying mechanism of hydrogen storage and release to examine the changes in the hydrogen storage properties of the system as it undergoes multiple hydrogen storage and release cycles, and to investigate in greater detail the mechanisms of capacity loss and other subtleties in the reactions. In particular, the recently-reported beneficial effect of the addition of nitrogen

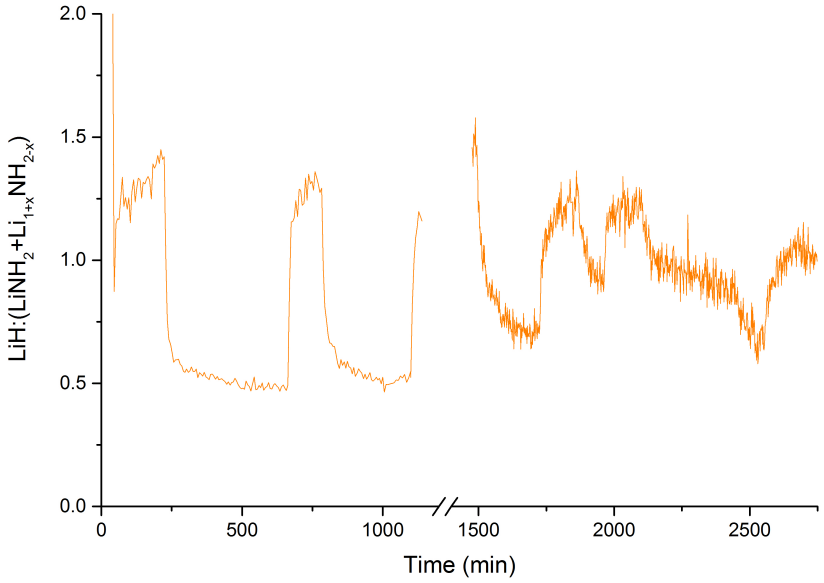

Figure 3.34: The ratio of the molar amount of lithium hydride to the sum of the molar amounts of lithium amide and the non-stoichiometric phases (including lithium imide) over the course of the reactions of the undoped Li-N-H sample, as determined by Rietveld analysis of the PXRD data.

on the cycling stability of the system is of significant interest [143].

3.4.1 Thermogravimetric and diffraction study of hydrogen cycling in the Li-N-H system

As a starting point for this investigation, the behaviour of the Li-N-H hydrogen store as it cycles under pure hydrogen was investigated. Samples were subject to hydrogenation-dehydrogenation cycles by IGA, and then a final cycle in the synchrotron X-ray beam. In contrast to the initial PXRD investigation, the conditions of the hydrogen storage and release reactions were kept constant for each cycle, to isolate the effect of the cycling. The IGA data are shown in Figure 3.35 for lithium nitride samples which underwent 1, 2, 5, 10, 25 and 45 cycles at 265 °C, with 3 bar hydrogen used for the hydrogenation. The downside of the use of IGA for performing the cycling reactions is that the sample is suspended in a mesh bucket in order to measure its mass. With many cycles moving between dynamic vaccum and 3 bar of gas pressure, there is potential for some material to be lost from the bucket — this may be the cause of some of the steady decrease in the sample mass over the course of each experiment. This does raise a concern as to whether the components of the sample are lost in the same ratio as they are present in the material, as any preferential loss of one component would cause a reduction in the capacity. It

is assumed here that there is no preferential loss.

As was observed in the *in situ* diffraction studies, the lithium nitride did not react completely on the first hydrogenation, and so the initial mass rise was not as large as would be expected from complete reaction. Otherwise, the classic behaviour of the Li-N-H system is observed, with only around half the initial hydrogen uptake recovered as the sample dehydrogenates to lithium imide rather than back to the nitride. With cycling, it is clear that the reversible hydrogen storage content changes. The relative amount of hydrogen released for each cycle in each sample is shown in Figure 3.36, given as a percentage of the first dehydrogenation. There is some spread evident in the results for the various samples, but the general trends are consistent. Each sample showed an initial rise in the hydrogen content, which can be attributed to extra capacity as the lithium nitride hydrogenates fully, as was observed over multiple cycles in the original *in situ* PXRD study. Following this initial rise, each of the samples then showed a steady decline in the reversible hydrogen content, dropping to 20.7 % of the original value after 45 cycles.

In addition to recording the magnitude of the mass changes, the IGA data allows for the kinetics of the hydrogenation and dehydrogenation reactions to be determined in a similar manner as was performed for the PXRD data. The mass data for the 45 cycle sample were fitted to the same exponential functions as were used in the previous analysis (Equations 3.3 and 3.4), except now represent the overall reaction rate, rather than the rate for a given species. The rate constants extracted for the hydrogenation and dehydrogenation reactions for every fifth cycle are shown in Figure 3.37. These results indicate that even though the capacity is seen to diminish with cycling, the hydrogenation kinetics were essentially unaltered and the dehydrogenation kinetics show a slight improvement over the course of the reaction.

Raman spectra of each of the samples at the end of their cycling experiment (left in the dehydrogenated state) are shown in Figure 3.38, and support the conclusion that the kinetics of the reactions were not adversely affected by the cycling process. Aside from the 45 cycle sample, which showed no strong Raman bands, each of the samples showed a strong imide N–H stretch band, with no significant peak from stoichiometric or non-stoichiometric amide N–H stretches as were reported earlier in this Chapter. The peak position does not vary over the first ten cycles, with a slight shift to a higher wavenumber in the 25 cycle sample, indicating that a similar extent of reaction was reached in the amide-imide phase at each stage in the cycling reaction.

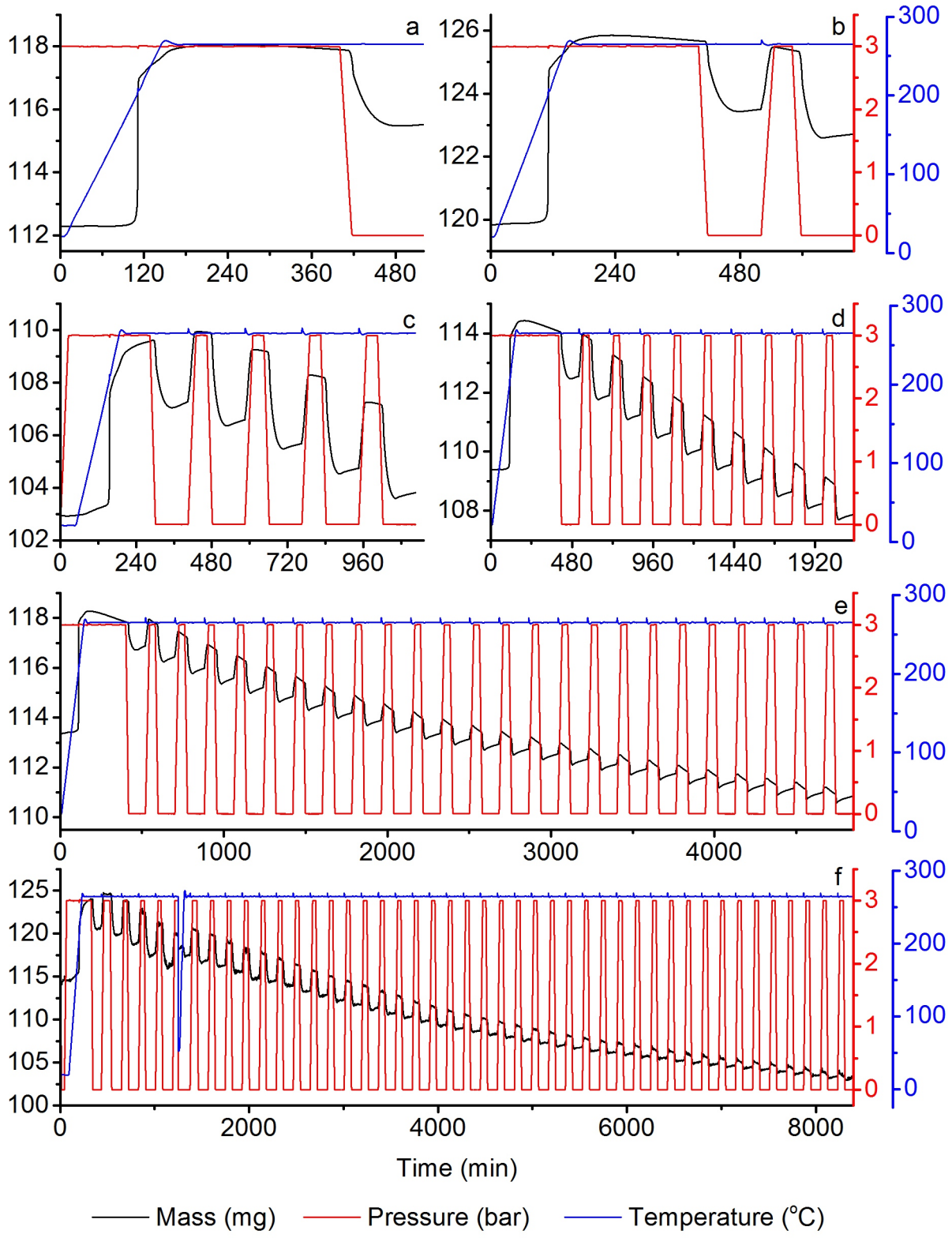

Figure 3.35: Plots of IGA data for a) 1 b) 2 c) 5 d) 10 e) 25 and f) 45 hydrogenation-dehydrogenation cycles of the Li-N-H system, showing the mass, pressure and temperature of the sample. Each sample was initially lithium nitride, and was subject to sucessive hydrogenation and dehydrogenation cycles.

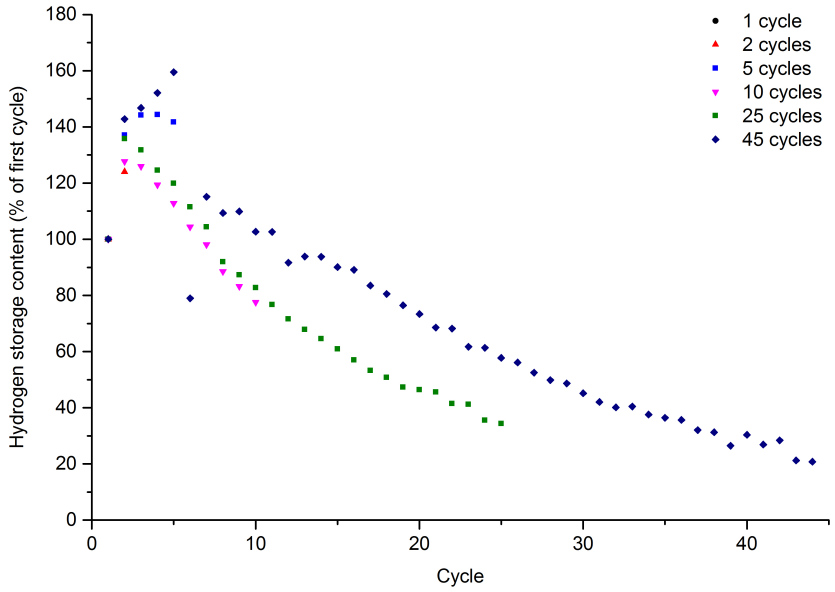

Figure 3.36: A plot of the weight percentage of hydrogen released from the Li-N-H samples over multiple hydrogenation-dehydrogenation cycles, expressed as a percentage of the release in the first dehydrogenation. The estimated standard deviation in the hydrogen storage content is ±0.2 %.

In turn, this suggests that the differences in the extent of reaction seen in the first *in situ* work were almost entirely due to the temperature and pressure conditions used, and not the number of cycles the sample had been through. The result also supports an explanation of the observed capacity loss as being due to one of the routes of nitrogen loss outlined earlier.

In order to better probe the capacity loss, the samples were each analysed by synchrotron PXRD, and underwent a hydrogenation-dehydrogenation cycle in the beam. Contour plots of selected segments of the diffraction patterns for each sample are shown in Figure 3.39 (Individual diffraction patterns showing the observed patterns and the calculated fit to the data for each sample in the hydrogenated state are given in Appendix D). The panels showing the lithium amide superlattice reflections indicate that these peaks become less prevalent at higher cycle numbers, indicating a lesser extent of hydrogenation with increasing cycling.

The lithium amide-imide panels show the familiar hydrogenation and dehydrogenation reaction paths through the continuum of intermediate intensity, reflecting the presence of the non-stoichiometric intermediate phases. Although the relative intensity of the peaks was seen to decrease as the cycles increase, the distribution of phases through the reactions was quite similar over the different cycles, corroborating the Raman spectra which showed similar imide peaks for each of the samples. Indeed, Rietveld analysis of the dehydrogenated samples gives a similar

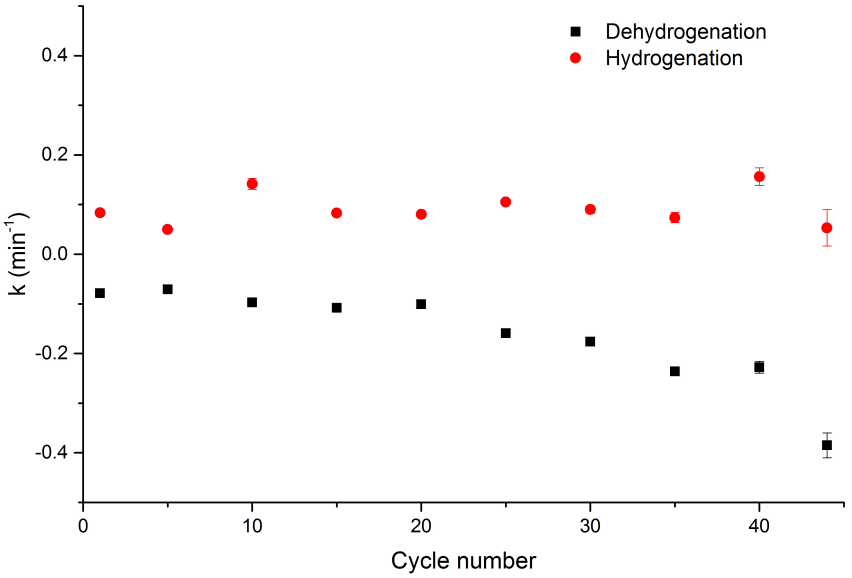

Figure 3.37: The rate constants extracted from exponential fits to the IGA data for selected cycles in the Li-N-H sample run for 45 hydrogenation-dehydrogenation cycles.

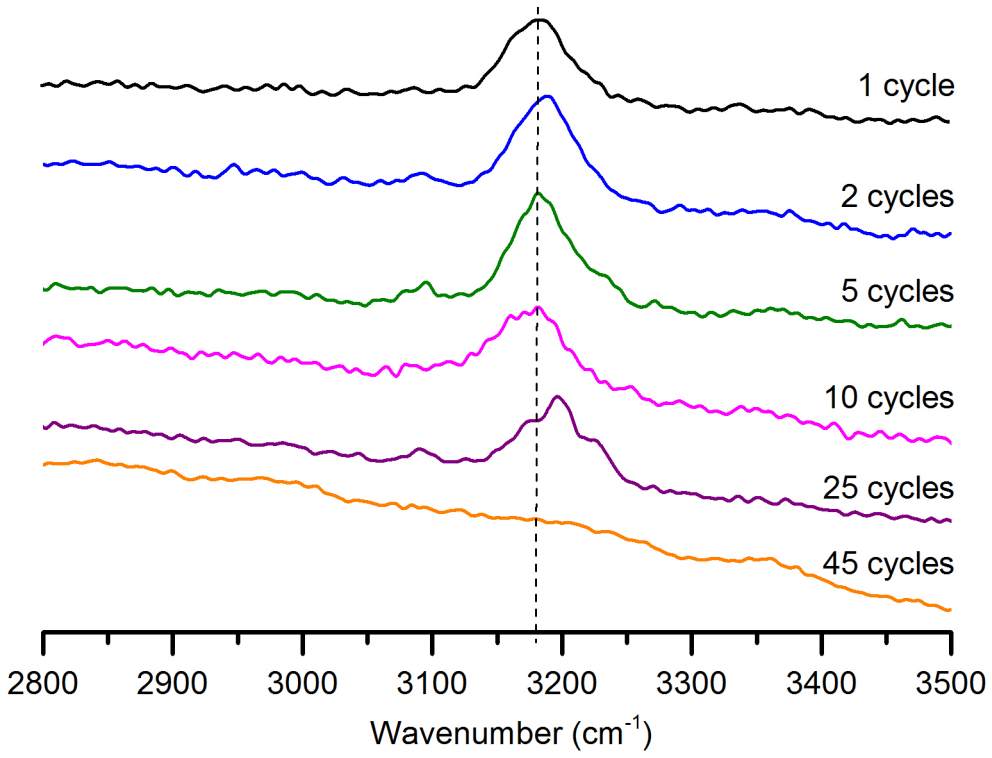

Figure 3.38: The N–H stretching region of the Raman spectra of the cycled Li-N-H samples. The position of the peak assigned to the N–H stretch of lithium imide is shown as a vertical dashed line.

Table 3.6: Average stoichiometry of the cycled Li-N-H samples in the dehydrogenated state.

Number of cycles	Average stoichiometry
1	$Li_{1.72}NH_{1.28}$
2	$Li_{1.82}NH_{1.18}$
5	$Li_{1.87}NH_{1.13}$
10	$Li_{1.84}NH_{1.16}$
25	$Li_{1.90}NH_{1.10}$
45	$Li_{1.61}NH_{1.39}$

average stoichiometry for each sample (given in Table 3.6), and shows that this stoichiometry is quite close to lithium imide for each sample except the 45 cycle sample, which showed an intermediate stoichiometry.

The similar progression in the non-stoichiometric intermediate phases seen in the contour plots of the amide-imide peaks indicates that the cycle number does not have a significant effect on the underlying mechanism. The differences seen in the extent of reaction between cycles in the original *in situ* study may be confined to a contrast between the first and second cycles, or could relate to the higher temperature used in those cycles.

The panels showing the lithium hydride peak are the most stark point of variation between the samples. The capacity loss recorded in the gravimetric analysis is reflected in the magnitude of the change in the lithium hydride peak intensity over the course of the reactions — this change diminished moving to higher cycle numbers. Although the variation in the magnitude of the peak was significantly smaller with cycling, the lithium hydride peak intensity itself was not diminished in the same way as the lithium amide-imide peaks, suggesting that there was an increasing proportion of lithium hydride in the sample with increasing cycle number. This qualititative assessment is supported by the relative molar amounts of the various crystalline phases extracted from the Rietveld analysis of the samples at the end of the hydrogenation reaction, shown in Figure 3.40. The cycle number listed is the number of hydrogenation-dehydrogenation cycles the sample had undergone prior to the final hydrogenation on the diffractometer.

Ideally, the lithium hydride to lithium amide ratio should be 2:1 in the hydrogenated state. Even in the first cycle, this ratio was larger than 2:1, with the proportion of lithium hydride increased significantly with cycling. Although there was some increase in the level of lithium

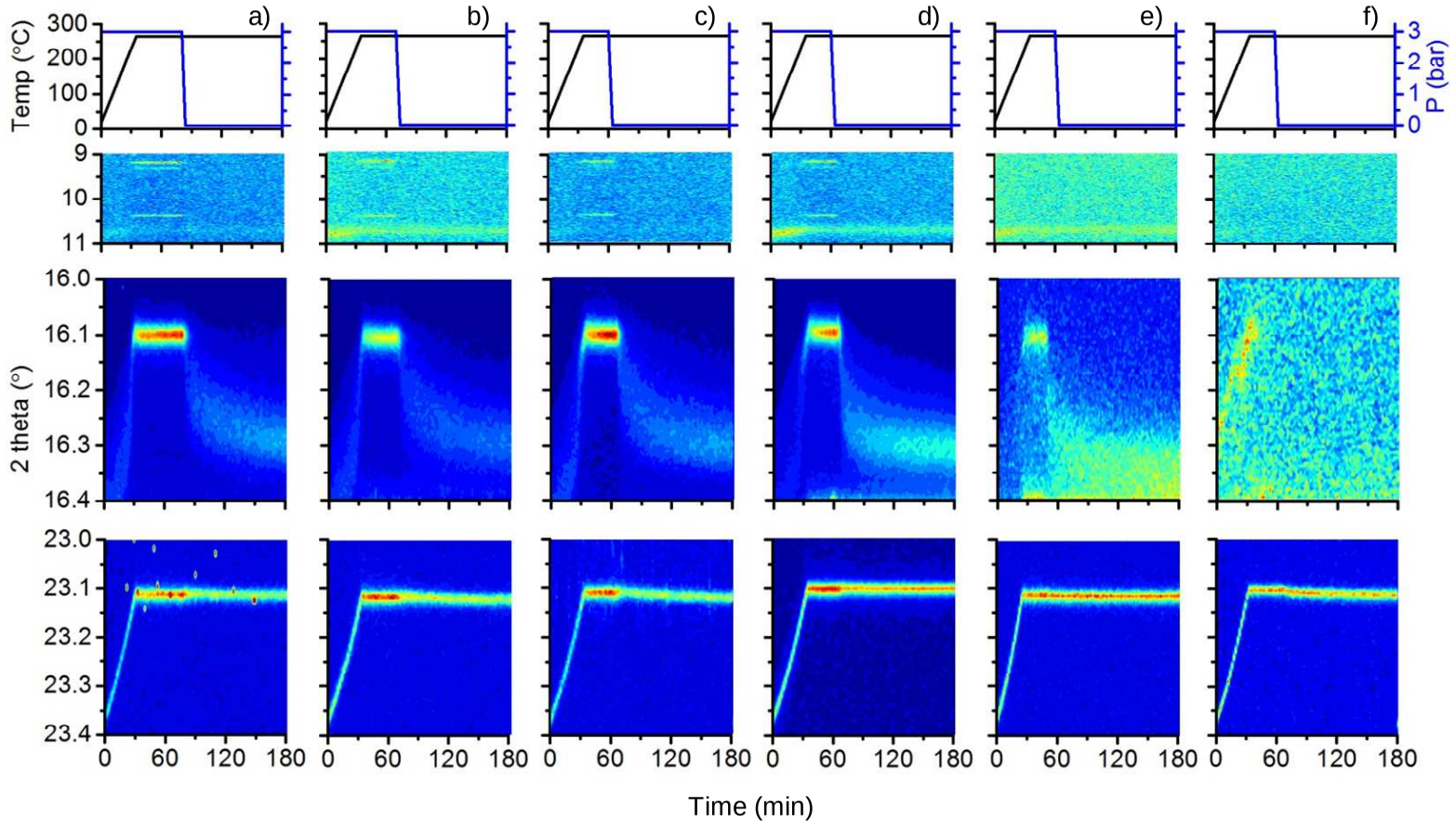

Figure 3.39: Contour plots of selected sections of the PXRD data for the hydrogenation-dehydrogenation of Li-N-H samples which had been previously subjected to a) 1 b) 2 c) 5 d) 10 e) 25 and f) 45 *ex situ* hydrogenation-dehydrogenation cycles. Each section displays (from top to bottom) the reaction conditions, the lithium amide superlattice reflection region, the lithium amide (112) and lithium imide (111) reflections and the lithium hydride (002) reflection.

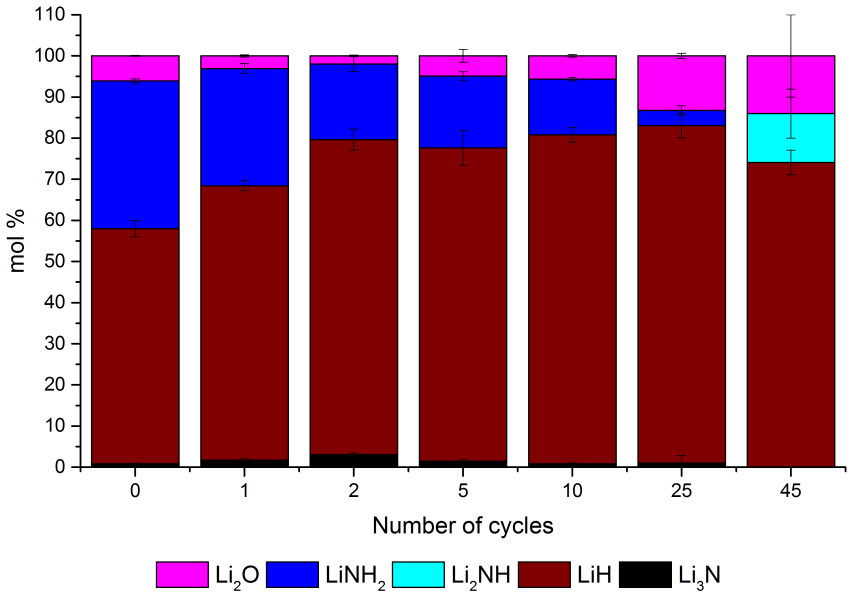

Figure 3.40: Relative molar amounts of each of the refined phases in the cycled Li-N-H samples after a 1 hour hydrogenation at 265 °C, 3 bar. The cycle number is the number of previous cycles.

oxide in the sample in the 25- and 45-cycle samples, it is not sufficient to account for all of the capacity loss seen. These data indicate that the formation of excess lithium hydride is a significant source of capacity loss in the Li-N-H system. This may also provide an explanation of the decreasing sample mass observed in the IGA data of all of the sample, as the conversion from lithium amide to lithium hydride would be associated with a decrease in the sample mass.

The precise mechanism of excess hydride formation (Equation 3.8 or 3.9) in operation remains unclear. There may be some indication from a comparison of experimental setups in the original PXRD experiment with these cycling experiments. In the original experiment, an excess of lithium hydride was not observed over the small number of cycles (3.34), however after an equivalent number of cycles in the IGA experiment, the effect was already clear. In the PXRD sample, ratio of the sample to the gas volume was significantly higher than in the *ex situ* cycling experiments, where the whole volume of the IGA instrument was filled with hydrogen. If the excess hydrogen is formed via the conversion of lithium amide to lithium hydride under hydrogen, the experimental setup may indicate why the effect was more pronounced in the IGA experiment.

3.4.2 The effect of additives: nitrogen gas

To date, the most detailed investigation of capacity changes in the Li-N-H system and the reasons for the formation of excess lithium hydride, was that of Lamb *et al.*, described earlier in this Chapter [143]. In order to investigate their findings on the effect of adding nitrogen to the hydrogenation gas stream, and to provide further insight into the causes of capacity loss in the Li-N-H system, the nitrogen-hydrogen gas mixtures used in that study were applied to a third set of *in situ* synchrotron PXRD experiments, on ID31 at the ESRF.

Their original study used pressure-composition isotherms to determine the capacity of the system. The application of PXRD here adds a new dimension to the investigation. In these experiments, IGA was not used due to the issues with sample loss and the potential for oxidation encountered for the pure hydrogen cycling study. Therefore, samples were subjected to a large number of hydrogenation-dehydrogenation cycles with *in situ* PXRD. Two samples were used, one for each of the nitrogen levels used by Lamb *et al* (100 ppm and 20 % nitrogen-in-hydrogen gas mixtures). As for the hydrogen-only cycling experiments, the sample temperature was kept constant throughout the reaction, and the same cycling procedure was used for each cycle.

Contour plots of selected regions of the diffraction patterns obtained are shown in Figure 3.41 for the 100 ppm nitrogen-in-hydrogen sample and Figure 3.42 for the 20 % nitrogen-in-hydrogen sample. Individual diffraction patterns showing the observed patterns and the calculated fit to the data for each sample at various points in the experiments are given in Appendix D. The contour plot for the 100 ppm sample shows the first five cycles, then a break while the synchrotron beam was down. The sample continued to be cycled during this beam-off period, and the second part of the contour plot shows the PXRD collected once the beam returned, for cycles 25–33. The 20 % sample did not have any such breaks in the data, and so the contour plot shows all of the 26 cycles performed for that sample. A high-frequency oscillation is apparent in the data shown in the contour plots — this is as a result of the instrumentation. In order to maximise the number of datasets captured for the reactions, diffraction data were collected both for the detector sweeping up and down through the specified angular range. There are different zero errors for each trajectory, hence the apparent 'wiggle' in the data.

Significant differences exist between the behaviour of these samples upon cycling compared with the pure hydrogen cycled sample, and there are clearly different effects from the two levels of

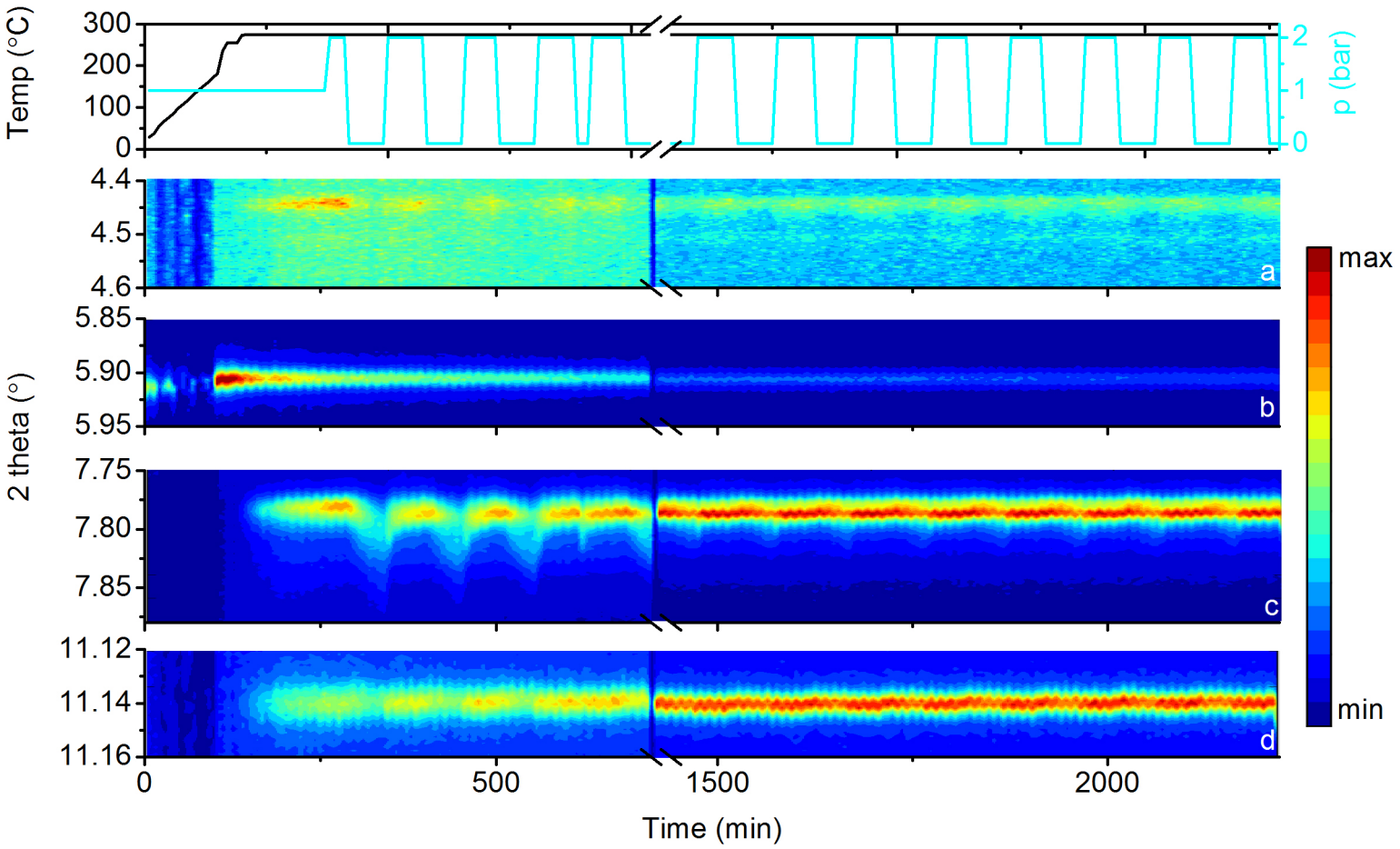

Figure 3.41: Contour plots of selected regions of the PXRD data for a Li-N-H sample exposed to 100 ppm nitrogen in hydrogen as the hydrogenation gas mixture. The top panel indicates the reaction conditions, and the contour plots show a) the (002) and (001) reflections of lithium amide b) the (001) reflection of alpha-lithium nitride c) the (112) reflection of lithium amide and the (111) of lithium imide and non-stoichiometric phases and d) the (002) reflection of lithium hydride.

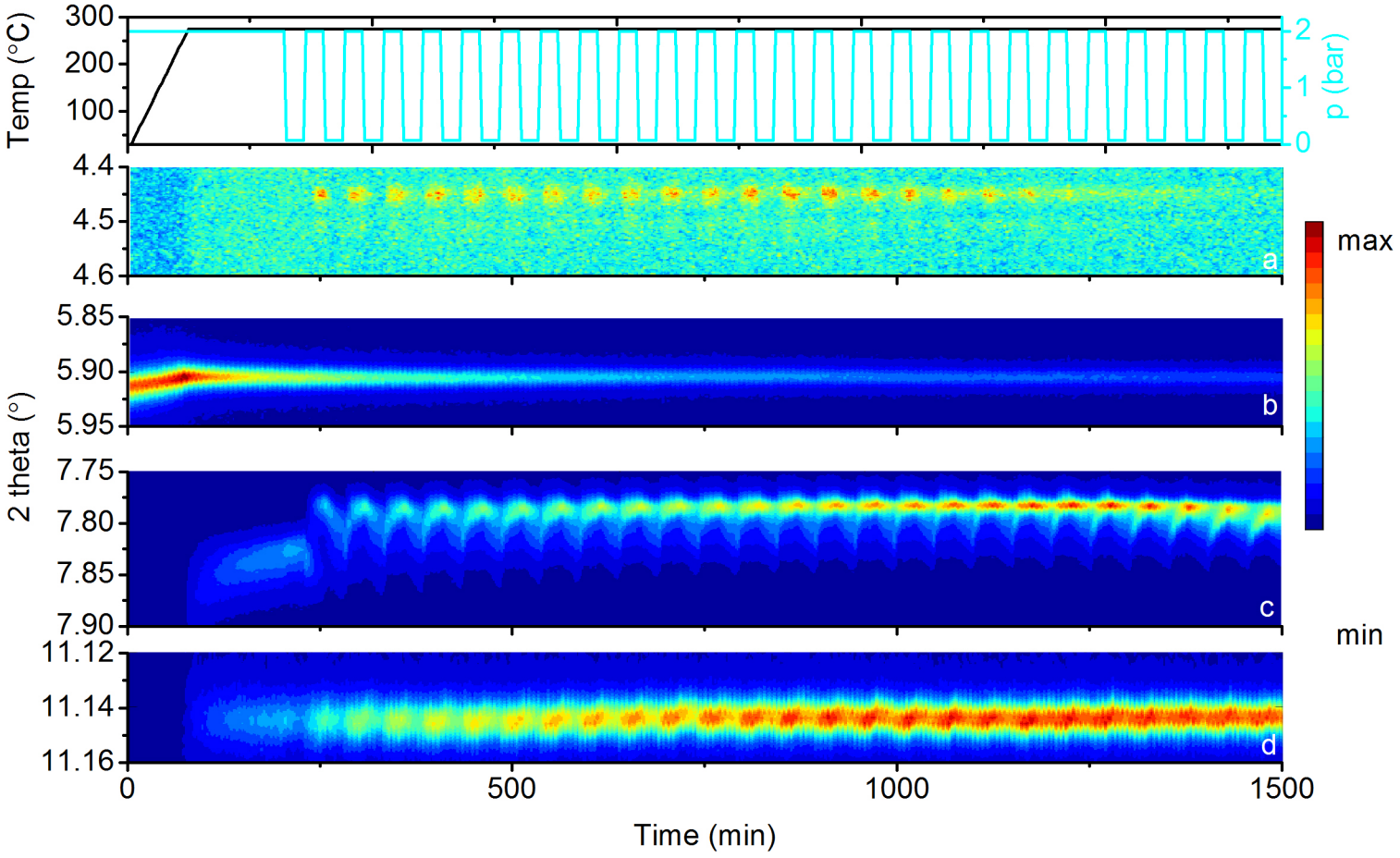

Figure 3.42: Contour plots of selected regions of the PXRD data for a Li-N-H sample exposed to 20% nitrogen in hydrogen as the hydrogenation gas mixture. The top panel indicates the reaction conditions, and the contour plots show a) the (002) and (001) reflections of lithium amide b) the (001) reflection of alpha-lithium nitride c) the (112) reflection of lithium amide and the (111) of lithium imide and non-stoichiometric phases and d) the (002) reflection of lithium hydride.

nitrogen in the hydrogenation gas stream. The initial hydrogenation of lithium nitride was starkly different for the two samples. The 100 ppm sample showed the expected hydrogenation directly to lithium amide, while the 20 % sample initially formed lithium imide, with apparent migration towards the amide as the reaction progressed. During the second hydrogenation reaction, the amide was formed. This effect is probably because of the lower partial pressure of hydrogen in this sample. While it is clear that the pressure of hydrogen (1.6 bar) is sufficient to hydrogenate to the amide, the equilibrium hydrogen pressure of the amide-imide dehydrogenation reaction is evidently not significantly lower than this pressure. This is consistent with published results of pressure-composition isotherms which indicate that the equilibrium hydrogen pressure of the reaction is 1.5 bar at 255 °C[98]. In the experimental setup used in this work (a narrow capillary) the hydrogen consumed in the hydrogenation reaction is a significant proportion of the gas volume around the sample, which may lead to an increase in the local nitrogen partial pressure, destabilising the amide.

This effect also appears to be evident in the latter stages of the cycling in the 20 % sample. The diffraction peak in the lithium amide-imide region in the hydrogenated state drifted away from lithium amide over the last three cycles, and the lithium amide superlattice peaks diminished over the last nine cycles. Consistent with the explanation of the initial hydrogenation to lithium imide, a similar increase in the nitrogen partial pressure around the sample during each hydrogenation reaction likely occurs. If the vacuum system does not completely evacuate the sample during dehydrogenation, then there may be a gradual accumulation of nitrogen in the sample volume, which will eventually cause the applied hydrogen pressure to be less than the equilibrium pressure, resulting in incomplete hydrogenation. Any future study would benefit from the use of higher hydrogen pressure if this effect were to be avoided over a large number of cycles.

As was observed in the original study, the 2-theta position of the lithium hydride peak varied during the reactions, with the lattice expanding during dehydrogenation, corroborating the evidence for the existence of a defect structure in lithium hydride during the dehydrogenation reaction. The magnitude of the hydride peak increased over the course of the initial cycles, which can be correlated with the disappearance of the lithium nitride phase, representing increasing hydrogenation of the sample. In the 20 % sample, the magnitude then decreased in line with the

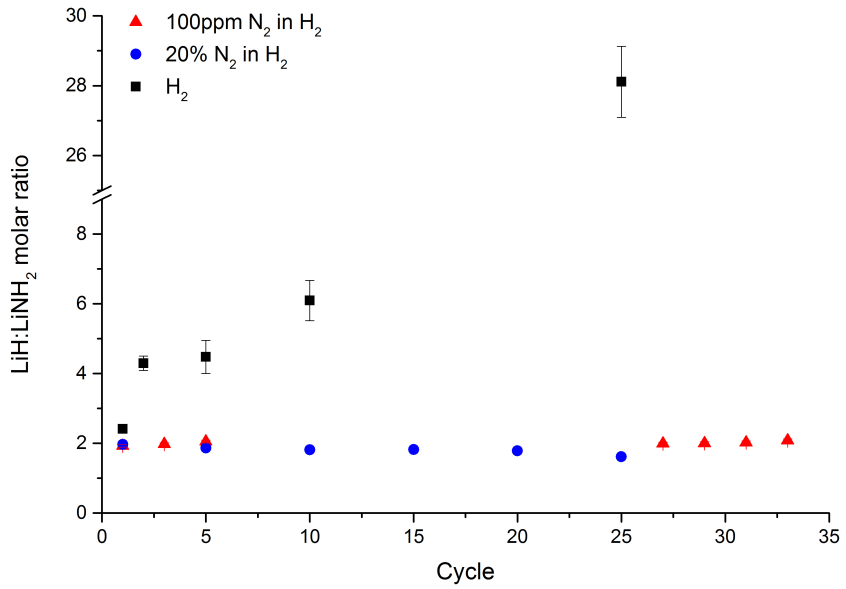

Figure 3.43: The molar ratio of lithium hydride to lithium amide over variable numbers of hydrogenation-dehydrogenation cycles, for each of the three hydrogenation gas mixtures used.

decreased extent of hydrogenation in the latter stages of the cycling experiment.

The addition of nitrogen to the hydrogenation gas stream had an effect on the cycle stability of the Li-N-H system. The magnitude of the amide-imide Bragg peaks was maintained to a much greater extent over the cycling than was the case for the pure hydrogen cycled samples. A plot of the ratio of lithium hydride to lithium amide in the hydrogenated state against cycle number for each of the three hydrogenation gas mixtures is shown in Figure 3.43, indicating that the addition of nitrogen completely suppressed the formation of excess hydride under the studied conditions, in contrast to the large excess formed using pure hydrogen.

While there is no direct evidence in these data of the formation of metallic lithium as advocated by Lamb *et al.* in any of the reaction processes (its presence would not be expected to be observed by PXRD given the melting point of lithium is 180 °C), it does provide some support to that hypothesis, given the absence of any other explanation for the role of nitrogen in preventing lithium hydride formation. However, our results do not exactly mirror those of Lamb *et al.* The authors reported that the hydrogen storage capacity increased with cycling under nitrogen-hydrogen mixtures, with the remarkable increase to the full hydrogen capacity of lithium nitride with 20 % nitrogen-in-hydrogen.

In the 100 ppm sample, the formation of excess lithium hydride appears to have been pre-

vented, but there was still capacity loss, with the dehydrogenation reaction significantly less complete in the latter cycles when compared with the initial ones. This may indicate that the lithium amide and lithium hydride particles were not sufficiently mixed. The 20 % sample did show a larger reversible hydrogen capacity as assessed by the extent of dehydrogenation to the imide. However, there was no increase in capacity observed beyond that of lithium imide. This may be due to the significant discrepancy in the number of cycles examined in the *in situ* PXRD study compared with the hundreds of cycles examined in the pressure-composition isotherm measurements. The increase in capacity beyond that of lithium imide implies a fundamental change to the reaction mechanism, which has not been observed in this work.

3.5 Conclusions and Further Work

Extensive *in situ* PXRD studies have provided a number of insights into the hydrogen storage and release properties of the Li-N-H system. These *in situ* data provide strong evidence for the transformation of lithium amide to lithium imide (and vice-versa) via a continuum of non-stoichiometric intermediates. The observation of these intermediates during the hydrogenation and dehydrogenation reactions provides supporting evidence for the proposed Frenkel defect mechanism for hydrogenation and dehydrogenation. The high resolution provided by synchrotron diffraction instrumentation also allowed for the determination of subtle changes in the crystal structures of lithium amide and lithium hydride during these reactions, pointing to possible defect structures in these phases.

The in situ examination of non-stoichiometry in the Li-N-H system has provided some insight into the relative stability of the non-stoichiometric continuum, indicating that the non-stoichiometry is kinetically-stabilised, unstable to phase separation into the parent structures of lithium amide and lithium imide. This instability resulted in some difficulty synthesising pure samples of these intermediate stoichiometry values, although the combined use of Raman spectroscopy and diffraction methods showed that these phases can be produced in isolation from the hydrogen storage and release reactions, and that in these phases, amide and imide anions coexist within the structure.

Further studies of the phases may provide significant insight into the behaviour of the Li-N-H

system — a more detailed exploration of the synthesis of non-stoichiometric Li-N-H compounds may explain the differences in lattice size trends between the *in situ* and *ex situ* work presented here, perhaps by identifying distinct defect structures in different synthesis methods, and would hopefully lead to the synthesis of pure phases. This would allow a thorough characterisation by total X-ray and neutron scattering, which would reveal the local structure of these phases, and the degree of order in their crystal structures. Nuclear magnetic resonance (NMR) spectroscopy could be used as an additional probe of the local structure of the lithium and hydrogen atoms in the non-stoichiometric phases, while ionic conductivity measurements would also be an important way to characterise their properties in relation to the reversibility of the Li-N-H system.

The results of this study emphasise the importance of ionic conductivity and topotactic reactions for facile reversibility in complex hydride materials. Clearly, the enhancement of this conductivity while maintaining mobility with cycling are key goals in the commercial development of the Li-N-H hydrogen store. Optimisation of this characteristic feature is the most promising route to a lowering of the practical operating temperature of the system. Indeed, studies on the insertion of halide anions into the lithium amide structure have delivered lower desorption temperatures[112]. Further work in this area is needed, ideally without the hydrogen storage capacity diminishment which naturally accompanies halide substitution.

Extension of the *in situ* PXRD studies to the effects of multiple hydrogenation-dehydrogenation cycles on the Li-N-H system showed the presence of an additional set of considerations beyond the basic mechanism are required in order to understand the practical performance of a solid-state hydrogen store. Cycling under pure hydrogen showed that, although the kinetics of the hydrogen storage and release reactions were maintained over 45 cycles, oxidation and the formation of excess lithium hydride did cause significant loss of capacity. The addition of nitrogen to the hydrogenation gas stream was effective in preventing the formation of lithium hydride.

While these results may provide indirect evidence in support of the hypothesis of the formation of metallic lithium, more investigation is required to ascertain the precise mechanism at play in these reactions. Particularly, clearer evidence for the existence (or lack) of lithium metal would be an important indicator as to the role of nitrogen. NMR spectroscopy seems an ideal tool for this type of investigation, given the characteristic features of metals in NMR spectra. *In situ* NMR studies of the hydrogenation and dehydrogenation of the Li-N-H system, and the

conversion of lithium amide to lithium hydride under hydrogen, may provide evidence for the presence of lithium metal. Gaining an understanding of these effects will be a crucial step in the practical development of the Li-N-H system. If the remarkable increases in hydrogen capacity can be reproduced and understood, the suitability of the Li-N-H system for practical application would be significantly enhanced.

Chapter 4

Structure, synthesis and decomposition of light metal amides

4.1 Overview and Experimental

In hydrogen storage applications light metal amides are almost exclusively studied as composite materials with lithium hydride. However, there is also value in the study of their behaviour in isolation, potentially giving a clearer description of the role of the amide as part of the composite material. The first section of this Chapter focuses on lithium amide and, in particular, the synthesis and decomposition reactions of the amide with examination by diffraction and gravimetric analysis methods. Following on from this work, the synthesis and structure of sodium amide, one of the few amides that shows hydrogen storage potential without the presence of a hydride, is investigated by neutron scattering measurements.

Firstly, the decomposition of lithium amide to lithium imide is reported. This reaction was investigated using multiple experimental methodologies. A 9.5 mg sample of lithium amide powder was placed in a 30 μL alumina crucible, and inserted into the DSC-TGA instrument (Section 2.3.3). The sample was heated to 700 °C at 5 °C min^{-1} under 30 sccm of argon gas flow with mass and heat flow data recorded simultaneously. Additionally, QGA data were recorded for the decomposition of a 1 g sample of lithium amide which was loaded into a stainless steel reactor and attached to the Quantitative Gas Analyser as described in Section 2.6. The sample was heated to 670 °C at 5 °C min^{-1} under and argon flow of 60 sccm. Structural data for the

decomposition reaction were collected using in situ PXRD on the I11 beamline at Diamond. A sample of lithium amide powder was loaded into a 0.7 mm borosilicate capillary, flame-sealed and loaded into a capillary holder. The capillary was attached to the diffractometer, and then heated using a hot air blower from room temperature to 600 °C at 10 °C min^{-1}. For this fast process, the second detector on I11 was used: the position-sensitive detector (PSD). The PSD is a strip-detector which can measure 90° of diffraction data simultaneously with an angular resolution of 0.05°. Diffraction patterns were collected in 30 second blocks for the duration of the heating experiment.

Reactions of each of lithium deuteride and sodium deuteride with deuterated ammonia to form the relevant amide were studied using NPD on the GEM instrument at ISIS. Lithium deuteride was used as received, sodium deuteride was synthesised by the reaction of sodium under 40–80 bar of deuterium gas at 700 °C for 24 hours. This experiment was performed in conjunction with the use of the IGA^n, as described in section 2.3.2. The metal deuteride sample (350 mg lithium deuteride, 450 mg sodium deuteride) were loaded into vanadium buckets which were attached to the IGA^n balance, and sealed using the quartz reactor. Once loaded onto GEM, an initial one hour background scan of the starting material was taken at room temperature. Both samples were then exposed to 1000 mbar of deuterated ammonia, and heated in various steps to the desired final temperature (300 °C for lithium deuteride, 175 °C for sodium deuteride). For the duration of the experiment, diffraction data sets were collected every three minutes. GEM detector banks 4 and 5 were used for the data analysis. Post reaction, each sample was transferred into a 6 mm vanadium can and measured for an hour at room temperature for use as a final data set.

The reactions of the metal hydrides/deuterides with ammonia were further investigated by reacting each of the possible mixtures of metal hydride/deuteride with deuterated/non-deuterated ammonia. Each sample was reacted with 1000 mbar of ammonia in the IGA^n apparatus heated to the same temperatures as used for the GEM experiment. The resulting powders were loaded into 0.7 mm borosilicate capillaries, and examined by Raman spectroscopy using a 532 nm laser, with two co-additions of two-second data collections. These measurements take advantage of the huge isotope effect for H-D substitutions in spectroscopy, where due to the fact that deuterium is double the mass of hydrogen, the equivalent vibration for N-H is approximately 1.4 times the

frequency of the deuterated analogue.

The structure of sodium amide was further investigated in two neutron scattering experiments. A sample of deuterated sodium amide was prepared by the reaction of sodium deuteride (prepared as above) with deuterated sodium amide in the IGAn apparatus, heating to 180 °C under 1100 mbar of ammonia until the mass reading showed a complete reaction. The sample was confirmed to be 98 % pure by PXRD analysis. This sample was loaded into a 10 mm vented vanadium can and inserted into the POLARIS diffractometer at ISIS. The sample was heated from 50–200 °C in 2 °C steps, with three minute diffraction datasets collected at each temperature. Neutron total scattering data were also collected on the solid and liquid phase of sodium amide using the NIMROD instrument at ISIS. All of the scattering in the experiment which is not due to the sample must be accounted for before the data for the sample can be analysed. Thus, two-hour data collections were performed on the empty instrument, the empty furnace, and the empty sample cell, with the furnace and sample cell collected at each temperature used in the experiment. The sample was then placed into the same 12 mm cylindrical vanadium can as was used for the empty can measurement, sealed with indium wire and attached to a centre stick. Scattering data for the sample were collected for four hours at room temperature, and then three hours at each of 200, 210 and 300 °C. The melting point of sodium amide is 210 °C. Data were processed using the GudrunN program[204], which is outlined in Section 2.4.4. These neutron total scattering data were compared to X-ray total scattering data collected on the silver source X'pert diffractometer. The sodium amide sample measured on this instrument was sealed in a 2 mm i.d. quartz capillary and attached to a goniometer, which allows the user to align the capillary with the X-ray beam. After aligning the sample, X-ray data were collected for 24 hours, and compared with equivalent datasets for the empty instrument, and an empty capillary using the GudrunX program[205], which is outlined in Section 2.4.4.

4.2 The synthesis and decomposition of lithium amide

The decomposition of lithium amide to lithium imide is a core component of the hydrogen release reaction in the Li-N-H system. In the mechanism outlined in the previous Chapter, the interconverion of amide and imide is the reason given for the formation of the non-stoichiometric

phases which underpin the facile reversibility of the hydrogen storage reactions. As such, the properties of this transformation are of significant interest, particularly whether the formation of non-stoichiometric intermediates is an integral part of the interconversion of the amide and imide, or whether it is isolated to the hydrogen storage and release reactions of the Li-N-H system.

Combined DSC and TGA data and QGA data for the decomposition of powder samples of lithium amide are shown in Figure 4.1a and b, respectively. The TGA data show a total mass loss of 33.8 %, compared with an expected mass loss of 37.1 %; the difference most likely attributable to the oxidation of the sample. The QGA data indicate that ammonia was the gas released in this decomposition, as would be expected. The nitrogen and hydrogen emitted between 300 and 550 °C are in a three to one ratio, representing ammonia decomposed into its constituents. The mass loss for this first process occurred in two steps, a low-temperature mass loss at 200–280 °C, which probably corresponds to desorption of adsorbed or loosely-held ammonia, followed by the main mass loss above 300 °C.

The DSC data show two endothermic transitions for this decomposition: a sharp peak centred on 368 °C corresponds to the melting of lithium amide, with the broad peak spanning the decomposition corresponding to the endothermic decomposition reaction ($\Delta H = 84.1\,\mathrm{kJ\,mol^{-1}}$). Correlation of these data with the mass loss shows that in bulk lithium amide the decomposition reaction accelerated rapidly following the onset of melting. This is in contrast to the reaction of the Li-N-H system, where the hydrogen release occurs entirely in the solid state. The onset temperature for the decomposition (*ca* 300 °C) in the isolated reaction was also significantly higher than that observed for hydrogen release in the Li-N-H system. It has been shown that the equilibrium vapour pressure of ammonia in lithium amide is very low prior to melting, and so even small amounts of ammonia adsorbed onto the particle surface will retard the decomposition in the solid state[224]. The effective removal of ammonia from the surface of lithium amide by the rapid reaction of lithium hydride with ammonia[230, 231] thus appears to be an important factor in lowering the temperature of the decomposition reaction, and therefore the hydrogen release temperature of the Li-N-H system.

A second decomposition event was observed in both datasets above 600 °C. While this temperature range is higher than the region of interest in this study, it is worth noting that the 1:1 mixture of nitrogen and hydrogen that evolves from the sample in the absence of any ammonia

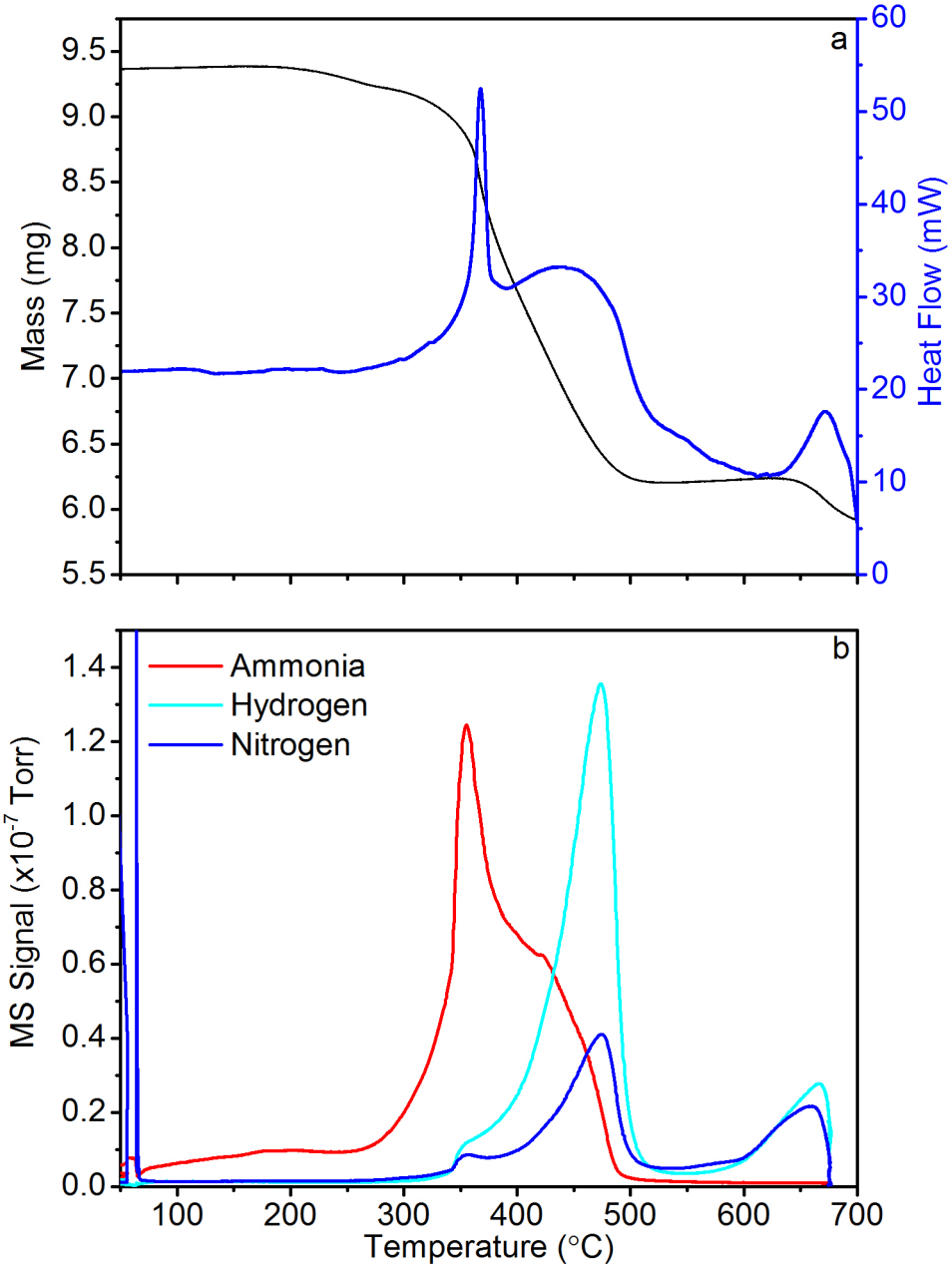

Figure 4.1: The decomposition of a powder sample of lithium amide as examined by a) combined DSC-TGA and b) QGA. Both experiments were performed under flowing argon.

signal supports the view that the decomposition of lithium imide does not form lithium nitride, as might be expected, but rather results in the formation of lithium nitride hydride (Li_4NH) according to Equation 4.1[113, 232].

$$2Li_2NH \rightarrow Li_4NH + \frac{1}{2}N_2 + \frac{1}{2}H_2 \tag{4.1}$$

A more detailed analysis of the gas species released during the decomposition to lithium imide was obtained using Temperature Programmed Desorption – Mass Spectrometry (TPD-MS) data obtained from single crystals of lithium amide grown by Dr Shige Isobe (Figure 4.2). Decomposition of the single crystal gives a very clear mass loss profile. While the emission of ammonia was the dominant process in the reaction, the collection of a range of gaseous species by mass spectrometry (MS) can provide further insights into the reaction mechanisms. Figure 4.2b shows the MS traces for each of the mass fragments collected, namely m/z= 2, 14, 15, 16, 17, 18 and 28, representing H_2, N, NH, NH_2, NH_3, NH_4 and N_2. Some of these fragments represent species which are expected to be produced in the decomposition of lithium amide, while others are more likely produced by fragmentation of one of these species in the ionisation source of the mass spectrometer. Each of the mass fragments displayed a similar profile over the course of the reaction, which is unsurprising given that a single process is expected for this reaction. However, it is possible to observe that the the initial mass loss below 370 °C was due only to ammonia, while hydrogen and nitrogen accompany the ammonia release in the main decomposition peak above 370 °C. This is consistent with the initial mass loss being attributed to the release of adsorbed ammonia, rather than decomposition of the amide itself. As discussed earlier in this Chapter, the presence of nitrogen and hydrogen is usually attributed to the decomposition of released ammonia. However, the possibility that a portion of these species could result from the formation of metallic lithium, as discussed for the Li-N-H system in Chapter 3, should not be ruled out.

The mass data can be effectively coupled to the variation in the mass spectrum as a function of temperature to give a fuller picture of the decomposition process. By weighting the signals from the different mass fragments by their mass, a good correlation between the negative of the first derivative of the mass loss and the summed, weighted MS signals can be seen (Figure 4.2c). A logarithmic plot of the data (Figure 4.2c, inset) shows that the correlation is good except at

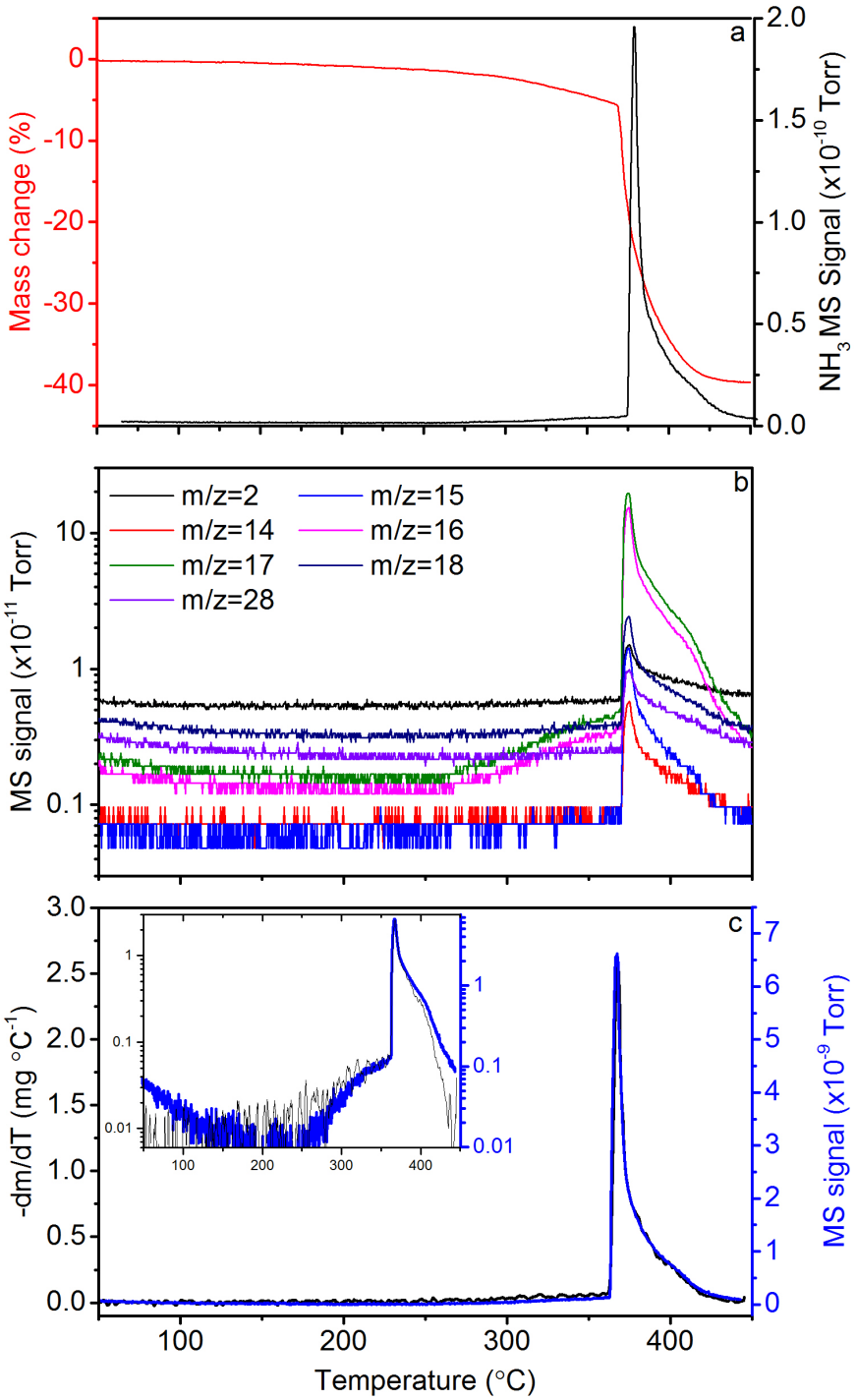

Figure 4.2: The decomposition of a single crystal of lithium amide, as assessed by TPD-MS, showing a) the mass loss and ammonia signal b) the various mass fragments analysed by mass spectrometry over the course of the reaction and c) a comparison of the negative of the rate of mass change with the mass-weighted sum of the mass spectrometry species, replicated on a logarithmic scale in the inset.

the highest temperatures, where the MS signals overestimate the mass loss. This may be because of residual gas coming through the instrument.

While this advanced data analysis has not revealed anything unexpected for the decomposition of lithium amide, the methodology could be applied to more complex systems to give some indication as to whether particular fragments are produced by distinct processes, giving insight into the decomposition pathway. The quantitative comparison of the MS signals with the mass loss detailed here could also be used to ascertain whether the examined mass fragments account for all of the mass losses observed.

In terms of investigating the formation of non-stoichiometric species as part of the decomposition of lithium amide, the fact that the sample melts at an early stage in the decomposition process makes the detection of these phases more difficult. As outlined earlier, the decomposition of lithium amide in the Li-N-H system occurs below its melting point, implying that the solid-state behaviour of lithium amide is of greater relevance to that reaction. The early stages of the decomposition reaction were studied by *in situ* synchrotron PXRD data collected on I11 at Diamond. Contour plots of the PXRD data for a number of the lithium amide Bragg peaks are shown in Figure 4.3. While the use of the lower-resolution PSD detector for these data makes detailed analysis difficult, it is possible to observe that in addition to the increase in the lattice parameter of the lithium amide as the sample was heated, the magnitude of the amide peaks decreased, and a peak was seen to branch off towards a smaller d-spacing. The fact that these peaks branched out from the amide peaks is a particularly strong indication of the presence of non-stoichiometry, rather than transition directly to the imide, as was observed in the *in situ* PXRD studies of the Li-N-H system.

These data indicate that the formation of non-stoichiometric phases is an intrinsic part of the decomposition of lithium amide. It seems reasonable to assume that the reverse reaction, the formation of lithium amide from the reaction of lithium imide and ammonia would proceed via the same non-stoichiometric phases (of course, studying this reaction would allow for the sample to be kept in the solid state for the entire process).

In the Li-N-H hydrogen storage system, lithium amide is also formed in the dehydrogenation reaction via the reaction of lithium hydride with ammonia, which is the hydrogen release step. The reactions of metal hydrides with ammonia have also recently attracted some interest as

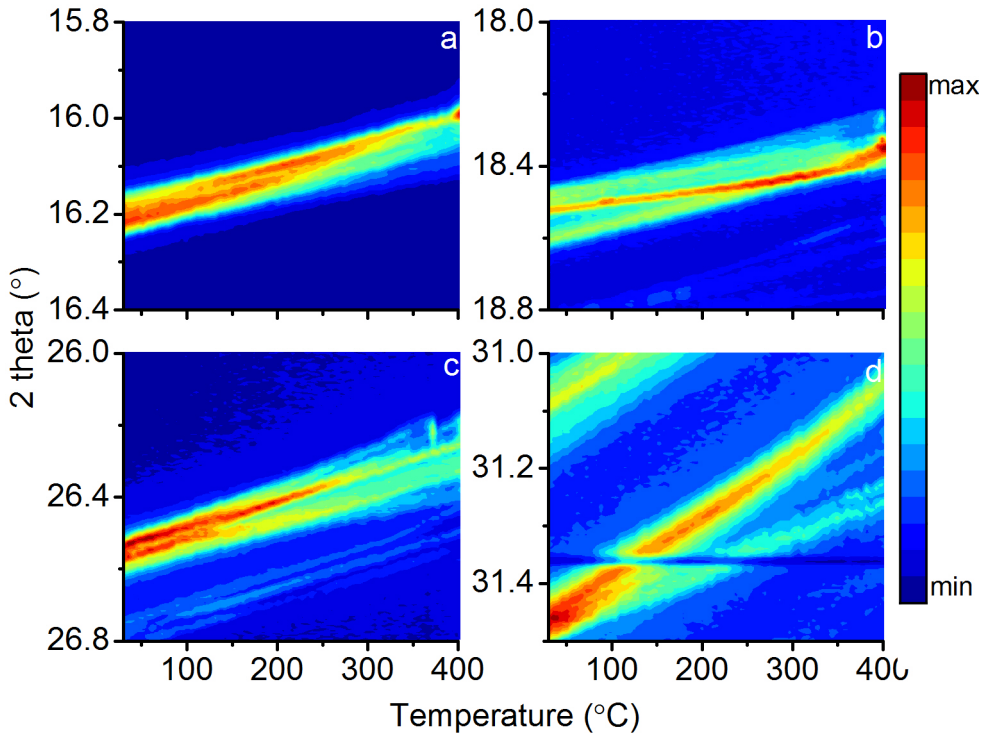

Figure 4.3: Contour plots of PXRD data for the decomposition of lithium amide showing the section of the data for the a) (112), b) (004), c) (024), and d) (312) lithium amide Bragg peaks.

a recyclable method of hydrogen storage in their own right[229, 233–235]. This reaction was investigated by a combination of IGA and NPD using the IGA^n instrument. The results of this experiment are shown in Figure 4.4. The IGA^n instrument records the reaction conditions (Figure 4.4a) and the mass of the sample (Figure 4.4e), while the NPD data (Figure 4.4b-d) were recorded on the GEM diffractometer at ISIS. For this experiment, the deuterated analogues were used to avoid the large backgrounds associated with hydrogen (^{1}H). Individual diffraction patterns of the sample at the beginning and end of the experiment showing the observed patterns and the calculated fit to the data are given in Appendix H, with crystallographic information used in the refinements given in Appendix A.

It can be seen that an increase in the sample mass was associated with the conversion of lithium deuteride to lithium amide, and also with the oxidation of the sample. At approximately 360 mins, the software controlling the temperature of the sample aborted, resulting in a momentary drop in the temperature of the sample, which can be observed as a decrease in the lattice parameter of the lithium deuteride. At around 720 mins, the pressure control was lost, resulting in the observed pressure drop as the sample reacted with the ammonia in the reactor.

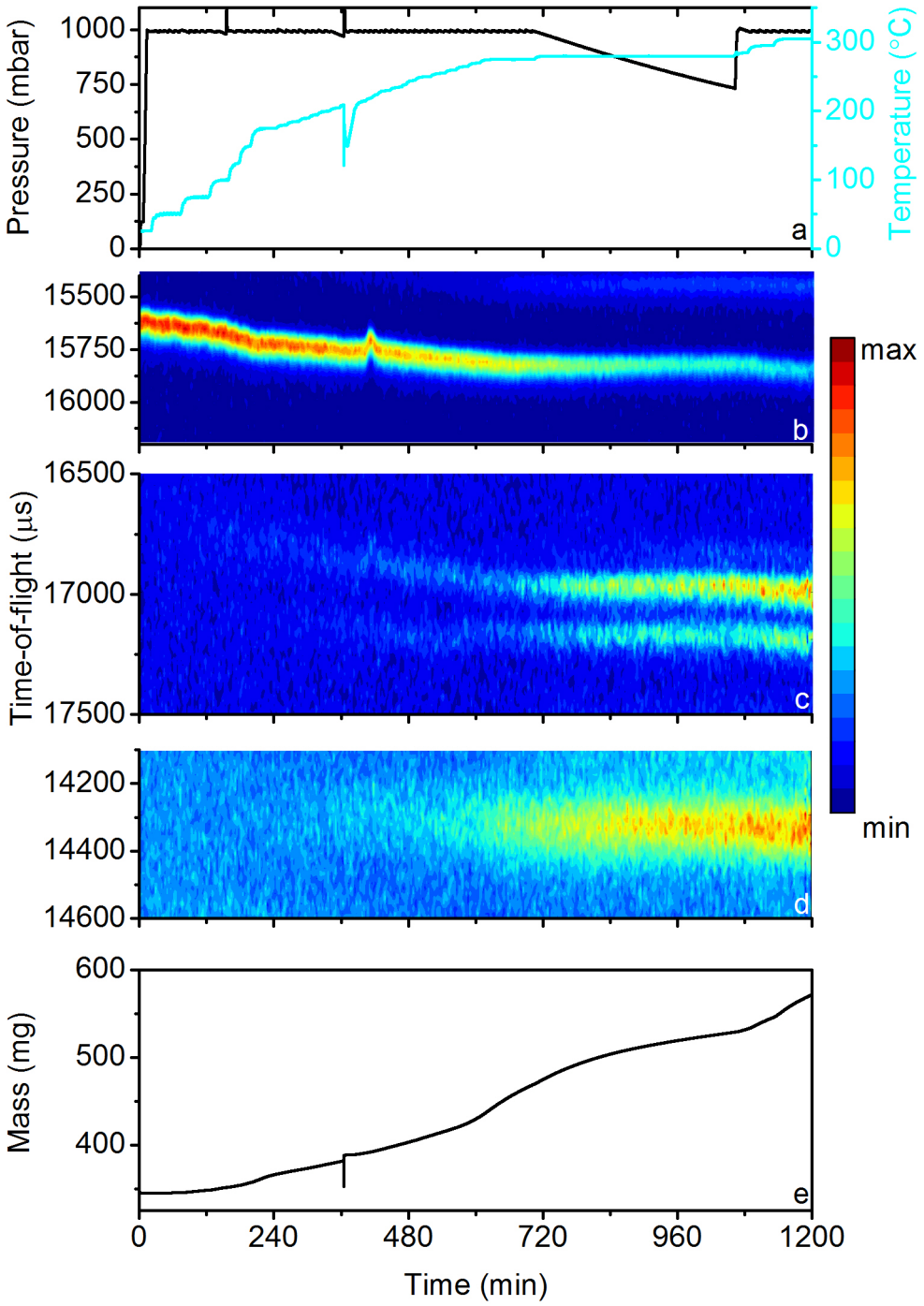

Figure 4.4: Combined IGA^n and *in situ* NPD experiment for the reaction of lithium deuteride with deuterated ammonia. The panels show a) the reaction conditions, NPD contour plots for b) lithium deuteride (111) c) lithium amide (002) and (004) and d) lithium oxide (111), and e) the mass of the sample. The error in the mass determined by the IGA^n is ± 0.05 mg.

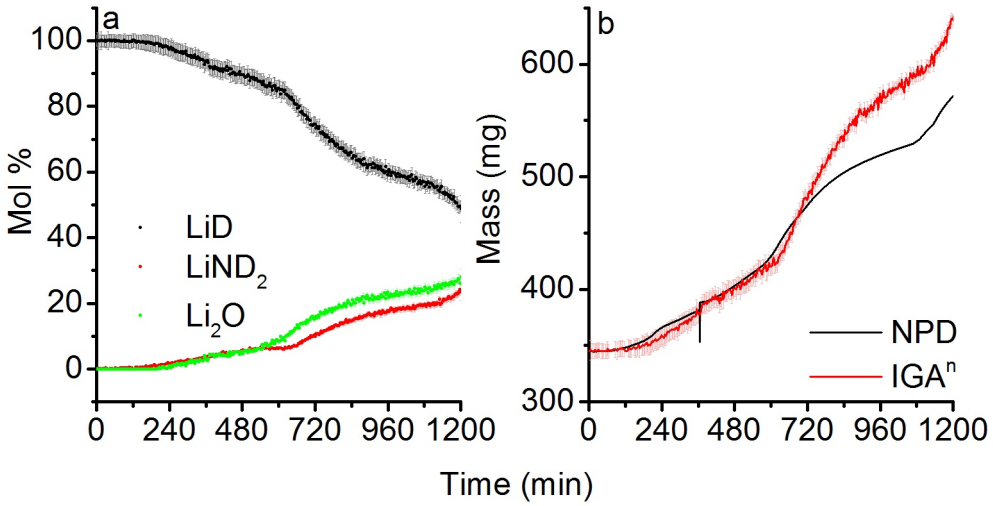

Figure 4.5: a) Relative molar amount of each of the crystalline phases present during the reaction of lithium deuteride with deuterated ammonia, extracted from Rietveld analysis of the NPD data, and b) a comparison of the mass of the sample as measured by the IGA^n compared with the mass expected from the composition of the sample derived from Rietveld analysis of the NPD data. The error in the mass determined by the IGA^n is ± 0.05 mg, , while the error in the mass determined by refinement of the neutron diffraction data is ± 25 mg.

Despite working at temperatures in the range of those used for hydrogen desorption in the Li-N-H system, the conversion of the deuteride to the amide was relatively slow, in contrast to the documented rapid reaction[231]. This apparent inconsistency probably results from the different nature of the hydride/deuteride particles in the Li-N-H system, where they are present as an intimate mixture of small particles with the amide. Here, the particle size was larger, and it appears that the reaction occured by the formation of a surface layer of amide on the deuteride, with further reaction requiring the diffusion of ammonia through this layer. This effect would be exacerbated by the evident oxidation of the sample, which would also passivate the surface of the deuteride particles, slowing the reaction kinetics. In the Li-N-H system, the lithium amide formed by the reaction of lithium hydride and ammonia is rapidly decomposed as the dehydrogenation reaction progresses, which helps to avoid the formation of a passivating layer on the hydride.

Rietveld analysis of the diffraction data shows the expected ammoniation of the lithium deuteride into lithium amide and lithium oxide (Figure 4.5a). The analysis suggests that there was significant oxidation of the sample, with the molar percentage of oxide exceeding that of the product amide.

The combined measurement of gravimetric and diffraction data gives an opportunity to validate the refinement. Based on the relative amount of each phase in the refined NPD data, the expected mass of the sample can be calculated. Identifying discrepancies between this value and the measured mass allows for the accuracy of the refinement to be assessed, as well as providing an indication of whether an analysis of the crystalline components is a full description of the system (a lower than expected mass from the refined phases may suggest that there are some amorphous phases present). The comparison does rest on the assumption that either i) all of the sample was in the neutron beam or ii) that the sample composition did not vary between the parts that are in and out of the beam. In most circumstances, this should be a reasonable assumption.

The expected mass calculated from the refinement of the NPD in this case is compared with the measured sample mass in Figure 4.5b, which shows that the expected and actual mass are well matched for the first half of the reaction, after which the expected mass is significantly in excess of the measured mass. In this case, the higher mass expected from the refinement most likely indicates that the amide or oxide phases were overestimated in the refinement. The most likely scenario is that the lithium oxide was overestimated, as its broader Bragg peaks are less reliably quantified and are highly correlated with the background.

One of the purposes of examining this reaction was to provide information about its mechanism, and in particular whether non-stoichiometric phases are involved. No evidence was observed in the NPD data for the formation of any cubic imide-like phases, with the superlattice reflections well-correlated with the appearance of the amide phase. Nor were any complex peak shapes observed, as was the case for the Li-N-H system. However, the resolution of the GEM diffractometer at ISIS is not as high as for synchrotron PXRD. This suggests that more subtle indications of stoichiometry variation are worth considering. These are shown in Figure 4.6. Figure 4.6a shows the lattice parameters of lithium amide and lithium deuteride over the course of the reaction. The change in the a lattice parameter of lithium amide mirrored that of lithium deuteride, indicating that the variation was fully accounted for by changes in the temperature.

A second check for non-stoichiometry is the c/a ratio for lithium amide, shown in Figure 4.6b. Progression from imide-like stoichiometry values to the amide would be expected to cause this ratio to increase from a value of 2.0 towards the ratio for stoichiometric amide of around

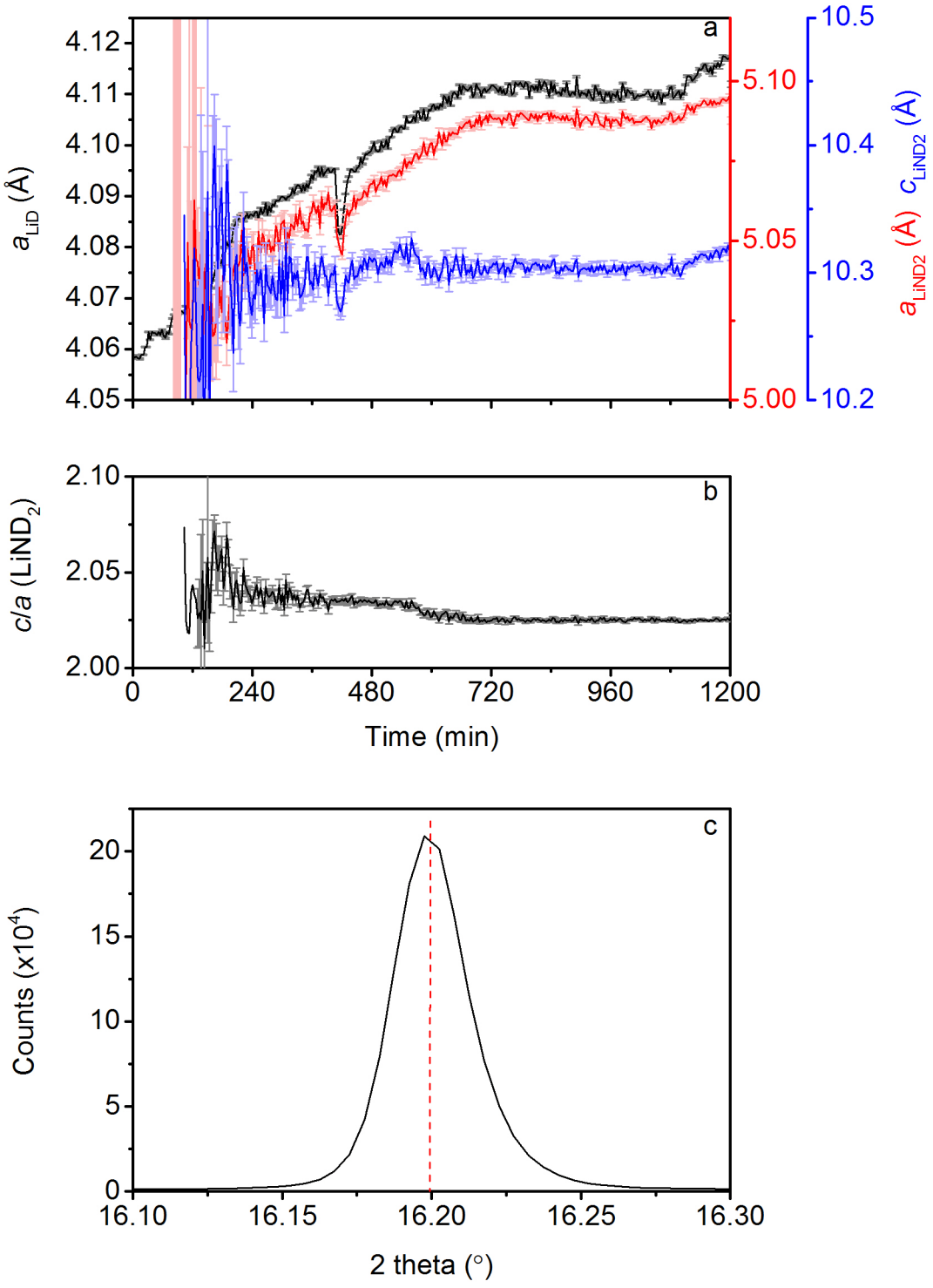

Figure 4.6: a) The lattice parameters idenitified from Rietveld analysis of NPD data of lithium deuteride and lithium amide during the reaction between lithium deuteride and deuterated ammonia, b) the c/a ratio for lithium amide and c) the lithium amide (112) peak in post-reaction PXRD analysis, with a dashed red line to indicate the peak position.

2.03. This was not observed in the c/a ratio in these data, with the value being quite stable close to that expected for the amide. The origin of a small step change in the ratio at around 580 minutes is unclear; the fact that the effect is not consistent across all of the detector banks[1] is indicative that the change in the ratio may be due to the analysis of the data. Therefore it is concluded that the c/a ratio provides strong evidence for the absence of non-stoichiometry.

This is perhaps unsurprising, given the previously determined lack of stoichiometric variability accommodated in the tetragonal amide phase. As a further check for the presence of non-stoichiometric phases, the post-reaction sample was analysed by synchrotron PXRD — the (112) peak of the lithium amide phase is shown in Figure 4.6c. The peak is only very slightly asymmetric towards the non-stoichiometric region, supporting the assessment that stoichiometric amide is formed by the reaction of lithium hydride and ammonia.

A further assessment of the reaction mechanism was sought by examining the Raman spectra of a series of the permutations of combinations of lithium hydride/deuteride and ammonia/deuterated ammonia. The samples were reacted using the IGA^n (without simultaneous NPD), and then analysed post reaction by Raman spectroscopy. Because the mass of deuterium is double that of hydrogen, there is a large difference in the reduced mass of the N–H bond compared with the N–D bond, resulting in well-separated vibrational bands. The N–D and N–H stretching regions of the Raman spectra are shown in Figure 4.7a and b, respectively.

There was no imide N–H stretch observed in the data, nor was there any variation in the position of the various amide stretch peaks between the samples which could indicate the presence of non-stoichiometric phases. This supports the conclusion drawn from the NPD analysis that stoichiometric amide is formed.

If these indications are correct, and stoichiometric amide is formed, then there are two obvious possibilities for amide formation from the reaction of lithium hydride and ammonia. The attraction between the hydride anion and the partial positive charge on the ammonia protons will encourage the formation of an activated complex. From the formation of this activated complex, two possible routes emerge. Firstly, that the hydride anion combines with one of the hydrogens on the ammonia molecule, producing hydrogen. In this case, mixtures of deuterated and hydrogenated species (LiD + NH_3 and LiH+ND_3) should result only in the emission of HD,

[1] There is a positive change in the ratio if a refinement of only bank 5 is completed, a negative change if only bank 4 is refined, and the pictured change for both banks refined simultaneously

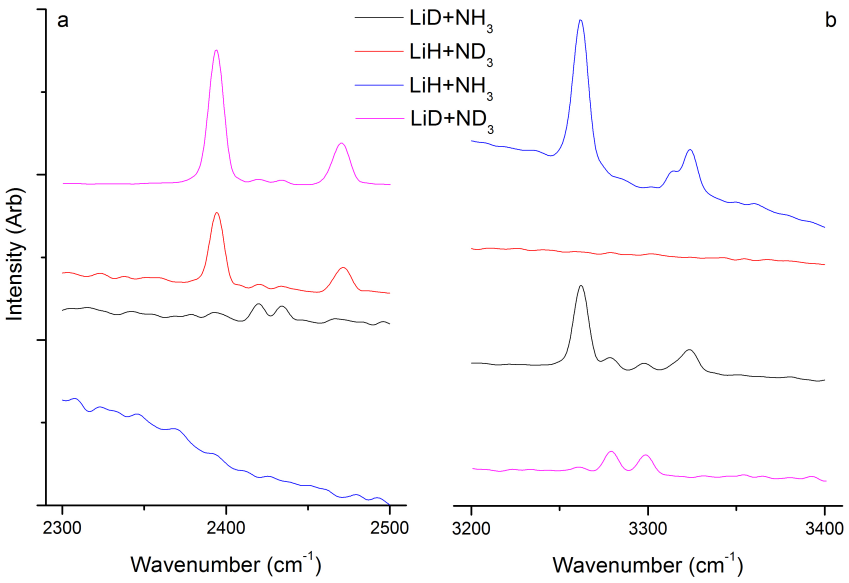

Figure 4.7: Raman spectra of lithium amide produced from the reaction of various isotope mixtures of lithium hydride and ammonia showing a) N–D and b) N–H stretching regions.

and the resultant amide should be contain only the hydrogen isotope contained in the ammonia. Alternatively, the hydrogen produced is a random combination of two of the hydrogen atoms from the four in the activated complex, which would result in a statistical mixture of isotopes in the hydrogen gas and the amide.

The combination of LiH and NH_3 gave the familiar N–H stretch bands: the strong symmetric stretch (3260 cm^{-1}) and two weaker asymmetric stretch bands (3313 and 3323 cm^{-1}). As expected, there are no peaks in the N-D region for this sample, since the isotopic abundance of deuterium in these samples was at the natural level (0.002 %). However, the combination of LiD and ND_3 gave a more complex spectrum. The expected amide stretches are found in the N–D region, but there are also additional low-intensity peaks in between these bands at 2425 and 2435 cm^{-1}, and similar intermediate bands in the N-H stretch region at 3280 and 3295 cm^{-1}. These bands are assigned to N–H or N–D stretches from a mixed NDH amide unit. The presence of these bands in the LiD + ND_3 sample implies that the lithium deuteride was not isotopically pure. These mixed isotope amide stretches are seen in the LiD + NH_3 sample also, and may be present in the LiH+ND_3 sample, although the peaks are not well distinguished from background noise.

The presence of these mixed amide N–H and N–D stretches supports the model of a statistical release of hydrogen atoms, rather than direct combination of one hydrogen from the hydride and

another from ammonia. The ratio of mixed amide units to pure units is less than the expected 1:4. However, the demonstrated exchange of hydrogen atoms between amides and ammonia may cause diminished peak intensities. Another important question is whether there can be exchange of hydrogen atoms between metal amides and hydrogen. If this is the case, then the first model could hold, with the mixed amide units accounted for by reabsorption of the emitted HD molecule. In respect to this, the results presented here are inconclusive.

4.3 The synthesis and structure of sodium amide

Sodium amide is not generally examined for its hydrogen storage properties, since its decomposition temperature is in excess of 400 °C. However, its decomposition reaction contrasts with lithium amide, as it does not form a stable imide. Instead, it decomposes directly to the metal, nitrogen and hydrogen (Equation 4.2). The emission of hydrogen without the need to create an amide-hydride composite removes a number of practical issues which are associated with composite materials, and avoids the problem of ammonia release. The reaction may also prove to be of increased interest if it is shown that decomposition to lithium metal is a reaction which occurs to some extent in the Li-N-H system.

$$NaNH_2 \rightarrow Na + \frac{1}{2}N_2 + H_2 \tag{4.2}$$

The synthesis of deuterated sodium amide from the deuteride and deuterated ammonia in the same manner as was performed for lithium amide, was also studied by IGA^n-NPD. The results of that experiment are shown in Figure 4.8. Figure 4.8a shows the reaction conditions,Figure 4.8b and c are contour plots of the (002) Bragg peak of sodium deuteride and the (202), (022) and (220) peaks of sodium amide, respectively, and Figure 4.8d shows the mass of the sample. There is a small gap in the NPD data at around 120 minutes when the neutron beam was off. Individual diffraction patterns of the sample at the beginning and end of the experiment showing the observed patterns and the calculated fit to the data are given in Appendix H, with crystallographic information used in the refinements given in Appendix A.

The IGA and NPD data show the reaction progressed as expected, with the sodium deuteride consumed as the amide formed. The NPD data suggest that the reaction progressed to comple-

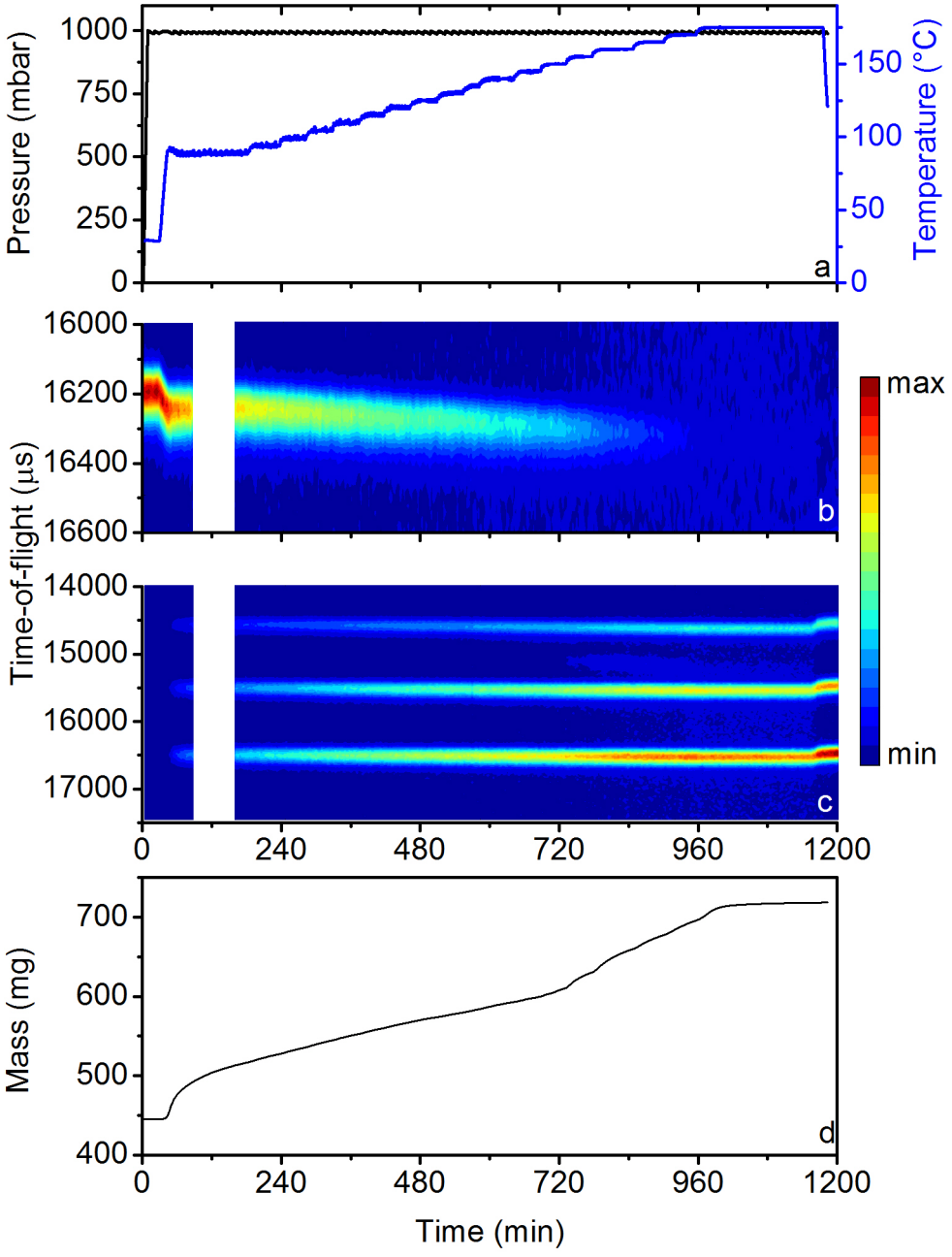

Figure 4.8: The combined IGA^n-NPD data for the reaction of sodium deuteride and deuterated ammonia. The panels show a) the reaction conditions b) the (002) peak of sodium deuteride c) the (202), (022) and (220) peaks of sodium amide and d) the mass of the sample. The error in the mass of the sample measured by the IGA^{n}is ± 0.05 mg.

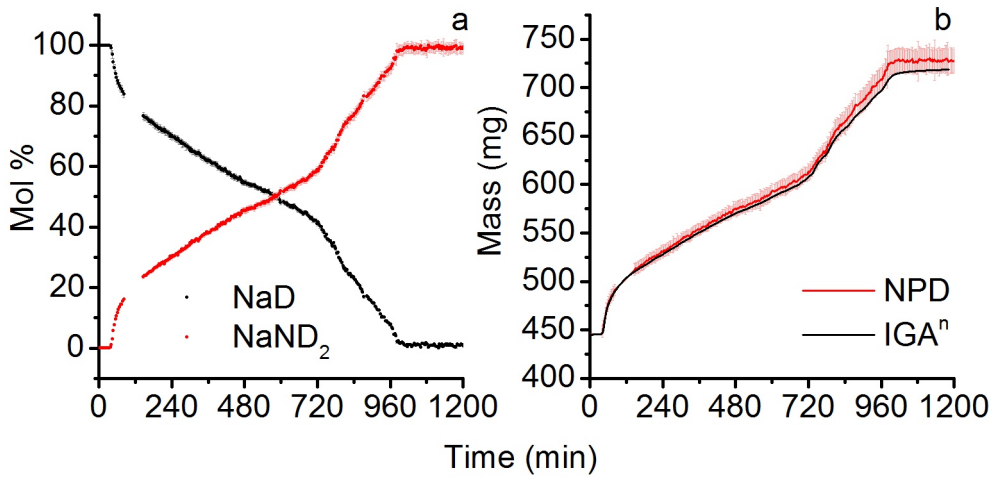

Figure 4.9: a) The relative molar amounts of the crystalline phases in the reaction of sodium deuteride with deuterated ammonia b) the comparison of the mass of the sample calculated from the phase composition in the NPD data with the actual mass of the sample measured by the IGA^n. The error in the mass determined by the IGA^n is ± 0.05 mg, while the error in the mass determined by refinement of the neutron diffraction data is ± 20 mg.

tion, which is corroborated by the mass increase. This is in contrast to the reaction of lithium deuteride. The difference in the extent of reaction is at least partially due to the oxidation of the lithium deuteride sample, which passivated the surface. The sodium deuteride sample did not suffer from any detectable oxidation.

Unsurprisingly, given the fact that sodium imide is not known to form, there are no indications from the NPD data that the reaction proceeded by anything other than a stoichiometric reaction. Given the Bragg peaks of the two phases are well separated, quantification of the reaction progress is straightforward. The relative molar amounts extracted from Rietveld analysis of the NPD data are shown in Figure 4.9a, with the comparison of the expected mass from the refinement and the actual mass measured by the IGA^n shown in Figure 4.9b. Given the absence of oxidation as a complicating factor in the quantification of the phases, it can be seen that the refinement reflects well the progression of the reaction as measured by the increase in the mass of the sample.

A set of Raman experiments using different isotopic substitutions for the reaction of the hydride with ammonia were conducted in the same manner as those performed with lithium hydride. The N–D and N–H stretching regions of the resulting Raman spectra are shown in Figure 4.10a and 4.10b, respectively. The results are analogous to those obtained for the lithium experiments, albeit at lower wavenumber than in lithium amide, reflecting a weaker N–H bond.

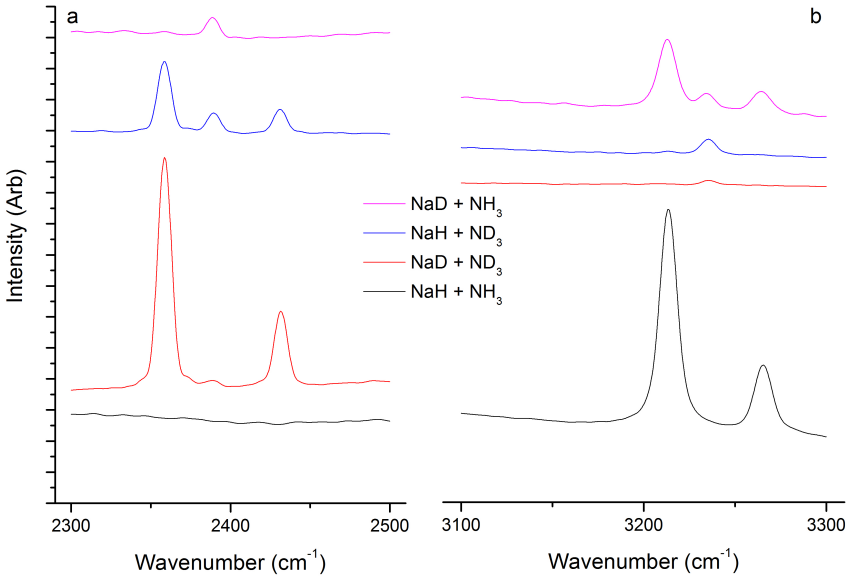

Figure 4.10: Raman spectra of sodium amide produced from the reaction of various isotope mixtures of sodium hydride and ammonia, showing a) N–D and b) N–H stretching regions.

The combination of NaH and NH_3 gave only amide N–H stretches at 3210 and 3260 cm^{-1} (symmetric and asymmetric stretches, repectively). The reaction of both deuterated analogues again gave a small impurity of a mixed NDH stretch in both the N–H (3240 cm^{-1}) and N–D (2390 cm^{-1}) regions, as well as the expected N–D amide stretch bands (2360 cm^{-1} and 2440 cm^{-1} for symmetric and asymmetric stretches, respectively). The mixed isotope reactions (NaH+ND_3, NaD+NH_3) gave similar results, with the major amide group being the pure form of the ammonia-derived hydrogen isotope, with a significant minority of mixed isotope amide stretch peaks.

With the same caveats as were discussed for the lithium samples, these results provide some support for the statistical distribution of the hydrogen atoms from the activated complex in the product amide phase.

The values of the lattice parameters of the sodium amide produced during the IGA-NPD reaction are shown in Figure 4.11. The a and c parameters increased in step with the temperature, with a thermal expansion of between 4 and 5 % between 50 and 200 °C. In contrast, the b lattice parameter changed by only 0.1 % over this temperature range. As well as showing this remarkable incompressibility, the small change which did occur had a curious behaviour, increasing until 120 °C (400 minutes) and then contracting for the remainder of the heating. This unusual behaviour merited further investigation into the variable-temperature behaviour of

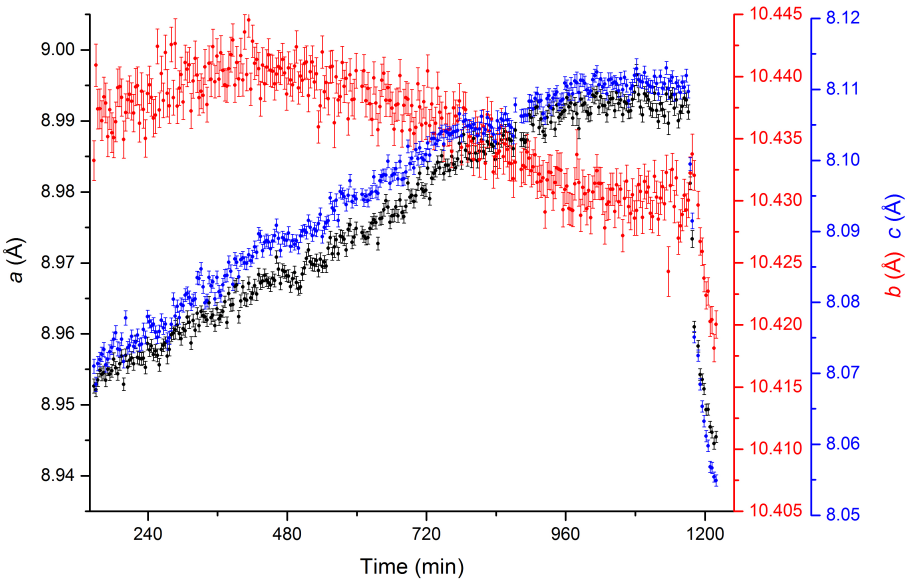

Figure 4.11: The cell parameters of sodium amide during the reaction between sodium deuteride and deuterated ammonia.

sodium amide.

The results of a NPD heating study of a sample of deuterated sodium amide on the POLARIS instrument are shown in Figure 4.12. Figure 4.12a shows a contour plot of the NPD data from detector bank 4 as a function of temperature, and Figure 4.12b is a corresponding plot of the lattice parameters of the amide extracted from Rietveld analysis of the diffraction data. The sample was heated up to the point where the sample began to melt (200 °C), as evidenced by the dramatic decrease in the intensity of the Bragg peaks in the later datasets. Individual diffraction patterns of the sample at the beginning and end of the experiment showing the observed patterns and the calculated fit to the data are given in Appendix I.

The lattice parameters of the sodium amide sample mirrored closely those observed in the synthesis of sodium amide from sodium deuteride and deuterated ammonia. The precise origin of the incompressibility and change in the expansion behaviour of the b lattice parameter is unclear. The volume of the unit cell (Figure 4.13) was unexpectedly constant over the first 10 °C of the heating, potentially reflecting a lack of thermal equilibrium between the thermocouple and the sample. However, after this initial discrepancy, the volume increased linearly throughout the experiment, giving no evidence of a phase transition. It is likely that Density Functional Theory calculations of the phonon density of states would be required to ascertain which phonons could

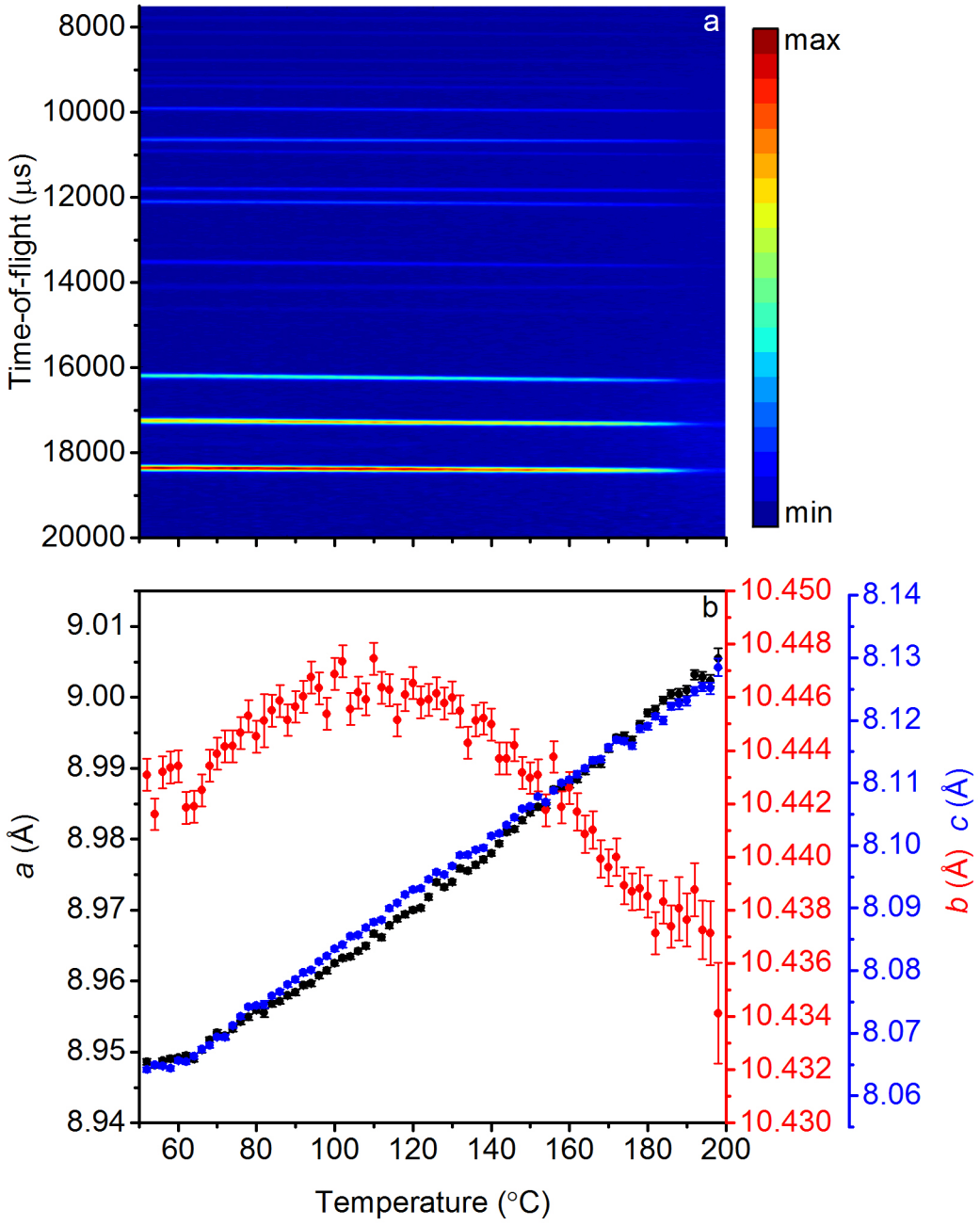

Figure 4.12: Results of a NPD heating study on sodium amide, showing a) a contour plot of the diffraction data from detector bank 4, and b) the values of the sodium amide lattice parameters extracted from Rietveld analysis of these diffraction data.

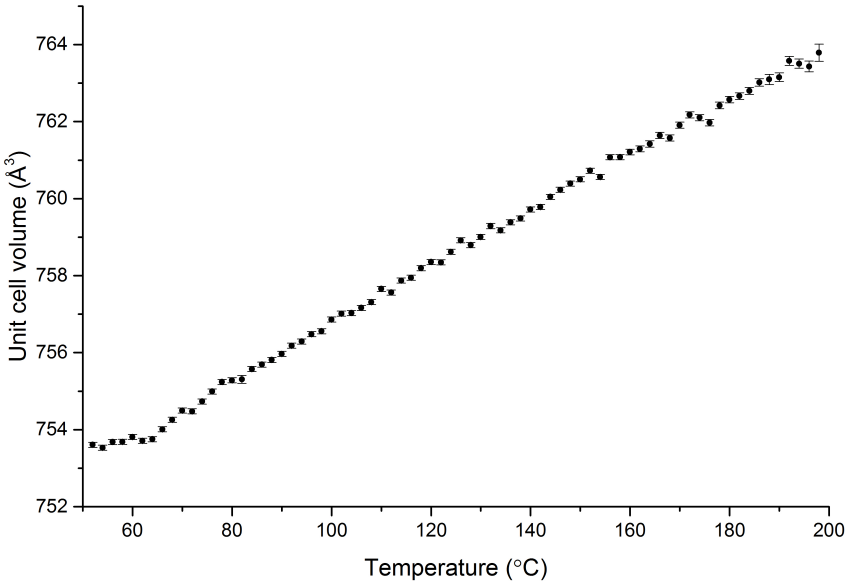

Figure 4.13: The variation of the sodium amide unit cell volume with temperature, derived from Rietveld analysis of NPD data.

be responsible for the observed lattice behaviour. Depending on which modes are responsible, variable temperature Inelastic Neutron Spectroscopy (INS) may also provide some insight into this behaviour.

Sodium amide crystallises with an orthorhombic unit cell (space group *Fddd*), shown in Figure 4.14. The nitrogen atoms form a pseudo body-centred cubic lattice, with the sodium atoms occupying tetrahedral sites. This results in unusually short sodium-sodium distances in the structure. In addition to the unusual lattice behaviour, the refinement of these NPD data reveals interesting motion of the atoms in the sodium amide structure. Initial refinements of the structure with anisotropic thermal parameters showed that the deuterium atoms have strong anisotropic librations. This was investigated in more detail through the construction of a structural model which incorporated these motions. The structure contains the repeated motif of an amide unit between two sodium atoms, illustrated in Figure 4.15. The deuterium sites in the structural model were setup in an arc around the nitrogen atom on a plane perpendicular to the Na-N-Na axis (Figure 4.15a), essentially allowing the amide unit to rotate around that axis. The occupancies of these sites were set to a Gaussian distribution, with the average libration angle described by the standard deviation of that distribution, σ. The amide bond angle (Ψ) was also allowed to vary (Figure 4.15b), along with the N–D bond length. All the atoms were

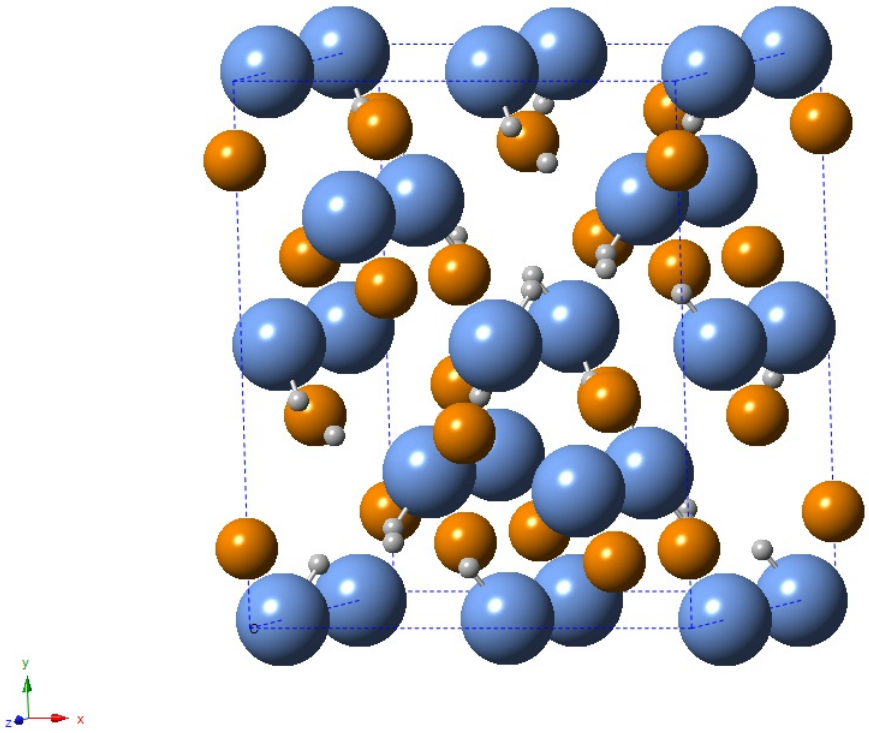

Figure 4.14: The crystal structure of sodium amide. Sodium atoms are shown in orange, nitrogen in blue and hydrogen in grey.

also given a refineable isotropic thermal parameter (β).

The results of the refinement of these values for the NPD data of the heating of sodium amide are shown in Figure 4.16. The refined libration angle at 50 °C (21.8°) indicates that there was significant thermal motion even close to room temperature. The magnitude of the libration increased steadily with increasing temperature, as anticipated. The isotropic thermal parameters also increased linearly with temperature; the temperature factor of the deuterium atoms was significantly larger than those of nitrogen and sodium. Since the libration is accounted for by the various deuterium positions, the large thermal parameter may indicate that the amide unit also tilts off the main axis of libration. This may also be reflected by the apparent shortening of the N–D bond observed in the refinement; decreasing bond lengths are not expected with increasing temperature, but if there is a significant tilting of the amide unit, then the deuterium positions included in the refinement will not account for this motion, and so a combination of a large thermal parameter and a slight shortening of the bond would improve the fit to the data.

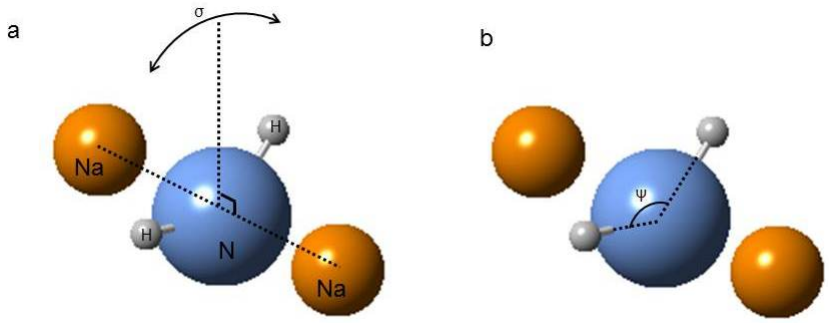

Figure 4.15: Parameters used to model the motion of the amide ion in Rietveld analysis. a) σ represents the libration of the amide ion in a plane perpendicular to the Na–N–Na line, and b)Ψ which represents the D–N–D bond angle.

The amide bond angle did not vary significantly with temperature, with only a slight increase observed from 160 °C, which is likely related to the approach to the melting point. The solid-state amide angle is around 102°, significantly less than the ideal tetrahedral bond angle (109.5°), reflecting the influence of the two lone pairs present on the nitrogen. There are no hydrogen bonds evident in the crystal structure of sodium amide, with the nearest intermolecular N-H distance being 3.17 Å. This absence of hydrogen bonding is consistent across the solid alkali metal amides[100]. However, in the melt, it is expected that the amide units may form hydrogen bonds, which would reduce the effect of the lone pairs on the geometry of the amide ion. The onset of melting and the associated formation of hydrogen bonds may provide an explanation for the increase in the bond angle observed in refinement of the NPD data.

In order to probe the structure of sodium amide in more detail, room temperature X-ray and neutron total scattering data were collected on samples of sodium amide and deuterated sodium amide, respectively. The neutron data were collected on the NIMROD instrument, while the X-ray data were collected on a silver-source laboratory X-ray diffractometer. Processing of the total scattering data allows for the computation of distribution functions, which describe the density of atoms at particular radial separations in the material. The radial distribution function, g(r), and the differential distribution function, D(r), for sodium amide are shown in Figure 4.17. The differential distribution function is shown to highlight the long-range correlations in the samples.

Examination of the room-temperature distribution functions demonstrates the complementary nature of X-ray and neutron scattering; the neutron measurement is dominated by the scattering of the nitrogen and deuterium, while the hydrogen is essentially invisible in the X-ray

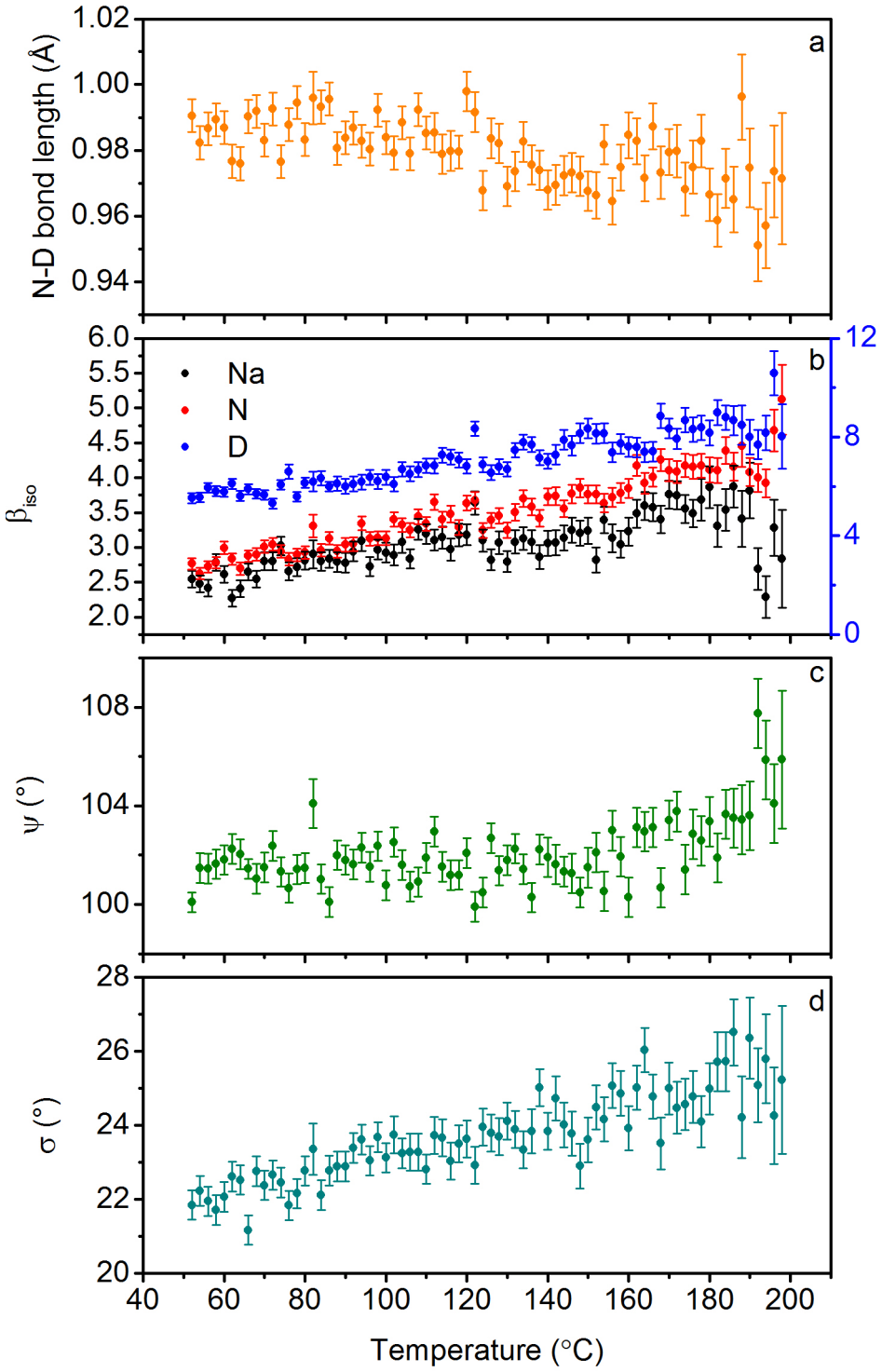

Figure 4.16: The outputs of Rietveld analysis of NPD data for the heating of sodium amide, showing variation in a) the N–D bond length, b) the isotropic thermal parameters of the atoms, c) the amide bond angle and d) the amide unit libration angle.

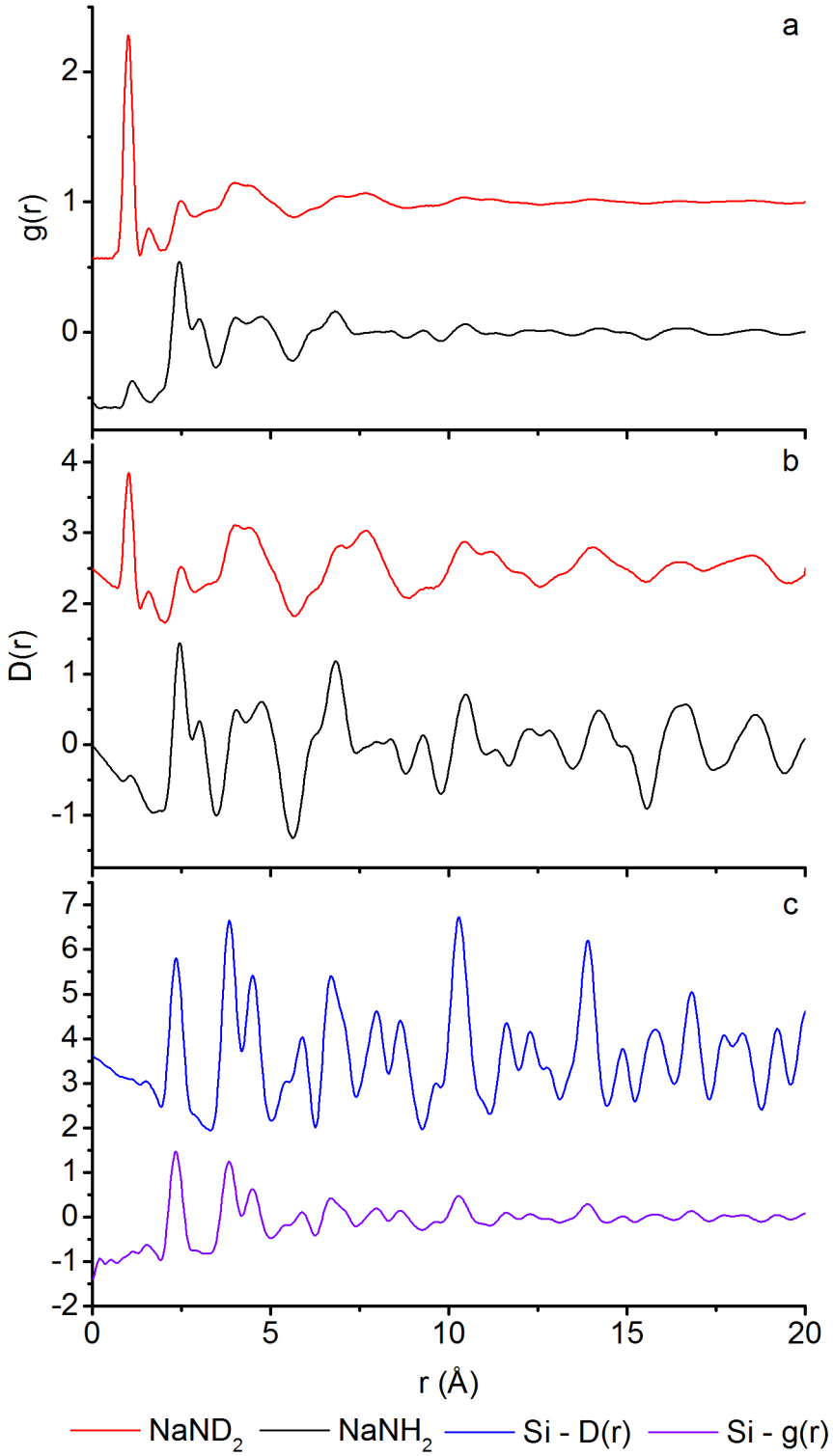

Figure 4.17: Room temperature a) radial and b) differential distribution functions of sodium amide, measured by neutron total scattering (red) and X-ray total scattering (black), compared with c) the radial and differential distribution functions of crystalline silicon measured by X-ray total scattering. The datasets are offset from each other for clarity.

measurement. The peaks at less than 5 Å separation are well understood from consideration of the unit cell of sodium amide. The first and largest peak in the neutron diffraction data at 0.99 Å is the N–D bond length, correlating well with the value obtained from the NPD data. The peak at around 1 Å in the X-ray data is unlikely to be a real feature since its position varies with changes in the cutoff radius used, and so is likely to be an artefact of the Fourier transform. The second peak in the neutron data at 1.58 Å is the D-D separation within a single amide anion. By simple geometry, this implies a D–N–D angle of 104°, which is slightly larger than the refined value of 102° determined from the NPD data. The first common peak between the neutron and X-ray distribution functions is at 2.45 Å, which is the expected distance for the closest sodium and nitrogen pair; at 3.00 Å, the closest sodium-sodium pair is observed. And so, the process of assigning peaks could continue. In short, the short-range correlations are as would be expected for crystalline sodium amide.

Beyond 5 Å, there are very few well-resolved peaks in the neutron g(r), with even the D(r) showing a rapid loss of sharp correlations. This indicates that the long-range structure of sodium amide has a high degree of disorder at room temperature. Again, the complementary nature of the two experiments is clear, with the X-ray distribution functions showing significantly greater long-range order than the neutron measurement. This is consistent with the results of the NPD experiment, which showed that the amide unit is highly mobile even at room temperature, while the sodium and nitrogen atoms are more ordered. Thus, the disorder is clear in the neutron pair distribution functions, but is not present to the same extent in the X-ray measurement.

Of course, great care must be taken when comparing results between different measurement techniques. An example of the distribution function of a highly ordered structure, crystalline silicon, is shown in Figure 4.17c for comparison with the X-ray distribution function of sodium amide. The sodium-nitrogen lattice is clearly less ordered than the silicon, but the main source of disorder in the sodium amide structure appears to be the amide unit itself.

Variable temperature neutron total scattering data were also collected for sodium amide. The distribution functions at 22 °C, 200 °C, 210 °C and 300 °C are shown in Figure 4.18, covering a range below and above the melting point (210 °C). Clearly the amide unit and the coordination to the first sodium ion were conserved as the sample passed through the melt transition, as would be expected. However, there was a significant change in the ordering in the solid phase between

Table 4.1: Positions of the first three peaks in the radial distribution function of deuterated sodium amide at various temperatures, calculated from neutron total scattering data collected on the NIMROD instrument. Lattice parameters given are from Rietveld refinement of POLARIS NPD data on the same sample.

$NaND_2$, space group Fddd							
Temp (°C)	*a* (Å)	*b* (Å)	*c* (Å)	N–D bond length (Å)	D–D distance (Å)	DND bond angle (°)	Na–N distance (Å)
22	8.9485(4)	10.4430(6)	8.0642(4)	1.003(1)	1.597(5)	103	2.46(1)
200	9.006(1)	10.434(2)	8.129(1)	1.021(2)	1.64(2)	110	2.45(1)
210	-	-	-	1.005(1)	1.57(1)	105	2.411(2)
300	-	-	-	1.008(1)	1.54(1)	101	2.41(1)

22 °C and 200 °C. Indeed, the distribution functions of the amide at 200 °C are more similar to those in the liquid phase than those at room temperature. This reflects the NPD data, which showed that the sample had undergone significant amorphisation by 200 °C. At this point, the long-range order in the structure collapses.

Sodium amide displays reasonably typical melt behaviour, with the distribution functions at the melting point and at 300 °C showing peaks and troughs which resemble the solid phase order, but are significantly broadened as a result of the large degree of disorder in the structure.

The peak positions of the first three peaks in the radial distribution function (N–D, D-D and Na-N distances) are recorded in Table 4.1, along with the amide bond angle implied by the D-D distance. The N–D bond length and Na-N distance remain constant across the temperature range other than a slight expansion seen in the 200 °C dataset. This dataset may be slightly anomalous, as further evidenced by the magnitude of the increase in the D-D distance, which implies a bond angle greater than in an ideal tetrahedron. Although an expansion of the bond angle may be expected due to the onset of hydrogen bonding as outlined earlier in this Chapter, and is consistent with the NPD data, the magnitude of the change is much larger than would be expected. Indeed, the values of the bond angle in the other datasets are significantly smaller. Overall, there is not a clear trend in the bond angle with temperature, which may indicate that the position of the D-D distance peak requires further investigation.

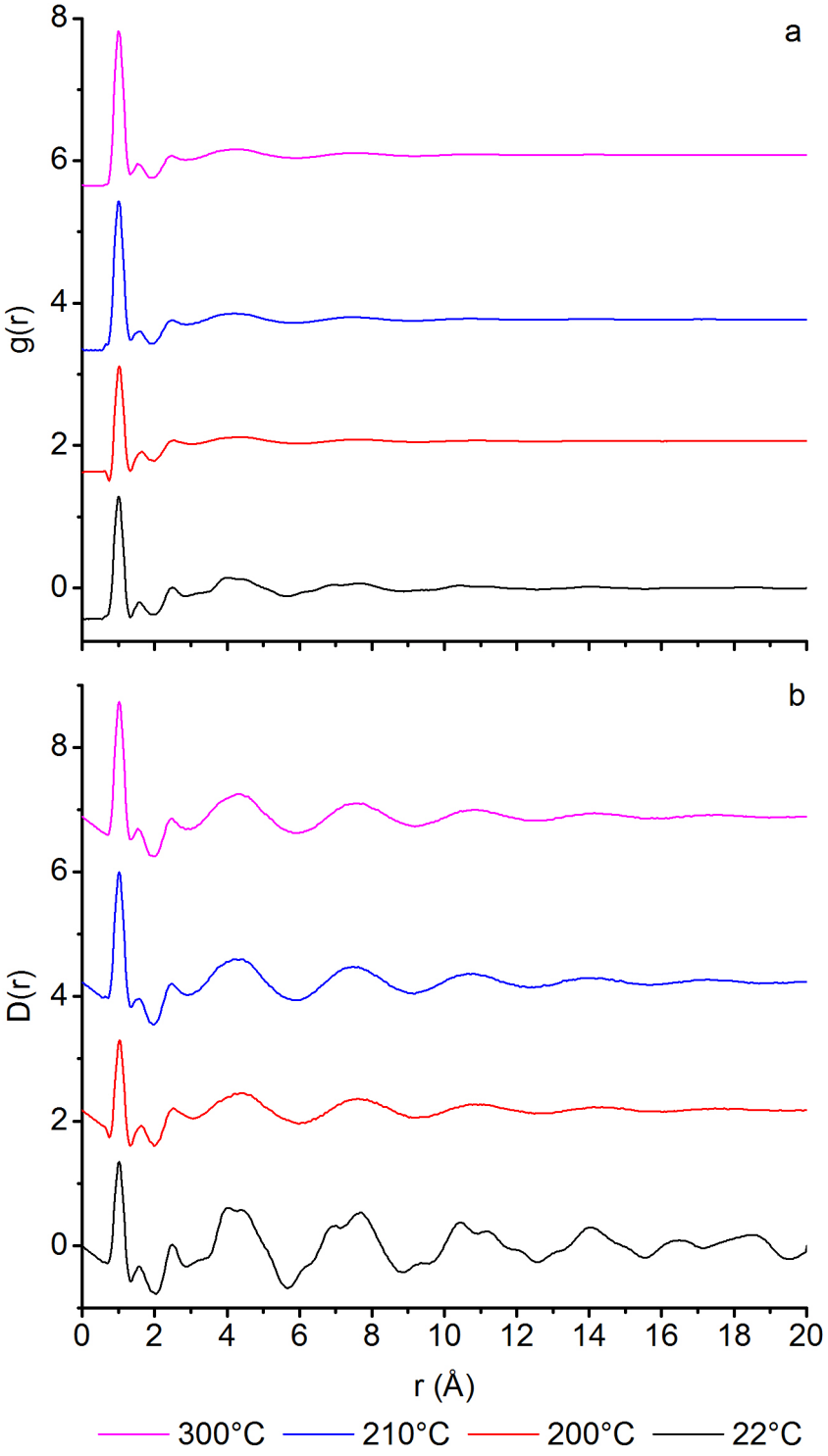

Figure 4.18: The variable temperature a) radial and b) differential distribution functions for deuterated sodium amide, measured by neutron total scattering.

4.4 Conclusions and Future Work

This Chapter has investigated the properties and reactions of lithium and sodium amide, and has utilised a combination of gravimetric analysis, X-ray and neutron scattering, and Raman spectroscopy to gain an insight into these systems. The additional value from the combination of gravimetric and diffraction analysis using the IGA^n, and the complementary nature of neutron and X-ray measurements have been clearly demonstrated.

Examination of the thermal decomposition of lithium amide showed that the formation of non-stoichiometric intermediates is an intrinsic property of the interconversion of lithium amide and lithium imide. Conversely, the production of lithium amide from the reaction of lithium hydride and ammonia showed no evidence for the bulk formation of non-stoichiometric phases.

Raman spectroscopy of mixed isotope reactions of lithium and sodium hydride with ammonia gave preliminary indications that the reactions progressed via the formation of an activated complex which emits a random selection of two of the hydrogen atoms present as a hydrogen molecule. Further investigations as to the role of reabsorption of emitted gas species are required to give a clearer picture of the mechanism of this reaction.

The investigation of the synthesis of sodium amide highlighted unusual dynamics in the b lattice parameter, showing significant incompressibility and a switch from positive to negative thermal expansion observed above 120 °C. This behaviour was reproduced in a simple NPD heating study of sodium amide. The generation of a phonon density of states based on the refined crystal structure of sodium amide would allow for the origins of this lattice behaviour to be established.

Refinement of the diffraction data from this study indicated a substantial degree of libration of the amide anion was present, even close to room temperature. This was corroborated by neutron total scattering measurements, which indicated a significant degree of long-range disorder of the amide units. Variable-temperature measurements showed that this disorder increased markedly as the melting point of the amide was approached. Complementary X-ray total scattering measurements revealed that the sodium and nitrogen lattice within sodium amide have significantly greater degree of long-range order than the amide units.

There is scope to expand upon these total scattering measurements. Low temperature measurements would allow for the ordered structure of sodium amide to be studied. Modelling

of this structure through techniques such as Empirical Potential Structure Refinement (EPSR) [236] could be used as a starting point for an analysis of the evolution of the disorder in the structure with increasing temperature, through to the liquid phase. This study would benefit from the collection of more variable-temperature data in order to probe the fascinating structural properties of this material.

Chapter 5

Metal amides and imides for ammonia decomposition

5.1 Overview and Experimental

Ammonia has long been dismissed as a potential hydrogen store because of concerns over its safety and the difficulties associated with the release of its stored hydrogen. In this Chapter, a new method for the decomposition of ammonia into hydrogen and nitrogen is introduced, based on the formation and decomposition of sodium amide. This method is a significant departure from traditional ammonia decomposition catalysis using rare earth metals, and invites reconsideration of ammonia as a hydrogen vector, or, indeed, a fuel in its own right. From this initial observation, the ammonia decomposition efficiencies of other Group I metal amides are reported, showing that even imide-forming amides such as lithium amide have good ammonia decomposition activity.

Ammonia conversion efficiencies of the materials reported in this Chapter were analysed by loading 0.5 g of the catalyst powder into a 46.9 cm^3 stainless steel reactor reactor, attached to the Quantitative Gas Analyser as described in Section 2.6. For experiments where silica/alumina-supported nickel or alumina-supported ruthenium was used, 0.5 g of catalyst was placed into the reactor after having been lightly ground to remove any agglomeration. The reactor was then sealed and transferred to a vertical tube furnace (Severn Thermal Solutions) and connected to the gas control panel. The panel was first flushed with argon, then evacuated up to the reactor, before flushing the panel and reactor with ammonia prior to heating. Typical experimental

programmes comprised varying the ammonia inlet flow at a given temperature or varying the temperature at a given ammonia inlet flow. For the silica/alumina-supported nickel and alumina-supported ruthenium experiments, the catalyst was first reduced under flowing ammonia for 5 hours at 680 °C. The mass spectrometer monitored the gas species coming off the reactor.

Samples of sodium amide, silica/alumina-supported nickel and alumina-supported ruthenium were used as received. Potassium amide was prepared by the reaction of potassium hydride with 1 bar of ammonia at 180 °C using the IGA^{n} or flowing gas setup as described in Section 2.2.1. Lithium magnesium imide and lithium calcium imide were prepared by ball-milling the mixture of lithium amide and the appropriate hydride (magnesium hydride or calcium hydride) for 4 hours at 400 rpm, followed by heating in an alumina crucible under flowing argon to 350 °C at 2 °C min^{-1} for 12 hours.

Post-reaction samples from sodium amide ammonia decomposition experiments were analysed using the POLARIS diffractometer at ISIS. The samples (~50 mg) were placed into 2 mm quartz capillaries, sealed with epoxy resin. Due to the small sample size and the fact that these samples were not deuterated, diffraction data on these samples were collected for four hours each.

The other POLARIS data presented in this thesis is an *in situ* NPD study of ammonia decomposition by lithium amide-lithium imide. Deuterated lithium amide was prepared by the reaction of deuterated ammonia with lithium nitride (Table 2.2), and then converted into deuterated lithium imide via reaction with lithium nitride (Table 2.3), with the final sample purity assessed as greater than 90 % by PXRD. Two variations of this experiment were carried out, using slightly different sample environments. In the first experiment, a 10 mm i.d. cylindrical stainless steel flow-through cell was chosen in order to maximise exposure of the ammonia gas to the powder sample. Approximately 2.5 g of deuterated lithium imide was held in the cell using porous stainless steel frits at the the top and bottom of the cell. Gas flow was directed in the bottom of the cell and flowed out of the top. This setup was adequate for flowing under argon, but during ammonia flow, problems were encountered with blockage of the cell. For this reason, a new cell was commissioned with the same dimensions as the first, but with the bottom of the cell having a solid seal. The gas flow setup was altered such that the gas flowed into the sample cell via a pipe which extended 10 mm down from the top of the cell into the cell volume, and out through a hole in the top of the cell. This minimised the potential for a

blockage of the cell, and allowed the collection of data under flowing ammonia. The cells were sealed using gold O-rings, and filled with sample in an argon-filled glove bag. In both cases, the cell was encased in a boron-nitride collimation shell, with extra gadolinium shielding. This setup removes the diffraction intensity from the stainless steel sample cell, but restricts the data collection to detector bank 4 of the instrument (~90°). For this study, these data were sufficient for a full analysis of the sample.

Once loaded, the sample was attached to the gas delivery panel described in Section 2.6, equipped with gas suppplies of argon, ammonia and deuterated ammonia. The outgas from the sample cell was monitored by mass spectrometry using the Quantitative Gas Analyser, again described in Section 2.6. The m/z values which were monitored were m/z = 2 (H_2), 3 (HD), 4 (D_2), 17 (NH_3), 18 (NH_2D), 19 (ND_2H), 20 (ND_3), 28 (N_2), 32 (O_2) and 40 (Ar). The gas line was evacuated up to the sample, filled with argon and then leak tested. Once tested, the sample was placed into the diffractometer, and collection of NPD data was initiated. The sample was measured for 75 minutes at room temperature under flowing argon (20 sccm). The sample was then heated under flowing argon first to 300 °C (2 °C min^{-1}), then to 500 °C. After stabilising at that temperature for approximately 30 minutes, the flow was then switched to deuterated ammonia at various flow rates and two temperatures (500 and 550 °C), and finally the sample was exposed to ammonia at 550 °C. The experimental conditions were also replicated using an empty cell to assess the background ammonia decomposition levels.

5.2 Sodium amide

While the use of the Li-N-H system as a hydrogen store has merit because of its highly reversible nature, the slow kinetics of its hydrogenation and dehydrogenation inhibit its applicability for use in transportation. The most demanding kinetics are those of hydrogenation; refuelling times which are of the order of a few minutes are required of hydrogen stores in order to remain consistent with the current refuelling paradigm[1]. The fast kinetics associated with the formation of the alkali metal amides from the reaction of their respective hydrides with ammonia leads to the concept of an improved method of solid-state hydrogen storage and release system using light

[1] It is worth noting here the different standard to which electric vehicles are held to, where hours-long recharging times are acceptable. This is probably due to the the greater flexibility of when and where recharging can occur.

metal amides whereby the refuelling process was achieved using ammonia, and then hydrogen was delivered via decomposition of the amide. However, the development of such a system using the Li-N-H system seems unlikely. While the spent store (as lithium imide) could be regenerated to lithium amide using ammonia, some means of introducing lithium hydride and creating an intimate mixture of the two materials on-board in order to produce hydrogen rather than ammonia would then be required. This seems highly impractical.

However, other alkali metal amides may be more promising candidates for this proposed system. Although extensively used as a reagent in a variety of synthesis processes[237], sodium amide ($NaNH_2$) has attracted only passing interest from the hydrogen storage community[78, 122, 238, 239]. Its low melting-point and high chemical reactivity make the conventional thermal analysis methods challenging. Moreover, its modest hydrogen capacity and high decomposition enthalpy ($\Delta H = 123.8\,kJ\ mol^{-1}$) suggest, on initial consideration, that sodium amide is an unattractive hydrogen storage candidate. However, as first observed by Titherley in 1894 and confirmed in 1937 by Sakurazawa and Hara, sodium amide decomposes on heating into its constituent elements: sodium, nitrogen gas and hydrogen gas[240, 241] (Equation 5.1). The formation of two gases results in an unusually large entropy change, $\Delta S = 200.9\ J\ K^{-1}\,mol^{-1}$, that leads to a modest theoretical decomposition temperature of 343 °C. Therefore, sodium amide should fulfil the requirements of the fast-refuelling system described above, with the regeneration of the sodium amide via reaction of sodium metal with ammonia (Equation 5.2).

$$NaNH_2 \rightarrow Na + \frac{1}{2}N_2 + H_2 \tag{5.1}$$

$$Na + NH_3 \rightarrow NaNH_2 + \frac{1}{2}H_2 \tag{5.2}$$

The extra hydrogen released during the formation of the amide results in a combined hydrogen storage capacity of 7.5 wt%, which is in excess of that of the Li-N-H system. This is an attractive prospect for vehicular hydrogen storage. However, the true potential of this system comes from looking at the net reaction of Equations 5.1 and 5.2: run concurrently, these two reactions should effect the chemical decomposition of ammonia by cycling between sodium amide and sodium metal (Equation 5.3). In 1894, Titherley noted this property in passing, stating that *"an*

interesting result is obtained on heating sodamide to dull redness... through which a current of ammonia is passing; the latter is continuously decomposed into its elements". Remarkably, this reaction has not been studied further, nor its use and application examined since.

$$2NH_3 \rightarrow N_2 + 3H_2 \tag{5.3}$$

It seems clear that the sodium amide should act as a catalyst for ammonia decomposition. In this circumstance, the hydrogen storage content of the amide is irrelevant. Ammonia is the hydrogen vector, and so the hydrogen density (17.8 wt%, 121 kg H_2 m^{-3} in liquid ammonia) is significantly higher than any of the light metal amides, and higher even than most of the borohydrides and amidoboranes examined for hydrogen storage. The use of ammonia also eliminates the need to consider the engineering difficulty of heat dissipation during the hydrogenation of the metal hydride material, since the ammonia would be synthesised externally.

Initially, the reactions described in Equations 5.1 and 5.2 were performed in isolation. QGA data for a) the decomposition of sodium amide under flowing argon and b) the reaction of sodium with flowing ammonia gas are shown in Figure 5.1. It can be seen that the decomposition of sodium amide to nitrogen and hydrogen occurs from 440 °C; the hydrogen and nitrogen occur in an approximate ratio of 2:1, as expected from Equation 5.1. Interestingly, nitrogen gas release occurs at 150 °C, which has not been reported previously. Since the total decomposition of the amide is observed at higher temperatures, there is no obvious process which would result in the loss of nitrogen from sodium amide. Thus, it is proposed that the nitrogen evolution observed at lower temperatures is the release of occluded nitrogen remnant from the commercial synthesis of the sodium amide. This analysis is supported by the fact that when sodium amide is decomposed, reformed *in situ* under ammonia (no nitrogen gas present), and then heated again, it does not show this nitrogen release feature. Sodium metal is the only product observed at the end of this reaction.

The formation of sodium amide from the reaction of sodium metal with ammonia proceeds as expected from Equation 5.2, with hydrogen release observed from 200 °C. In this setup, it appears that the sodium must be significantly above its melting point in order to break through the surface amide layer and expose fresh sodium metal for reaction. There is clearly a significant kinetic barrier to the reaction of a lump of solid sodium and gaseous ammonia, since the reaction

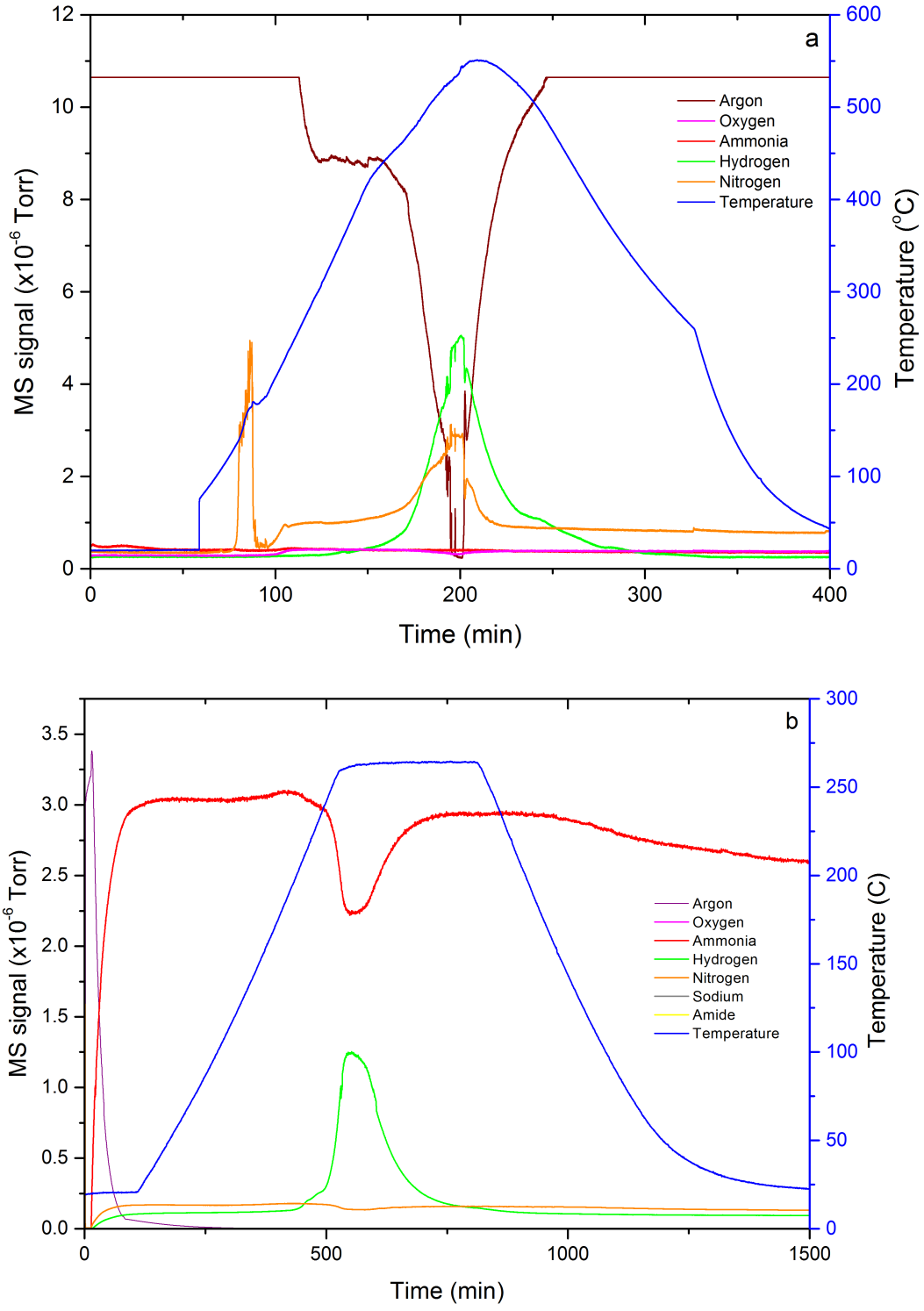

Figure 5.1: QGA data for a) the decomposition of sodium amide under flowing argon and b) the reaction of sodium with flowing ammonia gas in a stainless steel reactor. The temperature of the reactor is also indicated.

is performed on a large scale commercially by the decomposition of a sodium-ammonia solution at -33 °C. However, post-reaction analysis by PXRD showed sodium amide as the only crystalline phase present.

Having confirmed the individual reactions, running the reactions concurrently to effect ammonia decomposition was tested under flowing ammonia gas (20–60 sccm), using both sodium amide and sodium metal as initial reactants (Figure 5.2, panels a and b, respectively), with the outgas examined using QGA. The low-temperature behaviour shown in Figure 5.1 is also observed in this experiment: the sodium amide sample releases nitrogen at 155 °C, while a peak in the hydrogen signal is observed for the sodium sample at 330 °C, which is indicative of the formation of sodium amide. For both samples, at temperatures above 360 °C, appreciable decomposition of ammonia is observed.

Figure 5.3 shows the ammonia conversion percentage calculated from the QGA data for the experiments in Figure 5.2a and b, along with a similar experiment performed with a blank reactor. These data show that the extent of decomposition increases with increasing temperature and decreasing ammonia flow rate, as the rate of reaction and time in the reaction zone increase, respectively. The level of ammonia decomposition is also significantly in excess of that observed for the blank reactor. This is strong evidence for the catalytic effect of the sodium/sodium amide on the ammonia decomposition reaction as outlined above. The fact that the number of moles of ammonia decomposed in these experiments was over 100 times the number of moles of sodium amide, excludes the possibility of some other stoichiometric reaction as the source of the nitrogen and hydrogen produced.

Figure 5.2c and d show post-reaction NPD patterns collected using the POLARIS instrument. Rietveld analysis of these data found sodium amide as the major crystalline component in both samples, with a small amount of sodium (~12 wt%) detected in the sample originally present as sodium amide. The use of NPD also enables the stoichiometry of each amide sample to be evaluated, as although non-stoichiometry is not expected in sodium amide since it cannot form an imide, non-stoichiometric species have been shown to be an integral part of ammonia-mediated processes in the Li-N-H system, and so were deemed worthy of investigation. Rietveld analysis of the sodium amide phase in each neutron diffraction pattern returned hydrogen site occupancies of 0.99(4) for the sodium amide sample and 1.00(3) for the sodium sample, indicating that the

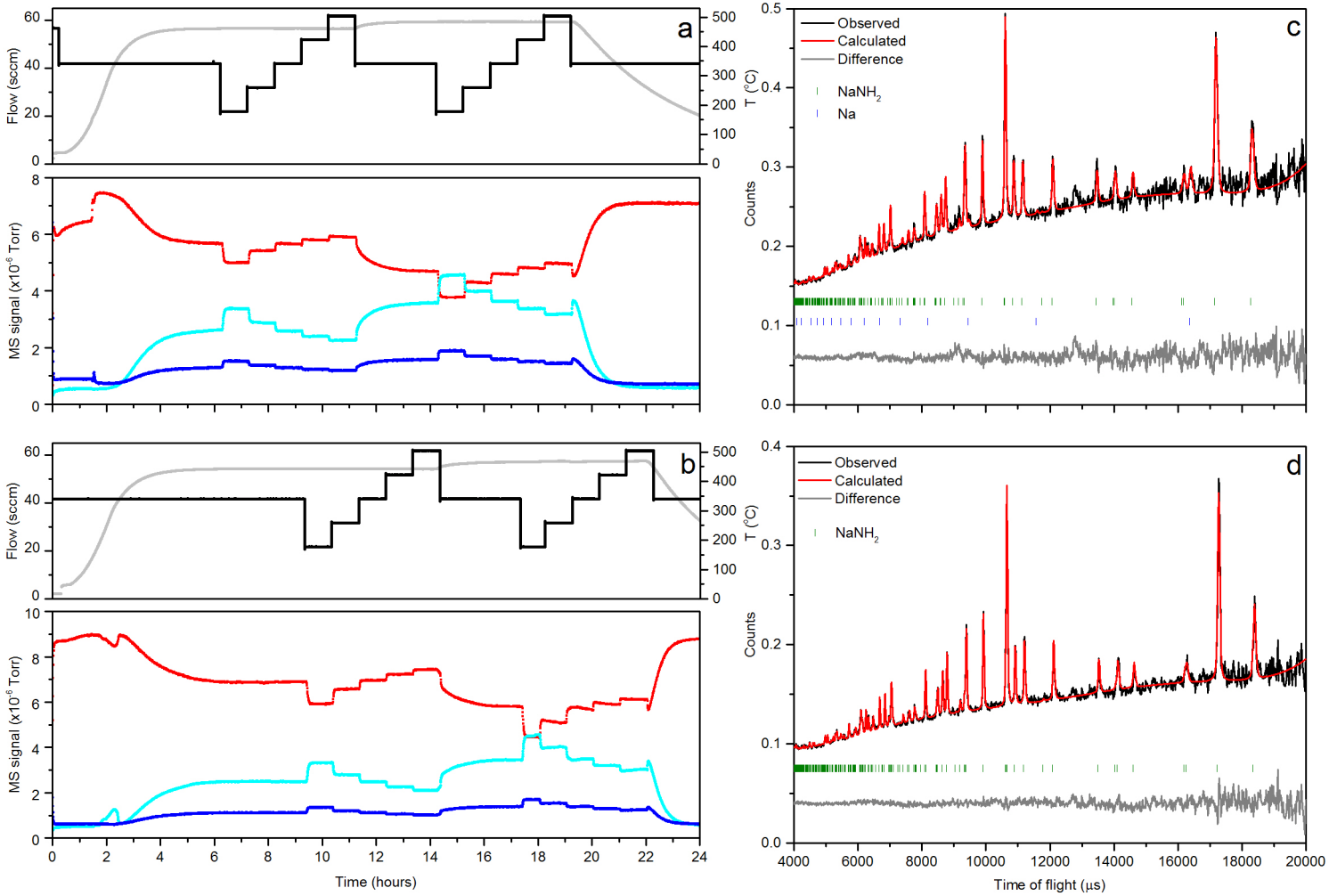

Figure 5.2: Ammonia decomposition reaction mass spectrometry traces for ammonia (red, m/z = 17), hydrogen (cyan, m/z = 2) and nitrogen (blue, m/z = 28) for the reaction of (a) 0.25 g of $NaNH_2$ and (b) 0.15 g of Na. The temperature (light grey) and ammonia flow rate (dark grey) during the experiment at atmospheric pressure are indicated in the top panels for each reaction. Neutron diffraction data, collected on post reaction material, for equivalent experiments based upon (c) 1.0 g $NaNH_2$ and (d) 0.6 g Na. The Rwp values for the fits to the data were 1.846 and 1.889, respectively. Adapted with permission from [206]. Copyright 2014 American Chemical Society.

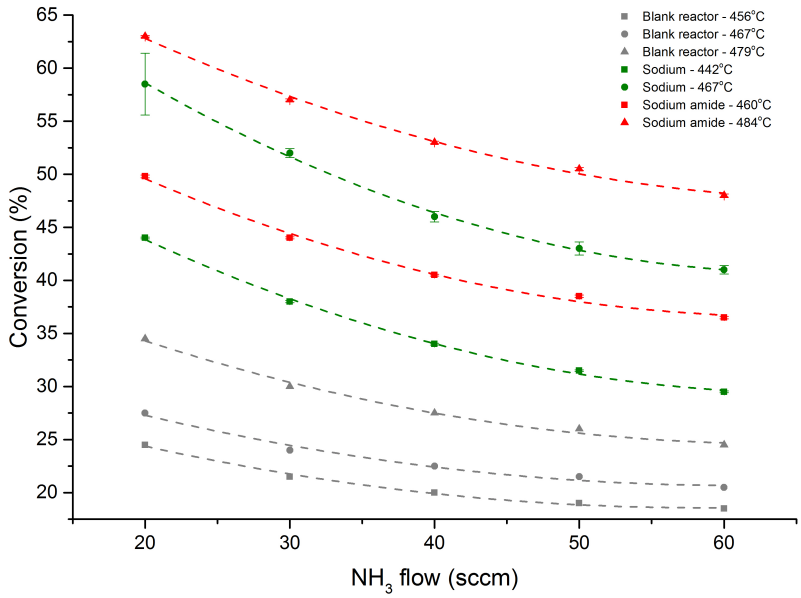

Figure 5.3: Variable flow rate ammonia decomposition efficiency (%) for the blank reactor (grey), the sodium metal (green) and sodium amide (red) at various temperatures. The shapes of the data point markers indicate the most appropriate temperature comparisons between the samples. The data are fitted to quadratic functions as a guide to the eye. These data were collected by Dr Sam Callear.

amide is indeed stoichiometric. Therefore it is reasonable to conclude from these results that the reaction scheme outlined in Equations 5.1 and 5.2 is a good description for the catalytic activity of sodium/sodium amide under flowing ammonia. This catalytic cycle is summarised in Figure 5.4.

Of course, post-reaction analysis does not necessarily indicate which species are present during the reaction. During heating, the QGA data indicate that the sodium sample forms sodium amide, and the sodium amide sample does not change other than the release of nitrogen at 155 °C. Given that the diffraction data indicate that the samples both end up as sodium amide post-reaction, and there is no obvious hydrogen peak or increase in the hydrogen to nitrogen ratio upon cooling or during the reaction, as would result from the conversion of sodium back to sodium amide (see Equation 5.2), it is likely that sodium amide is the dominant species present in the reactor at the temperatures of the experiments shown in Figure 5.2, with sodium produced as a transient, highly reactive species. This analysis is consistent with the endothermic amide decomposition reaction being the slower reaction (ammonia decomposition is not observed until this decomposition is favourable). Of course, as the reaction temperature is increased, the sample mixture would be expected to shift towards a greater proportion of sodium in the sample.

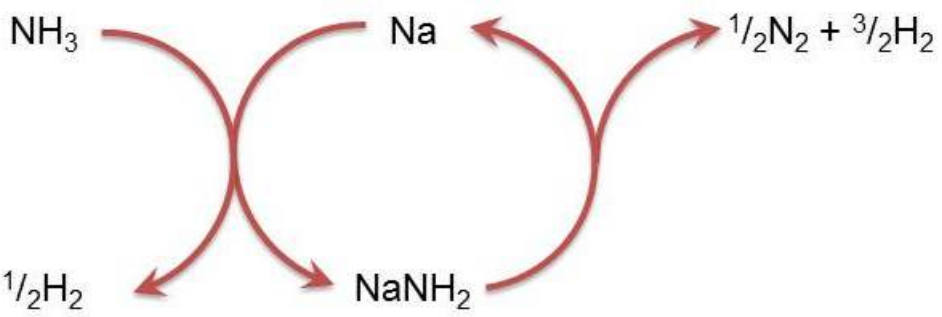

Figure 5.4: A catalytic cycle for the decomposition of ammonia by the formation and decomposition of sodium amide.

These experimental results suggest that the catalytic decomposition of ammonia by sodium amide is a clear departure from traditional surface catalysis methods. The activity of transition metals in heterogeneous catalysis is usually rationalised in terms of the ability of the metal centres to accept electron density from the gas molecules via their vacant or partially vacant d-orbitals. Sodium does not have access to d-orbitals, and so cannot function in this way. Alkali metal salts (usually nitrates, although at the reaction temperatures, either the oxide or hydroxide is the most likely species present) have been added to metal catalysts as so-called promoter species for ammonia formation and decomposition, and are very effective in this role[178, 181–189, 242]. However, the understanding of the mechanism for their effect is less clear. It has been postulated that they donate electron density to the active metal centre, which has the result of improving nitrogen desorption properties of the catalyst[181]. This appears to be very different to the action of sodium amide in this work.

The discovery of the ability of sodium amide to decompose ammonia in this way is of significant scientific interest. However, a number of ammonia decomposition catalysts are already well-known[171]. If sodium amide is to renew serious consideration of the use of ammonia for hydrogen delivery, then it must have high catalytic activity when compared with these materials. In order to determine the level of activity, a 0.5 g sample of sodium amide was heated under 60 sccm of ammonia, with similar experiments were conducted with equivalent masses of slilica/alumina-supported nickel and alumina-supported ruthenium catalysts. These results are shown in Figure 5.5. 90 % ammonia decomposition efficiency is observed at 500 °C using sodium amide, relative to 82 % and 58 % conversion at this temperature using the ruthenium and nickel catalysts respectively. Under the conditions of these experiments, the supported nickel catalyst

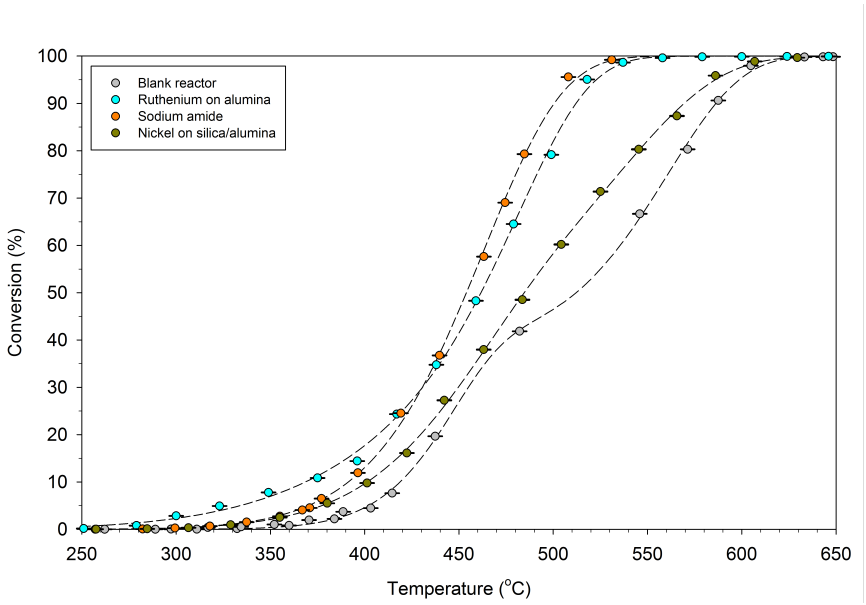

Figure 5.5: Comparison of ammonia conversion as a function of reaction temperature (between 250 °C and 650 °C) for the blank 46.9 cm^3 stainless steel reactor and when containing 0.5 g of $NaNH_2$, silica/alumina-supported nickel, and alumina-supported ruthenium, at an ammonia flow rate of 60 sccm. Error bars are generally smaller than the data points. Adapted with permission from [206]. Copyright 2014 American Chemical Society.

offers only marginal improvement over the performance of the blank stainless steel reactor. Indeed, the use of nickel is generally confined to high temperature (~900 °C) production of reducing atmospheres for metal heat treatment. Ruthenium is generally accepted to be the most active catalyst for the decomposition of ammonia. The variable-temperature decomposition efficiency of sodium amide is similar to that of the supported ruthenium catalyst, with superior performance at high conversion values, while the ruthenium catalyst is more active at lower temperatures.

The fits to the data shown in Figure 5.5 were obtained using a least-squares algorithm, which was used to optimise the parameters of single or bi-sigmoidal functions, corresponding to single process (Equation 5.4) and dual-process (Equation 5.5) reactions, respectively. The sigmoids relate the ammonia conversion efficiency (C) to the temperature (T, Kelvin) using a pre-exponential factor (A), an activation energy (E_a), and the universal gas constant (R). For the dual-process equation, a single parameter (α) is used to modifiy the magnitude of each of the processes. The values obtained for each of the curves are shown in Table 5.1. As can be seen, all of the curves, except that of sodium amide, are fit best by the dual-process function. The activation energies obtained from this fitting process are not dissimilar to those reported for similar catalysts in the literature, although there is a significant spread in the reported

values[243].

$$C = 1 - \exp\left[-\exp\left(\frac{A}{R} - \frac{E_a}{RT}\right)\right] \tag{5.4}$$

$$C = 1 - \alpha \exp\left[-\exp\left(\frac{A_1}{R} - \frac{E_{a1}}{RT}\right)\right] - (1-\alpha)\exp\left[-\exp\left(\frac{A_2}{R} - \frac{E_{a2}}{RT}\right)\right] \tag{5.5}$$

This way of obtaining the activation energy fits the conversion data directly, rather than using traditional Arrhenius plots, which plot the natural logarithm of the rate constant against the inverse of the temperature. For completeness, these plots are given in Figure 5.6. Not all of the conversion data were used to generate these plots, as the low- and high-conversion data points often did not follow the linear trend expected from the Arrhenius relationship. This is most likely due to the nature of the experimental data used to construct these plots. The Arrhenius equation relates the rate constant to the temperature. There are two sources of uncertainty in constructing Arrhenius plots from these experimental data. Firstly, the reaction rate is used rather than a rate constant, since the rate law is not currently known. This is sufficient if the rate law only depends on the partial pressure of ammonia. If the rate law depends on the concentrations of either of the products, then the fact that the use of the reaction rate rather than the rate constant does not account for these species will be problematic. Secondly, these rates are calculated from the conversion values and the ammonia flow rate, reflecting the average reaction rate. The actual profile of the ammonia conversion through the reactor hot zone is not measured directly. The result of this is that the rates measured at low and high conversion are likely to be subject to significant levels of uncertainty. Furthermore, those values are much more susceptible to the corrections made to the data for background levels, and so it is difficult to be confident in the the reaction rates determined in these regions. Therefore, the temperature range which encompasses the mid-range conversion values was used to generate Arrhenius plots. In these regions, linear Arrhenius behaviour is observed for each sample, and, as mentioned, the values for the activation energies correlate reasonably well with those extracted from the sigmoidal fits. Clearly, an experimental setup better suited to the collection of these data would be able to clarify these results. The use of higher flows would also help to minimise the error due to taking an average reaction rate. The identification of the number of processes and the

Table 5.1: Fitted parameters and their associated errors for the fitting of variable-temperature ammonia decomposition data of various catalyst species to single- or dual-process sigmoidal curves.

Sample	A_1	E_{a1}	A_2	E_{a2}
Blank reactor	0.25(2)	180(20)	0.20(2)	160(10)
Nickel on silica-alumina	0.15(2)	120(10)	0.20(2)	110(20)
Ruthenium on alumina	0.096(9)	67(10)	0.19(2)	150(10)
Sodium amide	0.16(1)	121(8)	-	-

values of the activation energies for those processes are in reasonable agreement with the values for the sigmoidal fits. Given that those fits account for the entire shape of the curve, they are more likely to give accurate results with these data.

A single decomposition process across the temperature range investigated here is consistent with the depiction of the activity of sodium amide-based ammonia decomposition as occurring by successive stoichiometric reactions with the catalyst, rather than convential surface catalysis. Although there is still a significant amount of debate as to the specifics of the kinetics of ammonia decomposition reactions on metal surfaces, there are numerous reports of discontinuities in the kinetics of the reaction with change in the temperature, including for iron/iron nitrides, nickel and ruthenium[244–248]. While a full discussion of the various kinetic models for ammonia decomposition in these systems would be a significant diversion at this point, it is worth noting that the reasons postulated for these changes in kinetics generally centre upon a variation in the rate determining step of the process from the combinative desorption of nitrogen to the dissociative adsorption of ammonia molecules (ie the breaking of an N–H bond)[244, 245]. For example, Tsai and Weinberg observed an activation energy of 180 kJ mol^{-1} at temperatures below 377 °C, which they associated with nitrogen desorption, and a much smaller activation energy of 28 kJ mol^{-1} above 477 °C, associated with ammonia adsorption[245]. Alternatively, changes in the reaction kinetics have been proposed to be due to hydrogen inhibition at low temperatures.

It is worth noting that the reactions reported in these previous studies were performed at much lower ammonia pressures, and that the experiments in this work were not specifically designed for kinetic analysis. However, the contrast of the single reaction process observed for sodium amide is perhaps indicative of a significantly different reaction mechanism compared with transition metal catalysts. Of course, the recombinative desorption of nitrogen and/or the

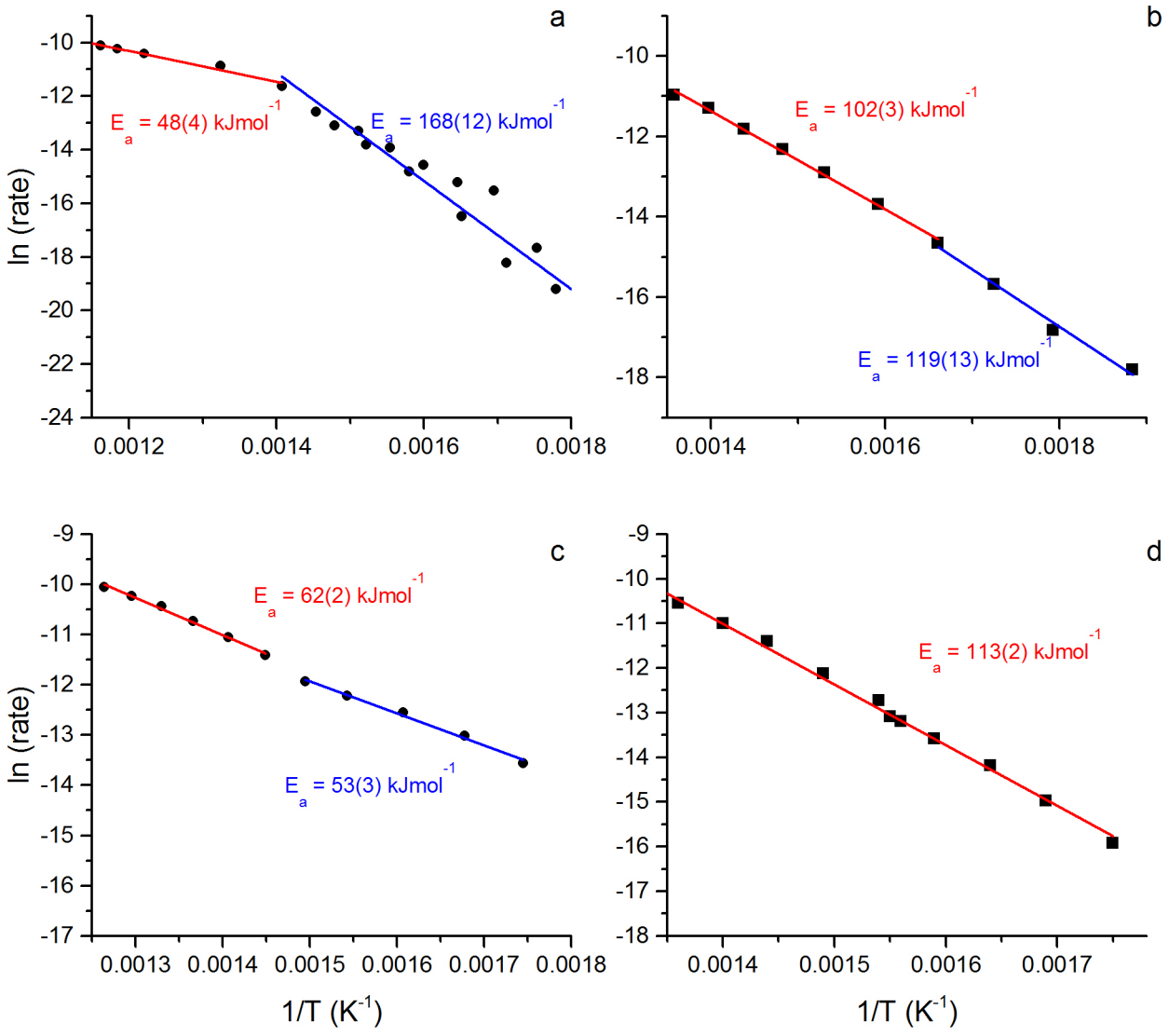

Figure 5.6: Arrhenius plots of the ammonia decompositon reactions of a) the blank reactor b) nickel on silica-alumina c) ruthenium on alumina and d) sodium amide, generated from the data presented in Figure 5.5, with the activation energy extracted for each identified process indicated on the plot.

cleavage of N–H bonds in ammonia (or the amide) may well be the rate determining step/s in the sodium amide process. However, if the rate determining step occurs as a bulk process rather than a surface-mediated one, as is suspected for sodium amide, this could mean that the kinetics are less affected by the occupation of surface sites by nitrogen or hydrogen as described for transition metal catalysts.

Recent catalytic studies have demonstrated that the ruthenium catalysts benefit from the development of more sophisticated supports[165], along with additive materials[185] and improved reactor design[158]. Indeed, the 2004 study by Yin *et al.*[175] of potassium hydroxide-modified ruthenium supported on a magnesia/carbon nanotube composite shows almost 100 % ammonia decomposition efficiency at 500 °C with 0.1 g of sample and an ammonia flow rate of 100 sccm. Nickel-ruthenium composite catalyst systems, which have been scaled up to kW-scale stationary cracking units, show a decomposition efficiency of 99.99 % at 500 °C and 485 sccm of ammonia using 20 g of catalyst in a packed tube reactor[163]. These results are evidently superior to those obtained for ruthenium and sodium amide in this study. However, the comparison in Figure 5.5 highlights the significant potential and impressive performance of sodium amide, with the unmodified powder achieving >90 % conversion at a lower temperature than that of the supported ruthenium catalyst. Given the simplicity of these experiments, there is clearly much scope for optimization of the operating parameters, reactor design and variation in the method of presenting the sodium amide catalyst, and so it is anticipated that sodium amide-based ammonia decomposition could perform as well as the best ruthenium-based catalysts.

One significant drawback in the use of sodium amide as a decomposition catalyst is the difficulty in containing the catalyst at the operating temperature of the reaction. As mentioned previously, sodium amide melts at 210 °C, and at temperatures of high ammonia conversion efficiency (in excess of 450 °C), it appears that the sample is present in the reactor as some form of aerosol. Upon completion of an experiment, recovery of sodium amide from the base of the reactor is generally less than 1 %, with powder found inside the outlet tube and associated pipework. Despite this fact, it is clear that during the reaction, the sample (or at least a fraction of it) is present in the hot zone of the reaction.

The results of a longer-duration ammonia decomposition experiment are shown in Figure 5.7, where the sample was kept at 475 °C for almost 60 hours. No appreciable drop in the ammonia

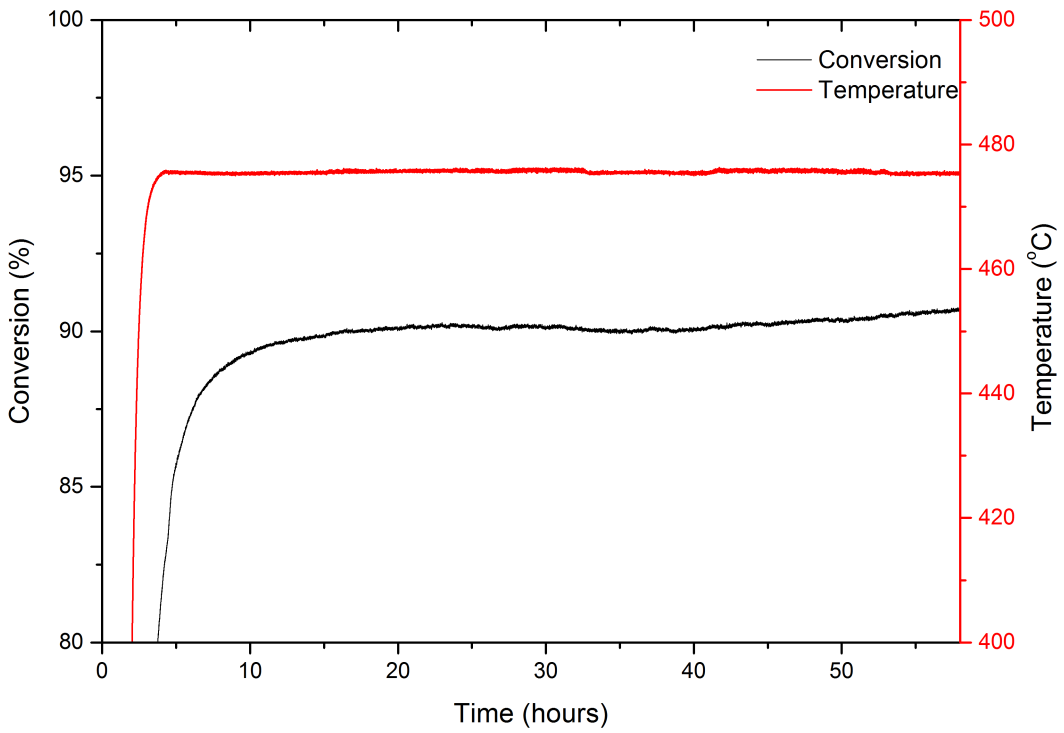

Figure 5.7: Long-duration experiment for 0.5 g sodium amide under 60 sccm of ammonia flow at 475 °C, showing the ammonia conversion efficiency (black) and temperature (red) as a function of time.

conversion efficiency was observed over that time. However, it should be noted that this is a fairly moderate temperature and a very low flow rate compared with what would be required for kW-scale reactors. Experiments at higher flow rates (500 sccm) at the same temperature have shown that sample loss is observed over timescales similar to this long-duration experiment. Even these conditions are some way from the flow rates required for a working system, but it is clear that the poor containment of the sodium amide would not be acceptable for a vehicle which is expected to run for thousands of hours. Without some form of transparent reactor to monitor the behaviour of the sample *in situ*, it is difficult to know exactly what would be the best strategy to contain the amide. It could be that the sample migrates while it is present as sodium, or as the amide. Both sodium (melting point = 98 °C) and sodium amide would be expected to be molten at the temperature of operation, however the vapour pressure of sodium at 520 °C is only 10 mbar[249], so it seems likely that sodium amide is the volatile species, with a boiling point of 400 °C[250]. It seems probable that some kind of reflux environment develops, with the sodium amide volatilising and then condensing at the top of the reactor/in the exhaust pipe where the temperature rapidly drops below the melting point of both sodium and sodium

amide. If this is indeed the case, a different heating design whereby the lower part of the reactor is heated to the reaction temperature, and the upper part is heated to slightly above the melting point of the amide, may help to contain the sample. Altering the temperature that this cooler section is held at might also confirm whether sodium, sodium amide or both species are the cause of the material loss. Containing the sample in a high gas flow is also problematic, and may rely on filters which can block quite easily.

Chemical containment is another potential route which may provide a means of trapping the sodium/sodium amide, whilst also potentially enhancing the activity through a higher surface area and/or favourable interactions with the scaffold. Although sodium amide has been shown to be able to be synthesised in silica gel[251], it reacts with silica when heated to form a mixture of sodium silicides. While this does contain the sodium, it does not allow it to reform the amide, and so the conversion efficiency is not as good. Containment in porous carbon materials has been achieved through various means for the Li-N-H system, resulting in lower decomposition temperatures and altered decomposition pathways compared with the bulk sample[252–254]. Pursuit of these materials for the containment and enhancement of sodium amide may be a productive future research focus.

Despite these challenges, and assuming the conversion levels required for the relevant application can be achieved, sodium amide would not require better or even equivalent performance to a ruthenium-based catalyst to be useful in a practical system. This is due to the fact that sodium is so much more abundant than ruthenium; at current prices, a kilogram of sodium amide costs roughly \$1–5, wheareas ruthenium costs three orders of magnitude more than this. Any progress to improve the kinetics and catalyst containment of the sodium amide process will only serve to improve the comparison with the current systems.

Sodium amide clearly shows significant potential as a new class of catalyst for the effective, efficient and inexpensive decomposition of ammonia into hydrogen and nitrogen. Low temperature fuel cells, either alkaline fuel cells (AFCs) or proton exchange membrane-based (PEM), are well placed to utilize the hydrogen produced. It is worth outlining the challenge of developing these systems for use in transportation. Based on a fuel cell running at 45 % total power efficiency, with an ammonia cracker running at 65 % energy efficiency, the US DoE estimate that a 1 kW fuel cell (scaled down from their estimate for a 100 kW system) requires a 13.5 L min^{-1}

(13500 sccm) hydrogen supply[155]. The highest hydrogen output reported by David *et al* [206] is 475 sccm (63.3 % conversion of a 500 sccm ammonia flow). Therefore, to deliver 13500 sccm of hydrogen, the parallel operation of (13500/475 = 28.4) 29 of the sodium amide ammonia decomposition reactors used in this work would be required. The total volume of 29 reactors would be 29 × 21.3 cm^3 = 618 cm^3. As each reactor contains 0.5 g of sodium amide, 14.5 g of sodium amide would be needed to supply 29 reactors. These extrapolated figures are for 1 kW only, a fuel cell vehicle would require in the region of 35–100 kW of power. At the flow rates reported in this thesis, sodium amide would not yet translate into a workable solution for such a vehicle. However, the potential for the optimisation of the reactor design and the material properties of the amide itself seems to suggest that this is not an unreasonable starting point for the development of a commercial system.

In addition to the practical difficulties of creating a system which can efficiently and effectively process such a high ammonia flow rate, the hydrogen gas stream must be of extremely high purity. PEM fuel cells are highly intolerant to trace levels of >100 ppb ammonia[102] and, therefore, the scale-up described above would further require the reuse or capture of a significant amount of ammonia from the product gas stream. This requirement would hold even for ammonia tolerant fuel cells such as AFCs[162], since the emission of large amounts of ammonia into the atmosphere is not tolerable from a health or environmental perspective. Although solid-state ammonia capture materials which can hold large weight percentages of ammonia are well-known[149, 157, 255], the more desirable scenario would be to increase the efficiency of the sodium amide ammonia conversion in order to reduce the requirements for these clean-up methods.

For a system such as sodium amide, the direct combustion of ammonia is, perhaps, the most attractive short-term option as it removes the need to generate a pure hydrogen stream. As mentioned in Chapter 1, ammonia alone is difficult to ignite, but a 2.5 wt% hydrogen-in-ammonia mixture is sufficient to enable ammonia combustion[159]. Indeed, a recent high-performance car achieved a range of 180 km with a 30 litre ammonia tank[256]. A good estimate of the ammonia flow rate required to drive this car is 3×10^5 sccm. In order to produce a 2.5 wt% hydrogen mixture, approximately 14 % conversion of the ammonia stream is required. If we consider the same sodium amide decomposition reactor (21.3 cm^3 reactor under 500 sccm of ammonia flow) working at 63.3 % conversion efficiency, then diverting 25 % of the total ammonia flow

through this reactor will give 16 % conversion. It follows that if 25 % of the flow required for the sports car is $3 \times 10^5 \times 0.25 = 7.5 \times 10^4$ sccm, then (7.5x10^4/500) 150 of these reactors would need to operate in parallel to achieve 15 % conversion of the total ammonia flow. This would equate to a total reactor volume of 150 $\times$ 21.3 cm^3 = 3195 cm^3. Given each reactor requires 0.5 g of sodium amide, this would require 75 g of the amide in total. Depending on the energy efficiency, a larger proportion of the gas could also flow through reactors operating at lo1wer temperatures. Whatever the precise configuration, these calculations indicate that ammonia-based transportation is achievable. With the levels calculated here, the cost of the sodium amide catalyst would be incidental as a proportion of the cost of the ammonia cracker, let alone the entire system.

5.3 Potassium amide

A logical extension of the activity of sodium amide towards the decomposition of ammonia is that the other alkali metal amides that decompose to the metal, nitrogen and hydrogen should also display ammonia decomposition activity. The amides of potassium, rubidium and caesium are all thought to decompose by this method, although none of these reactions have been studied in any significant detail, in part due to their chemical reactivity (similar to that outlined for sodium amide) and the particularly significant hazards associated with working with rubidium and caesium. Each of these metals is less attractive than sodium in terms of cost and abundance. However, their performance may be instructive in terms of understanding the parameters which might affect the ammonia decomposition efficiency.

The potassium amide ammonia decomposition efficiency was determined using the same method that was described for the sodium amide sample, except that these tests were completed in nickel-coated reactors. Again, 0.5 g samples of each of the catalysts were placed inside the reactor and heated under a constant 60 sccm flow of ammonia, with the ammonia conversion shown in Figure 5.8a. As predicted, the potassium amide also shows appreciable ammonia decomposition efficiency, and is superior to sodium amide across the temperature range investigated. The corresponding Arrhenius plot is shown in Figure 5.8b, and again identifies a single reaction process with an activation energy of 70.6 kJ mol^{-1}, which is significantly lower than that of sodium

amide.

Given what is known about the mechanism of this reaction, the improved performance of the potassium amide relative to sodium amide can be rationalised in terms of the way the amide behaves as it is heated. A comparitive TGA plot for sodium amide and potassium amide is shown in Figure 5.9. As mentioned earlier, the physical properties of the amides make it difficult to perform this analysis reliably, and thus the actual value of the mass loss for each amide is not instructive. The samples migrate out of the bucket, so the mass loss is always higher than would be expected. However, the onset of decomposition can be observed for each sample. It is clear that potassium amide decomposes at a lower temperature than sodium amide, with an onset temperature of around 300 °C compared with 420 °C for sodium amide. Given the apparent likelihood that the decomposition of the amide is the rate-determining reaction, this may explain why potassium amide has faster ammonia decomposition kinetics than sodium amide.

Another potential explanation for the enhanced activity of potassium amide is that the melting point of the potassium amide (330 °C) is higher than sodium amide (210 °C)[100, 229]. This trend is the opposite to what would be expected based purely on the ionic radii; one would expect that the amide with the smaller cation (sodium amide) would have a larger lattice enthalpy due to its higher charge density, and therefore stronger attraction between it and the amide anion. However, this is not the case. There is not a clear explanation for the anomalously low sodium amide melting point — the rest of the melting points of the alkali metal amides are reported to follow the trend predicted by the charge density of the cation[100].

The effect of this difference in melting points may mean that molten potassium amide is less 'mobile' than sodium amide, resulting in a greater proportion of the sample remaining in the hot zone where it can decompose the ammonia. There is some evidence to support this from the potassium amide experiments. Firstly, the TGA trace shows that, prior to the decomposition, the potassium amide mass is much more stable than that of the sodium amide, which slowly decreases prior to the decomposition. Secondly, the recovery of potassium amide post reaction for ammonia decomposition experiments conducted in this work is generally higher than for sodium amide, at around 25 %.

The trends discussed here could be explored more fully by the examination the decomposition and ammonia decomposition behaviour of rubidium and caesium amide. Particularly, it would be

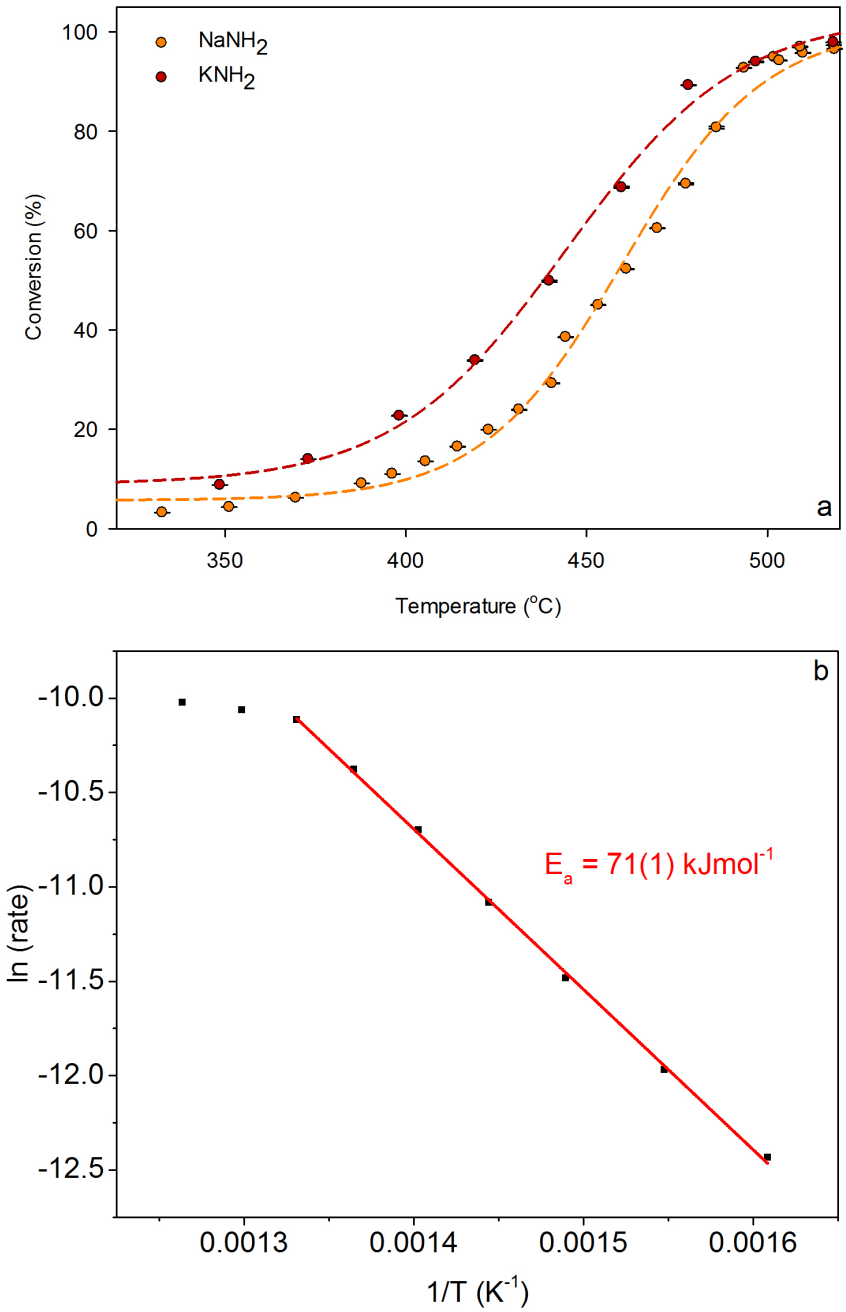

Figure 5.8: a) Comparison of ammonia conversion as a function of reaction temperature (between 250 °C and 520 °C) within a 46.9 cm^3 nickel-coated stainless steel reactor for 0.5 g of KNH_2, and $NaNH_2$ at an ammonia flow rate of 60 sccm and b) the Arrhenius plot for the KNH_2 data, with the activation energy included on the plot. Error bars are generally smaller than the data points.

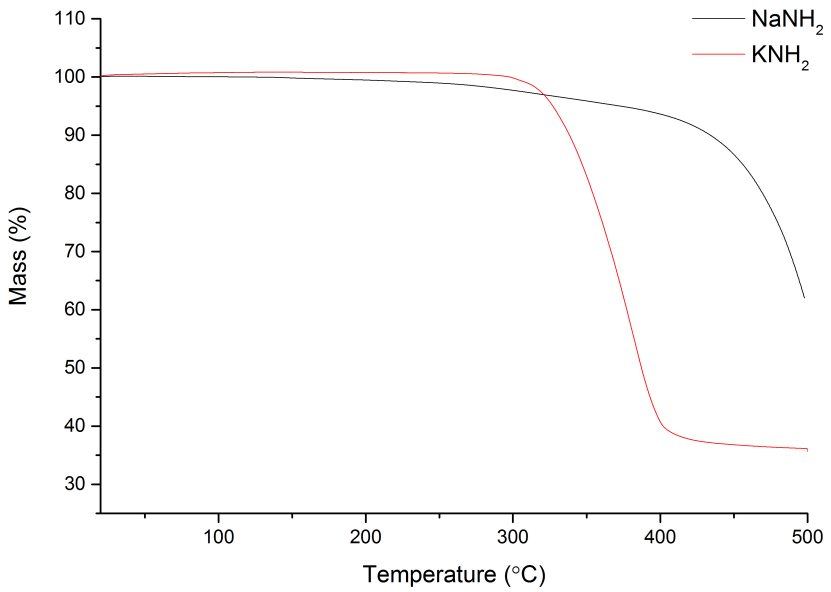

Figure 5.9: TGA data for $NaNH_2$ and KNH_2 collected under flowing argon, with a linear heating rate of 1 °C min^{-1}.

interesting to ascertain whether potassium is the most active of the Group I amides, since it has been found to be the most effective promoter for traditional ammonia decomposition catalysts.

5.4 Lithium amide - imide

The generalised mechanism proposed for the sodium-based system involves the cracking of ammonia through the concurrent decomposition and formation of the amide (MNH_2) from the metal (M), as shown in Equations 5.6 and 5.7. As shown in the previous sections of this Chapter, other alkali metal amides that decompose via a similar mechanism also display appreciable ammonia decomposition activity.

$$MNH_2 \rightarrow M + 0.5N_2 + H_2 \tag{5.6}$$

$$M + NH_3 \rightarrow MNH_2 + 0.5H_2 \tag{5.7}$$

Conversely, amides which form the corresponding imide upon heating would not be expected to show this kind of stoichiometric ammonia decomposition. As discussed earlier, the decomposition of lithium amide is dominated by the formation of lithium imide; as such, it would not be

expected to show appreciable ammonia decomposition according to the mechanism described for the other alkali metal amides. Indeed, its activity was initially tested as a negative control.

The ammonia decomposition activity of lithium amide was examined in an identical manner to that described for the other amides, with ammonia gas flowing over the amide contained within a stainless steel reactor. The variable-temperature ammonia decomposition efficiency of 0.5 g lithium amide compared with an equivalent mass of sodium amide, supported nickel and ruthenium catalysts, and the empty reactor is shown in Figure 5.10a. The ammonia flow rate was constant at 60 sccm for all of the samples. Far from acting as a negative control, lithium amide gives high conversion at moderate temperatures, reaching 90.7 % conversion at 458 °C, compared with 54.9 % for sodium amide, 53.7 % for ruthenium on alumina, and 34.0 % for the blank reactor. Although less active than the supported ruthenium catalyst at low temperatures; lithium amide shows a steeper conversion curve than the other systems in Figure 5.10, which is indicative of a higher activation energy for the reaction. Indeed, the Arrhenius plot for lithium amide (Figure 5.10b) shows that the activation energy for the reaction is 123.4 kJ mol^{-1}, which is significantly larger than the value determined for both sodium amide and potassium amide. The superior performance of lithium amide, however, is a timely reminder that while comparison of activation energies is a useful guide for explaining the kinetic effects of modifications to a particular system, it must be treated carefully as a comparator between systems. Clearly, the characteristics associated with the pre-exponential factor are crucial for determining the performance of a catalyst.

It is apparent that lithium amide has superior ammonia decomposition activity at high conversion rates. The precise mechanism by which it decomposes ammonia is significantly less obvious. Other than the work presented in Chapter 4, the decomposition of lithium amide on its own has received only limited attention to date; its examination has largely been confined to its role in the production of hydrogen in the lithium amide – lithium hydride hydrogen storage system[113, 132, 134, 257, 258]. These studies generally consider the decomposition of lithium amide under an inert atmosphere. Investigation of the behaviour of lithium amide under an ammonia atmosphere is limited to a single study of the thermodynamic parameters of the reaction through the measurement of pressure-composition isotherms[124].

In order to probe the decomposition of lithium amide, TGA experiments were performed

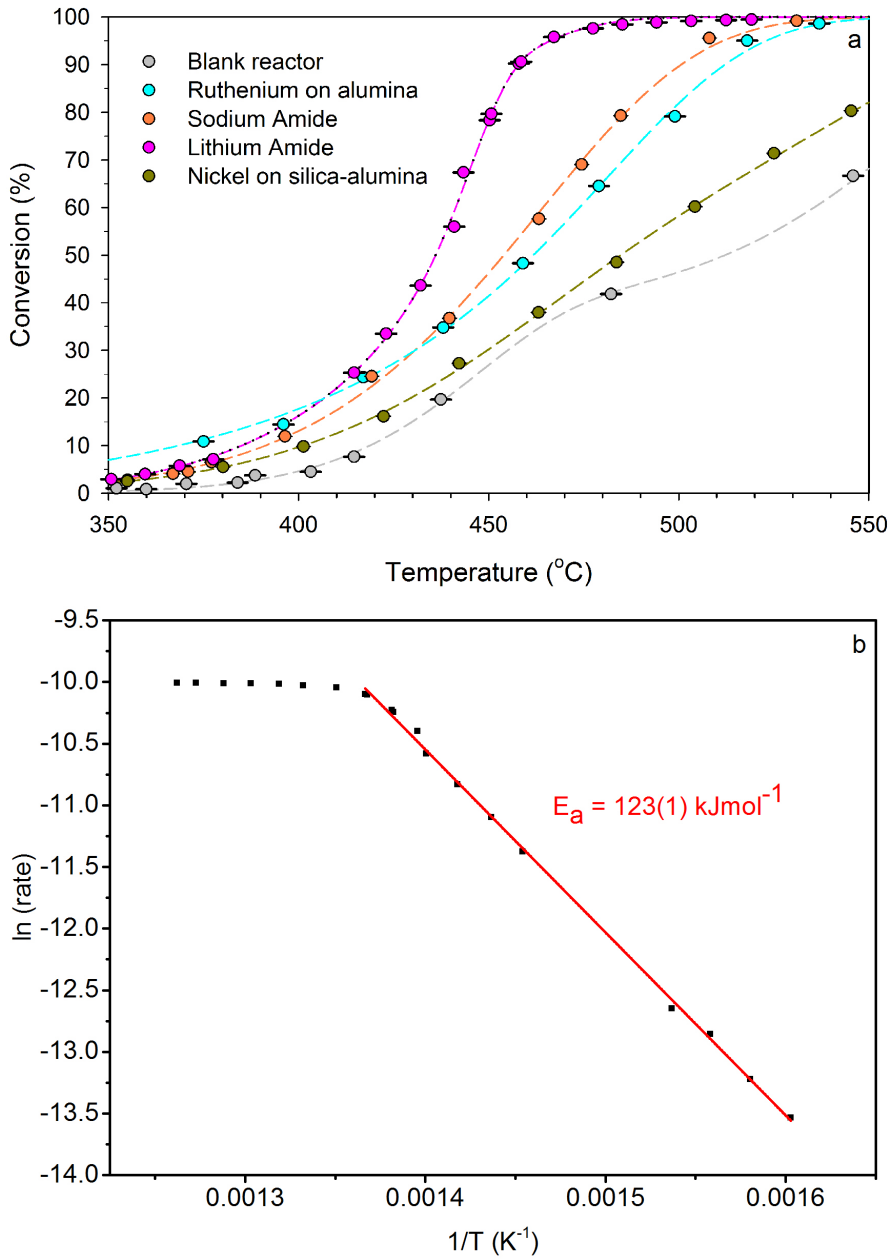

Figure 5.10: a) Comparison of ammonia conversion as a function of reaction temperature (between 350 °C and 550 °C) for the blank 46.9 cm^3 stainless steel reactor and when containing 0.5 g of $LiNH_2$, $NaNH_2$, silica/alumina-supported nickel, and alumina-supported ruthenium, at an ammonia flow rate of 60 sccm, with dashed lines showing sigmoidal fits to the data, and b) the Arrhenius plot for the $LiNH_2$ data, with the activation energy included on the plot. Error bars are generally smaller than the data points.

under 1 bar argon and ammonia atmospheres between 50–450 °C, the results of which are shown in Figure 5.11. The decomposition of lithium amide is delayed under an ammonia atmosphere, as would be expected. Nevertheless, under both argon and ammonia the expected lithium imide product is obtained, as evidenced by the percentage mass loss observed. A comparison of Figures 5.10 and 5.11 indicates that lithium amide will have partially or completely decomposed to lithium imide in the temperature region where it is active in the decomposition of ammonia. Indeed, in the experiments with lithium amide, there is a reproducible peak in the gas outflow data at approximately 460 °C, shown in Figure 5.12. It is difficult to be authoritative about the exact nature of this peak since there is a significant amount of background ammonia signal, and the peak appears in the context of increasing outflow due to higher levels of ammonia decomposition. However, the reproducible temperature of this peak, and the degree to which it correlates with the temperature at which decomposition is expected from the gravimetric data indicates that it may be due to ammonia release from the decomposition of lithium amide. This could be an important factor in determining the feasibility of using alkali metal amides for ammonia decomposition. Lithium amide melts at 360 °C, which, although significantly higher than the melting point of sodium amide (210 °C), does not completely avoid the difficulties that are encountered with the effective containment of the catalyst. However, lithium imide is solid up to the point of its decomposition at around 600 °C[113, 232], and so may prove easier to contain.

Of course, this inference is somewhat simplistic given that, in the TGA experiment, the amount of ammonia present is so far in excess of the lithium amide sample that the decomposition can be reasonably considered to be under an ammonia atmosphere, whereas in the decomposition experiments, the atmosphere around the sample is a variable mixture of ammonia, nitrogen and hydrogen. As such, an *in situ* probe is the most reliable means for determining the active state of the system. Neutron powder diffraction (NPD) measurements of a deuterated lithium imide sample (Li_2ND) were performed using a stainless steel flow-through cell. Although this apparatus is slightly different from that used in the experiments for Figure 5.10, the flow-through setup ensures that the bulk of the sample is exposed to ammonia, such that the data collected should relate to the sample in contact with ammonia.

Figure 5.13 shows a section of the NPD data showing the (111) and (002) reflections of Li_2ND, along with the temperature, gas flow, input gas species and the refined a lattice parameter of

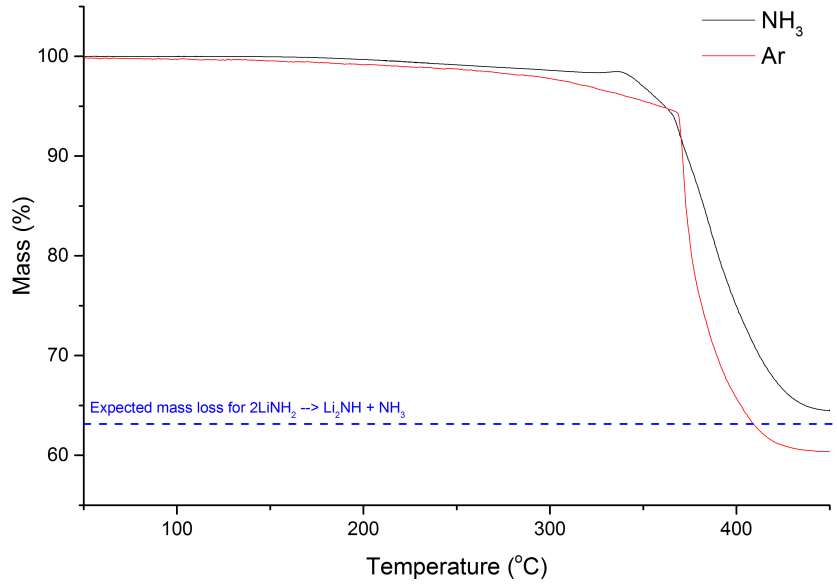

Figure 5.11: TGA data showing the comparison between the decomposition of $LiNH_2$ under ammonia (black) and argon (red). The expected mass loss expected from decomposition to Li_2NH is shown as a dashed blue line.

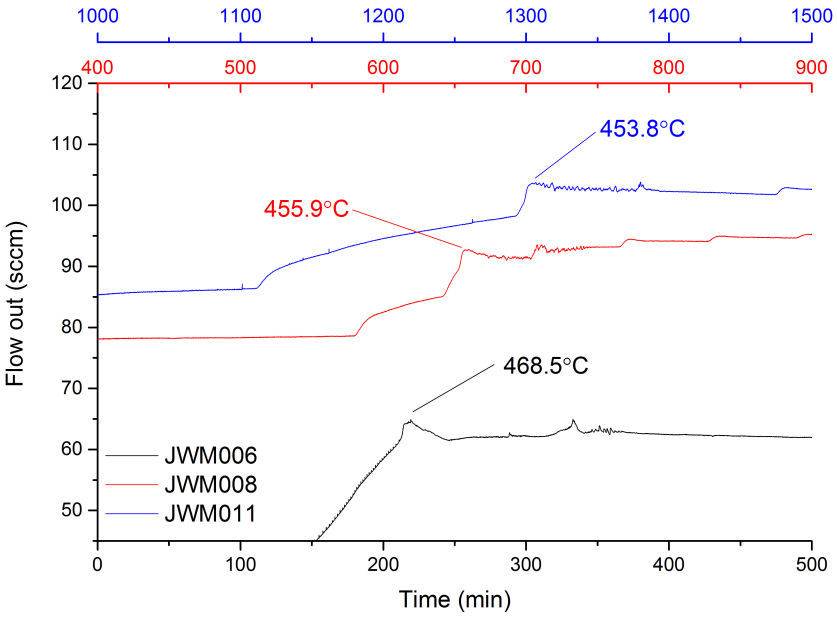

Figure 5.12: Gas out flow data for three ammonia decomposition experiments with 0.5 g of $LiNH_2$ in a 46.9 cm^3 stainless steel reactor, showing peaks in the flow which apppear to be in addition to the expected rise with temperature, and potentially are indicative of decomposition of the amide.

the Li_2ND extracted via a Pawley refinement of the diffraction data[259]. Individual diffraction patterns of the sample at the beginning and end of the experiment showing the observed patterns and the calculated fit to the data are given in Appendix J. The difficulty in attempting to keep the Li_2ND sample solid is that it must be heated under argon to a temperature at which the formation of the amide (which would melt) is unfavourable. As such, the sample was heated to 500 °C under argon, and remained crystalline throughout this heating process.

Upon the introduction of deuterated ammonia, ND_3, at approximately 12 hours, the intensity of the Li_2ND Bragg peaks changes dramatically – firs(one standard deviation)tly the sample appears to melt or amorphise, which is indicative of the formation of amide-like species. The flow-through cell suffered significant blockage at this point. Thus, in the absence of further ND_3 flow, the sample reforms solid Li_2ND, and the Bragg intensity returns. This unblocked the cell, exposing the sample to further ND_3, which causes the sample to melt, and so this cycle of blocking and unblocking was repeated a number of times before it was decided to elevate the temperature of the sample under an argon atmosphere in an effort to reform crystalline Li_2ND and thus unblock the cell. Heating of the sample to 550 °C achieved this goal and the reintroduction of ND_3 23 hours into the experiment did not result in the loss of Bragg peak intensity, nor the blocking of the sample cell. The ammonia decomposition efficiency at 500 °C was approximately 50 %, increasing to 74 % at 550 °C, compared with 23 % and 39 % using the same reaction conditions with the blank sample cell (see Appendix K). Clearly the sample was involved in the enhanced decomposition of the ammonia in this experiment. Interestingly, the efficiencies for both the empty reactor and the catalyst are lower than those presented in Figure 5.10. This may be as a result of the different geometry of the reaction zone and may also be a consequence of the difference in the reaction kinetics moving between NH_3 and ND_3. This effect will be discussed in more detail later.

The lithium amide-imide system is known to form a continuum of non-stoichiometric intermediates ($Li_{1+x}NH_{2-x}$, $0 \leq x \leq 1$) which have the same average cubic structure as high-temperature lithium imide, but with an increased cubic lattice parameter as the stoichiometry approaches that of lithium amide[136, 137]. Therefore, the lattice parameter, displayed in Figure 5.13, is a good guide to the stoichiometry of the sample when measured under isothermal conditions. The variation of the lattice parameter and the temperature for a portion of the experiment is

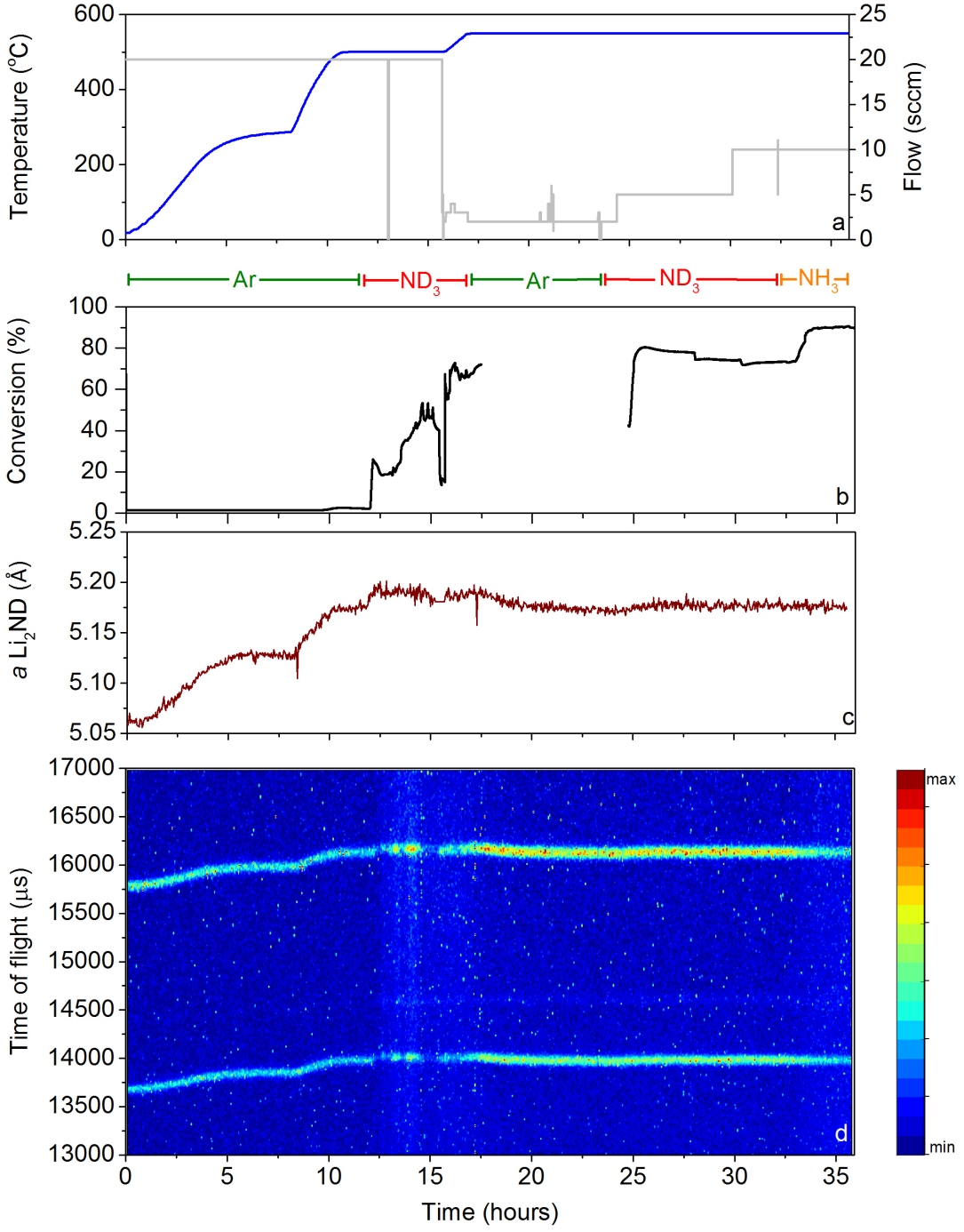

Figure 5.13: Neutron powder diffraction experiment. a) temperature (blue) and gas flow set point (grey), along with the input gas species listed below, b) the ammonia conversion percentage c) *a* lattice parameter from Pawley refinement of NPD data and d) contour plot of the neutron diffraction data showing the (111) and (002) Bragg peaks of Li_2ND. The colour bar to the right gives an indication of the scattering intensity. The error in the lattice parameter is ±0.001Å, while the error in the ammonia conversion is ±0.2%.

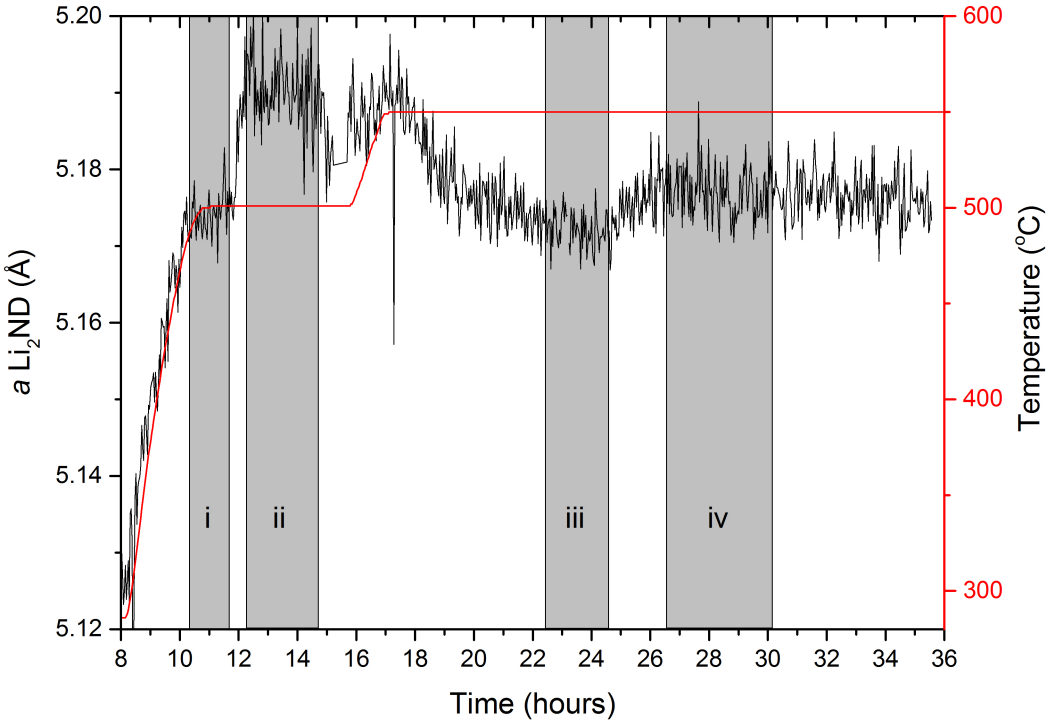

Figure 5.14: Variation of the a lattice parameter of Li_2ND (black) over the course of the experiment. The temperature of the sample (red) is shown for comparison. The shaded regions (i)–(iv) were summed and analysed individually by Rietveld analysis to determine the lattice parameter and sample stoichioimetry more accurately. The error in the lattice parameter is ±0.001Å.

shown in more detail in Figure 5.14. The datasets in the shaded areas (i)–(iv) were summed and analysed by Rietveld refinement to determine more accurately the lattice parameter and stoichiometry of the sample. The results from these refinements are shown in Table 5.2.

The behaviour of the lattice parameter shows that the addition of ND_3, both at 500 °C and 550 °C, results in an increase in the lattice parameter of the Li_2ND. Furthermore, when the sample is exposed to argon from 17–24 hours, the lattice parameter decreases. We postulate that these changes are due to a change in the stoichiometry of the sample as outlined above. In contrast

Table 5.2: Refined values for the lattice constant and average stoichiometry of the Li_2ND sample

Segment	Temp (°C)	Gas	a Li_2ND (Å)	p value / Average Stoichiometry
i	500	Ar	5.174(3)	0.00(3) / $Li_{1.998}ND_{1.002}$
ii	500	ND_3	5.190(5)	0.37(3) / $Li_{1.63}ND_{1.37}$
iii	550	Ar	5.172(2)	0.19(2) / $Li_{1.81}ND_{1.19}$
iv	550	ND_3	5.177(3)	0.24(2) / $Li_{1.76}ND_{1.24}$

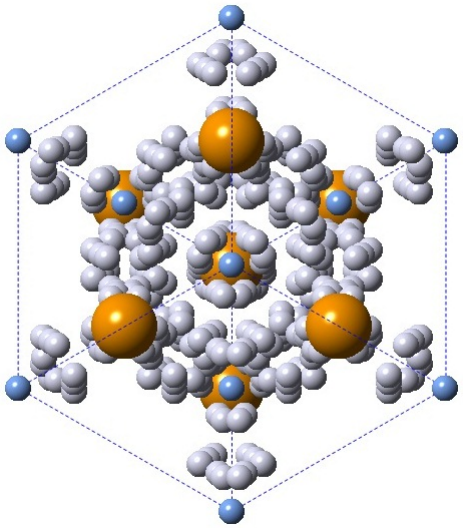

Figure 5.15: Cubic $LiND_2$ structure, orientated along the (111) direction. Lithium ions are shown in orange, nitrogen in blue and deuterium in grey.

to the previous X-ray scattering investigations, where the scattering of the hydrogen atoms could essentially be ignored, the deuterium provides a significant proportion of the scattering in the NPD experiment. This affords the opportunity to determine the stoichiometry of the sample through Rietveld analysis, but also requires a more carefully-constructed analysis to account for the presence of the D atoms. In order to achieve this, the tetragonal $LiND_2$ structure was translated into a cubic anti-fluorite cell (the Li_2ND structure), resulting in a cell with half-occupied lithium sites and D atoms on two disordered sites around the N with gaps along the (111) directions, shown in Figure 5.15.

The translation of the $LiND_2$ structure into the cubic form allowed for the continuum of stoichiometry between Li_2ND and $LiND_2$ to be modelled as a single phase in the Rietveld analysis. The two D sites illustrated in Figure 5.15 were used as the "amide" sites, with the normal single D site for Li_2ND (slightly shorter N–D bond) used as the "imide" site. A single parameter, p ($0 \leq p \leq 1$; 0=Li_2ND, 1=$LiND_2$) was refined to allow variation in the occupancy of these sites between fully-occupied amide D sites and a fully-occupied imide D site. The p value also determined the lithium occupancy in the structure, ranging from full occupancy when p=0 to half-occupied when p=1. In this way, the value of p reflects the average stoichiometry of the sample. The refined p values for the various segments are shown in Table 5.2. Full details of the crystallographic model used are given in Appendix A.

As a check on the stoichiometry value obtained from the Rietveld refinement, the change in the lattice parameter can be compared with the change observed in the previous *in situ* PXRD study on the decomposition of the Li-N-H hydrogen store detailed in Chapter 3. There, the increase in the lattice parameter from lithium imide to lithium amide is approximately 1.5 % at 290 °C. Assuming a linear variation in the lattice parameter with stoichiometry change, the stoichiometry predicted from the magnitude of the changes in the lattice constant mirror those obtained from the Rietveld analysis well, predicting a stoichiometry of $Li_{1.79}ND_{1.21}$ for segment (ii) (i.e a 0.31 % increase in a from segment (i)) and $Li_{1.75}ND_{1.25}$ for segment (iv) (i.e. a 0.097 % increase in a from segment (iii)). Some discrepancy might be expected from this comparison given that the XRD study compared lithium amide and lithium imide rather than their deuterated analogues in this study, and was also examined at a lower temperature. The isotope effect would be expected to be relatively minor, especially given the use of percentage changes in the lattice parameter, and the lattice parameters of both phases change linearly with temperature. The most significant inconsistency between the two methods of determining the stoichiometry arises from comparison of the lattice parameters in segments (i) and (iii). The lattice parameter in segment (iii) is smaller than that in segment (i) despite being at a higher temperature and possessing more amide-like stoichiometry. One hypothesis for the origin of this discrepancy is that because the sample underwent a melting process between 12 and 15 hours, it may have been altered in such a way as to cause the change in the lattice parameter. This hypothesis is supported by the increase in the intensity of the Bragg peaks after 17 hours (i.e. after solidification) compared with the original pattern from the sample as observed in Figure 5.13c.

The stoichiometry values determined from the p value/lattice parameter could simply be indicative of the equilibrium position of the decomposition of lithium amide to lithium imide under the mixed ammonia-hydrogen-nitrogen atmosphere. Alternatively, it may give some insight into the mechanism by which the lithium amide-imide system decomposes ammonia. Comparison of Figures 5.10 and 5.11 indicates that the decomposition of ammonia becomes favourable once lithium amide is no longer stable. Although lithium amide is known to decompose to form lithium imide, there have been recent suggestions (discussed in Chapter 3) that metallic lithium can form in small quantities along the phase space between lithium imide and lithium amide; this was the explanation of the effect of the presence of nitrogen in the hydrogenation gas stream on

the hydrogen storage capacity of the Li-N-H system[143]. If this is the case, and lithium metal is present under the conditions used in this study, then its ammonia decomposition activity could be rationalised in a similar manner to sodium amide, after all, following an analogous mechanism to Equations 5.6 and 5.7.

The validation of these hypotheses requires further experimental evidence. An isotope exchange experiment was conducted between 28 and 36 hours during the NPD experiment, with the flow through the Li_2ND sample switched from ND_3 to NH_3 at 32.5 hours. It can be seen in Figure 5.13 that the signal-to-noise ratio of the neutron diffraction data decreases steadily after this time. This is a consequence of increased background counts from the incoherent scattering of neutrons by hydrogen which replaces deuterium in the Li_2ND structure; as hydrogen has an incoherent neutron scattering cross section that is more than ten times larger than deuterium[194].

As with the determination of the stoichiometry of the sample, the progress of the isotope exchange reaction can be quantified more precisely through Rietveld analysis. In this case, the stoichiometry of the sample was fixed, and a set of hydrogen positions were added to the structure, identical in location and thermal parameter to the deuterium positions. A single parameter was used to determine the fractional occupancy of H/D. As can be seen in Figure 5.16a, the deuterium occupancy remains close to 1.0 until the NH_3 is introduced, and then undergoes a steady decline for the remainder of the experiment; the lattice parameter mirrors this behaviour. At the point at which the experiment was terminated, the refinement of the NPD data suggests that 58 % of the deuterium in the structure had been replaced by hydrogen.

To corroborate this analysis, a value for the extent of deuterium-to-hydrogen substitution was calculated from the gas flow and mass spectrometry data: the average ND_3 flow is 5.7 sccm for the 210 minutes of the exchange reaction, giving a total volume of approximately 1200 cm^3. The conversion of NH_3 in that period is around 90 %, giving a volume of reacted NH_3 of 1080 cm^3. Given the density of ammonia gas at STP is 0.771 gL^{-1}, the mass of reacted NH_3 is 0.832 g, which corresponds to 0.049 moles. The mass of the Li_2ND sample was 2.7 g, which corresponds to 0.090 moles. If there is a net exchange of one H from each NH_3 molecule that is decomposed by the sample for a D in Li_2ND, then the gas flow and QGA data would suggest that 54 % of the D in the Li_2ND sample was replaced. This value is in remarkably good agreement with the NPD data.

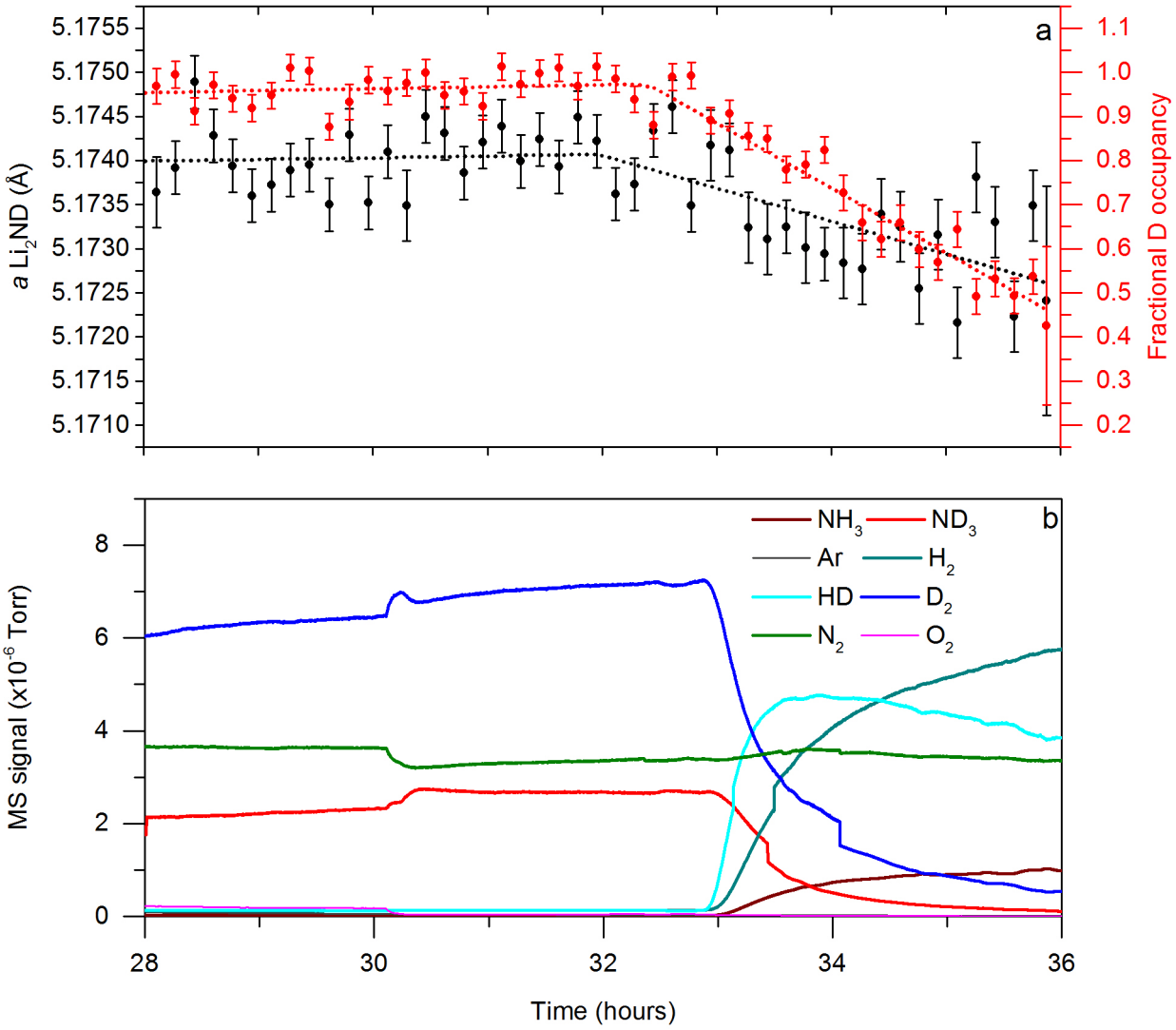

Figure 5.16: Lithium imide D-H exchange experiment. a) The fractional D occupancy (red) and a lattice parameter (black) of the Li_2ND b) QGA data as a function of experiment time.

The QGA data in Figure 5.16b provides a third piece of evidence for the isotope exchange reaction. HD (m/z=3) is observed in the QGA data shortly after the introduction of the NH_3 and for the duration of the isotope experiment. The only sources of deuterium in the experiment are Li_2ND, ND_3 and D_2. Although the gaseous species will exchange to give an HD signal, the signal persists after the ND_3 and D_2 reach very low levels, implying that deuterium from the Li_2ND is a significant proportion of the HD signal.

The net exchange of one hydrogen per NH_3 molecule would seem to indicate that the decomposition of ammonia by $LiNH_2$-Li_2NH can be described using a set of stoichiometric reactions. The simplest overall reaction that fulfils this criterion would be Equation 5.8. Given the potential for isotopic scrambling, it is not possible to use the QGA data to provide an accurate account of the gas species produced. Equally, it is difficult to envisage stoichiometric reactions based on an assumption of the likely possible species produced, which give rise to the ratios of gaseous species given in Equation 5.8.

$$Li_2ND + NH_3 \longleftrightarrow Li_2NH + HD + \frac{1}{2}H_2 + \frac{1}{2}N_2 \tag{5.8}$$

Of course, it is unlikely that only one hydrogen interacts with the sample: given that the stoichiometry of the sample is observed to deviate from line-phase Li_2ND during the reaction, it is evident that when the Li_2ND is exposed to NH_3 there will be some amide formation, as described in Equation 5.9. If the decomposition of the ammonia is via lithium metal in a mechanism analogous to Equations 5.6 and 5.7, then there is no clear path for stoichiometric incorporation of a single hydrogen from each NH_3 molecule as a result of these reactions. It is known that the energy barrier for the migration of protons between amide and imide groups is quite low[140, 141]. If the rate of diffusion of hydrogen into the imide structure according to Equation 5.10 is significantly faster than that of the ammonia decomposition, then hydrogen would be expected to be incorporated into the Li_2ND structure. However, this mechanism would incorporate more than one hydrogen per NH_3. The precise mechanism of ammonia decomposition needs further investigation.

$$Li_2ND + NH_3 \longleftrightarrow LiNDH + LiNH_2 \tag{5.9}$$

$$NDH^- + ND^{2-} \longleftrightarrow ND^{2-} + NDH^- \tag{5.10}$$

The temperature and flow conditions were kept constant under both ND_3 and NH_3 for the exchange experiment. Examination of the QGA data shows that the conversion for the ND_3 was 79.89 %, while under NH_3, the conversion was 86.93 %. One experimental explanation for this discrepancy could be that ND_3/NH_3 or D_2/H_2 have different ionisation sensitivities in the QGA system (the same sensitivity factors are used for the deuterated analogues as for the natural abundance species). However, such a significant difference seems unlikely to be solely due to this, and so we may conclude that there are truly different conversion levels for the two species, and that there is a kinetic isotope effect. This observation would indicate that the deuterium and hydrogen are involved in the rate determining step of the ammonia decomposition reaction, either as the breaking of N-H/D bonds, H/D diffusion or H_2/D_2 formation/desorption.

Identifying the steps involved in the reaction and their associated energies and activation energies will require a more detailed experimental and computational modelling investigation. For example, the magnitude of the kinetic isotope effect could give an indication as to the nature of the process involving the H/D atoms, but this would require the determination of the initial rates of reaction, not the average rates which can be calculated from the conversion data. However, some insight can be gained by combining the results of this isotope exchange reaction with computational studies of the Li-N-H system. In each of the substantive Density Functional Theory studies on the decomposition of $LiNH_2$, the hydrogen is involved in the rate-determining step.[140–142, 260] Miceli *et al.* found that the cleavage of the N–H bond to form an interstitial proton had the equal-highest activation energy together with that of the formation of the lithium ion Frenkel defect pair[141], while Wang *et al.* and Hazrati *et al.* determined it to have significantly higher activation energy than the lithium pair[140, 260]. Hoang *et al.* proposed two different mechanisms: for large particles, the cleavage of the N-H bond was again the rate-determining step, and for small particles, diffusion of H^+ to the surface of the particle had the highest activation energy[142]. All of these mechanisms would be expected to show a kinetic isotope effect; the observation of such an effect in the ammonia decomposition reaction for lithium imide is consistent with these analyses, and may indicate that the elementary steps used to explain the reaction mechanism of hydrogen storage and release in the Li-N-H system may go

some way to explaining the mechanism of ammonia decomposition using lithium amide-imide.

From the perspective of practicality, the ability to keep the amide catalyst solid at high temperatures has important implications, potentially giving a lithium-based catalyst an additional advantage over the sodium system. Working with a solid catalyst allows for the traditional catalysis routes to higher turnover frequency, such as nanosizing and complex support structures, to be explored. The task of containing the catalyst is also significantly simpler. A typical experimental run with the sodium amide catalyst (99.75 % conversion, 600 °C, 100 sccm NH_3) results in material recoveries as low as 0.1 %, as the sodium amide ends up coating the reactor and outlet tubing with a fine coating of powder. In contrast, lithium imide, which is heated to 500°C under argon in order to avoid amide formation when switching to ammonia, shows material recoveries in excess of 80% after similar reaction conditions (99.85 % conversion, 590 °C, 100 sccm NH_3). While heating under inert gas is not a practical solution for a transportation application, it does demonstrate the principle that an imide catalyst can be contained more effectively than the amide.

The use of lithium amide-imide is more expensive than sodium amide because of the greater scarcity of lithium compared with sodium. However, it remains significantly cheaper than precious metal-based catalysts, and offers higher ammonia decomposition activity than sodium amide. Its activity towards ammonia decomposition is important for two main reasons. First, it provides an example of an amide-based ammonia decomposition reagent which can be solid during operation. Solids are simpler to deal with in a practical catalytic system, and, academically, are easier to probe. Secondly, it shows that the range of active materials extends into imide-forming amides, opening up a rich vein of new materials and a diverse range of chemistry to explore.

5.5 Lithium-calcium imide and lithium-magnesium imide

By analogy to sodium and potassium amide, the choice of amides which decompose at a lower temperatures than lithium amide may result in more active ammonia decomposition catalysts. The activity of the lithium amide - imide system enables the use of imide-forming amides, which, through their greater propensity to remain solid, are more practical choices than amides which

will be molten or aerosol-like at the temperature of operation. Calcium and magnesium amides decompose at significantly lower temperatures than the alkali metal amides, and so would be good choices based on that criterion[261]. However, the combination of the lithium system with calcium and magnesium to form ternary compounds may be even more attractive, combining the more favourable thermodynamics of the calcium amd magnesium imides with the fact that both materials only form imides, not amides. As such, they seem good targets for both practical and active ammonia decomposition catalysts.

Lithium-magnesium imide ($Li_2Mg(NH)_2$) and lithium-calcium imide ($Li_2Ca(NH)_2$) are formed by the reaction of lithium amide and magnesium/calcium hydride (Equation 5.11). These ternary imides have been previously investigated for their reversible hydrogen storage content[127, 262–267], with a focus on the lithium magnesium imide due to its higher gravimetric hydrogen content (5.5 wt%).

$$2LiNH_2 + (Mg/Ca)H_2 \rightarrow Li_2(Mg/Ca)(NH)_2 + 2H_2 \tag{5.11}$$

The hydrogen storage and release reactions in the lithium-magnesium system are reversible under more moderate conditions, which may be indicative of their potential activity as ammonia decomposition catalysts. Furthermore, *in situ* XPD studies on lithium-magnesium imide indicate that, under argon, the sample remains solid at high temperature, undergoing two solid-solid phase transitions upon heating to 500 °C[265]. There are no published data on the temperature stability of lithium-calcium imide.

Difficulty was encountered obtaining pure samples of these ternary imides, despite replication of previously reported synthesis methods. For both samples, the highest purity obtained was approximately 60 %, with impurities of the starting materials. Examples of the PXRD patterns obtained for these samples are shown in Figure 5.17. Variation of ball-milling times, reaction times, temperatures and the atmosphere of the reaction were unsuccessful in improving the purity beyond this level.

The level of purity obtained was deemed sufficient to give an indication of the ammonia decomposition activity of each of the ternary imides. As such, the variable-temperature ammonia decomposition efficiency of 0.5 g of the impure lithium-calcium imide and lithium-magnesium imide were each tested in the same manner as that described before. These results are shown

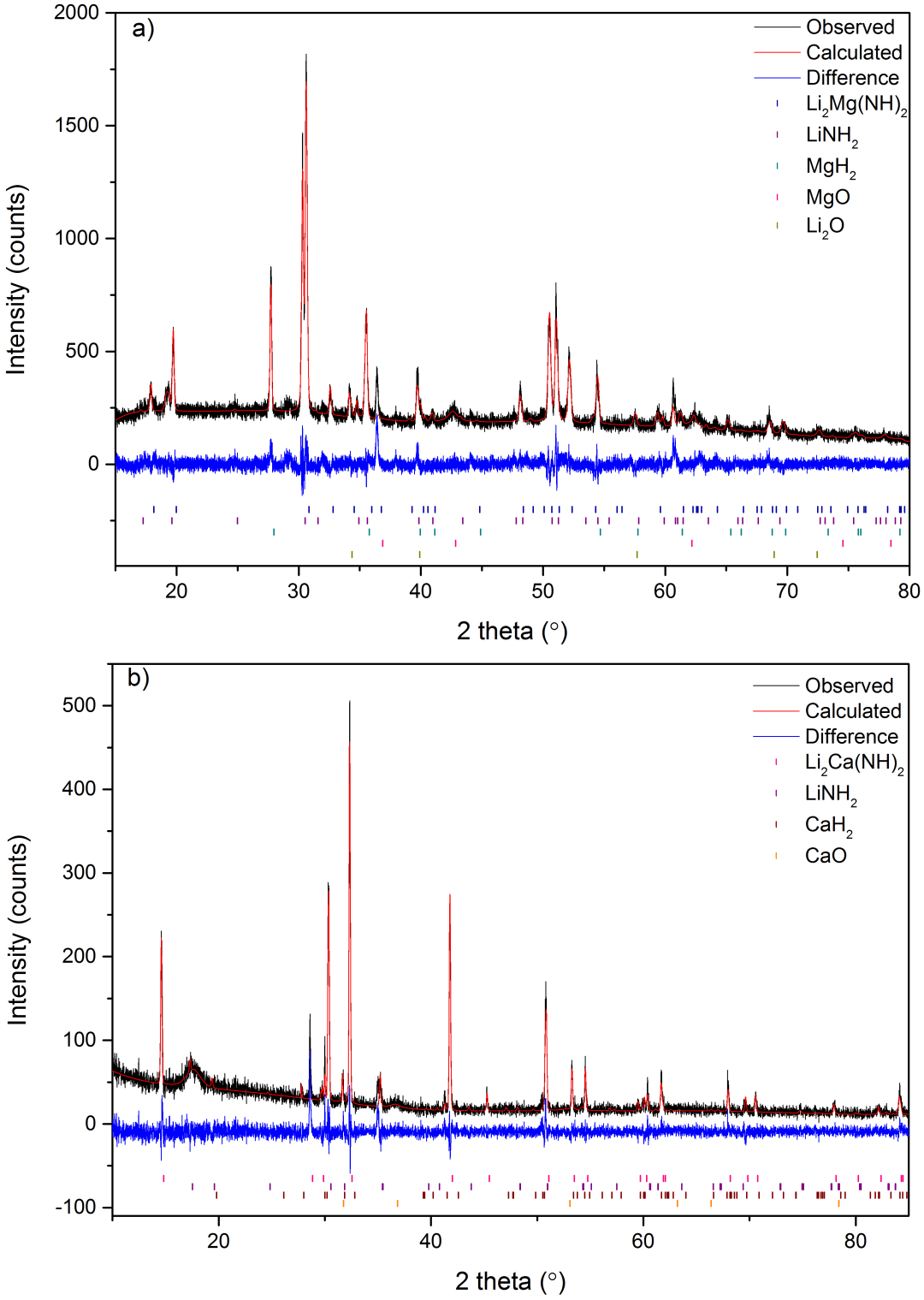

Figure 5.17: PXRD patterns for as-synthesised samples of a) $Li_2Mg(NH)_2$ and b) $Li_2Ca(NH)_2$.The Rwp values for the fits to the data were 9.290 and 18.792, respectively.

in Figure 5.18a, along with those of lithium amide and sodium amide, for comparison. The performance of both ternary imides are superior at low temperatures to that of the other amides tested. Above 430 °C, the lithium-magnesium imide conversion efficiency tails off compared with the other amides, while the lithium-calcium imide tracks the performance of lithium amide-imide quite closely. Unfortunately, the ternary imides did not improve upon the performance of lithium amide-imide in terms of decomposition efficiency at high conversion levels.

The Arrhenius plots for lithium-calcium imide (Figure 5.18c) shows a similar single process, as was observed for the other amides. However, lithium-magnesium imide (Figure 5.18b) appears to consist of two separate processes. Whether these are differences in the rate determining step, or a change in the sample, is difficult to say without further information.

Surprisingly, the recovery of the lithium-magnesium imide was very poor (less than 5 %). There are a few possible causes of this poor recovery: firstly, the sample may simply melt above 500 °C. Secondly, the presence of impurities of lithium amide (which shows poor recovery), could have caused the imide to dissolve. Thirdly, the imide may react with ammonia to form an amide which itself is molten at the temperatures of these experiments. The behaviour of these mixed imides has never been studied under ammonia. These would be important data to collect with a pure sample of the imide. This poor recovery may explain the tail-off in decomposition efficiency at high temperatures.

In contrast, the recovery of the lithium-calcium imide was almost complete (96 %). This is significant in light of the fact that the decomposition performance was equivalent to lithium amide-imide, making it the equal-most active ammonia decomposition catalyst presented in this work. Because the lithium-calcium imide does not appear to readily form an amide, it does not require heating under argon to achieve good recovery values, as is required for lithium amide-imide samples. This indicates that the lithium-calcium imide could be more readily applied to a practical device, and would be compatible with support architecture to improve its activity.

The high degree of recovery of the lithium-calcium imide sample is somewhat surprising given the impure nature of the starting material. The most abundant impurity in the sample was lithium amide, which would not be expected to be recovered. The fact that almost all of the mass was recovered at the end of the experiment implies that the lithium amide reacted with the lithium-calcium imide in the course of the ammonia decomposition reaction, since the previous

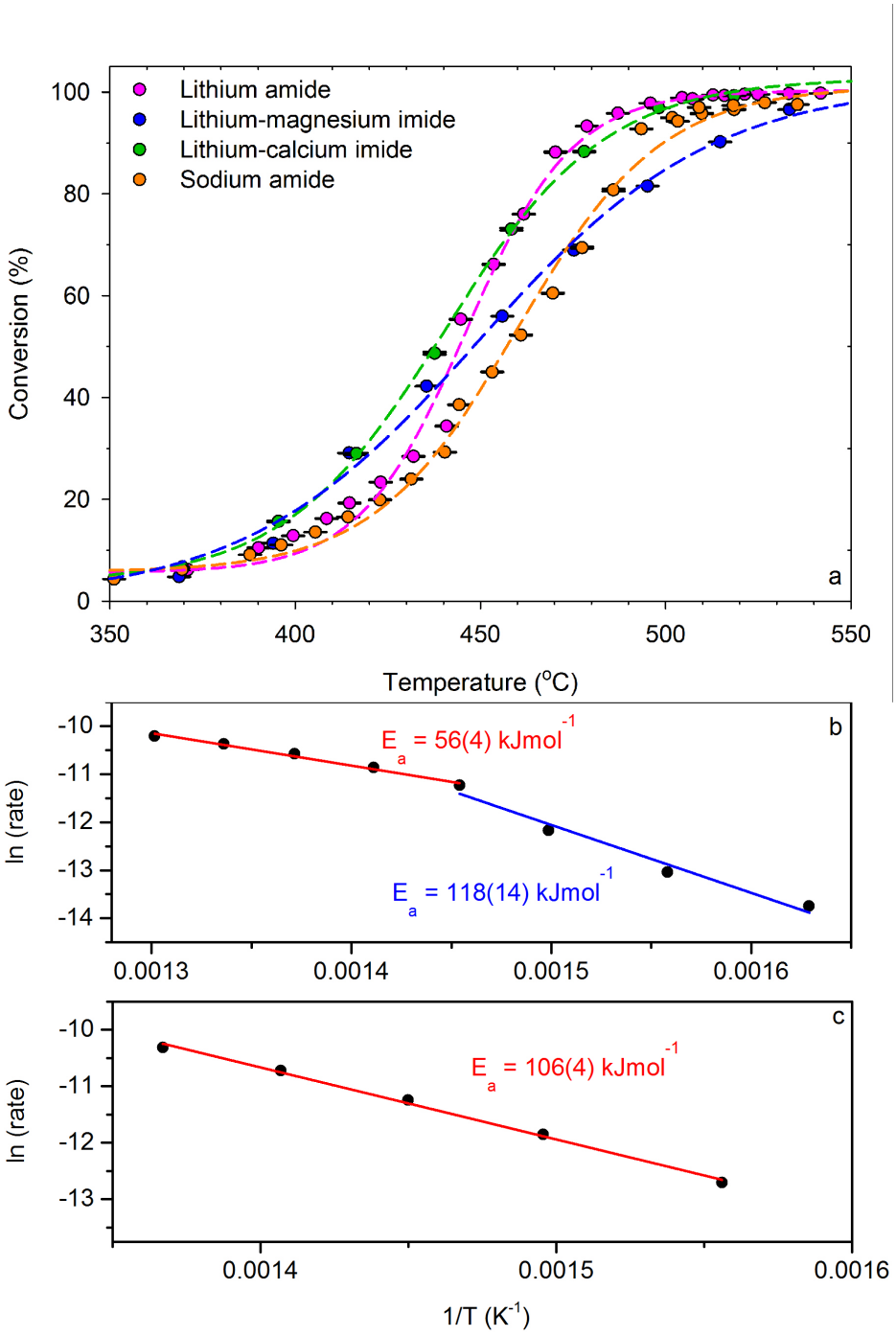

Figure 5.18: a) Comparison of ammonia conversion as a function of reaction temperature (between 300 °C and 600 °C) for the blank 46.9 cm^3 nickel-coated stainless steel reactor and 0.5 g of $Li_2Mg(NH)_2$, $Li_2Ca(NH)_2$, $LiNH_2$ and $NaNH_2$ at an ammonia flow rate of 60 sccm, with dashed lines indicating a sigmoidal fit to the data, and Arrhenius plots for b) $Li_2Mg(NH)_2$ and c) $Li_2Ca(NH)_2$ with the activation energies included on the graphs for each process identified.

experience with lithium amide would suggest it would not remain in the base of the reactor by the end of the experiment. The post-reaction PXRD pattern (Figure 5.19) is somewhat ambiguous. The original lithium-calcium imide phase is no longer present, and the pattern is dominated by a set of peaks associated with a cubic structure, with a minor set of peaks from a second phase. As discussed in depth in Chapter 3, lithium amide adopts an ordered derivative of the anti-fluorite structure. Calcium imide, by nature of the 1:1 stoichiometry and relative ionic radii of the calcium and imide ions, adopts a rock salt (face-centred cubic) structure. While the structures can be distinguished on this basis, they have very similar unit cell sizes, and so many of their Bragg peaks are essentially coincident. The simplest explanation of the PXRD pattern for the post-reaction sample is that it is a mixture of lithium amide and calcium imide. The fit agrees reasonably well with this structural model, with the presence of the (002) superlattice reflection of lithium amide, and a strong (002) reflection for the rock salt structure. Although it is difficult to be certain, Rietveld analysis of the PXRD data using this model gives an approximate 1:1 molar ratio between the two species, which gives the correct ratio of lithium to calcium as was present in the starting material.

The surprising aspect of this result is that it is not clear why the presence of the calcium imide would cause the lithium amide-imide to be better contained than it is in isolation. It is also unclear under which conditions the lithium-calcium imide separates into lithium imide and calcium imide, and whether this is an artifact of the ammonia decomposition, or whether this is simply a temperature-dependent effect. An *in situ* diffraction study would be instructive in addressing these questions. Nevertheless this result indicates that calcium imide is likely to show good ammonia decomposition performance.

5.6 Conclusions and further work

In this chapter, light metal amides and imides have been discussed as a new class of ammonia decomposition catalysts. The comparative activities of the species are summarised in Table 5.3. All of the amides and imides investigated, except lithium-magnesium imide, show superior high-temperature ammonia decomposition to sample ruthenium and nickel-based catalysts in the reactor geometry used in this study. Ruthenium is a more active ammonia decomposition

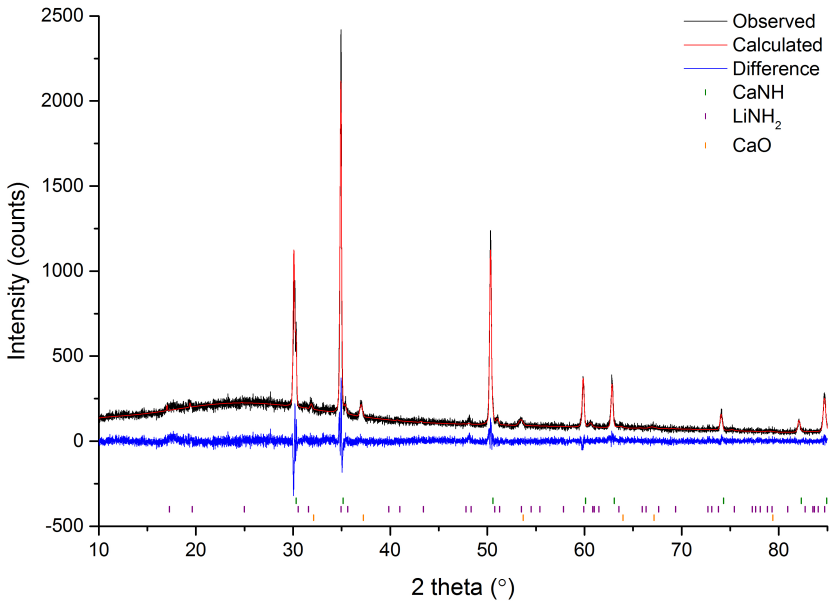

Figure 5.19: PXRD pattern for the $Li_2Ca(NH)_2$ sample recovered after ammonia decomposition reaction. The Rwp for the fit to the data was 10.515.

catalyst at lower temperatures. The temperatures at which 90 % ammonia decomposition is reached (T90 %) for each sample indicate that the lithium amide-imide catalyst is the most active on a mass-for-mass basis in the results presented.

Sodium and potassium amide, which decompose to their constituent elements upon heating, appear to decompose ammonia via two concurrent stoichiometric reactions: the synthesis and subsequent decomposition of the amide via the metal. This type of reaction mechanism is a clear departure from traditional surface catalysis. For the imides and imide-forming amide (lithium amide), the mechanism is less clear, although isotope exchange experiments with neutron powder

Table 5.3: A summary of ammonia decomposition characteristics of the amides and imides presented in this chapter. $T_{90\%}$ is the temperature at which 90% ammonia decomposition occurs under 60 sccm of ammonia flow in a nickel-coated 45 cm^3 stainless steel reactor. The recovery is the average percentage of the starting mass of the catalyst recovered from the reactor at the end of the experiment, and is a guide to the volatility of the catalyst.

Species	$T_{90\%}$ (°C)	E_{act} (kJ mol^{-1})	Recovery (%)
$NaNH_2$	493	113(2)	<1
KNH_2	481	71(1)	25
$LiNH_2 - Li_2NH$	472	123(1)	<1 (amide), 80 (imide)
$Li_2Ca(NH)_2$	480	106(4)	96
$Li_2Mg(NH)_2$	514	120(10), 56(4)	<5

diffraction on the lithium amide-imide have indicated that the bulk of the sample is involved in the reaction, and hint at a stoichiometric isotope exchange reaction, despite the clearly-identified presence of non-stoichiometric phases during the ammonia decomposition reaction. A kinetic isotope effect observed for decomposition of ND_3 versus NH_3 suggests hydrogen or the N–H bond is involved in the rate determining step of the ammonia decomposition in both sodium amide and lithium amide-imide reactions. Differences in the activity of sodium and potassium amide can also be rationalised in terms of the strength of the N–H bond and the volatility of the material.

Containment of the active catalyst appears to be the principal practical hurdle for the use of lithium, sodium and potassium amides, as well as the lithium-magnesium amide, with very low recovery of the catalyst material post-reaction. Careful control of the reaction conditions of lithium imide resulted in greater recovery, showing the importance of keeping the catalyst solid during the reaction. There is significant scope for trying to encapsulate these amide and imide materials, and to decorate the solid ones onto support architectures.

To date, the most promising amide/imide catalyst appears to be lithium-calcium imide, which is solid across the range of temperatures studied here, and shows very similar ammonia decomposition activity to lithium amide-imide. Since it appears to be solid throughout the reaction, it is also a prime candidate for a range of *in situ* techniques, such as neutron and X-ray powder diffraction.

The amide catalysts are some way from a kW-scale practical device. Although these materials show significant promise, their performance is not yet optimised to the same extent as current metal catalyst systems. The key challenges to improve the prospects of widespread application are: to raise the conversion efficiency to minimise the need for clean-up and maximise the potential for use in PEM fuel cell applications, to search for novel methods of containing volatile amides/metals, and to improve the kinetics (turnover frequency) of the decomposition reaction in order to lower the temperature of operation, which will in turn improve the system efficiency.

The use of amides and imides is a distinctively new method for ammonia decomposition, with significant opportunities for new research. Most of the work presented here involves the determination of the basic ammonia decomposition performance of a range of amide and imide materials. This application of light metal amides is the intersection of two pre-existing research

fields: the storage of hydrogen in light metal amides and their composites, and the catalytic decomposition of ammonia. As such, the lessons from each of these fields can be employed to improve the action of metal amides. For example, if it can be determined that the decomposition of the amide is the rate determining reaction for some of these amides, improving the kinetics of ammonia decomposition may be achieved by employing knowledge from the hydrogen storage community about additives which promote the decomposition of amides[103, 104, 106, 108, 112, 113].

Further information about the reaction mechanisms at play in these new catalysts will be instrumental in any effort to improve their activity. More detailed kinetic studies, spectroscopic analysis and further *in situ* studies will be key to gaining this information.

Of course, since the hydrogen density of the amide is no longer the primary concern, new avenues of amide research are of particular interest. Here there is significant scope to review and build on the substantial body of synthetic work over the past sixty years [268–272], and to explore the periodic properties of the amides in the context of their ammonia decomposition activity. The benefits of the use of many of the light elements in terms of cost are clear, but other materials may outperform them, or offer other practical advantages such as reduced water sensitivity. Given the promising results obtained in this initial study, it seems possible that an amide or imide material will provide the answer for cheap and effective ammonia decomposition and thus on-demand hydrogen production.

Chapter 6

Conclusion

Light metal amides have the potential to play important roles in the implementation of a sustainable energy system which uses hydrogen as an energy vector. While hydrogen vehicles can, and will, be produced using highly-pressurised gas fuel tanks, the development of a solid-state material which meets the requirements for on-board reversible hydrogen storage remains an important target because of the enhanced design flexibility, reduced safety considerations and simpler infrastructure conferred by its use.

Among existing complex metal hydride-based materials, the light metal amide systems are arguably the most promising candidates for practical application. This thesis has explored in substantial detail the impressive reversibility of the Li-N-H hydrogen storage system through the extensive application of *in situ* diffraction techniques. These studies have shown clearly that the hydrogenation and dehydrogenation of the Li-N-H system is well described by a Frenkel defect mechanism that results in the bulk formation of non-stoichiometric intermediate phases. These intermediates appear to be crucial in facilitating the facile reversibility of the hydrogen storage reactions.

The high resolution and intensity offered by synchrotron PXRD has facilitated the examination of the dynamic behaviour of these phases, highlighting their instability relative to the ordered parent phases. Attempts to further investigate the properties of the non-stoichiometric phases encountered difficulties with the synthesis of pure, narrow stoichiometry distribution samples. These results, to some extent, reflect the stability variations identified in the *in situ* studies. However, there would be clear benefits to further probing their behaviour - in particular, devel-

oping an understanding of the local structure of the phases and their relative ionic mobility may provide important insights into their role in the Li-N-H system.

The importance of ionic mobility and the conservation of topology as the basis of reversibility should inform the future investigation of complex hydride hydrogen stores. However, if the Li-N-H system itself is to find practical application with low temperature fuel cell systems, it is clear that the kinetics of the hydrogenation and dehydrogenation reactions must be improved. An important starting point would be the optimisation of the ionic mobility of lithium amide and the non-stoichiometric phases, in particular. A more detailed investigation of how this behaviour changes in mixed metal amide-hydride composites, which often show superior low temperature behaviour to the Li-N-H system may lead to improvements in their performance, and the development of an important understanding of the variation in ionic mobility within amide systems. Efforts to modify the mobility of the Li-N-H system, either through bulk changes to the crystal structure or through the use of additives, should be expanded.

The influence of additives on the performance of the Li-N-H system is an under-investigated and poorly-understood area. The results presented in Chapter 3 indicate that titanium (III) chloride has a demonstrable effect on the behaviour of the system, but that the reason for its activity is still not well understood. A dual approach to this investigation, comprising a screening program of a range of possible additive materials, and computational and experimental studies to enhance understanding of their effects, may help achieve the necessary improvements in the reaction kinetics.

The Li-N-H system has the highest hydrogen capacity demonstrated over many hundreds of cycles of any complex hydride hydrogen store to date. Despite its facile reversiblity, it is not immune to the loss of capacity with cycling. In this work, it has been shown that oxidation and the formation of excess lithium hydride, either via the direct reaction of lithium amide with hydrogen or by loss of ammonia during the decomposition of lithium amide, are the primary sources of this capacity loss. Over 45 cycles, the reaction kinetics did not diminish appreciably, with the two aforementioned factors the only identifiable reasons for the observed drop in the reversible hydrogen content.

The improvement of the reversible hydrogen content upon cycling with the addition of nitrogen to the hydrogenation gas mixture may be the most important recent development in the

Li-N-H system. The *in situ* diffraction data presented in this study confirm that the addition of nitrogen does prevent the formation of excess lithium hydride under the conditions studied here. However, the discrepancies between this work and the previously published study, primarily the lack of observation of an increase in the reversible hydrogen content with cycling in this work, warrants further investigation. It is clear that the *in situ* diffraction method can provide valuable information on changes with cycling, and so it would be worthwhile to extend the study of the effect of nitrogen to much larger cycle numbers in order to ascertain whether an enhanced hydrogen storage capacity is observed.

While this thesis has provided a detailed exploration of the structural behaviour of the Li-N-H system by diffraction methods, there is significant scope to employ spectroscopic techniques to examine many of the addressed research questions. NMR spectroscopy could be used to give insight into the local structure of non-stoichiometric phases, and would potentially provide a more conclusive answer as to whether lithium metal is formed during the hydrogenation and dehydrogenation reactions of the Li-N-H system. Although the collection of high-temperature *in situ* NMR data is experimentally challenging, they would be an important measurement to complement the diffraction data reported here. It is clear that there are subtleties in the reactions of the Li-N-H system which have not been fully elucidated, and future investigations should focus on these effects.

Although there remain many research paths to be pursued in the development of solid-state hydrogen storage materials, it is possible that the challenging array of target properties for vehicular hydrogen storage may never be reached in a single material. In the case of the Li-N-H system, even if the reaction kinetics can be improved to the extent that the temperature of operation falls within the range outlined by the U.S. DoE, it may be that the complicated cooling equipment needed to dissipate the heat of refuelling will mean that the system is not favoured over compressed hydrogen. While the search for amide materials with lower reaction enthalpy values would help mitigate this effect, alternatives to solid-state hydrogen storage need to be seriously considered.

In this context, the second major strand of this thesis has considered the use of ammonia as an energy (and hydrogen) vector. Light metal amides are a new class of catalyst for the decomposition of ammonia into nitrogen and hydrogen for energy applications. The range of

amide and imide materials studied all show appreciable ammonia decomposition activity, with comparable conversion efficiencies to a ruthenium-based catalyst, which is widely acknowledged as the most active transition metal catalyst. They also show significant potential for that activity to be optimised. For sodium and potassium amide, the principal challenge is to contain the catalyst effectively, while all of the materials would benefit from research efforts aimed at improving the kinetics of the ammonia decomposition reaction. This would allow the system to operate at lower temperatures, improving its energy efficiency.

The application of these hydrogen storage materials as ammonia decomposition catalysts may draw together research strategies from the hydrogen storage community with those of traditional catalysis research. For example, promoting the decomposition of metal amide materials through the the use of additives, nanoconfinement and composite systems, all strategies previously used to enhance their hydrogen storage properties, may be effective in improving the ammonia decomposition activity of those amides. Likewise, approaches drawn from catalysis such as the use of support architectures may be applied to the amide-imide catalyst systems.

Free from the restriction of using only light elements in the amide in order to maximise the gravimetric hydrogen storage capacity, a wider range of metal amide chemistry should be explored in order to screen for more active and practical catalyst materials and understand their periodic properties. For the materials already described in this work, there remains significant scope to develop a deeper understanding of the mechanism by which these catalysts operate, as the mechanisms appear to be significantly different to traditional metal catalysts. The diffraction studies in this work suggest that there is variation in the mechanism of ammonia decomposition between different amide species, particularly between imide-forming and metal-forming amides. The deepening of this understanding will, in turn, provide the opportunity to develop more active catalyst materials.

Undeniably, these materials offer a cost-effective method for the decomposition of ammonia using readily available materials. Hopefully, this discovery will spur renewed consideration of the potential of ammonia as an attractive energy store for transport and grid-balancing applications.

This thesis demonstrates the value of not only investigating the 'headline' properties of energy storage materials (e.g. the gravimetric hydrogen content or ammonia decomposition efficiency), but also examining the mechanisms which underpin those characteristics. In particular, *in situ*

analysis techniques enabled by improved sample environments has been shown to provide unique insight into the function of energy materials. These methodological advances can be applied to a wide range of investigations covering the full spectrum of scientific research, from the understanding of fundamental properties to the probing of practical performance and degradation. The knowledge generated from their use will undoubtedly help facilitate our transition to a sustainable energy system. Light metal amides are clearly versatile energy materials, and may play an important role in that process.

Bibliography

[1] Malik, K. Human development report 2013. Tech. Rep., United Nations Development Program (2013).

[2] The World Bank. Electric power consumption (kWh per capita). URL `http://data.worldbank.org/indicator/EG.USE.ELEC.KH.PC`. (Date accessed: August 2013).

[3] Kolasinski, K. W. Frontiers of surface science. *Current Opinion in Solid State and Materials Science* **10**, 129–131 (2006).

[4] International Energy Agency. World energy outlook 2013—executive summary. Tech. Rep., International Energy Agency (2013).

[5] Department of Economic and Social Affairs, Population Division, U. N. World population prospects the 2012 revision. Tech. Rep., United Nations (2013).

[6] International Energy Agency. Energy technology perspectives 2012 pathways to a clean energy system executive summary. Tech. Rep., International Energy Agency (2012).

[7] International Energy Agency. CO_2 emissions from fuel combustion highlights 2013. Tech. Rep. (2013).

[8] Field, C. B. Climate change 2014: Impacts, adaptation, and vulnerability. summary for policymakers. Tech. Rep. March, Intergovernmental Panel on Climate Change (2014).

[9] McKinsey & Company. A portfolio of power-trains for Europe: a fact-based analysis. Tech. Rep. (2011).

[10] Orimo, S., Nakamori, Y., Eliseo, J. R., Züttel, A. & Jensen, C. M. Complex hydrides for hydrogen storage. *Chem. Rev.* **107**, 4111–4132 (2007).

[11] Jain, I. P., Jain, P. & Jain, A. Novel hydrogen storage materials: A review of lightweight complex hydrides. *J. Alloys Compd.* **503**, 303–339 (2010).

[12] David, W. I. F. Effective hydrogen storage: a strategic chemistry challenge. *Faraday Discuss.* **151**, 399–414 (2011).

[13] Edwards, P. P., Kuznetsov, V. L., Johnson, S. R., Lodge, M. T. J. & Jones, M. O. Sustainable hydrogen energy. In Jamasb, T., Nuttall, W. & Pollitt, M. (eds.) *Future Technologies for a Sustainable Electricity System* (Cambridge University Press, Cambridge, 2006).

[14] Holladay, J. D., Hu, J., King, D. L. & Wang, Y. An overview of hydrogen production technologies. *Catal. Today* **139**, 244–260 (2009).

[15] Züttel, A., Remhof, A., Borgschulte, A. & Friedrichs, O. Hydrogen: the future energy carrier. *Philos. Trans. R. Soc. London, Ser. A* **368**, 3329–3342 (2010).

[16] Little, A. D. Guidance for transportation technologies: Fuel choice for fuel cell vehicles. Tech. Rep. (2002).

[17] Melaina, M. & Penev, M. Hydrogen station cost estimates. Tech. Rep. September, National Renewable Energy Laboratory (2013).

[18] Spendelow, J. & Marcinkoski, J. DOE fuel cell technologies office record. Tech. Rep., United States Department of Energy (2013).

[19] U.S. Department of Energy. Hydrogen and fuel cell technologies FY14 budget at-a-glance. Tech. Rep., U.S Department of Energy (2014).

[20] US Department of Energy. Targets for onboard hydrogen storage systems for light-duty vehicles. Tech. Rep. September (2009).

[21] Dillon, A. C., Jones, K. M., Bekkedahl, T. A., Kiang, C. H., Bethune, D. S. & Heben, M. J. Storage of hydrogen in single-walled carbon nanotubes. *Nature* **386**, 377–379 (1997).

[22] Iijima, S. & Yudasaka, M. Nano-aggregates of single-walled graphitic carbon nano-horns. *Chem. Phys. Lett.* **309**, 165–170 (1999).

[23] Yang, Z., Xia, Y. & Mokaya, R. Enhanced hydrogen storage capacity of high surface area zeolite-like carbon materials. *J. Am. Chem. Soc.* **129**, 1673–1679 (2007).

[24] Sevilla, M., Alam, N. & Mokaya, R. Enhancement of hydrogen storage capacity of zeolite-templated carbons by chemical activation. *J. Phys. Chem. C* **114**, 11314–11319 (2010).

[25] Sevilla, M., Fuertes, A. B. & Mokaya, R. High density hydrogen storage in superactivated carbons from hydrothermally carbonized renewable organic materials. *Energy Environ. Sci.* **4**, 1400–11410 (2011).

[26] Chambers, A., Park, C., Baker, R. T. K. & Rodriguez, N. M. Hydrogen storage in graphite nanofibers. *J. Phys. Chem. B* **102**, 4253–4256 (1998).

[27] Chen, P., Wu, X., Lin, J. & Tan, K. L. High H_2 uptake by alkali-doped carbon nanotubes under ambient pressure and moderate temperatures. *Science* **285**, 91–93 (1999).

[28] Pinkerton, F. E., Wicke, B. G., Olk, C. H., Tibbetts, G. G., Meisner, G. P., Meyer, M. S. & Herbst, J. F. Thermogravimetric measurement of hydrogen absorption in alkali-modified carbon materials. *J. Phys. Chem. B* **104**, 9460–9467 (2000).

[29] Wang, L. & Yang, R. T. New sorbents for hydrogen storage by hydrogen spillover – a review. *Energy Environ. Sci.* **1**, 268–279 (2008).

[30] Prins, R. Hydrogen spillover. Facts and Fiction. *Chem. Rev.* **112**, 2714–2738 (2012).

[31] Cheng, H., Chen, L., Cooper, A. C., Sha, X. & Pez, G. P. Hydrogen spillover in the context of hydrogen storage using solid-state materials. *Energy Environ. Sci.* **1**, 338–354 (2008).

[32] Rosi, N. L., Eckert, J., Eddaoudi, M., Vodak, D. T., Kim, J., O'Keeffe, M. & Yaghi, O. M. Hydrogen storage in microporous metal-organic frameworks. *Science* **300**, 1127–1129 (2003).

[33] Kaye, S. S., Dailly, A., Yaghi, O. M. & Long, J. R. Impact of preparation and handling

on the hydrogen storage properties of Zn_4O(1,4-benzenedicarboxylate)$_3$ (MOF-5). *J. Am. Chem. Soc.* **129**, 14176–14177 (2010).

[34] Suh, M. P., Park, H. J., Prasad, T. K. & Lim, D.-W. Hydrogen storage in metal-organic frameworks. *Chem. Rev.* **112**, 782–835 (2012).

[35] Thomas, K. M. Adsorption and desorption of hydrogen on metal-organic framework materials for storage applications: comparison with other nanoporous materials. *Dalton Trans.* 1487–1505 (2009).

[36] Scully, J., Yuan, D. & Zhou, H.-C. The current status of hydrogen storage in metal-organic frameworks—updated. *Energy Environ. Sci.* **4**, 2721–2735 (2011).

[37] Farha, O. K., Yazaydın, A. O., Eryazici, I., Malliakas, C. D., Hauser, B. G., Kanatzidis, M. G., Nguyen, S. T., Snurr, R. Q. & Hupp, J. T. De novo synthesis of a metal-organic framework material featuring ultrahigh surface area and gas storage capacities. *Nat. Chem.* **2**, 944–948 (2010).

[38] Furukawa, H., Ko, N., Go, Y. B., Aratani, N., Choi, S. B., Choi, E., Yazaydın, A. O., Snurr, R. Q., O'Keeffe, M., Kim, J. & Yaghi, O. M. Ultrahigh porosity in metal-organic frameworks. *Science* **329**, 424–428 (2010).

[39] Yan, Y., Lin, X., Yang, S., Blake, A. J., Dailly, A., Champness, N. R., Hubberstey, P. & Schröder, M. Exceptionally high H_2 storage by a metal-organic polyhedral framework. *Chem. Commun.* 1025–1027 (2009).

[40] Cheon, Y. E. & Suh, M. P. Selective gas adsorption in a microporous metal-organic framework constructed of Co_4^{II} clusters. *Chem. Commun.* 2296–2298 (2009).

[41] Zhong, D.-C., Lin, J.-B., Lu, W.-G., Jiang, L. & Lu, T.-B. Strong hydrogen binding within a 3d microporous metal-organic framework. *Inorg. Chem.* **48**, 8656–8658 (2009).

[42] Dietzel, P. D. C., Besikiotis, V. & Blom, R. Application of metal-organic frameworks with coordinatively unsaturated metal sites in storage and separation of methane and carbon dioxide. *J. Mater. Chem.* **19**, 7362–7370 (2009).

[43] Zhou, W., Wu, H. & Yildirim, T. Enhanced H_2 adsorption in isostructural metal-organic frameworks with open metal sites: strong dependence of the binding strength on metal ions. *J. Am. Chem. Soc.* **130**, 15268–15269 (2008).

[44] Farha, O. K., Eryazici, I., Jeong, N. C., Hauser, B. G., Wilmer, C. E., Sarjeant, A. A., Snurr, R. Q., Nguyen, S. T., Yazaydın, A. O. & Hupp, J. T. Metal-organic framework materials with ultrahigh surface areas: is the sky the limit? *J. Am. Chem. Soc.* **134**, 15016–15021 (2012).

[45] Yang, S., Lin, X., Blake, A. J., Thomas, K. M., Hubberstey, P., Champness, N. R. & Schröder, M. Enhancement of H_2 adsorption in Li^+-exchanged co-ordination framework materials. *Chem. Commun.* 6108–6110 (2008).

[46] Himsl, D., Wallacher, D. & Hartmann, M. Improving the hydrogen-adsorption properties of a hydroxy-modified mil-53(Al) structural analogue by lithium doping. *Angew. Chem. Int. Ed.* **48**, 4639–4642 (2009).

[47] Yang, S., Callear, S. K., Ramirez-Cuesta, A. J., David, W. I. F., Sun, J., Blake, A. J., Champness, N. R. & Schröder, M. Pore with gate: modulating hydrogen storage in metal-organic framework materials via cation exchange. *Faraday Discuss.* **151**, 19–36 (2011).

[48] Bae, Y.-S. & Snurr, R. Q. Optimal isosteric heat of adsorption for hydrogen storage and delivery using metal-organic frameworks. *Microporous Mesoporous Mater.* **132**, 300–303 (2010).

[49] Kamazawa, K., Aoki, M., Noritake, T., Miwa, K., Sugiyama, J., Towata, S.-I., Ishikiriyama, M., Callear, S. K., Jones, M. O. & David, W. I. F. In-operando neutron diffraction studies of transition metal hydrogen storage materials. *Adv. Energy Mater.* **3**, 39–42 (2013).

[50] Toyota Motor Corporation. Technology file: Fuel cell vehicle (2014). URL `http://www.toyota-global.com/innovation/environmental_technology/technology_file/fuel_cell_hybrid.html`. (Date accessed: February 13, 2014).

[51] Oelerich, W., Klassen, T. & Bormann, R. Metal oxides as catalysts for improved hydrogen sorption in nanocrystalline Mg-based materials. *J. Alloys Compd.* **315**, 237–242 (2001).

[52] Oelerich, W., Klassen, T. & Bormann, R. Comparison of the catalytic effects of V, V_2O_5, V_n, and V_c on the hydrogen sorption of nanocrystalline Mg. *J. Alloys Compd.* **322**, L5–L9 (2001).

[53] Barkhordarian, G., Klassen, T. & Bormann, R. Fast hydrogen sorption kinetics of nanocrystalline Mg using Nb_2O_5 as catalyst. *Scripta Mater.* **49**, 213–217 (2003).

[54] Moser, D., Bull, D. J., Sato, T., Noréus, D., Kyoi, D., Sakai, T., Kitamura, N., Yusa, H., Taniguchi, T., Kalisvaart, W. P. & Notten, P. Structure and stability of high pressure synthesized Mg-TM hydrides (tm=Ti, Zr, Hf, V, Nb and Ta) as possible new hydrogen rich hydrides for hydrogen storage. *J. Mater. Chem.* **19**, 8150–8161 (2009).

[55] Takasaki, T., Kyoi, D., Kitamura, N., Tanase, S. & Sakai, T. Reversible hydrogen storage property and structural analysis for face-centered cubic hydride $Mg_{0.82}Zr_{0.18}H_2$ prepared by gigapascal hydrogen pressure method. *J. Phys. Chem. B* **111**, 14102–14106 (2007).

[56] McPhy energy. Solid hydrogen storage (2014). URL `http://www.mcphy.com/en/products/solid-hydrogen-storage/`. (Date accessed: June 15, 2014).

[57] Bogdanović, B. & Schwickardi, M. Ti-doped alkali metal aluminium hydrides as potential novel reversible hydrogen storage materials. *J. Alloys Compd.* **253–254**, 1–9 (1997).

[58] Blomqvist, A., Araújo, C. M., Jena, P. & Ahuja, R. Dehydrogenation from 3d-transition-metal-doped $NaAlH_4$: Prediction of catalysts. *Appl. Phys. Lett.* **90**, 141904 (2007).

[59] Kang, X. D., Wang, P., Song, X. P., Yao, X. D., Lu, G. Q. & Cheng, H. M. Catalytic effect of Al_3Ti on the reversible dehydrogenation of $NaAlH_4$. *J. Alloys Compd.* **424**, 365–369 (2006).

[60] Lee, G.-J., Shim, J.-H., Whan, Y. C. & Lee, K. S. Reversible hydrogen storage in $NaAlH_4$ catalyzed with lanthanide oxides. *Int. J. Hydrogen Energy* **32**, 1911–1915 (2007).

[61] Naik, M., Rather, S., Zacharia, R., So, C. S., Hwang, S. W., Kim, A. R. & Nahm, K. S. Comparative study of dehydrogenation of sodium aluminum hydride wet-doped with $ScCl_3$, $TiCl_3$, VCl_3, and $MnCl_2$. *J. Alloys Compd.* **471**, L16–L22 (2009).

[62] Pukazhselvan, D., Hudson, M. S. L., Gupta, B. K., Shaz, M. A. & Srivastava, O. N. Investigations on the desorption kinetics of Mm-doped $NaAlH_4$. *J. Alloys Compd.* **439**, 243–248 (2007).

[63] Anton, D. L. Hydrogen desorption kinetics in transition metal modified $NaAlH_4$. *J. Alloys Compd.* **357**, 400–404 (2003).

[64] Berseth, P. A., Harter, A. G., Zidan, R., Blomqvist, A., Araújo, C. M., Scheicher, R. H., Ahuja, R. & Jena, P. Carbon nanomaterials as catalysts for hydrogen uptake and release in $NaAlH_4$. *Nano Lett.* **9**, 1501–1505 (2009).

[65] Bogdanović, B., Brand, R. A., Marjanović, A., Schwickardi, M. & Tölle, J. Metal-doped sodium aluminium hydrides as potential new hydrogen storage materials. *J. Alloys Compd.* **302**, 36–58 (2000).

[66] Srinivasan, S. S., Brinks, H. W., Hauback, B. C., Sun, D. & Jensen, C. M. Long term cycling behavior of titanium doped $NaAlH_4$ prepared through solvent mediated milling of NaH and Al with titanium dopant precursors. *J. Alloys Compd.* **377**, 283–289 (2004).

[67] Bellosta von Colbe, J. M., Metz, O., Lozano, G. A., Pranzas, P. K., Schmitz, H. W., Beckmann, F., Schreyer, A., Klassen, T. & Dornheim, M. Behavior of scaled-up sodium alanate hydrogen storage tanks during sorption. *Int. J. Hydrogen Energy* **37**, 2807–2811 (2012).

[68] Johnson, T. A., Jorgensen, S. W. & Dedrick, D. E. Performance of a full-scale hydrogen-storage tank based on complex hydrides. *Faraday Discuss.* **151**, 327–352 (2011).

[69] Mosher, D. A., Tang, X., Brown, R. J., Arsenault, S., Saitta, S., Laube, B. L., Dold, R. H. & Anton, D. L. High density hydrogen storage system demonstration using $NaAlH_4$ based complex compound hydrides final report. Tech. Rep., U.S. Department of Energy (2007).

[70] David, W. I. F., Callear, S. K., Jones, M. O., Aeberhard, P. C., Culligan, S. D., Pohl, A. H., Johnson, S. R., Ryan, K. R., Parker, J. E., Edwards, P. P., Nuttall, C. J. & Amieiro-Fonseca, A. The structure, thermal properties and phase transformations of the

cubic polymorph of magnesium tetrahydroborate. *Phys. Chem. Chem. Phys.* **14**, 11800–11807 (2012).

[71] Li, H.-W., Yan, Y., Orimo, S.-I., Züttel, A. & Jensen, C. M. Recent progress in metal borohydrides for hydrogen storage. *Energies* **4**, 185–214 (2011).

[72] Brinks, H. W., Fossdal, A. & Hauback, B. C. Adjustment of the stability of complex hydrides by anion substitution. *J. Phys. Chem. C* **112**, 5658–5661 (2008).

[73] Nakamori, Y., Li, H., Miwa, K., Towata, S. & Orimo, S. Syntheses and hydrogen desorption properties of metal-borohydrides $M(BH_4)_n$ (m=Mg, Sc, Zr, Ti, and Zn; n=2–4) as advanced hydrogen storage materials. *Mater. Trans.* **47**, 1898–1901 (2006).

[74] Matsunaga, T., Buchter, F., Miwa, K., Towata, S., Orimo, S. & Züttel, A. Magnesium borohydride: A new hydrogen storage material. *Renewable Energy* **33**, 193–196 (2008).

[75] Graetz, J. & Hauback, B. C. Recent developments in aluminum-based hydrides for hydrogen storage. *MRS Bull.* **38**, 473–479 (2013).

[76] Nickels, E. A., Jones, M. O., David, W. I. F., Johnson, S. R., Lowton, R. L., Sommariva, M. & Edwards, P. P. Tuning the decomposition temperature in complex hydrides: synthesis of a mixed alkali metal borohydride. *Angew. Chem. Int. Ed.* **47**, 2817–2819 (2008).

[77] Kojima, Y., Matsumoto, M., Kawai, Y., Haga, T., Ohba, N., Miwa, K., Towata, S.-I., Nakamori, Y. & Orimo, S.-I. Hydrogen absorption and desorption by the Li-Al-N-H system. *J. Phys. Chem. B* **110**, 9632–6 (2006).

[78] Chater, P. A., Anderson, P. A., Prendergast, J. W., Walton, A., Mann, V. S. J., Book, D., David, W. I., Johnson, S. R. & Edwards, P. P. Synthesis and characterization of amide-borohydrides: New complex light hydrides for potential hydrogen storage. *J. Alloys Compd.* **446–447**, 350–354 (2007).

[79] Chater, P. A., David, W. I. F., Johnson, S. R., Edwards, P. P. & Anderson, P. A. Synthesis and crystal structure of $Li_4BH_4(NH_2)_3$. *Chem. Commun.* **4**, 2439–41 (2006).

[80] Meisner, G. P., Scullin, M. L., Balogh, M. P., Pinkerton, F. E. & Meyer, M. S. Hydrogen release from mixtures of lithium borohydride and lithium amide: a phase diagram study. *J. Phys. Chem. B* **110**, 4186–4192 (2006).

[81] Nakamori, Y., Ninomiya, A., Kitahara, G., Aoki, M., Noritake, T., Miwa, K., Kojima, Y. & Orimo, S. Dehydriding reactions of mixed complex hydrides. *J. Power Sources* **155**, 447–455 (2006).

[82] Aoki, M., Miwa, K., Noritake, T., Kitahara, G., Nakamori, Y., Orimo, S. & Towata, S. Destabilization of $LiBH_4$ by mixing with $LiNH_2$. *Appl. Phys. A* **80**, 1409–1412 (2005).

[83] Xiong, Z., Yong, C. K., Wu, G., Chen, P., Shaw, W., Karkamkar, A., Autrey, T., Jones, M. O., Johnson, S. R., Edwards, P. P. & David, W. I. F. High-capacity hydrogen storage in lithium and sodium amidoboranes. *Nat. Mater.* **7**, 138–141 (2008).

[84] Diyabalanage, H. V. K., Nakagawa, T., Shrestha, R. P., Semelsberger, T. A., Davis, B. L., Scott, B. L., Burrell, A. K., David, W. I. F., Ryan, K. R., Jones, M. O. & Edwards, P. P. Potassium(i) amidotrihydroborate: structure and hydrogen release. *J. Am. Chem. Soc.* **132**, 11836–11837 (2010).

[85] Sutton, A. D., Burrell, A. K., Dixon, D. A., Garner, I., E. B., Gordon, J. C., Nakagawa, T., Ott, K. C., Robinson, J. P. & Vasiliu, M. Regeneration of ammonia borane spent fuel by direct reaction with hydrazine and liquid ammonia. *Science* **331**, 1426–1429 (2011).

[86] Xia, G., Tan, Y., Chen, X., Guo, Z., Liu, H. & Yu, X. Mixed-metal (li, al) amidoborane: synthesis and enhanced hydrogen storage properties. *J. Mater. Chem. A* **1**, 1810–1820 (2013).

[87] Tang, Z., Chen, X., Chen, H., Wu, L. & Yu, X. Metal-free catalysis of ammonia-borane dehydrogenation/regeneration for a highly efficient and facilely recyclable hydrogen-storage material. *Angewandte Chemie (International ed. in English)* **52**, 5832–5 (2013).

[88] Liu, X., McGrady, G. S., Langmi, H. W. & Jensen, C. M. Facile cycling of Ti-doped $LiAlH_4$ for high performance hydrogen storage. *J. Am. Chem. Soc.* **131**, 5032–5033 (2009).

[89] Liu, X., Beattie, S. D., Langmi, H. W., McGrady, G. S. & Jensen, C. M. Ti-doped $LiAlH_4$ for hydrogen storage: Rehydrogenation process, reaction conditions and microstructure evolution during cycling. *Int. J. Hydrogen Energy* **37**, 10215–10221 (2012).

[90] Li, S., Tang, Z., Gong, Q., Yu, X., Beaumont, P. R. & Jensen, C. M. Phenyl introduced ammonium borohydride: synthesis and reversible dehydrogenation properties. *J. Mater. Chem.* **22**, 21017–21023 (2012).

[91] Chong, M., Karkamkar, A., Autrey, T., Orimo, S.-I., Jalisatgi, S. & Jensen, C. M. Reversible dehydrogenation of magnesium borohydride to magnesium triborane in the solid state under moderate conditions. *Chem. Commun.* **47**, 1330–1332 (2011).

[92] Severa, G., Rönnebro, E. & Jensen, C. M. Direct hydrogenation of magnesium boride to magnesium borohydride: demonstration of >11 weight percent reversible hydrogen storage. *Chem. Commun.* **46**, 421–423 (2010).

[93] Rönnebro, E. & Majzoub, E. Discovery and development of metal hydrides for reversible on-board storage sandia program overview. Tech. Rep., Sandia National Laboratories (2008).

[94] Ngene, P., van den Berg, R., Verkuijlen, M. H. W., de Jong, K. P. & de Jongh, P. E. Reversibility of the hydrogen desorption from $NaBH_4$ by confinement in nanoporous carbon. *Energy Environ. Sci.* **4**, 4108–4115 (2011).

[95] Yan, Y., Au, Y. S., Rentsch, D., Remhof, A., de Jongh, P. E. & Züttel, A. Reversible hydrogen storage in $Mg(BH_4)_2$/carbon nanocomposites. *J. Mater. Chem. A* **1**, 11177–11183 (2013).

[96] Ngene, P., van Zwienen, M. & de Jongh, P. E. Reversibility of the hydrogen desorption from $LiBH_4$: a synergetic effect of nanoconfinement and Ni addition. *Chem. Commun.* **46**, 8201–8203 (2010).

[97] Lappert, M., Protchenko, A., Power, P. & Seeber, A. *Metal Amide Chemistry* (John Wiley and Sons, 2008).

[98] Chen, P., Xiong, Z., Luo, J., Lin, J. & Tan, K. L. Interaction of hydrogen with metal nitrides and imides. *Nature* **420**, 302–304 (2002).

[99] Dafert, F. W. & Miklauz, R. Über einige neue verbindungen von stickstoff und wasserstoff mit lithium. *Monatsh. Chem. Verw. Tl.* **31**, 981–996 (1910).

[100] Juza, R. Amides of the alkali and the alkaline earth metals. *Angew. Chem. Int. Ed.* **3**, 471–481 (1964).

[101] Osborn, W., Markmaitree, T. & Shaw, L. L. The long-term hydriding and dehydriding stability of the nanoscale $LiNH_2$+LiH hydrogen storage system. *Nanotechnology* **20**, 204028 (2009).

[102] Uribe, F. A., Gottesfeld, S. & Zawodzinski, J., T. A. Effect of ammonia as potential fuel impurity on proton exchange membrane fuel cell performance. *J. Electrochem. Soc.* **149**, A293–A296 (2002).

[103] Ichikawa, T., Isobe, S., Hanada, N. & Fujii, H. Lithium nitride for reversible hydrogen storage. *J. Alloys Compd.* **365**, 271–276 (2004).

[104] Ichikawa, T., Hanada, N., Isobe, S., Leng, H. Y. & Fujii, H. Hydrogen storage properties in Ti catalyzed Li-N-H system. *J. Alloys Compd.* **404–406**, 435–438 (2005).

[105] Ichikawa, T., Leng, H. Y., Isobe, S., Hanada, N. & Fujii, H. Recent development on hydrogen storage properties in metal-N-H systems. *J. Power Sources* **159**, 126–131 (2006).

[106] Isobe, S., Ichikawa, T., Hanada, N., Leng, H. Y., Fichtner, M., Fuhr, O. & Fujii, H. Effect of Ti catalyst with different chemical form on Li-N-H hydrogen storage properties. *J. Alloys Compd.* **404–406**, 439–442 (2005).

[107] Nayebossadri, S., Aguey-Zinsou, K. F. & Guo, Z. X. Effect of nitride additives on Li-N-H hydrogen storage system. *Int. J. Hydrogen Energy* **36**, 7920–7926 (2011).

[108] Isobe, S., Ichikawa, T., Kojima, Y. & Fujii, H. Characterization of titanium based catalysts in the Li-N-H hydrogen storage system by x-ray absorption spectroscopy. *J. Alloys Compd.* **446-447**, 360–362 (2007).

[109] Tsumuraya, T., Shishidou, T. & Oguchi, T. First-principles study on lithium and magnesium nitrogen hydrides for hydrogen storage. *J. Alloys Compd.* **446–447**, 323–327 (2007).

[110] Isobe, S., Hino, S., Ichikawa, T. & Kojima, Y. Identifying catalyst in Li-N-H system by x-ray absorption spectroscopy. *Appl. Phys. Lett.* **99**, 013101 (2011).

[111] Zhang, T., Isobe, S., Wang, Y., Hashimoto, N. & Ohnuki, S. A solid-solid reaction enhanced by an inhomogeneous catalyst in the (de)hydrogenation of a lithium-hydrogen-nitrogen system. *RSC Adv.* **3**, 6311–6314 (2013).

[112] Anderson, P. A., Chater, P. A., Hewett, D. R. & Slater, P. R. Hydrogen storage and ionic mobility in amide-halide systems. *Faraday Discuss.* **151**, 271–284 (2011).

[113] Zhang, J. & Hu, Y. H. Decomposition of lithium amide and lithium imide with and without anion promoter. *Ind. Eng. Chem. Res.* **50**, 8058–8064 (2011).

[114] Shaw, L. L., Ren, R., Markmaitree, T. & Osborn, W. Effects of mechanical activation on dehydrogenation of the lithium amide and lithium hydride system. *J. Alloys Compd.* **448**, 263–271 (2008).

[115] Varin, R. A., Jang, M. & Polanski, M. The effects of ball milling and molar ratio of LiH on the hydrogen storage properties of nanocrystalline lithium amide and lithium hydride ($LiNH_2$ + LiH) system. *J. Alloys Compd.* **491**, 658–667 (2010).

[116] Hu, J. Z., Kwak, J. H., Yang, Z., Osborn, W., Markmaitree, T. & Shaw, L. L. Investigation of mechanical activation on Li-N-H systems using ^{6}Li magic angle spinning nuclear magnetic resonance at ultra-high field. *J. Power Sources* **182**, 278–283 (2008).

[117] Lu, C., Hu, J., Kwak, J. H., Yang, Z., Ren, R., Markmaitree, T. & Shaw, L. L. Study the effects of mechanical activation on Li-N-H systems with ^{1}H and ^{6}Li solid-state NMR. *J. Power Sources* **170**, 419–424 (2007).

[118] Osborn, W., Markmaitree, T., Shaw, L. L., Hu, J.-Z., Kwak, J. & Yang, Z. Low temperature milling of the $LiNH_2$ + LiH hydrogen storage system. *Int. J. Hydrogen Energy* **34**, 4331–4339 (2009).

[119] Lowton, R. L., Jones, M. O., David, W. I. F., Johnson, S. R., Sommariva, M. & Edwards, P. P. The synthesis and structural investigation of mixed lithium/sodium amides. *J. Mater. Chem.* **18**, 2355–2360 (2008).

[120] Chu, H., Xiong, Z., Wu, G., He, T., Wu, C. & Chen, P. Hydrogen storage properties of Li-Ca-N-H system with different molar ratios of $LiNH_2/CaH_2$. *Int. J. Hydrogen Energy* **35**, 8317–8321 (2010).

[121] Tokoyoda, K., Hino, S., Ichikawa, T., Okamoto, K. & Fujii, H. Hydrogen desorption/absorption properties of Li-Ca-N-H system. *J. Alloys Compd.* **439**, 337–341 (2007).

[122] Xiong, Z., Hu, J., Wu, G. & Chen, P. Hydrogen absorption and desorption in Mg-Na-N-H system. *J. Alloys Compd.* **395**, 209–212 (2005).

[123] Nakamori, Y., Kitahara, G. & Orimo, S. Synthesis and dehydriding studies of Mg-N-H systems. *J. Power Sources* **138**, 309–312 (2004).

[124] Hino, S., Ichikawa, T. & Kojima, Y. Thermodynamic properties of metal amides determined by ammonia pressure-composition isotherms. *J. Chem. Thermodyn.* **42**, 140–143 (2010).

[125] Dolci, F., Napolitano, E., Weidner, E., Enzo, S., Moretto, P., Brunelli, M., Hansen, T., Fichtner, M. & Lohstroh, W. Magnesium imide : Synthesis and structure determination of an unconventional alkaline earth imide from decomposition of magnesium amide. *Inorg. Chem.* **50**, 1116–1122 (2011).

[126] Lu, J., Fang, Z. Z., Choi, Y. J. & Sohn, H. Y. Potential of binary lithium magnesium nitride for hydrogen storage applications. *J. Phys. Chem. C* **111**, 12129–12134 (2007).

[127] Janot, R., Eymery, J.-B. & Tarascon, J.-M. Investigation of the processes for reversible hydrogen storage in the Li-Mg-N-H system. *J. Power Sources* **164**, 496–502 (2007).

[128] Leng, H. Y., Ichikawa, T., Hino, S., Hanada, N., Isobe, S. & Fujii, H. New Metal-N-H system composed of $Mg(NH_2)_2$ and LiH for hydrogen storage. *J. Phys. Chem. B* **108**, 8763–8765 (2004).

[129] Leng, H., Ichikawa, T. & Fujii, H. Hydrogen storage properties of Li-Mg-N-H systems with different ratios of $LiH/Mg(NH_2)_2$. *The J. Phys. Chem. B* **110**, 12964–12968 (2006).

[130] Nakamori, Y., Kitahara, G., Miwa, K., Ohba, N., Noritake, T., Towata, S. & Orimo, S. Hydrogen storage properties of Li-Mg-N-H systems. *J. Alloys Compd.* **404–406**, 396–398 (2005).

[131] Chen, P., Xiong, Z., Luo, J., Lin, J. & Tan, K. L. Interaction between lithium amide and lithium hydride. *J. Phys. Chem. B* **107**, 10967–10970 (2003).

[132] Ichikawa, T., Hanada, N., Isobe, S., Leng, H. & Fujii, H. Mechanism of novel reaction from $LiNH_2$ and LiH to Li_2NH and H_2 as a promising hydrogen storage system. *J. Phys. Chem. B* **108**, 7887–7892 (2004).

[133] Isobe, S., Ichikawa, T., Hino, S. & Fujii, H. Hydrogen desorption mechanism in a Li-N-H system by means of the isotopic exchange technique. *J. Phys. Chem. B* **109**, 14855–8 (2005).

[134] Hu, Y. H. & Ruckenstein, E. Ultrafast reaction between LiH and NH_3 during H_2 storage in Li_3N. *J. Phys. Chem. A* **107**, 9737–9739 (2003).

[135] Hu, J. Z., Kwak, J. H., Yang, Z., Osborn, W., Markmaitree, T. & Shaw, L. L. Probing the reaction pathway of dehydrogenation of the $LiNH_2$+LiH mixture using in situ ^1H NMR spectroscopy. *J. Power Sources* **181**, 116–119 (2008).

[136] David, W. I. F., Jones, M. O., Gregory, D. H., Jewell, C. M., Johnson, S. R., Walton, A. & Edwards, P. P. A mechanism for non-stoichiometry in the lithium amide/lithium imide hydrogen storage reaction. *J. Am. Chem. Soc.* **129**, 1594–1601 (2007).

[137] Makepeace, J. W., Jones, M. O., Callear, S. K., Edwards, P. P. & David, W. I. F. In situ x-ray powder diffraction studies of hydrogen storage and release in the Li-N-H system. *Phys. Chem. Chem. Phys.* **16**, 4061–4070 (2014).

[138] Farley, T. W. D., Hayes, W., Hull, S., Hutchings, M. T. & Vrtis, M. Investigation of thermally induced Li^+ ion disorder in Li_2O using neutron diffraction. *J. Phys.: Condens. Matter* **3**, 4761–4781 (1991).

[139] Li, W., Wu, G., Xiong, Z., Feng, Y. P. & Chen, P. Li^+ ionic conductivities and diffusion mechanisms in Li-based imides and lithium amide. *Phys. Chem. Chem. Phys.* **14**, 1596–1606 (2012).

[140] Hazrati, E., Brocks, G., Buurman, B., de Groot, R. A. & de Wijs, G. A. Intrinsic defects and dopants in $LiNH_2$: a first-principles study. *Phys. Chem. Chem. Phys.* **13**, 6043–6052 (2011).

[141] Miceli, G., Cucinotta, C. S., Bernasconi, M. & Parrinello, M. First principles study of the $LiNH_2/Li_2NH$ transformation. *J. Phys. Chem. C* **114**, 15174–15183 (2010).

[142] Hoang, K., Janotti, A. & Van de Walle, C. G. Mechanisms for the decomposition and dehydrogenation of Li amide/imide. *Phys. Rev. B* **85**, 064115 (2012).

[143] Lamb, J., Chandra, D., Chien, W.-M., Phanon, D., Penin, N., Černý, R. & Yvon, K. Mitigation of hydrogen capacity losses during pressure cycling of the Li_3N-H system by the addition of nitrogen. *J. Phys. Chem. C* **115**, 14386–14391 (2011).

[144] U.S. Department of Energy. DOE targets for onboard hydrogen storage systems for light-duty vehicles. Tech. Rep., U.S. Department of Energy (2009).

[145] Erisman, J. W., Sutton, M. A., Galloway, J., Klimont, Z. & Winiwarter, W. How a century of ammonia synthesis changed the world. *Nat. Geosci.* **1**, 636–639 (2008).

[146] Green, J., L. An ammonia energy vector for the hydrogen economy. *Int. J. Hydrogen Energy* **7**, 355–359 (1982).

[147] Avery, W. H. A role for ammonia in the hydrogen economy. *Int. J. Hydrogen Energy* **13**, 761–773 (1988).

[148] Lan, R., Irvine, J. T. S. & Tao, S. Ammonia and related chemicals as potential indirect hydrogen storage materials. *Int. J. Hydrogen Energy* **37**, 1482–1494 (2012).

[149] Klerke, A., Christensen, C. H., Nørskov, J. K. & Vegge, T. Ammonia for hydrogen storage: challenges and opportunities. *J. Mater. Chem.* **18**, 2304 (2008).

[150] Christensen, C. H., Johannessen, T., Sørensen, R. Z. & Nørskov, J. K. Towards an ammonia-mediated hydrogen economy? *Catal. Today* **111**, 140–144 (2006).

[151] Industrial Efficiency Technology Database. Ammonia (2014). URL `http://ietd.iipnetwork.org/content/ammonia`. (Date accessed: June 15, 2014).

[152] GOV.UK. Fuel consumption (env01) (2014). URL `https://www.gov.uk/government/statistical-data-sets/env01-fuel-consumption`. (Date accessed January 20, 2015).

[153] U.S. Energy Information Administration. How much gasoline does the united states consume? (2014). URL `http://www.eia.gov/tools/faqs/faq.cfm?id=23&t=10`. (Date accessed January 20, 2015).

[154] Lan, R., Irvine, J. T. S. & Tao, S. Synthesis of ammonia directly from air and water at ambient temperature and pressure. *Sci. Rep.* **3**, 1145 (2013).

[155] Thomas, G. & Parks, G. Potential roles of ammonia in a hydrogen economy. Tech. Rep., U.S. Department of Energy (2006).

[156] Consultants, Q. Comparative quantitative risk analysis of motor gasoline, LPG, and anhydrous ammonia as an automotive fuel. Tech. Rep. (2009).

[157] Christensen, C. H., Sørensen, R. Z., Johannessen, T., Quaade, U. J., Honkala, K., Elmøe, T. D., Køhler, R. & Nørskov, J. K. Metal ammine complexes for hydrogen storage. *J. Mater. Chem.* **15**, 4106–4108 (2005).

[158] Sørensen, R. Z., Nielsen, L. J. E., Jensen, S., Hansen, O., Johannessen, T., Quaade, U. & Christensen, C. H. Catalytic ammonia decomposition: miniaturized production of CO_x-free hydrogen for fuel cells. *Catal. Commun.* **6**, 229–232 (2005).

[159] Mørch, C. S., Bjerre, A., Gøttrup, M. P., Sorenson, S. C. & Schramm, J. Ammonia/hydrogen mixtures in an SI-engine: Engine performance and analysis of a proposed fuel system. *Fuel* **90**, 854–864 (2011).

[160] Lutz, A. E., Larson, R. S. & Keller, J. O. Thermodynamic comparison of fuel cells to the carnot cycle. *Int. J. Hydogen Energy* **27**, 1103–1111 (2002).

[161] van Hassel, B. A., Pasini, J. M., McGee, R. C., Karra, J. R., Limarga, A. M., Holowczak, J., Fedchenia, I., Khalil, J., Rampone, J. C. & Brown, R. Advancement of systems designs and key engineering technologies for materials based hydrogen storage. Tech. Rep. (2012).

[162] Hejze, T., Besenhard, J. O., Kordesch, K., Cifrain, M. & Aronsson, R. R. Current status of combined systems using alkaline fuel cells and ammonia as a hydrogen carrier. *J. Power Sources* **176**, 490–493 (2008).

[163] Hacker, V. & Kordesch, K. Ammonia crackers. In Vielstich, W., Lamm, A. & Gasteiger, H. A. (eds.) *Handbook of Fuel Cells—Fundamentals, Technology and Applications*, vol. 3, 121–127 (John Wiley & Sons, Ltd, Chichester, 2003).

[164] Ganley, J. C., Thomas, F. S., Seebauer, E. G. & Masel, R. I. A priori catalytic activity correlations: the difficult case of hydrogen production from ammonia. *Catal. Lett.* **96**, 117–122 (2004).

[165] Schüth, F., Palkovits, R., Schlögl, R. & Su, D. S. Ammonia as a possible element in an energy infrastructure: catalysts for ammonia decomposition. *Energy Environ. Sci.* **5**, 6278–6289 (2012).

[166] Hansgen, D. A., Vlachos, D. G. & Chen, J. G. Using first principles to predict bimetallic catalysts for the ammonia decomposition reaction. *Nat. Chem.* **2**, 484–489 (2010).

[167] Appl, M. Ammonia. In *Ullmann's Encyclopedia of Industrial Chemistry* (Wiley-VCH, Weinheim, 2006), online edn.

[168] Choudhary, T. V., Sivadinarayana, C. & Goodman, D. W. Production of CO_x-free hydrogen for fuel cells via step-wise hydrocarbon reforming and catalytic dehydrogenation of ammonia. *Chem. Eng. J.* **93**, 69–80 (2003).

[169] Yin, S.-F., Zhang, Q.-H., Xu, B.-Q., Zhu, W.-X., Ng, C.-F. & Au, C. T. Investigation on the catalysis of CO_x-free hydrogen generation from ammonia. *J. Catal.* **224**, 384–396 (2004).

[170] Zhang, J., Müller, J.-O., Zheng, W., Wang, D., Su, D. & Schlögl, R. Individual Fe-Co

alloy nanoparticles on carbon nanotubes: Structural and catalytic properties. *Nano Lett.* **8**, 2738–2743 (2008).

[171] Yin, S. F., Xu, B. Q., Zhou, X. P. & Au, C. T. A mini-review on ammonia decomposition catalysts for on-site generation of hydrogen for fuel cell applications. *Appl. Catal., A* **277**, 1–9 (2004).

[172] Yin, S.-F., Xu, B.-Q., Ng, C.-F. & Au, C.-T. Nano Ru/CNTs: a highly active and stable catalyst for the generation of CO_x-free hydrogen in ammonia decomposition. *Appl. Catal., B* **48**, 237–241 (2004).

[173] Yin, S.-F., Xu, B.-Q., Wang, S.-J. & Au, C.-T. Nanosized Ru on high-surface-area superbasic ZrO_2-KOH for efficient generation of hydrogen via ammonia decomposition. *Appl. Catal., A* **301**, 202–210 (2006).

[174] Zhang, J., Xu, H., Ge, Q. & Li, W. Highly efficient Ru/MgO catalysts for NH_3 decomposition: Synthesis, characterization and promoter effect. *Catal. Commun.* **7**, 148–152 (2006).

[175] Yin, S. F., Xu, B. Q., Wang, S. J., Ng, C. F. & Au, C. T. Magnesia-carbon nanotubes (MgO-CNTs) nanocomposite: novel support of Ru catalyst for the generation of CO_x-free hydrogen from ammonia. *Catal. Lett.* **96**, 113–116 (2004).

[176] Li, Y., Yao, L., Song, Y., Liu, S., Zhao, J., Ji, W. & Au, C.-T. Core-shell structured microcapsular-like Ru@SiO_2 reactor for efficient generation of CO_x-free hydrogen through ammonia decomposition. *Chem. Commun.* **46**, 5298–300 (2010).

[177] Lorenzut, B., Montini, T., Pavel, C. C., Comotti, M., Vizza, F., Bianchini, C. & Fornasiero, P. Embedded Ru@ZrO_2 catalysts for H_2 production by ammonia decomposition. *ChemCatChem* **2**, 1096–1106 (2010).

[178] Wang, S. J., Yin, S. F., Li, L., Xu, B. Q., Ng, C. F. & Au, C. T. Investigation on modification of Ru/CNTs catalyst for the generation of CO_x-free hydrogen from ammonia. *Appl. Catal., B* **52**, 287–299 (2004).

[179] Hashimoto, K. & Toukai, N. Decomposition of ammonia over a catalyst consisting of ruthenium metal and cerium oxides supported on y-form zeolite. *J. Mol. Catal. A: Chem.* **161**, 171–178 (2000).

[180] García-García, F. R., Guerrero-Ruiz, A., Rodríguez-Ramos, I., Goguet, A., Shekhtman, S. O. & Hardacre, C. TAP studies of ammonia decomposition over Ru and Ir catalysts. *Phys. Chem. Chem. Phys.* **13**, 12892–12899 (2011).

[181] Hinrichsen, O., Rosowski, F., Hornung, A., Muhler, M. & Ertl, G. The kinetics of ammonia synthesis over Ru-based catalysts. *J. Catal.* **165**, 33–44 (1997).

[182] Jedynak, A., Kowalczyk, Z., Szmigiel, D., Raróg, W. & Zieliński, J. Ammonia decomposition over the carbon-based iron catalyst promoted with potassium. *Appl. Catal., A* **237**, 223–226 (2002).

[183] Kowalczyk, Z., Jodzis, S., Raróg, W., Zieliński, J. & Pielaszek, J. Effect of potassium and barium on the stability of a carbon-supported ruthenium catalyst for the synthesis of ammonia. *Appl. Catal., A* **173**, 153–160 (1998).

[184] Kowalczyk, Z., Jodzis, S., Raróg, W., Zieliński, J., Pielaszek, J. & Presz, A. Carbon-supported ruthenium catalyst for the synthesis of ammonia. the effect of the carbon support and barium promoter on the performance. *Appl. Catal., A* **184**, 95–102 (1999).

[185] Raróg-Pilecka, W., Szmigiel, D., Kowalczyk, Z., Jodzis, S. & Zielinski, J. Ammonia decomposition over the carbon-based ruthenium catalyst promoted with barium or cesium. *J. Catal.* **218**, 465–469 (2003).

[186] Raróg, W., Kowalczyk, Z., Sentek, J., Skladanowski, D. & Zieliński, J. Effect of K, Cs and Ba on the kinetics of NH_3 synthesis over carbon-based ruthenium catalysts. *Catal. Lett.* **68**, 163–168 (2000).

[187] Raróg, W., Kowalczyk, Z., Sentek, J., Skladanowski, D., Szmigiel, D. & Zieliński, J. Decomposition of ammonia over potassium promoted ruthenium catalyst supported on carbon. *Appl. Catal., A* **208**, 213–216 (2001).

[188] Szmigiel, D., Bielawa, H., Kurtz, M., Hinrichsen, O., Muhler, M., Raróg, W., Jodzis, S., Kowalczyk, Z., Znak, L. & Zielinski, J. The kinetics of ammonia synthesis over ruthenium-based catalysts: The role of barium and cesium. *J. Catal.* **205**, 205–212 (2002).

[189] Jedynak, A., Szmigiel, D., Raróg, W., Zieliński, J., Pielaszek, J., Dłużewski, P. & Kowalczyk, Z. Potassium-promoted carbon-based iron catalyst for ammonia synthesis. effect of Fe dispersion. *Catal. Lett.* **81**, 213–218 (2002).

[190] Thompson, S. P., Parker, J. E., Potter, J., Hill, T. P., Birt, A., Cobb, T. M., Yuan, F. & Tang, C. C. Beamline I11 at Diamond: a new instrument for high resolution powder diffraction. *Rev. Sci. Instrum.* **80**, 075107 (2009).

[191] Parker, J. E., Potter, J., Thompson, S. P., Lennie, A. R. & Tang, C. C. In situ gas supply system on the powder diffraction beamline I11 at Diamond Light Source. *Materials Science Forum* **706–709**, 1707–1712 (2012).

[192] Arblaster, J. W. Crystallographic properties of platinum. *Platinum Met. Rev.* **41**, 12–21 (1997).

[193] Hubbell, J. H. & Overbro, I. Relativistic atomic form factors and photon coherent scattering cross sections. *J. Phys. Chem. Ref. Data* **8**, 69–105 (1979).

[194] National Institute of Standards and Technology. Neutron scattering lengths and cross sections. URL `http://www.ncnr.nist.gov/resources/n-lengths/`. (Date accessed: July 13 2014).

[195] Hannon, A. C. Results on disordered materials from the general materials diffractometer, gem, at isis. *Nucl. Instrum. Methods Phys. Res., Sect. A* **551**, 88–107 (2005).

[196] Hull, S., Smith, R. I., David, W. I. F., Hannon, A. C., Mayers, J. & Cywinski, R. The polaris powder diffractometer at isis. *Physica B* **180–181**, 1000–1002 (1992).

[197] Bowron, D. T., Soper, A. K., Jones, K., Ansell, S., Birch, S., Norris, J., Perrott, L., Riedel, D., Rhodes, N. J., Wakefield, S. R., Botti, A., Ricci, M.-A., Grazzi, F. & Zoppi, M. NIMROD: The Near and InterMediate Range Order Diffractometer of the ISIS second target station. *Rev. Sci. Instrum.* **81**, 033905 (2010).

[198] Rietveld, H. M. A profile refinement method for nuclear and magnetic structures. *J. Appl. Crystallogr.* **2**, 65–71 (1969).

[199] Coelho, A. A. TOPAS Academic, Version 4.1 (1992-2004). URL `http://www.topas-academic.net/`. Coelho Software, Brisbane.

[200] Marquardt, D. W. An algorithm for least-squares estimation of nonlinear parameters. *J. Soc. Ind. Appl. Math.* **11**, 431–441 (1963).

[201] Coelho, A. A. A bound constrained conjugate gradient solution method as applied to crystallographic refinement problems. *J. Appl. Crystallogr.* **38**, 455–461 (2005).

[202] David, W. I. F. (personal communication).

[203] Ikeda, S. & Carpenter, J. M. Wide-energy-range, high-resolution measurements of neutron pulse shapes of polyethylene moderators. *Nucl. Instrum. Methods Phys. Res., Sect. A* **239**, 536–544 (1985).

[204] Soper, A. K. GudrunN, Version 5 (2012). URL `http://www.isis.stfc.ac.uk/instruments/sandals/data-analysis/gudrun8864.html/`.

[205] Soper, A. K. GudrunX, Version 5 (2012). URL `http://www.isis.stfc.ac.uk/instruments/sandals/data-analysis/gudrun8864.html/`.

[206] David, W. I. F., Makepeace, J. W., Callear, S. K., Hunter, H. M. A., Taylor, J. D., Wood, T. J. & Jones, M. O. Hydrogen production from ammonia using sodium amide. *J. Am. Chem. Soc.* **136**, 13082–13085 (2014).

[207] Palumbo, O., Paolone, A., Cantelli, R. & Chandra, D. Lithium nitride as hydrogen storage material. *Int. J. Hydrogen Energy* **33**, 3107–3110 (2008).

[208] Isobe, S., Ohnuki, S., David, W. I. F., Gutmann, M., Jones, M. O., Edwards, P. P., Ichikawa, T. & Kojima, Y. Variable temperature neutron diffraction studies of single crystals of $LiND_2$. *Int. J. Hydrogen Energy* **36**, 7909–7913 (2011).

[209] Zhang, F., Wang, Y. & Chou, M. Y. Theoretical investigation of intermediate phases between Li_2NH and $LiNH_2$. *Phys. Rev. B* **82**, 094112 (2010).

[210] Crivello, J.-C., Gupta, M., Černý, R., Latroche, M. & Chandra, D. Density functional study of Li_4NH and $Li_{1.5}NH_{1.5}$ as intermediary compounds during hydrogenation of Li_3N. *Phys. Rev. B* **81**, 104113 (2010).

[211] Yoon, D. N. & Lazarus, D. Pressure dependence of ionic conductivity in KCl, NaCl, KBr, and NaBr. *Phys. Rev. B* **5**, 4935–4945 (1972).

[212] Symeonides, C. I. Defect volume for Schottky defect formation and cation vacancy migration in LiH. *J. Alloys Compd.* **478**, 820–822 (2009).

[213] Khawam, A. & Flanagan, D. R. Solid-state kinetic models: basics and mathematical fundamentals. *J. Phys. Chem. B* **110**, 17315–17328 (2006).

[214] Lide, D. R. (ed.) *CRC Handbook of Chemistry and Physics, 88th Edition* (CRC Press, 2007).

[215] Isobe, S., Ichikawa, T., Tokoyoda, K., Hanada, N., Leng, H., Fujii, H. & Kojima, Y. Evaluation of enthalpy change due to hydrogen desorption for lithium amide/imide system by differential scanning calorimetry. *Thermochim. Acta* **468**, 35–38 (2008).

[216] Hino, S., Ogita, N., Udagawa, M., Ichikawa, T. & Kojima, Y. Thermodynamic properties of lithium amide under hydrogen pressure determined by raman spectroscopy. *J. Appl. Phys.* **105**, 023527 (2009).

[217] Motors, T. Your questions answered—Tesla Motors. URL `http://www.teslamotors.com/goelectric#charging`. (Date accessed: June 30, 2013).

[218] Blomqvist, A., Araújo, C. M., Scheicher, R., Srepusharawoot, P., Li, W., Chen, P. & Ahuja, R. Hydrogen as promoter and inhibitor of superionicity: A case study on Li−N−H systems. *Phys. Rev. B* **82**, 1–5 (2010).

[219] Bull, D. J., Weidner, E., Shabalin, I. L., Telling, M. T. F., Jewell, C. M., Gregory, D. H. & Ross, D. K. Pressure-dependent deuterium reaction pathways in the Li-N-D system. *Phys. Chem. Chem. Phys.* **12**, 2089–2097 (2010).

[220] Huq, A., Richardson, J. W., Maxey, E. R. & Chandra, D. Structural studies of deuteration and dedeuteration of Li_3N by use of in situ neutron diffraction. *J. Phys. Chem. C* **111**, 10712–10717 (2007).

[221] Chaudhuri, S., Graetz, J., Ignatov, A., Reilly, J. J. & Muckerman, J. T. Understanding the role of Ti in reversible hydrogen storage as sodium alanate: a combined experimental and density functional theoretical approach. *J. Am. Chem. Soc.* **128**, 11404–11415 (2006).

[222] Bale, C. W. The li-ti (lithium-titanium) system. *Bull. Alloy Phase Diagr.* **10**, 135–138 (1989).

[223] Tsumuraya, T., Shishidou, T. & Oguchi, T. Theoretical analysis of x-ray absorption spectra of Ti compounds used as catalysts in lithium amide/imide reactions. *Phys. Rev. B* **77**, 235114 (2008).

[224] Pinkerton, F. E. Decomposition kinetics of lithium amide for hydrogen storage materials. *J. Alloys Compd.* **400**, 76–82 (2005).

[225] Shaw, L. L., Osborn, W., Markmaitree, T. & Wan, X. The reaction pathway and rate-limiting step of dehydrogenation of the $LiHN_2$ + LiH mixture. *J. Power Sources* **177**, 500–505 (2008).

[226] Hu, Y. H. & Ruckenstein, E. Ultrafast reaction between Li_3N and $LiNH_2$ to prepare the effective hydrogen storage material Li_2NH. *Ind. Eng. Chem. Res.* **45**, 4993–4998 (2006).

[227] Michigoe, A., Hasegawa, T., Ogita, N., Ichikawa, T., Kojima, Y., Isobe, S. & Udagawa, M. Raman scattering study of hydrogen storage material $LiNH_2$. *J. Phys. Soc. Jpn.* **81**, 094603 (2012).

[228] Song, Y. & Guo, Z. Electronic structure, stability and bonding of the Li-N-H hydrogen storage system. *Phys. Rev. B* **74**, 195120 (2006).

[229] Yamamoto, H., Miyaoka, H., Hino, S., Nakanishi, H., Ichikawa, T. & Kojima, Y. Recyclable hydrogen storage system composed of ammonia and alkali metal hydride. *Int. J. Hydrogen Energy* **34**, 9760–9764 (2009).

[230] Markmaitree, T., Osborn, W. & Shaw, L. Comparisons between MgH_2- and LiH-containing systems for hydrogen storage applications. *Int. J. Hydrogen Energy* **33**, 3915–3924 (2008).

[231] Markmaitree, T., Osborn, W. & Shaw, L. L. Comparative studies of reaction rates of NH_3 with MgH_2 and lih. *J. Power Sources* **180**, 535–538 (2008).

[232] Zhang, J. & Hu, Y. H. Intermediate species and kinetics of lithium imide decomposition. *Int. J. Hydrogen Energy* **37**, 10467–10472 (2012).

[233] Miyaoka, H., Ichikawa, T., Hino, S. & Kojima, Y. Compressed hydrogen production via reaction between liquid ammonia and alkali metal hydride. *Int. J. Hydrogen Energy* **36**, 8217–8220 (2011).

[234] Miyaoka, H., Fujii, H., Yamamoto, H., Hino, S., Nakanishi, H., Ichikawa, T. & Kojima, Y. Improvement of reaction kinetics by metal chloride on ammonia and lithium hydride system. *Int. J. Hydrogen Energy* **37**, 16025–16030 (2012).

[235] Kojima, Y., Tange, K., Hino, S., Isobe, S., Tsubota, M., Nakamura, K., Nakatake, M., Miyaoka, H., Yamamoto, H. & Ichikawa, T. Molecular hydrogen carrier with activated nanohydride and ammonia. *J. Mater. Res.* **24**, 2185–2190 (2009).

[236] Soper, A. K. Paartial structure factors from disordered materials diffraction data: An approach using empirical potential structure refinement. *Phys. Rev. B* **72**, 104204 (2005).

[237] Caubere, P. Applications of sodamide-containing "complex bases" in organic synthesis. *Acc. Chem. Res.* **7**, 301–308 (1974).

[238] Liu, A. & Song, Y. In situ high-pressure study of sodium amide by raman and infrared spectroscopies. *J. Phys. Chem. B* **115**, 7–13 (2011).

[239] Sheppard, D. A., Paskevicius, M. & Buckley, C. E. Hydrogen desorption from the $NaNH_2$-MgH_2 system. *J. Phys. Chem. C* **115**, 8407–8413 (2011).

[240] Titherley, A. W. Sodium, potassium, and lithium amides. *J. Chem. Soc.* **65**, 504–522 (1894).

[241] Sakurazawa, K. & Hara, R. The synthesis of sodium amide from its elements and the thermal decomposition of it, ii. *J. Soc. Chem. Ind. Jpn. Suppl.* **40**, 10 (1937).

[242] Aika, K.-I., Kawahara, T., Murata, S. & Onishi, T. Promoter effect of alkali metal oxides and alkali earth metal oxides on active carbon-supported ruthenium catalyst for ammonia synthesis. *Bull. Chem. Soc. Jpn.* **63**, 1221–1225 (1990).

[243] Chellappa, A. S., Fischer, C. M. & Thomson, W. J. Ammonia decomposition kinetics over Ni-Pt/Al_2O_3 for pem fuel cell applications. *Appl. Catal., A* **227**, 231–240 (2002).

[244] McCabe, R. W. Kinetics of ammonia decomposition on nickel. *J. Catal.* **79**, 445–450 (1983).

[245] Tsai, W. & Weinberg, W. H. Steady-state decomposition of ammonia on the Ru(001) surface. *J. Phys. Chem.* **91**, 5302–5307 (1987).

[246] Vajo, J. J., Tsai, W. & Weinberg, W. H. Steady-state decomposition of ammonia on the Pt(110)-(1 $\times$ 2) surface. *J. Phys. Chem.* **90**, 6531–6535 (1986).

[247] Prasad, V., Karim, A. M., Arya, A. & Vlachos, D. G. Assessment of overall rate expressions and multiscale, microkinetic model uniqueness via experimental data injection: Ammonia decomposition on Ru / γ-Al_2O_3 for hydrogen production. *Ind. Eng. Chem. Res.* **48**, 5255–5265 (2009).

[248] Bradford, M. C. J., Fanning, P. E. & Vannice, M. A. Kinetics of NH_3 decomposition over well dispersed Ru. *J. Catal.* **172**, 479–484 (1997).

[249] Fink, J. K. & Leibowwitz, L. Thermodynamic and transport properties of sodium liquid and vapor. Tech. Rep. (1995).

[250] Perry, D. L. *Handbook of Inorganic Compounds, Second Edition* (CRC Press, 2011).

[251] Ogilvie, A. D., Makepeace, J. W., Hore, K., Ramirez-Cuesta, A. J., Apperley, D. C., Mitchels, J. M., Edwards, P. P. & Sartbaeva, A. Catalyst-free synthesis of sodium amide nanoparticles encapsulated in silica gel. *Chem. Phys.* **427**, 61–65 (2013).

[252] Demir-Cakan, R., Tang, W. S., Darwiche, A. & Janot, R. Modification of the hydrogen storage properties of Li_3N by confinement into mesoporous carbons. *Energy Environ. Sci.* **4**, 3625–3631 (2011).

[253] Xia, G., Li, D., Chen, X., Tan, Y., Tang, Z., Guo, Z., Liu, H., Liu, Z. & Yu, X. Carbon-coated Li_3N nanofibers for advanced hydrogen storage. *Adv. Mater.* **25**, 6238–6244 (2013).

[254] Yoshida, A., Yoshimura, H., Terada, T., Nakayama, Y., Kuno, H., Miyao, T. & Naito, S. Preparation of graphite supported Li-N-H hydrogen storage material from Li-graphite intercalation compound and their unique hydrogen release property. *Int. J. Hydrogen Energy* **36**, 6751–6755 (2011).

[255] Johnson, S. R., David, W. I. F., Royse, D. M., Sommariva, M., Tang, C. Y., Fabbiani, F. P. A., Jones, M. O. & Edwards, P. P. The monoammoniate of lithium borohydride, $Li(NH_3)BH_4$: an effective ammonia storage compound. *Chem. Asian J.* **4**, 849–854 (2009).

[256] Marangoni. Toyota GT86-R marangoni eco explorer: sport and technology in the new 2013 show car, fitted with marangoni "M-Power EvoRed" tyres (2013). URL `http://www.marangonipress.com/SinglePR.aspx?prid=545`. (Date accessed: February 28, 2013).

[257] Palumbo, O., Paolone, A., Rispoli, P., D'Orazio, A., Cantelli, R. & Chandra, D. The decomposition reaction of lithium amide studied by anelastic spectroscopy and thermogravimetry. *Int. J. Mater. Res.* **99**, 487–490 (2008).

[258] Markmaitree, T., Ren, R. & Shaw, L. L. Enhancement of lithium amide to lithium imide transition via mechanical activation. *J. Phys. Chem. B* **110**, 20710–20718 (2006).

[259] Pawley, G. S. Unit-cell refinement from powder diffraction scans. *J. Appl. Cryst.* **14**, 357–361 (1981).

[260] Wang, J., Du, Y., Xu, H., Jiang, C., Kong, Y., Sun, L. & Liu, Z.-K. Native defects in $LiNH_2$: A first-principles study. *Phys. Rev. B* **84**, 024107 (2011).

[261] Leng, H. Y., Ichikawa, T., Hino, S., Hanada, N., Isobe, S. & Fujii, H. Synthesis and

decomposition reactions of metal amides in metal-N-H hydrogen storage system. *J. Power Sources* **156**, 166–170 (2006).

[262] Bhattacharya, S., Wu, G., Chen, P., Feng, Y. P. & Das, G. P. Lithium calcium imide [$Li_2Ca(NH)_2$] for hydrogen storage: Structural and thermodynamic properties. *J. Phys. Chem. B* **112**, 11381–11384 (2008).

[263] Wu, H. Structure of ternary imide $Li_2Ca(NH)_2$ and hydrogen storage mechanisms in amide-hydride system. *J. Am. Chem. Soc.* **130**, 6515–6522 (2008).

[264] Pottmaier, D., Dolci, F., Orlova, M., Vaughan, G., Fichtner, M., Lohstroh, W. & Baricco, M. Hydrogen release and structural transformations in $LiNH_2$-MgH_2 systems. *J. Alloys Compd.* **509**, 5719–5723 (2011).

[265] Rijssenbeek, J., Gao, Y., Hanson, J., Huang, Q., Jones, C. & Toby, B. Crystal structure determination and reaction pathway of amide- hydride mixtures. *J. Alloys Compd.* **454**, 233–244 (2008).

[266] Durojaiye, T., Hayes, J. & Goudy, A. Rubidium hydride: An exceptional dehydrogenation catalyst for the lithium amide/magnesium hydride system. *J. Phys. Chem. C* **117**, 6554–6560 (2013).

[267] Wang, J., Liu, T., Wu, G., Li, W., Liu, Y., Araújo, C. M., Scheicher, R. H., Blomqvist, A., Ahuja, R., Xiong, Z., Yang, P., Gao, M., Pan, H. & Chen, P. Potassium-modified $Mg(NH_2)_2$/2LiH system for hydrogen storage. *Angew. Chem. Int. Ed.* **48**, 5828–5832 (2009).

[268] Flacke, F., Kockelmann, W. & Jacobs, H. Synthesis and crystal structure determination of $Na_2[Sn(NH_2)_6]$ and $Na_2[Sn(ND_2)_6]$ by x-ray and neutron diffraction. *J. Alloys Compd.* **255**, 149–154 (1997).

[269] Jacobs, H., Kockelkorn, J. & Birkenbeul, J. Struktur und eigenschaften der ternären metallamide $NaCa(NH_2)_3$, $KBa(NH_2)_3$, $RbBa(NH_2)_3$, $RbEu(NH_2)_3$ und $RbSr(NH_2)_3$. *J. Less Common Met.* **87**, 215–224 (1982).

[270] Jacobs, H. & Fröhling, B. $Na_2Mn(NH_2)_4$: Ein neuer schichtenstrukturtyp. *Z. Anorg. Allg. Chem.* **623**, 1108–1112 (1997).

[271] Juza, R. & Schumacher, H. Zur kenntnis der erdalkalimetallamide. *Z. Anorg. Allg. Chem.* **324**, 278–286 (1963).

[272] Ali, S. I. Reactions of silicon tetrabromide and -iodide with potassium amide in liquid ammonia. *Z. Anorg. Allg. Chem.* **379**, 68–71 (1970).

Appendix A

Crystallographic Details

Crystallographic parameters used for Rietveld refinement of diffraction data in this thesis. All listed lattice parameters are in Angstrom units.

Lithium amide ($LiNH_2$), $I\bar{4}$, a=b=5.04309(7), c=10.2262(3), $\alpha = \beta = \gamma = 90°$					
Atom	Wycoff site	x	y	z	Occupancy
Li (1)	2a	0	0	0	1
Li (2)	2d	0	0.5	-0.25	1
Li (3)	4f	0	0.5	0.003	1
N	8g	-0.234	-0.246	-0.113	1
H (1)	8g	-0.23	-0.18	-0.194	1
H (2)	8g	-0.37	-0.35	-0.118	1
*Analogous structure used for deuterated lithium amide, $LiND_2$					
Lithium imide (Li_2NH), $Fm\bar{3}m$, a=b=c=5.0769, $\alpha = \beta = \gamma = 90°$					
Atom	Wycoff site	x	y	z	Occupancy
Li	8c	0.25	0.25	0.25	1

N	4a	0	0	0	1
*H atoms omitted for XRD analysis					
Non-stoichiometric Li-N-H ($Li_{1+x}NH_{2-x}$, $0 \leq x \leq 1$), $Fm\bar{3}m$, a=b=c=x*a_{imide}+(1-x)*a_{amide}, $\alpha = \beta = \gamma = 90°$					
Atom	Wycoff site	x	y	z	Occupancy
Li	8c	0.25	0.25	0.25	0.5+0.5*x
N	4a	0	0	0	1
*H atoms omitted for XRD analysis					
Lithium hydride (LiH), $Fm\bar{3}m$, a=b=c=4.08321(6), $\alpha = \beta = \gamma = 90°$					
Atom	Wycoff site	x	y	z	Occupancy
Li	4a	0	0	0	1
H	4b	0.5	0.5	0.5	1
*Analogous structure used for deuterated lithium hydride (LiD)					
Lithium oxide (Li_2O), $Fm\bar{3}m$, a=b=c=4.610, $\alpha = \beta = \gamma = 90°$					
Atom	Wycoff site	x	y	z	Occupancy
Li	8c	0.25	0.25	0.25	1
O	4a	0	0	0	1
Deuterated lithium imide-amide ($Li_{2-p}NH_{1+p}$, $0 \leq p \leq 1$), $Fm\bar{3}m$, a=b=c=approx. 5.0769, $\alpha = \beta = \gamma = 90°$					
Atom	Wycoff site	x	y	z	Occupancy
Li	8c	0.25	0.25	0.25	1-p/2
N	4a	0	0	0	1

D (1)	192l	0.163	0.106	0.058	(1-p)/48
D (2)	96j	0	-0.081	0.186	p/24
D (3)	96j	0.165	0.118	0	p/24

Sodium hydride (NaH), $Fm\bar{3}m$, a=b=c=4.89, $\alpha = \beta = \gamma = 90°$

Atom	Wycoff site	x	y	z	Occupancy
Na	4a	0	0	0	1
H	4b	0.5	0.5	0.5	1

*Analogous structure used for deuterated sodium hydride (NaD)

Sodium amide ($NaNH_2$), $Fddd$, a= 8.949(6), b=10.456(5), c=8.061(4), $\alpha = \beta = \gamma = 90°$

Atom	Wycoff site	x	y	z	Occupancy
Na	16f	0	0.1442	0	1
N	16g	0	0	0.2344	1
H	32h	0.0388	0.9386	0.3166	1

*Analogous structure used for deuterated sodium amide ($NaND_2$)

Sodium (Na), $Im\bar{3}m$, a=b=c=4.30, $\alpha = \beta = \gamma = 90°$

Atom	Wycoff site	x	y	z	Occupancy
Na	2a	0	0	0	1

Lithium magnesium imide ($Li_2Mg(NH)_2$), $Iba2$, a=9.8937, b=4.9914, c=5.2238, $\alpha = \beta = \gamma = 90°$

Atom	Wycoff site	x	y	z	Occupancy
Li (1)	8c	-0.001	0.5074	0.2495	0.28125
Mg (1)	8c	-0.001	0.5074	0.2495	0.21875
Li (2)	8c	0.2563	0.0016	0.7547	0.71875

Mg (2)	8c	0.2563	0.0016	0.7547	0.28125
N	8c	0.1330	0.2766	0.010	1
H	8c	0.0610	0.1482	-0.0657	1

Lithium calcium imide ($Li_2Ca(NH)_2$), $P\bar{3}m1$,
a=b=3.5664(3), c=5.9540(8), $\alpha = \beta = \gamma = 90°$

Atom	Wycoff site	x	y	z	Occupancy
Ca	1b	0	0	0.5	1
Li	2d	0.3333	0.6667	0.8841	1
N	2d	0.3333	0.6667	0.2565	1

*Hydrogen atoms were omitted

Calcium imide (CaNH), $Fm\bar{3}m$, a=b=c=5.143(1),
$\alpha = \beta = \gamma = 90°$

Atom	Wycoff site	x	y	z	Occupancy
Ca	4a	0	0	0	1
N	4b	0.5	0.5	0.5	1
H	24e	0	0	0.35	0.167

Titanium (III) chloride ($TiCl_3$), $P\bar{3}1m$, a=b=6.14, c=5.85,
$\alpha = \beta = \gamma = 90°$

Atom	Wycoff number	x	y	z	Occupancy
Ti	2c	0.3333	0.6667	0	1
Cl	6k	0.3333	0	-0.25	1

Appendix B

Selected diffraction patterns 1: *In situ* diffraction on Li-N-H system

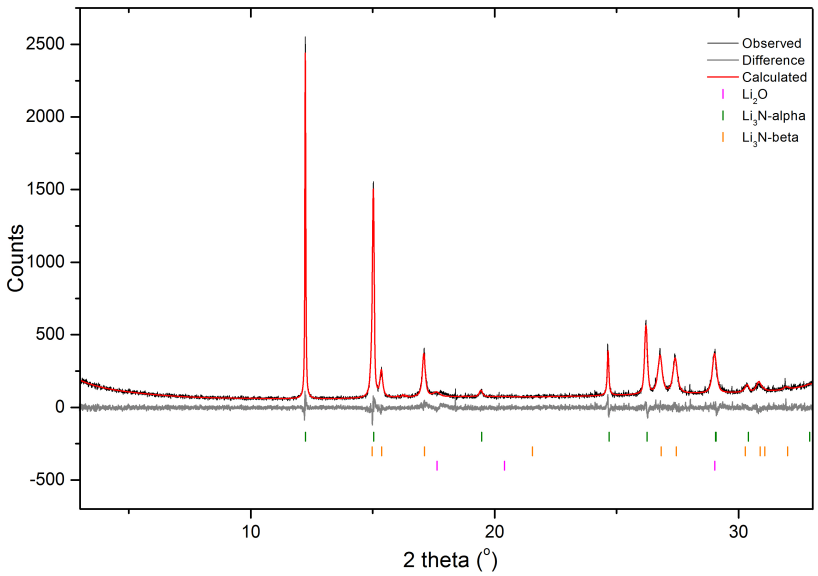

Figure B.1: X-ray powder diffraction pattern (3 minutes) of the Li-N-H system at the beginning of Process A in Table 3.1 (lithium nitride starting material). Tick marks indicate the phases refined in the Rietveld analysis. The observed pattern is shown in black, the calculated pattern in red, and the difference between the two patterns is shown in grey. The Rwp for the fit to the data was 8.291.

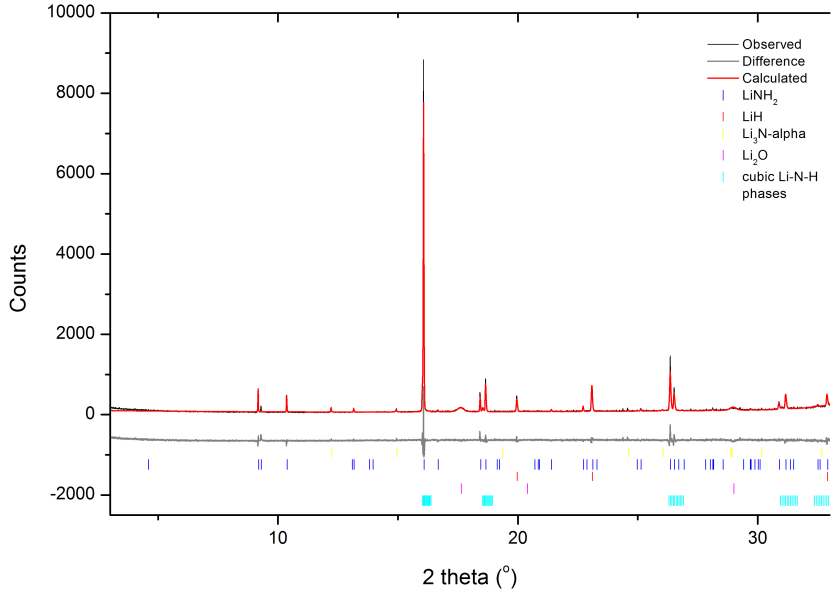

Figure B.2: X-ray powder diffraction pattern (3 minutes) of the Li-N-H system at the beginning of Process B in Table 3.1. Tick marks indicate the phases refined in the Rietveld analysis. The observed pattern is shown in black, the calculated pattern in red, and the difference between the two patterns is shown in grey. The Rwp for the fit to the data was 9.143.

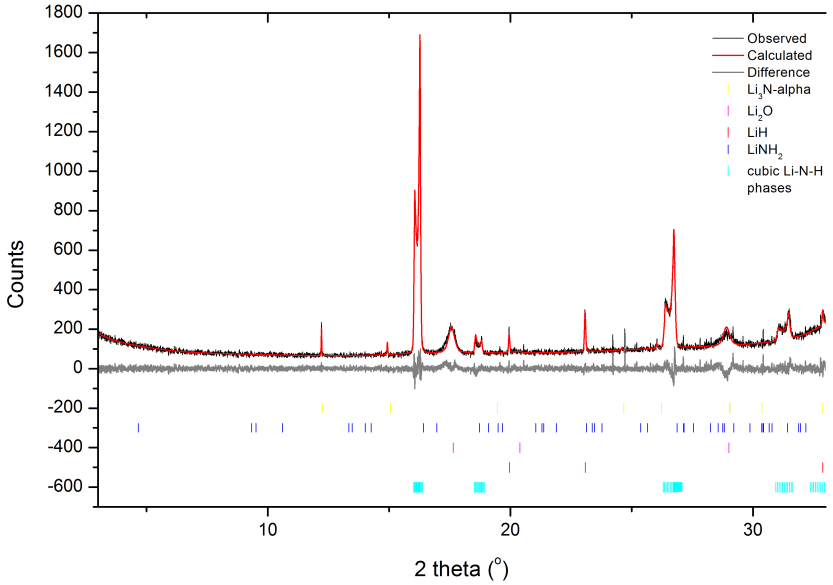

Figure B.3: X-ray powder diffraction pattern (3 minutes) of the Li-N-H system at the beginning of Process C in Table 3.1. Tick marks indicate the phases refined in the Rietveld analysis. The observed pattern is shown in black, the calculated pattern in red, and the difference between the two patterns is shown in grey. The Rwp for the fit to the data was 8.466.

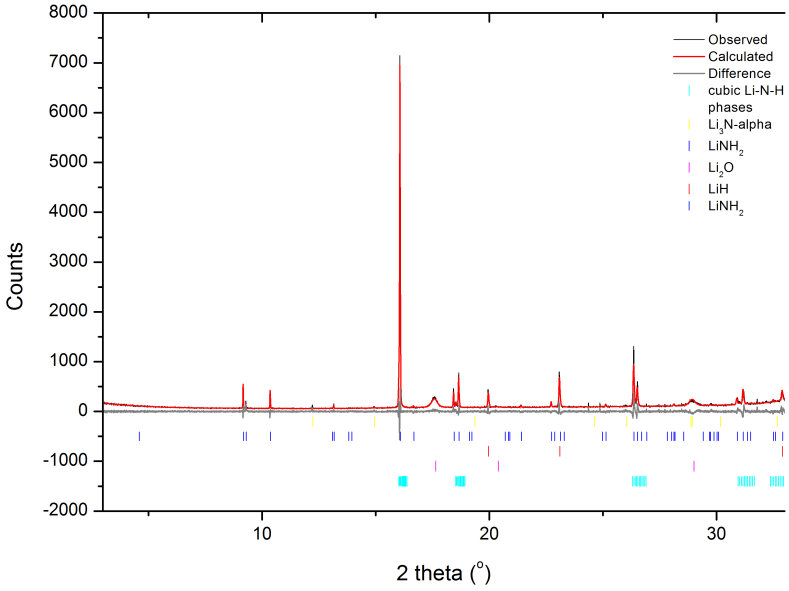

Figure B.4: X-ray powder diffraction pattern (3 minutes) of the Li-N-H system at the beginning of Process D in Table 3.1. Tick marks indicate the phases refined in the Rietveld analysis. The observed pattern is shown in black, the calculated pattern in red, and the difference between the two patterns is shown in grey. The Rwp for the fit to the data was 9.402.

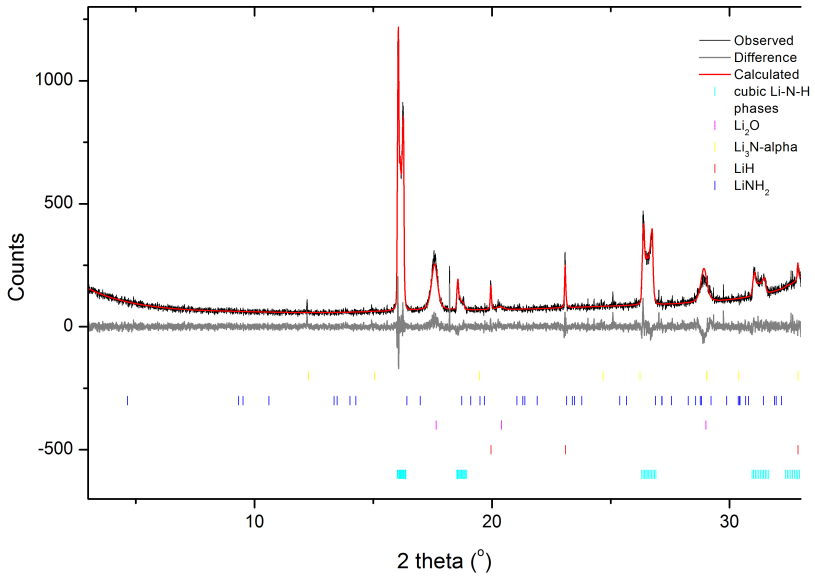

Figure B.5: X-ray powder diffraction pattern (3 minutes) of the Li-N-H system at the beginning of Process E in Table 3.1. Tick marks indicate the phases refined in the Rietveld analysis. The observed pattern is shown in black, the calculated pattern in red, and the difference between the two patterns is shown in grey. The Rwp for the fit to the data was 8.782.

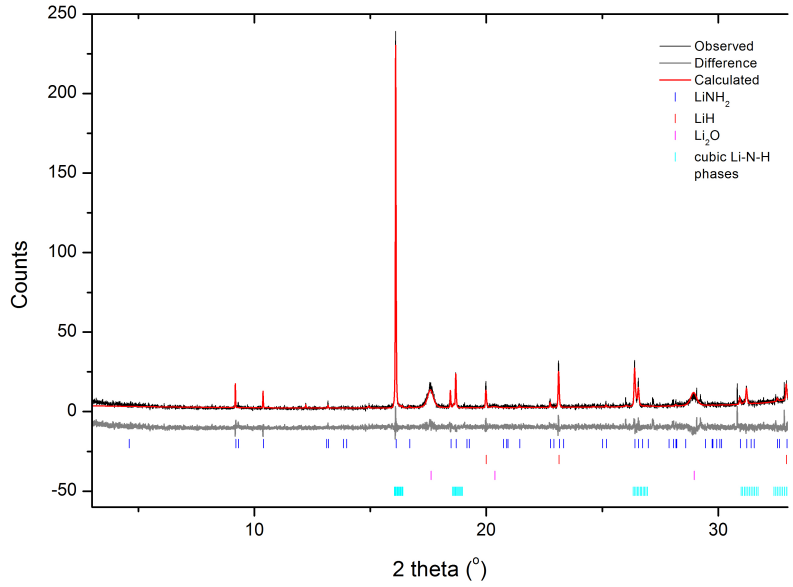

Figure B.6: X-ray powder diffraction pattern (1 minute) of the Li-N-H system at the beginning of Process F in Table 3.1. Tick marks indicate the phases refined in the Rietveld analysis. The observed pattern is shown in black, the calculated pattern in red, and the difference between the two patterns is shown in grey. The Rwp for the fit to the data was 20.239.

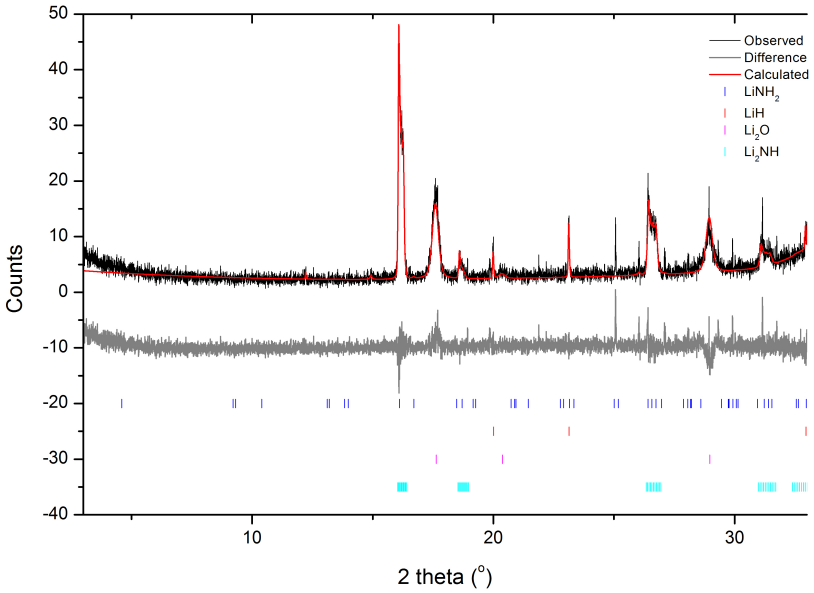

Figure B.7: X-ray powder diffraction pattern (1 minute) of the Li-N-H system at the beginning of Process G in Table 3.1. Tick marks indicate the phases refined in the Rietveld analysis. The observed pattern is shown in black, the calculated pattern in red, and the difference between the two patterns is shown in grey. The Rwp for the fit to the data was 20.4.

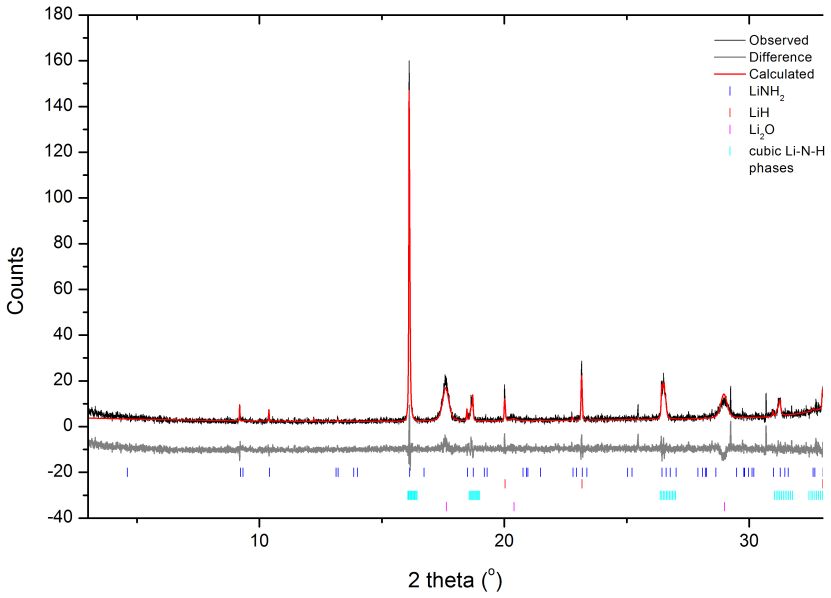

Figure B.8: X-ray powder diffraction pattern (1 minute) of the Li-N-H system at the beginning of Process H in Table 3.1. Tick marks indicate the phases refined in the Rietveld analysis. The observed pattern is shown in black, the calculated pattern in red, and the difference between the two patterns is shown in grey. The Rwp for the fit to the data was 20.042.

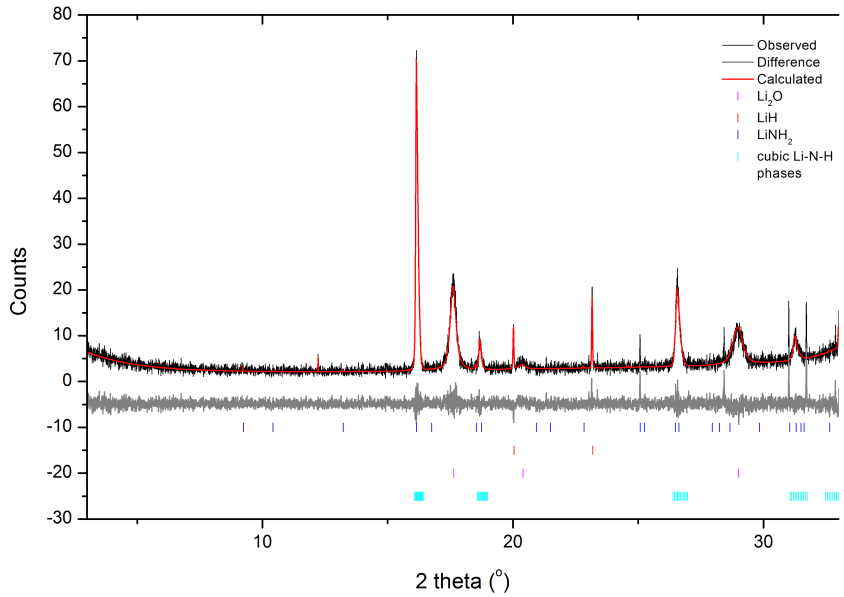

Figure B.9: X-ray powder diffraction pattern (1 minute) of the Li-N-H system at the beginning of Process I in Table 3.1. Tick marks indicate the phases refined in the Rietveld analysis. The observed pattern is shown in black, the calculated pattern in red, and the difference between the two patterns is shown in grey. The Rwp for the fit to the data was 19.896.

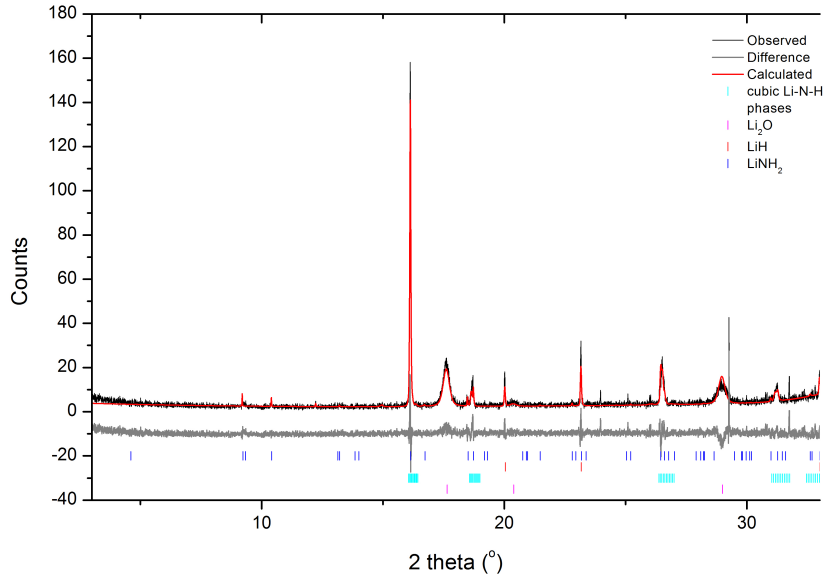

Figure B.10: X-ray powder diffraction pattern (1 minute) of the Li-N-H system at the beginning of Process J in Table 3.1. Tick marks indicate the phases refined in the Rietveld analysis. The observed pattern is shown in black, the calculated pattern in red, and the difference between the two patterns is shown in grey. The Rwp for the fit to the data was 20.527.

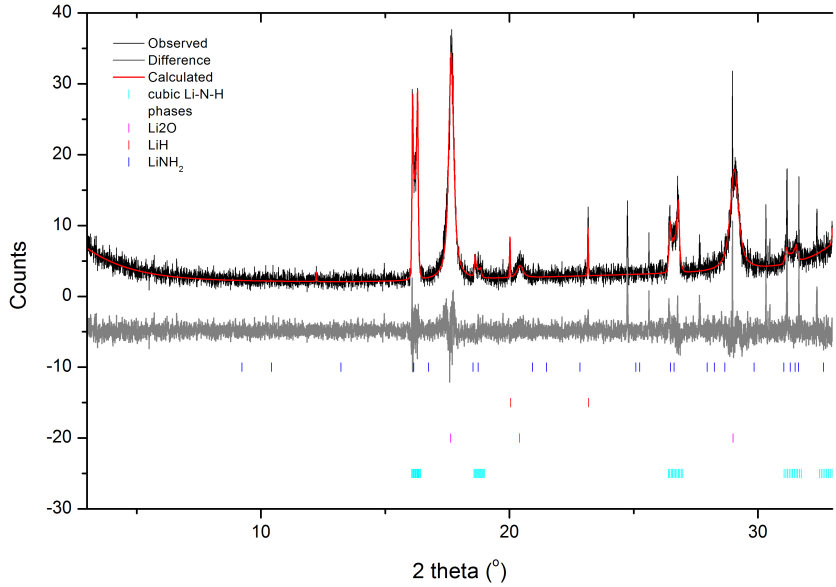

Figure B.11: X-ray powder diffraction pattern (1 minute) of the Li-N-H system at the beginning of Process K in Table 3.1. Tick marks indicate the phases refined in the Rietveld analysis. The observed pattern is shown in black, the calculated pattern in red, and the difference between the two patterns is shown in grey. The Rwp for the fit to the data was 20.661.

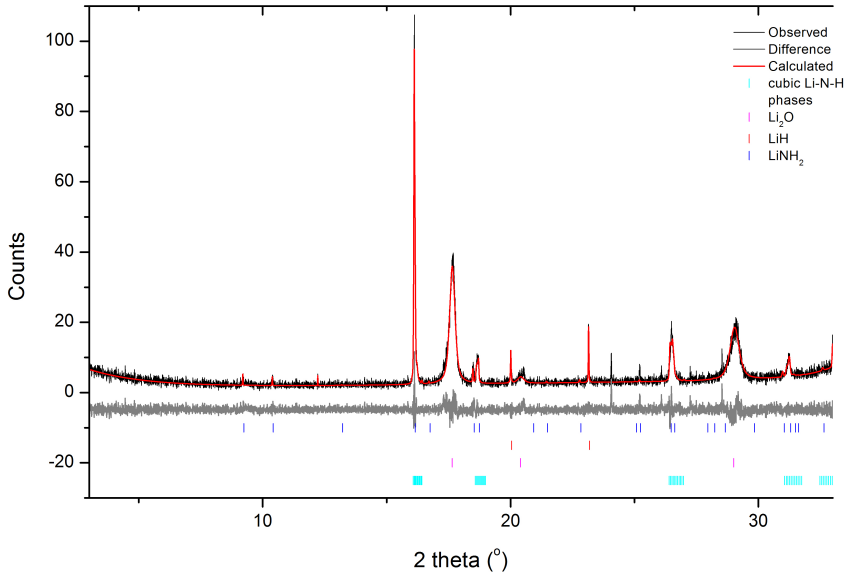

Figure B.12: X-ray powder diffraction pattern (1 minute) of the Li-N-H system at the end of Process K in Table 3.1. Tick marks indicate the phases refined in the Rietveld analysis. The observed pattern is shown in black, the calculated pattern in red, and the difference between the two patterns is shown in grey. The Rwp for the fit to the data was 20.176.

Appendix C

Selected diffraction patterns 2: *In situ* diffraction on $TiCl_3$-doped Li-N-H system

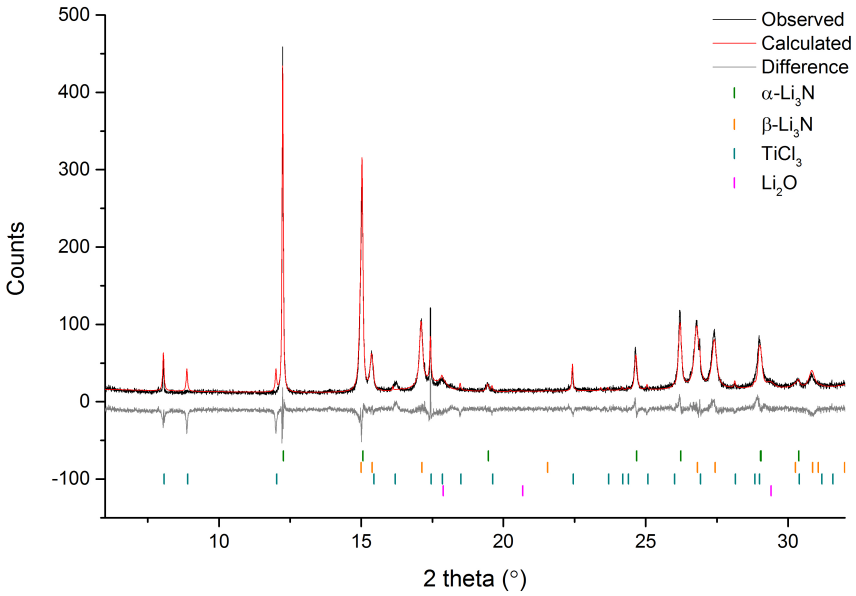

Figure C.1: X-ray powder diffraction pattern (1 minute) of the $TiCl_3$-doped Li-N-H system at the beginning of Process L in Table 3.3 (doped lithium nitride starting material). Tick marks indicate the phases refined in the Rietveld analysis. The observed pattern is shown in black, the calculated pattern in red, and the difference between the two patterns is shown in grey. The Rwp for the fit to the data was 16.099.

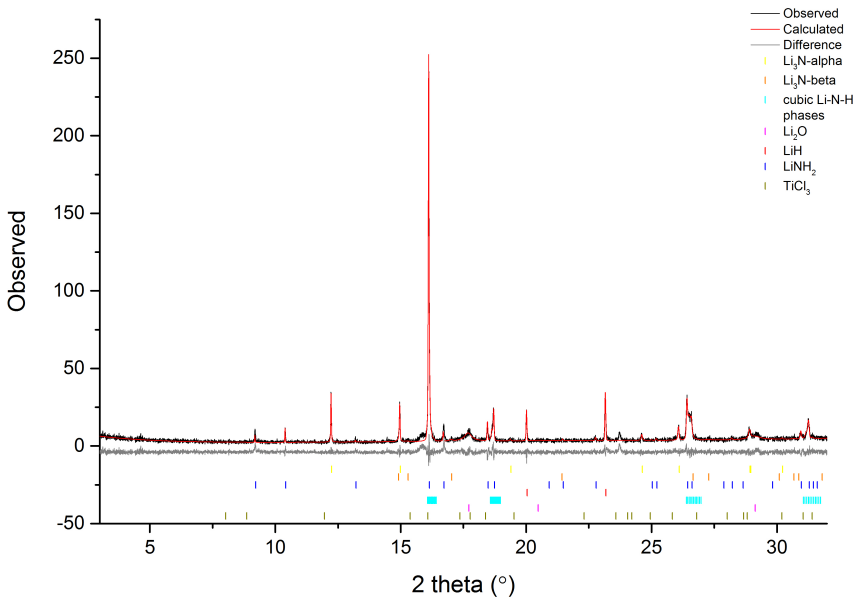

Figure C.2: X-ray powder diffraction pattern (1 minute) of the $TiCl_3$-doped Li-N-H system at the beginning of Process M in Table 3.3 (doped lithium nitride starting material). Tick marks indicate the phases refined in the Rietveld analysis. The observed pattern is shown in black, the calculated pattern in red, and the difference between the two patterns is shown in grey. The Rwp for the fit to the data was 20.308.

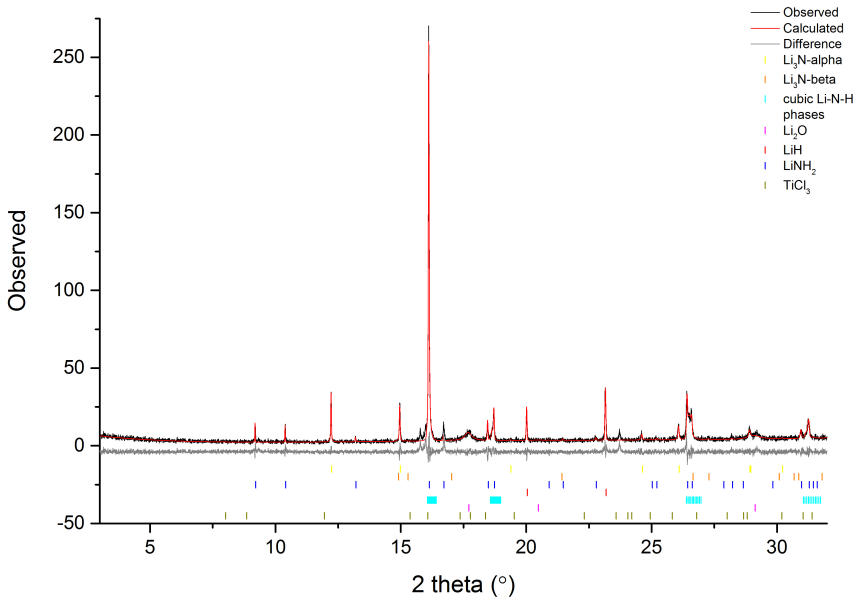

Figure C.3: X-ray powder diffraction pattern (1 minute) of the $TiCl_3$-doped Li-N-H system at the beginning of Process N in Table 3.3 (doped lithium nitride starting material). Tick marks indicate the phases refined in the Rietveld analysis. The observed pattern is shown in black, the calculated pattern in red, and the difference between the two patterns is shown in grey. The Rwp for the fit to the data was 20.633.

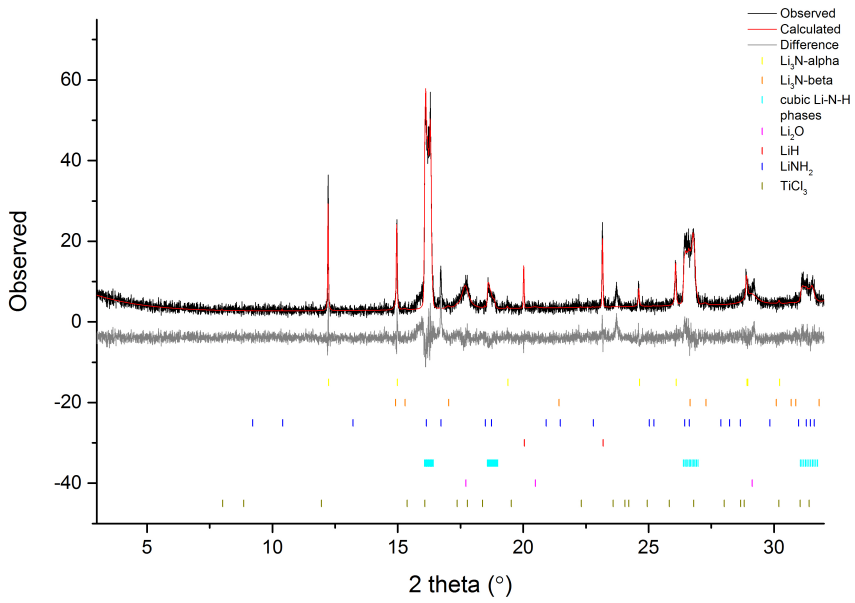

Figure C.4: X-ray powder diffraction pattern (1 minute) of the $TiCl_3$-doped Li-N-H system at the beginning of Process O in Table 3.3 (doped lithium nitride starting material). Tick marks indicate the phases refined in the Rietveld analysis. The observed pattern is shown in black, the calculated pattern in red, and the difference between the two patterns is shown in grey. The Rwp for the fit to the data was 19.704.

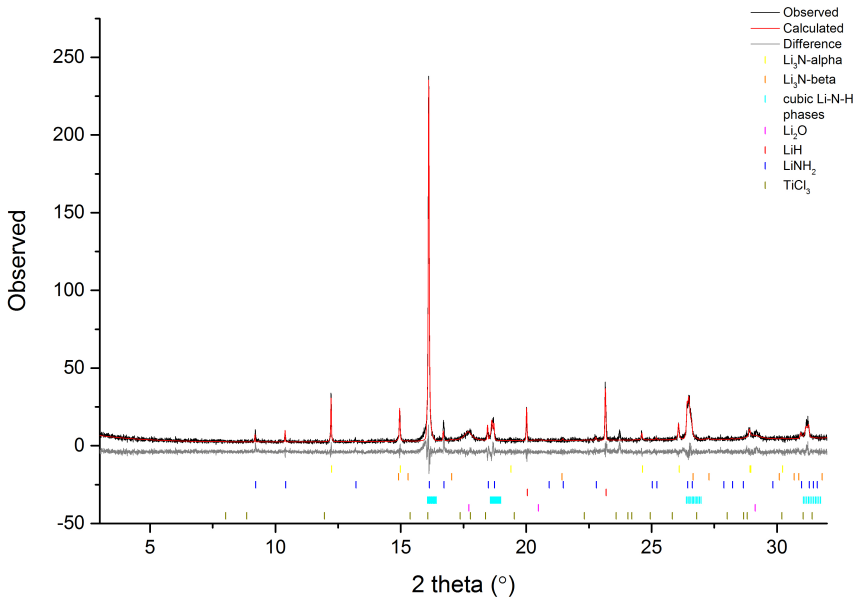

Figure C.5: X-ray powder diffraction pattern (1 minute) of the $TiCl_3$-doped Li-N-H system at the beginning of Process P in Table 3.3 (doped lithium nitride starting material). Tick marks indicate the phases refined in the Rietveld analysis. The observed pattern is shown in black, the calculated pattern in red, and the difference between the two patterns is shown in grey. The Rwp for the fit to the data was 20.271.

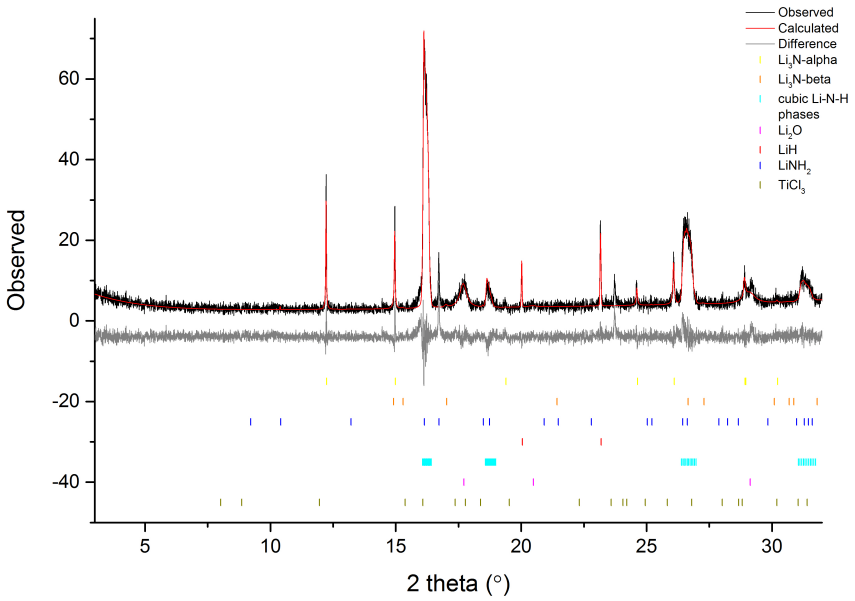

Figure C.6: X-ray powder diffraction pattern (1 minute) of the $TiCl_3$-doped Li-N-H system at the beginning of Process Q in Table 3.3 (doped lithium nitride starting material). Tick marks indicate the phases refined in the Rietveld analysis. The observed pattern is shown in black, the calculated pattern in red, and the difference between the two patterns is shown in grey. The Rwp for the fit to the data was 19.530.

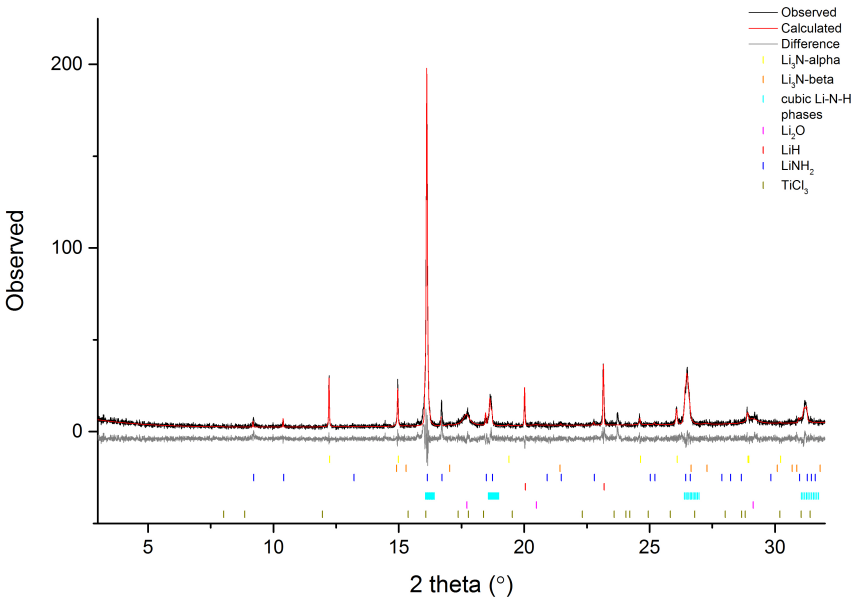

Figure C.7: X-ray powder diffraction pattern (1 minute) of the $TiCl_3$-doped Li-N-H system at the end of Process Q in Table 3.3 (doped lithium nitride starting material). Tick marks indicate the phases refined in the Rietveld analysis. The observed pattern is shown in black, the calculated pattern in red, and the difference between the two patterns is shown in grey. The Rwp for the fit to the data was 20.306.

Appendix D

Selected diffraction patterns 3: *In situ* diffraction on cycled Li-N-H system samples

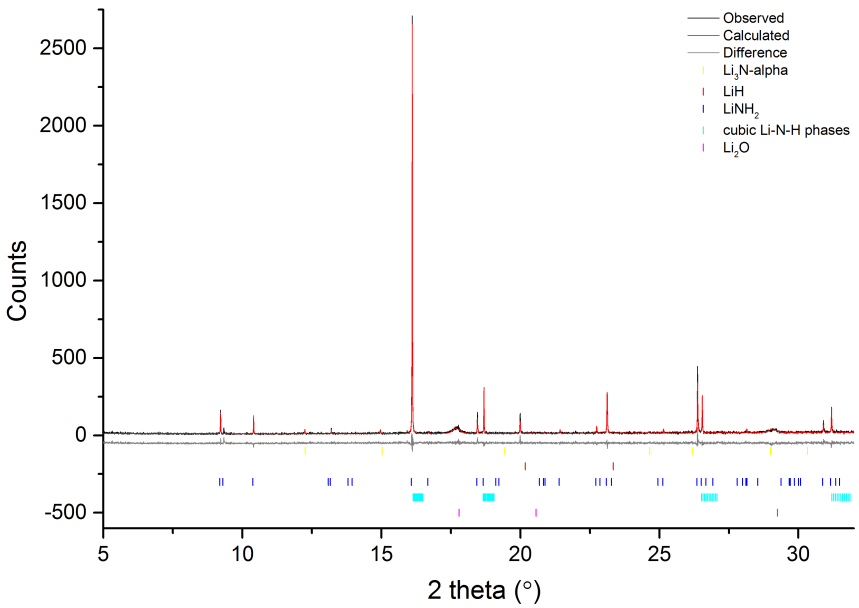

Figure D.1: Typical X-ray powder diffraction pattern (1 minute) of a hydrogen-cycled Li-N-H sample taken at Diamond at the end of the in situ hydrogenation reaction. Tick marks indicate the phases refined in the Rietveld analysis. The observed pattern is shown in black, the calculated pattern in red, and the difference between the two patterns is shown in grey. The Rwp for the fit to the data was 21.746.

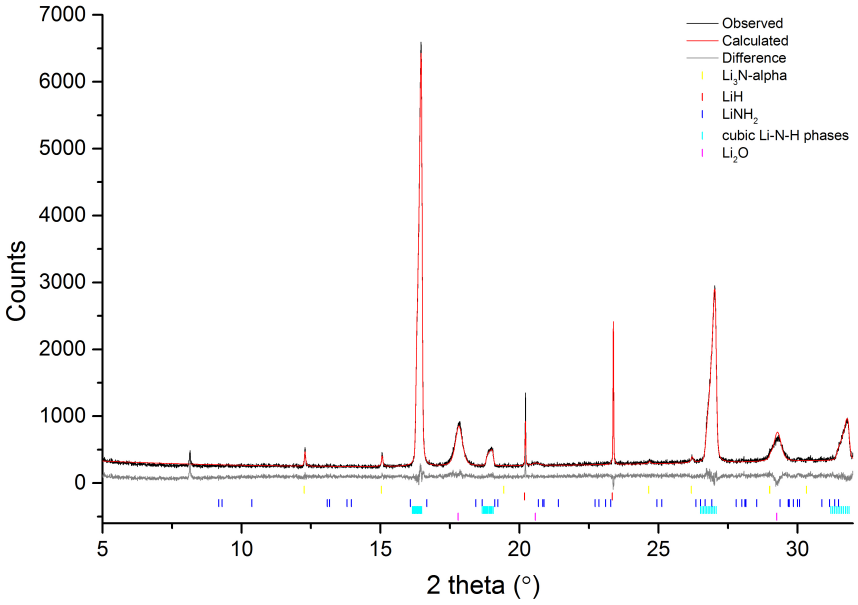

Figure D.2: Typical X-ray powder diffraction pattern (20 minutes) of a hydrogen-cycled Li-N-H sample taken at Diamond at the end of the in situ dehydrogenation reaction. Tick marks indicate the phases refined in the Rietveld analysis. The observed pattern is shown in black, the calculated pattern in red, and the difference between the two patterns is shown in grey. The Rwp for the fit to the data was 7.342.

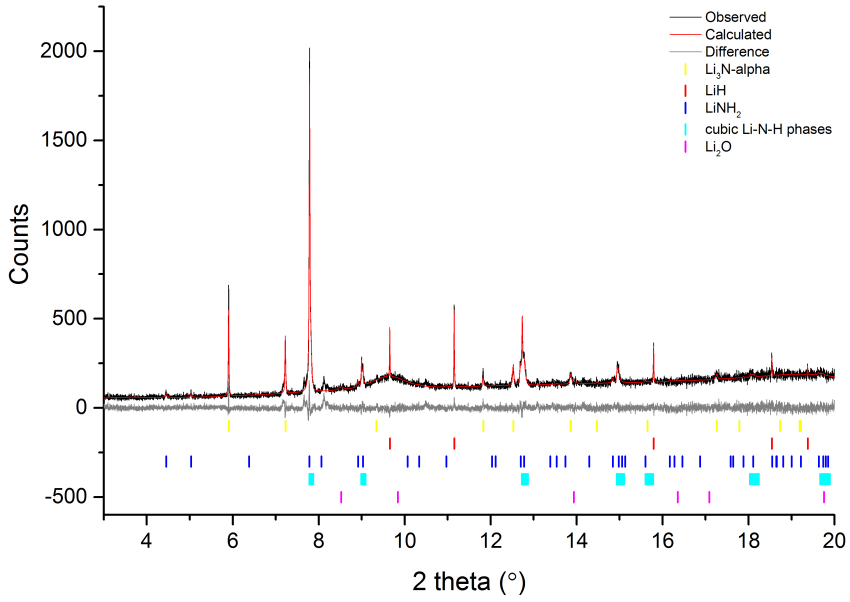

Figure D.3: X-ray powder diffraction pattern (3 minutes) of the 100ppm nitrogen-in-hydrogen-cycled Li-N-H sample taken at the ESRF at the end of the in situ hydrogenation reaction of the 5th hydrogenation-dehydrogenation cycle. Tick marks indicate the phases refined in the Rietveld analysis. The observed pattern is shown in black, the calculated pattern in red, and the difference between the two patterns is shown in grey. The Rwp for the fit to the data was 9.224.

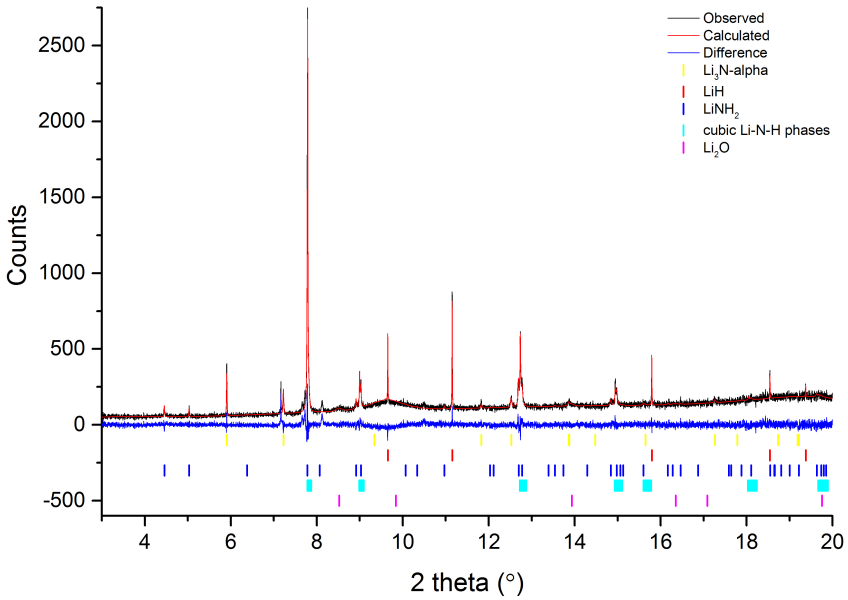

Figure D.4: X-ray powder diffraction pattern (3 minutes) of the 100ppm nitrogen-in-hydrogen-cycled Li-N-H sample taken at the ESRF at the end of the in situ hydrogenation reaction of the 33rd hydrogenation-dehydrogenation cycle. Tick marks indicate the phases refined in the Rietveld analysis. The observed pattern is shown in black, the calculated pattern in red, and the difference between the two patterns is shown in grey. The Rwp for the fit to the data was 10.394.

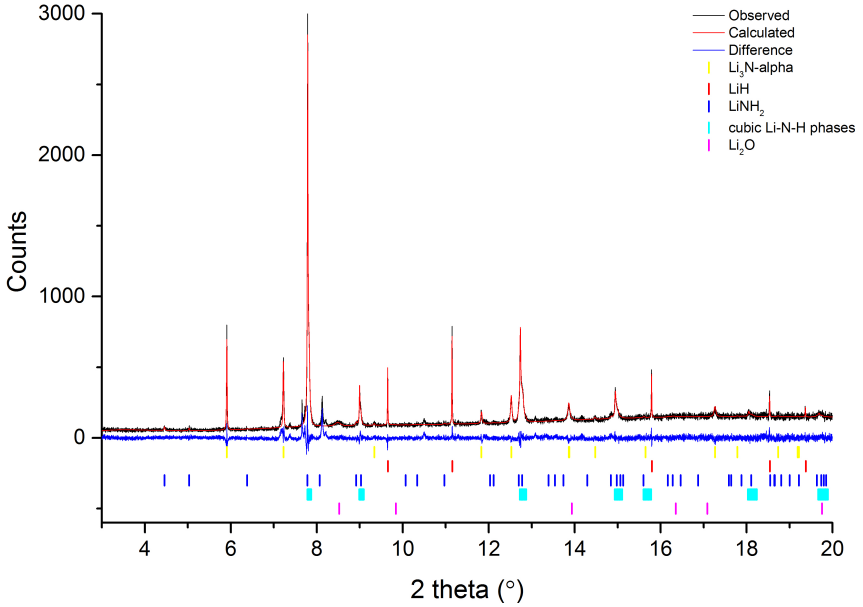

Figure D.5: X-ray powder diffraction pattern (3 minutes) of the 20% nitrogen-in-hydrogen-cycled Li-N-H sample taken at the ESRF at the end of the in situ hydrogenation reaction of the 5th hydrogenation-dehydrogenation cycle. Tick marks indicate the phases refined in the Rietveld analysis. The observed pattern is shown in black, the calculated pattern in red, and the difference between the two patterns is shown in grey. The Rwp for the fit to the data was 11.102.

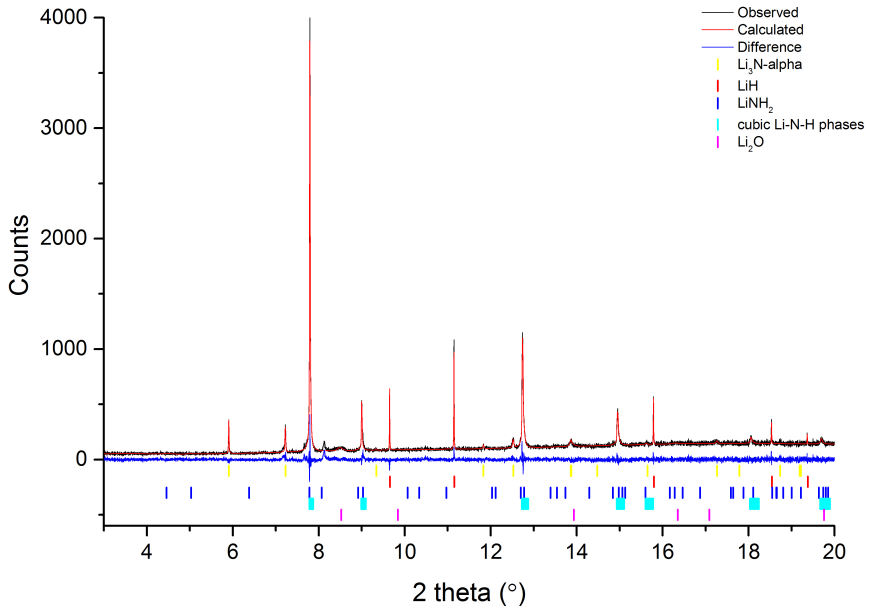

Figure D.6: X-ray powder diffraction pattern (3 minutes) of the 20% nitrogen-in-hydrogen-cycled Li-N-H sample taken at the ESRF at the end of the in situ hydrogenation reaction of the 25th hydrogenation-dehydrogenation cycle. Tick marks indicate the phases refined in the Rietveld analysis. The observed pattern is shown in black, the calculated pattern in red, and the difference between the two patterns is shown in grey. The Rwp for the fit to the data was 9.967.

Appendix E

Lithium hydride pressure response

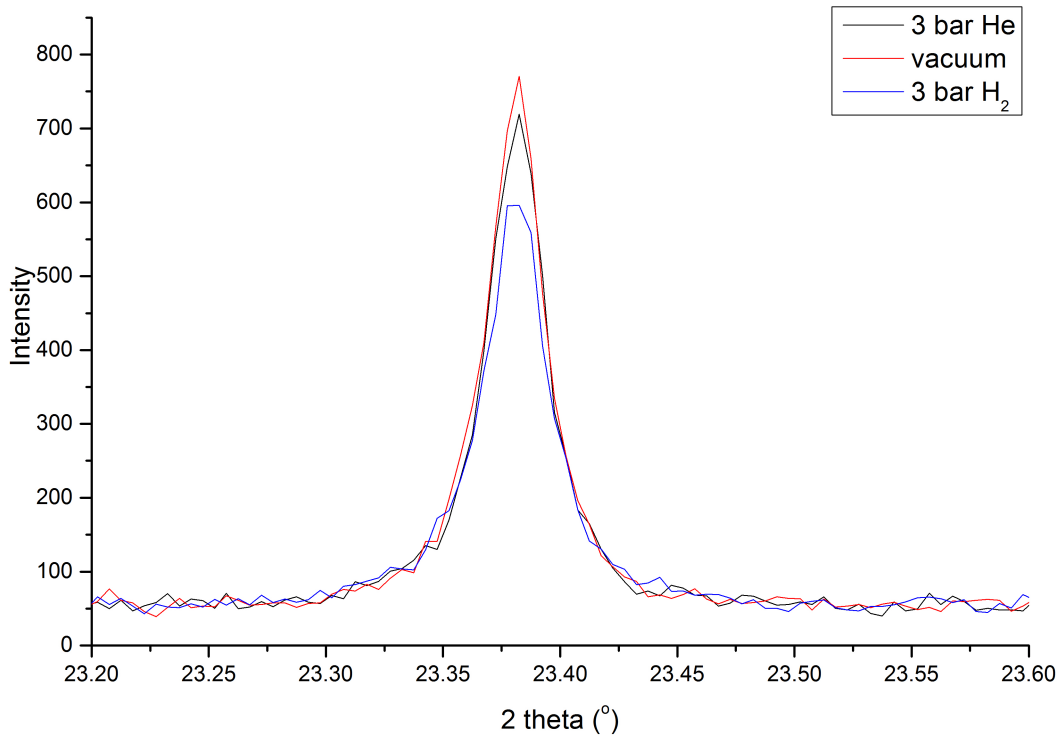

Figure E.1: PXRD data showing the lithium hydride (002) under 3 bar of helium (black), dynamic vaccum (red), and 3 bar of hydrogen gas (blue).

Appendix F

Li-N-H Arrhenius plots

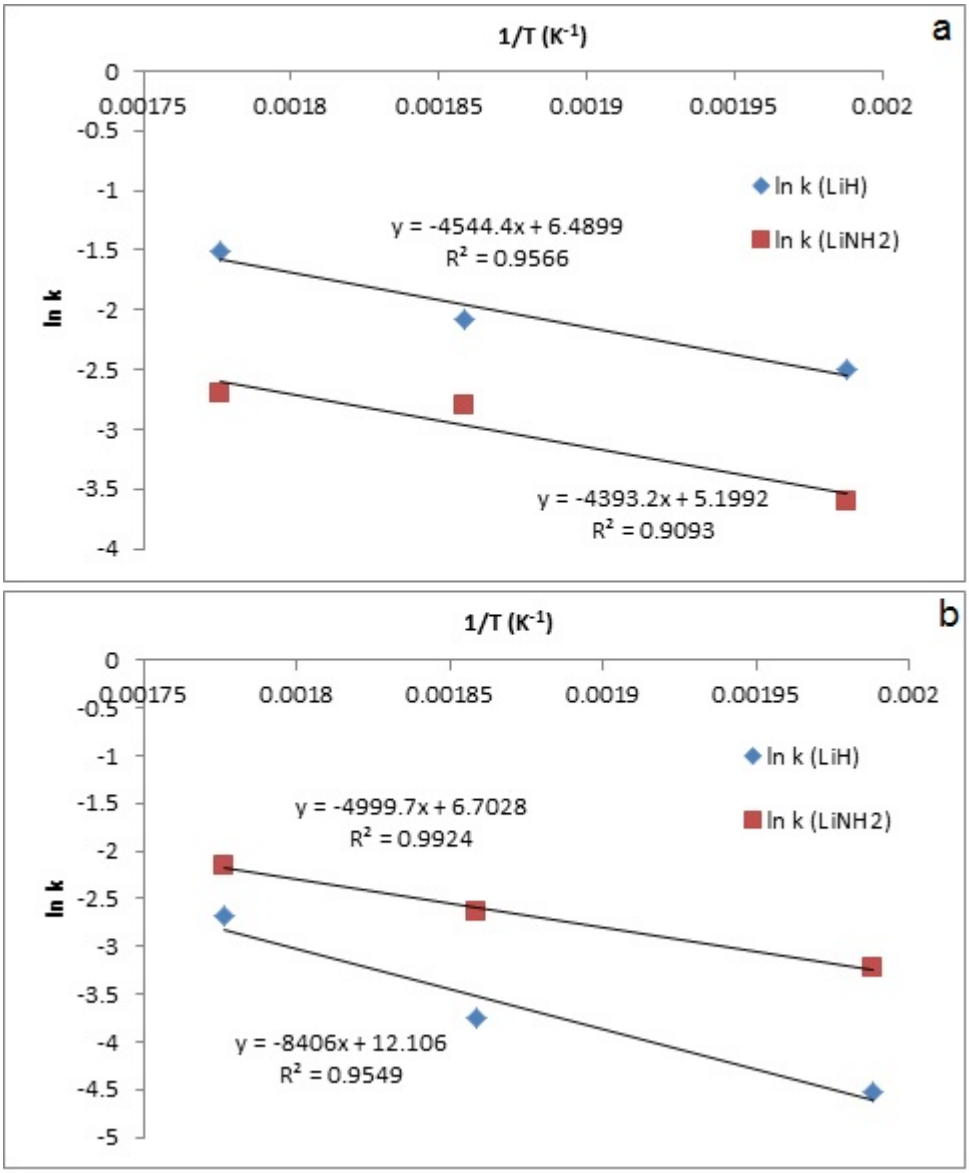

Figure F.1: Arrhenius plots for the extracted rate constant value (k) against the temperature (T) for a) the hydrogenation reactions (processes C, E and G) and b) dehydrogenation reactions (average of processes B and D, process F and average of processes H and J). The slope of each line is $-Ea/R$, where Ea is the activation energy, and R is the Universal Gas Constant.

Appendix G

PXRD Pattern of $TiCl_3(NH_3)_3$

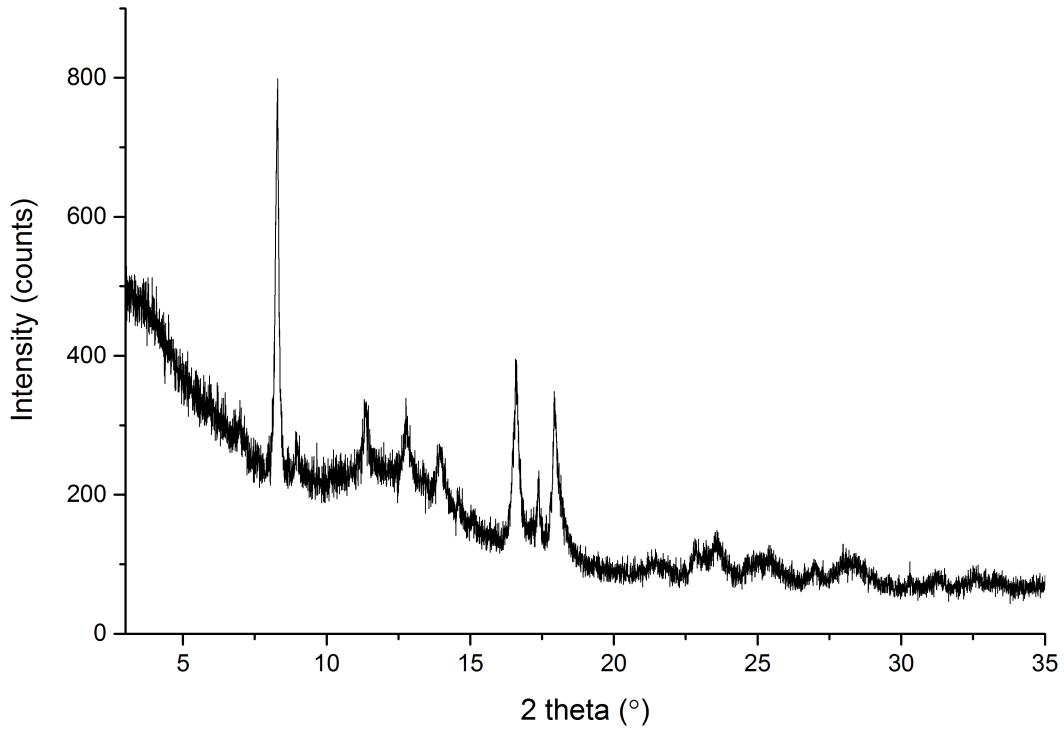

Figure G.1: PXRD pattern of triammoniate of titanium (III) chloride, coollected on I11 at Diamond.

Appendix H

Selected diffraction patterns 4: *In situ* neutron powder diffraction on LiD/NaD + ND_3 samples

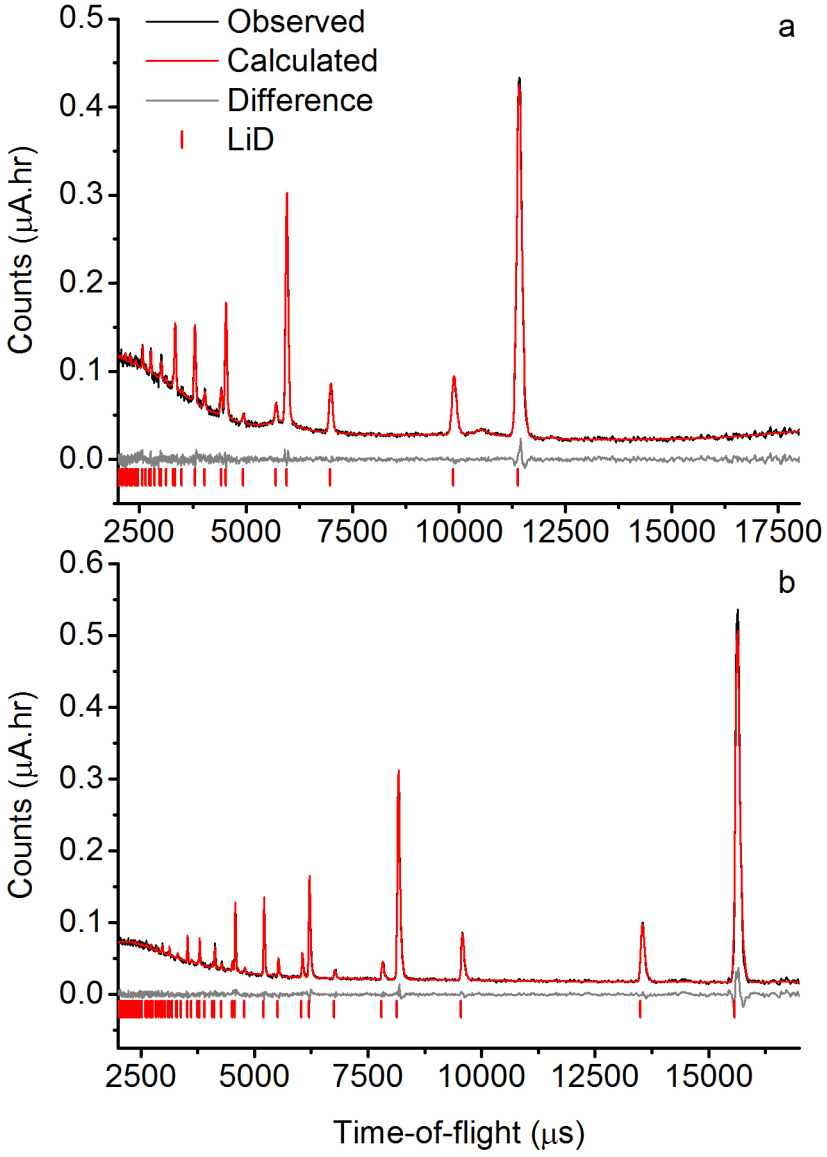

Figure H.1: Neutron powder diffraction patterns (3 minutes) of the initial lithium deuteride sample taken at the ISIS Facility, showing data from detector banks a) four and b) five of the GEM instrument. Tick marks indicate the peak positions of phases refined in the Rietveld analysis. The observed pattern is shown in black, the calculated pattern in red, and the difference between the two patterns is shown in grey. The Rwp for the combined fit to the data was 4.315.

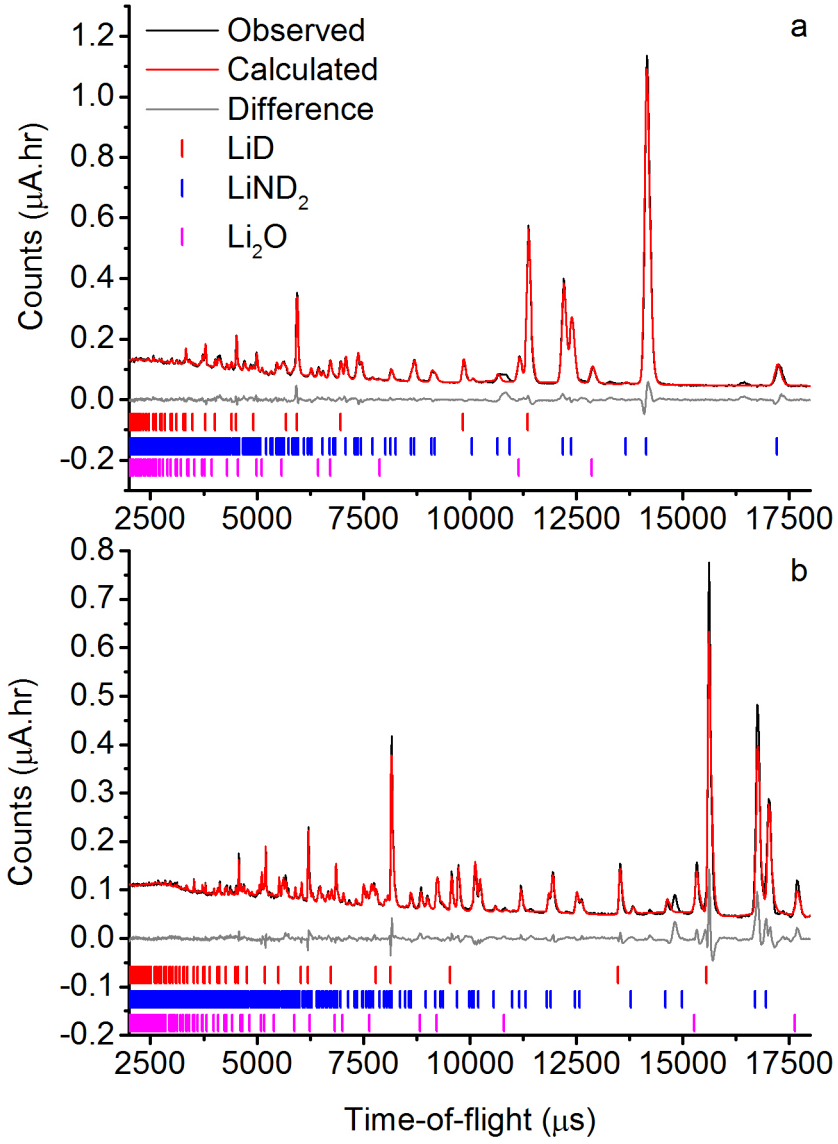

Figure H.2: Neutron powder diffraction patterns (3 minutes) of the lithium deuteride sample at the end of the ammoniation reaction, taken at the ISIS Facility, showing data from detector banks a) four and b) five of the GEM instrument. Tick marks indicate the peak positions of phases refined in the Rietveld analysis. The observed pattern is shown in black, the calculated pattern in red, and the difference between the two patterns is shown in grey. The Rwp for the combined fit to the data was 4.564.

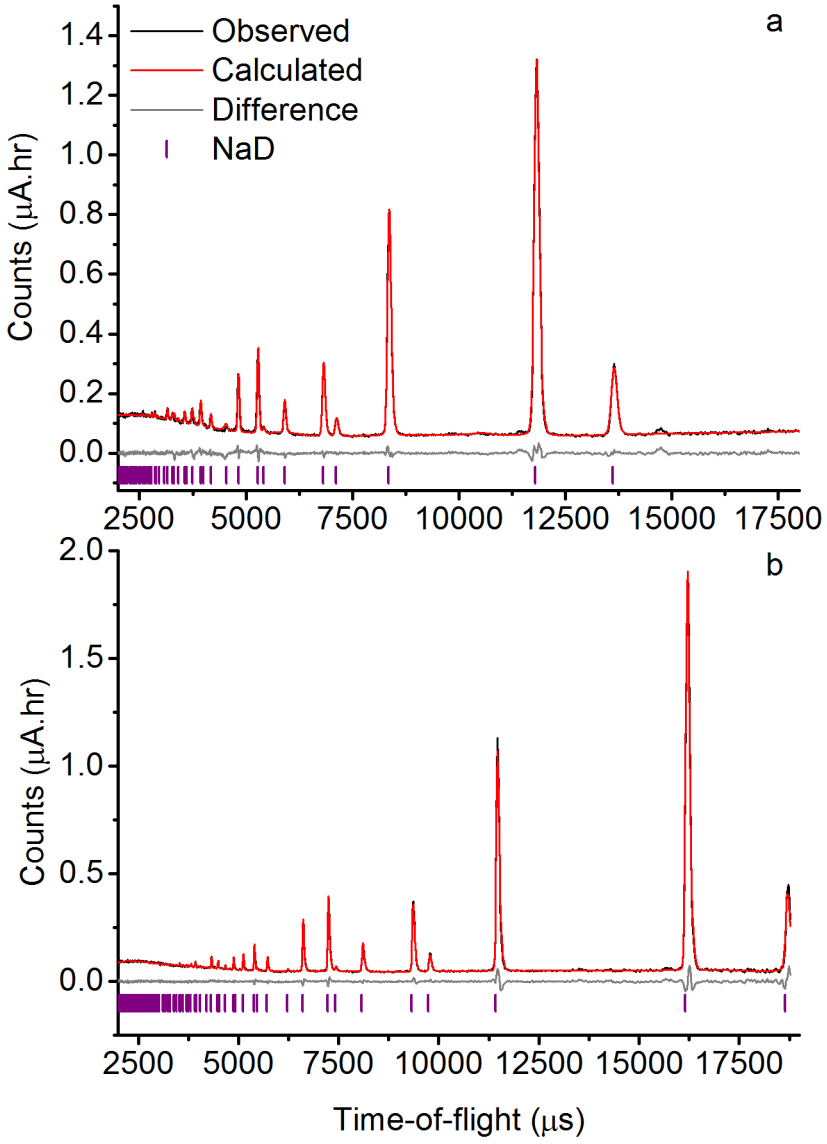

Figure H.3: Neutron powder diffraction patterns (3 minutes) of the initial sodium deuteride sample taken at the ISIS Facility, showing data from detector banks a) four and b) five of the GEM instrument. Tick marks indicate the peak positions of phases refined in the Rietveld analysis. The observed pattern is shown in black, the calculated pattern in red, and the difference between the two patterns is shown in grey. The Rwp for the combined fit to the data was 4.535.

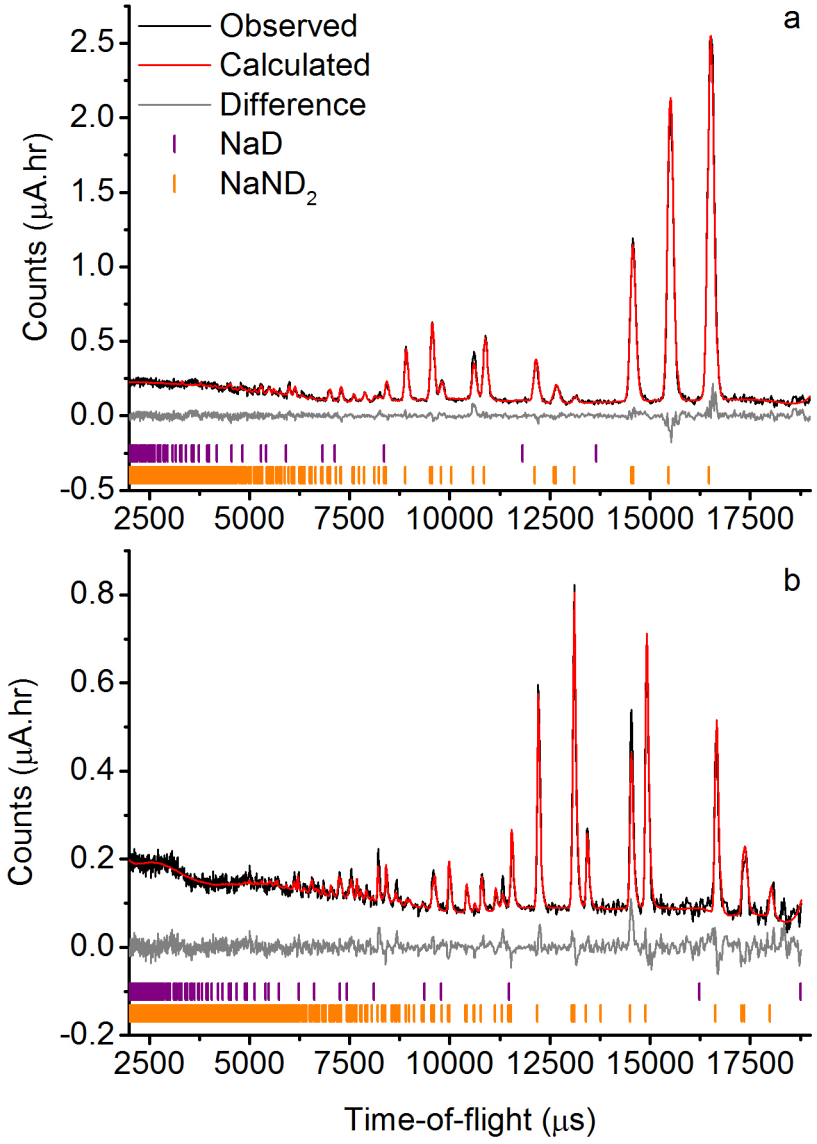

Figure H.4: Neutron powder diffraction patterns (3 minutes) of the sodium deuteride sample at the end of the ammoniation reaction, taken at the ISIS Facility, showing data from detector banks a) four and b) five of the GEM instrument. Tick marks indicate the peak positions of phases refined in the Rietveld analysis. The observed pattern is shown in black, the calculated pattern in red, and the difference between the two patterns is shown in grey. The Rwp for the combined fit to the data was 7.631.

Appendix I

Selected diffraction patterns 5: Neutron powder diffraction heating study on $NaND_2$

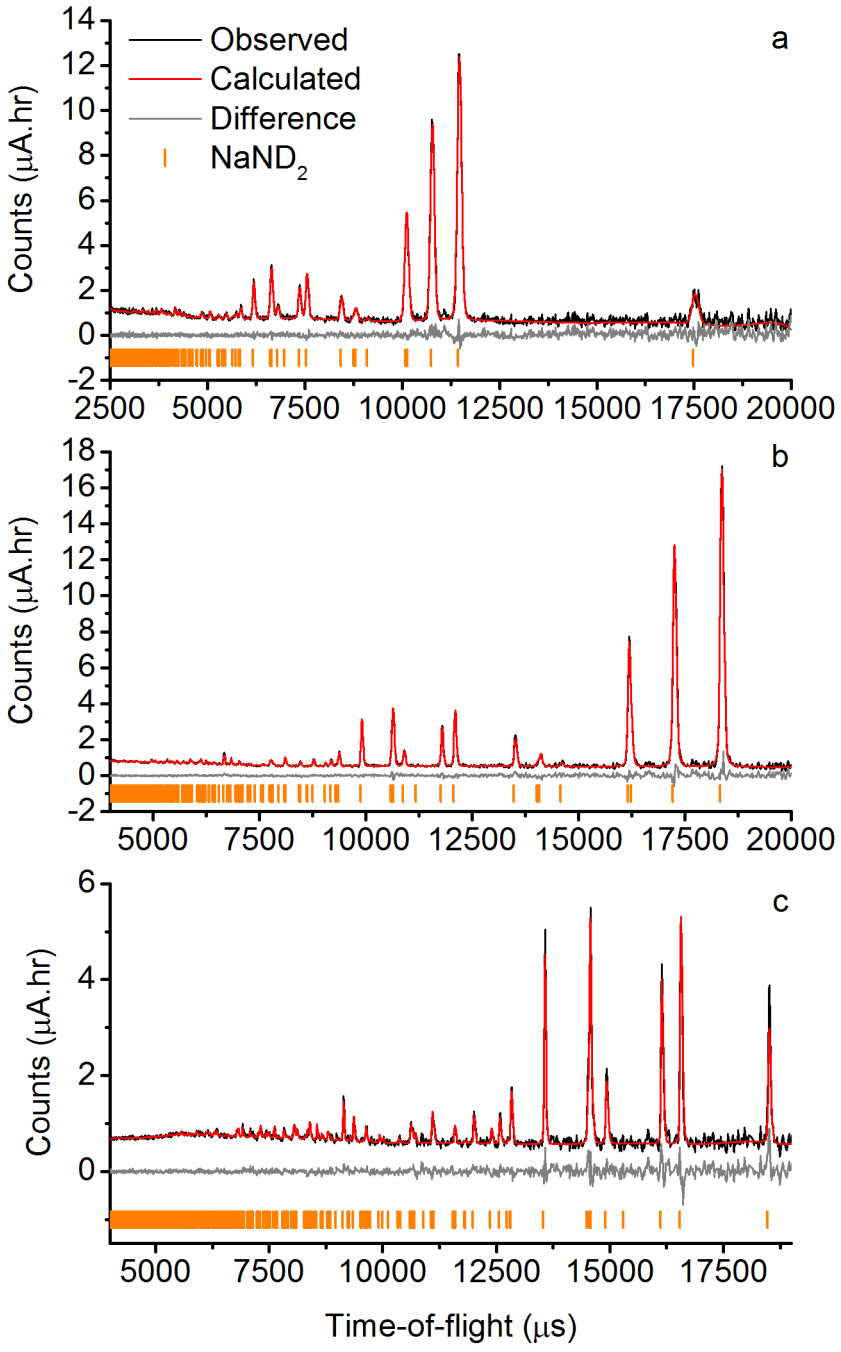

Figure I.1: Neutron powder diffraction patterns (3 minutes) of the sodium amide sample at 50 °C, taken at the ISIS Facility, showing data from detector banks a) three b) four and c) five of the POLARIS instrument. Tick marks indicate the peak positions of phases refined in the Rietveld analysis. The observed pattern is shown in black, the calculated pattern in red, and the difference between the two patterns is shown in grey. The Rwp for the combined fit to the data was 5.038.

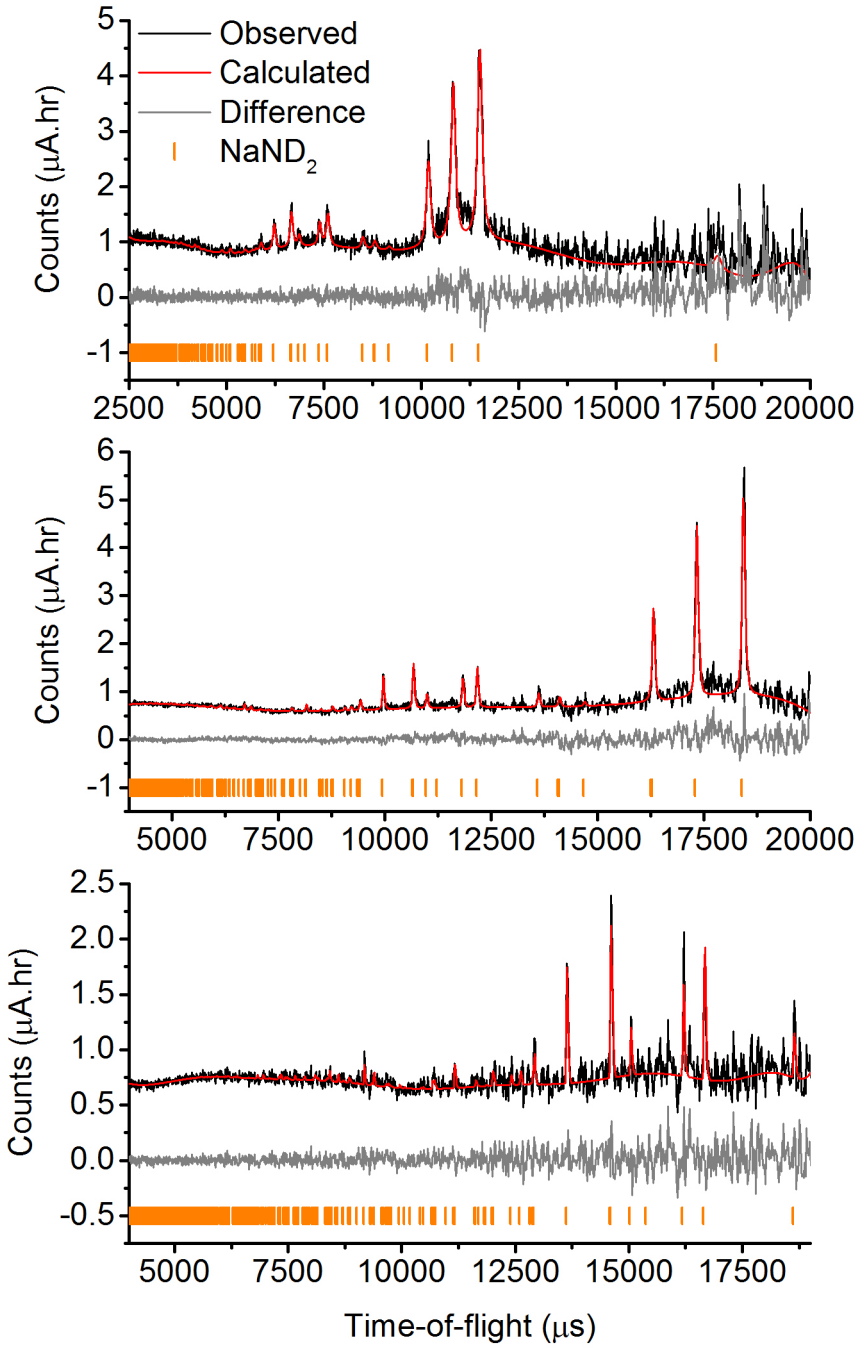

Figure I.2: Neutron powder diffraction patterns (3 minutes) of the sodium amide sample at 200 °C, taken at the ISIS Facility, showing data from detector banks a) three b) four and c) five of the POLARIS instrument. Tick marks indicate the peak positions of phases refined in the Rietveld analysis. The observed pattern is shown in black, the calculated pattern in red, and the difference between the two patterns is shown in grey. The Rwp for the combined fit to the data was 5.897.

Appendix J

Selected diffraction patterns 6: *In situ* neutron powder diffraction on Li_2ND ammonia decomposition catalyst

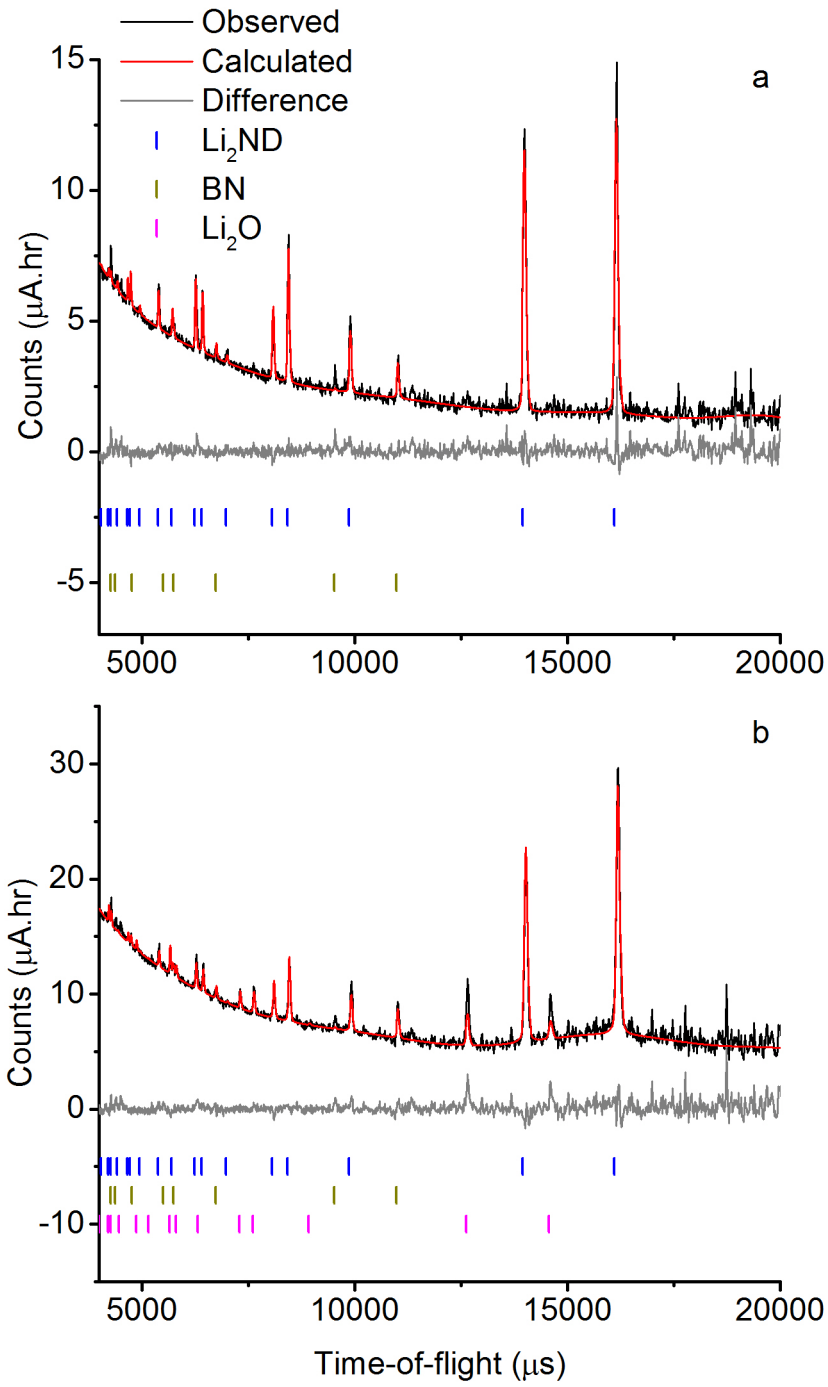

Figure J.1: Neutron powder diffraction patterns of the lithium imide sample taken at the ISIS Facility, showing data from detector bank four of the POLARIS instrument. Data shown are regions a) i and b) ii from Figure 5.14. Tick marks indicate the peak positions of phases refined in the Rietveld analysis. The observed pattern is shown in black, the calculated pattern in red, and the difference between the two patterns is shown in grey. The Rwp value for the fits to the data were 3.835 and 3.124, respectively.

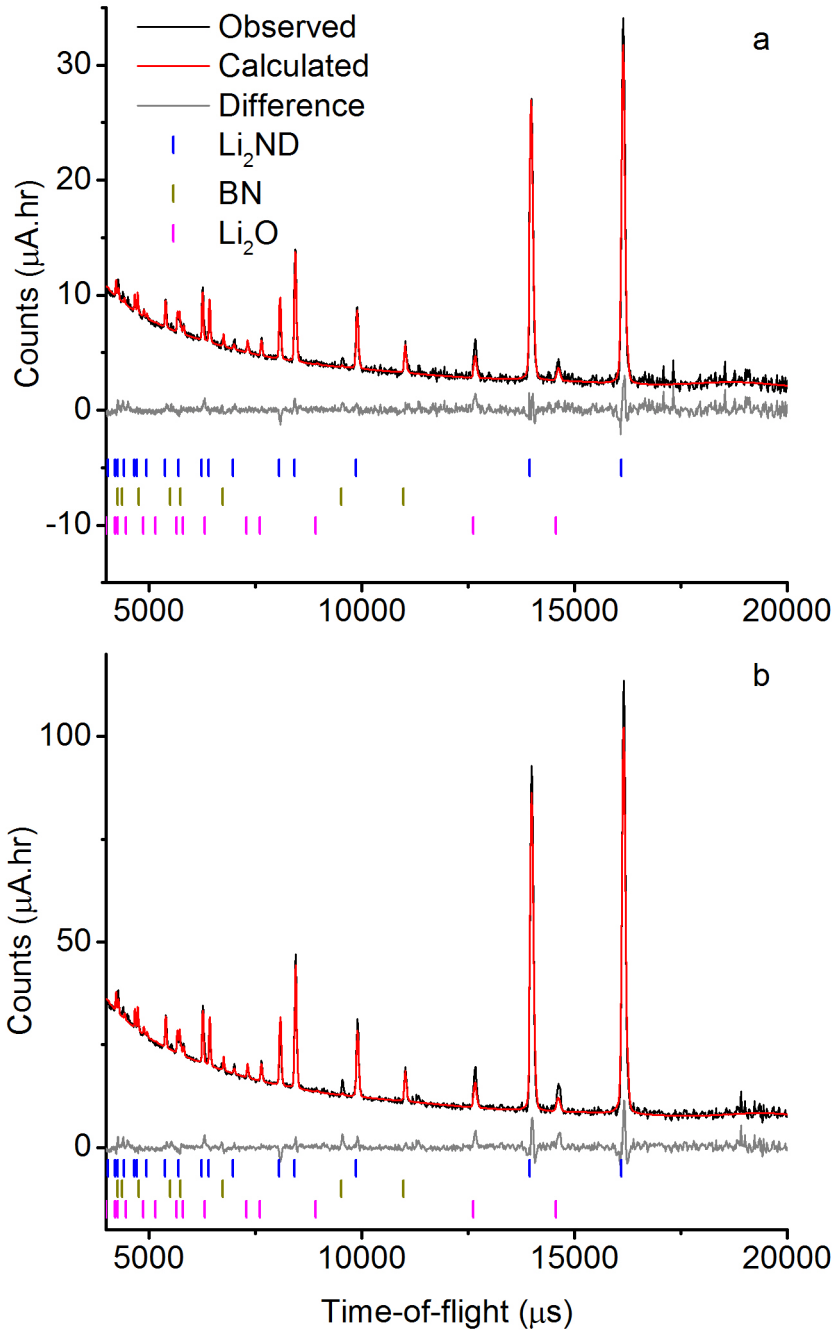

Figure J.2: Neutron powder diffraction patterns of the lithium imide sample taken at the ISIS Facility, showing data from detector bank four of the POLARIS instrument. Data shown are regions a) iii and b) iv from Figure 5.14. Tick marks indicate the peak positions of phases refined in the Rietveld analysis. The observed pattern is shown in black, the calculated pattern in red, and the difference between the two patterns is shown in grey. The Rwp value for the fits to the data were 3.482 and 3.237, respectively.

Appendix K

Ammonia decomposition in blank POLARIS cell

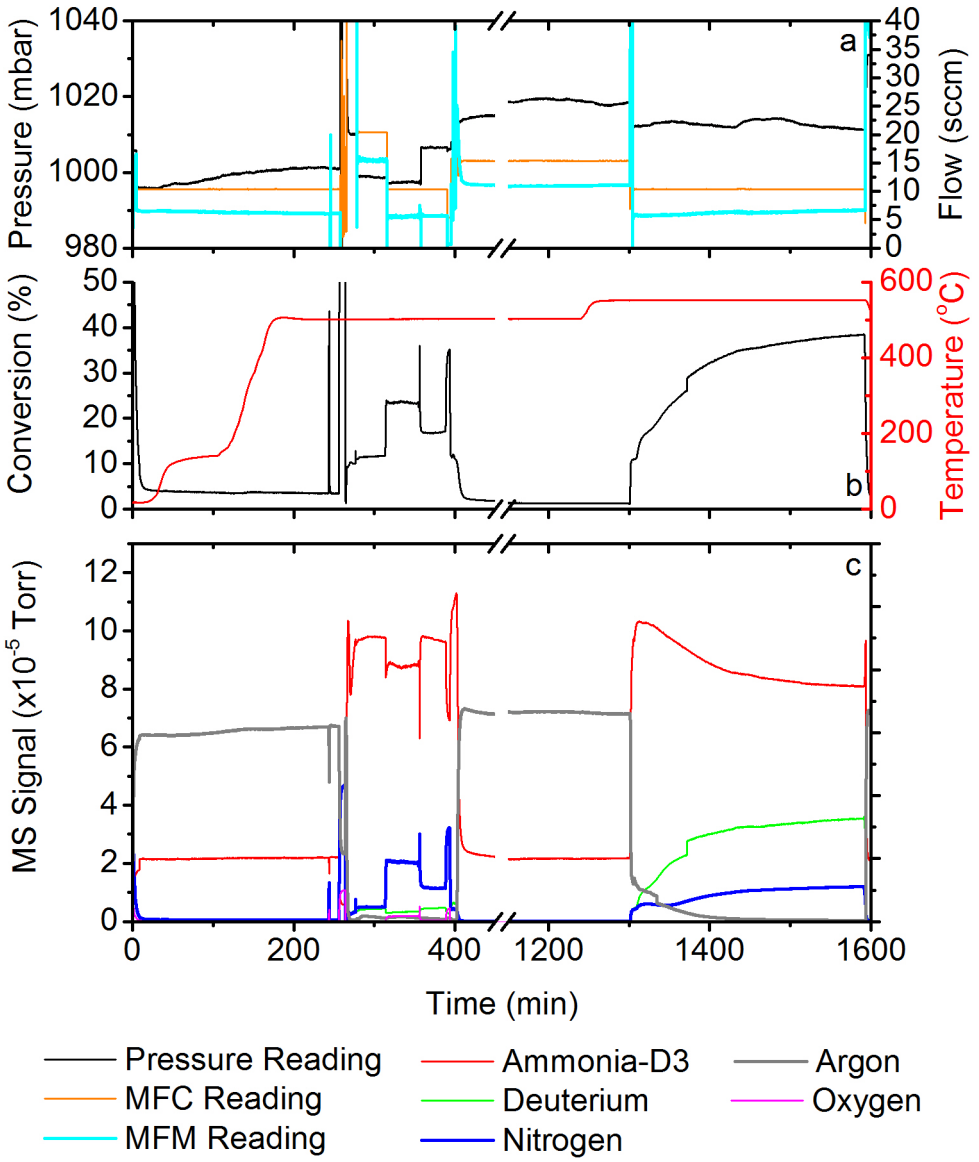

Figure K.1: The results of the ammonia decomposition reaction using the blank POLARIS flow through sample cell, showing a) pressure and flow data, b) the temperature of the cell and ammonia conversion percentage and c) the QGA data for the selected m/z values.

Appendix L

Publications arising from this work

1. Makepeace JW, Jones MO, Callear SK, Edwards PP and David WIF, 'In situ X-ray powder diffraction studies of hydrogen storage and release in the Li-N-H system' Physical Chemistry Chemical Physics (2014) 16(9), 4061-4070

2. David WIF, Makepeace JW, Callear SK, Hunter HMA, Taylor JD, Wood TJ and Jones MO, 'Hydrogen production from ammonia using sodium amide' Journal of the American Chemical Society (2014) 136 (38), 13082–13085